

Lecture Notes in Production Engineering

Berend Denkena · Adrian Rienäcker
Gunter Knoll · Friedrich-Wilhelm Bach
Hans Jürgen Maier · Eduard Reithmeier
Friedrich Dinkelacker *Editors*

Microstructuring of Thermo- Mechanically Highly Stressed Surfaces

Final Report of the DFG Research Group
576

 Springer

Lecture Notes in Production Engineering

More information about this series at <http://www.springer.com/series/10642>

Berend Denkena • Adrian Rienäcker • Gunter Knoll
Friedrich-Wilhelm Bach • Hans Jürgen Maier
Eduard Reithmeier • Friedrich Dinkelacker
Editors

Microstructuring of Thermo-Mechanically Highly Stressed Surfaces

Final Report of the DFG Research Group 576

 Springer

Editors

Berend Denkena
Leibniz Universität Hannover
Institut für Fertigungstechnik und
Werkzeugmaschinen IFW
Garbsen, Germany

Friedrich-Wilhelm Bach
Hans Jürgen Maier
Institut für Werkstoffkunde IW
Leibniz Universität Hannover
Garbsen, Germany

Friedrich Dinkelacker
Institut für Technische Verbrennung ITV
Leibniz Universität Hannover
Hannover, Germany

Adrian Rienäcker
Gunter Knoll
Lehrstuhl für Maschinenelemente und
Tribologie IMK
Universität Kassel
Kassel, Germany

Eduard Reithmeier
Institut für Mess- und
Regelungstechnik IMR
Leibniz Universität Hannover
Hannover, Germany

ISSN 2194-0525

ISBN 978-3-319-09691-9

DOI 10.1007/978-3-319-09692-6

Springer Cham Heidelberg New York Dordrecht London

ISSN 2194-0533 (electronic)

ISBN 978-3-319-09692-6 (eBook)

Library of Congress Control Number: 2014949153

© Springer International Publishing Switzerland 2015

This work is subject to copyright. All rights are reserved by the Publisher, whether the whole or part of the material is concerned, specifically the rights of translation, reprinting, reuse of illustrations, recitation, broadcasting, reproduction on microfilms or in any other physical way, and transmission or information storage and retrieval, electronic adaptation, computer software, or by similar or dissimilar methodology now known or hereafter developed. Exempted from this legal reservation are brief excerpts in connection with reviews or scholarly analysis or material supplied specifically for the purpose of being entered and executed on a computer system, for exclusive use by the purchaser of the work. Duplication of this publication or parts thereof is permitted only under the provisions of the Copyright Law of the Publisher's location, in its current version, and permission for use must always be obtained from Springer. Permissions for use may be obtained through RightsLink at the Copyright Clearance Center. Violations are liable to prosecution under the respective Copyright Law.

The use of general descriptive names, registered names, trademarks, service marks, etc. in this publication does not imply, even in the absence of a specific statement, that such names are exempt from the relevant protective laws and regulations and therefore free for general use.

While the advice and information in this book are believed to be true and accurate at the date of publication, neither the authors nor the editors nor the publisher can accept any legal responsibility for any errors or omissions that may be made. The publisher makes no warranty, express or implied, with respect to the material contained herein.

Printed on acid-free paper

Springer is part of Springer Science+Business Media (www.springer.com)

Preamble

The fuel consumption of a modern combustion engine is one of the most important purchase criteria in contemporary society. Increasing oil prices and exhaust emissions taxes force the automotive industry to continuously improve the vehicle engines. The fuel consumption is closely related to the frictional losses of an engine. New material pairings or constructive modifications of the piston group can reduce such losses. Another innovative concept to lower the frictional forces is the microstructuring of thermo-mechanically highly stressed surfaces. Within an interdisciplinary research group sponsored by the German Research Foundation, scientists at the Leibniz Universität Hannover and Universität Kassel have been working together to investigate this research topic. This final report presents their findings and offers scope for further discussion.

On behalf of the DFG research group 576,

Hannover, 1st of October, 2013

B. Denkena

(spokesman of the DFG research group 576)

Acknowledgement

The presented investigations were undertaken with the support of the German Research Foundation within the scope of the “Microstructuring of Thermo-Mechanically Highly Stressed Surfaces” research group (DFG Research Group 576).

Contents

Formula symbols and abbreviations	IX
1 Introduction.....	1
2 Project overview	2
2.1 Consortium.....	2
2.2 Starting situation and need for action.....	4
2.3 Summary of main results	7
3 Methods and models for the design of microstructures	9
- <i>G. Knoll, A. Rienäcker, S. Brandt, H. Fast</i>	
3.1 Objective and approach	9
3.2 Comparison between Computational Fluid Dynamics and the Reynolds equation	9
3.3 Investigation of dimple geometry and arrangement	11
3.4 Simulation model for piston ring friction coefficient test rig.....	18
3.5 Design and validation of a test engine simulation model	20
3.6 Conclusion	27
4 Microstructuring by means of cutting processes.....	28
- <i>B. Denkena, J. Kästner, T. Göttching</i>	
4.1 Objective and approach	28
4.2 Experimental set-up – fly-cutting tests	29
4.3 High-quality cutting of micro-dimples	33
4.4 Inner structuring of rotationally symmetrical components	46
4.5 Conclusion	56
5 Microstructured thermally sprayed surfaces	58
- <i>Fr.-W. Bach, K. Möhwald, M. Erne, C. Hübsch, H. J. Maier</i>	
5.1 Objective	58
5.2 Experimental	58
5.3 Outer coating of rotationally symmetric components	60
5.4 Inner coating of rotationally symmetric components	74
5.5 Tribological testing of the inner coating of cylinder liners	89
5.6 Conclusion	91

6	Surface characterisation based on optical metrology.....	93
	<i>- E. Reithmeier, M. Kästner, M. Bretschneider, O. Abo-Namous, F. Engelke</i>	
6.1	Objective and approach.....	93
6.2	Measurement techniques	94
6.3	Measurement of machined micro-dimples.....	97
6.4	Measurement of thermal sprayed surfaces.....	109
6.5	Multi-measurement methods	111
6.6	Conclusion.....	116
7	Tribological mechanisms of microstructures	119
7.1	Tribological mechanisms of machined micro-dimples under planar contact conditions	119
	<i>- B. Denkena, J. Kästner, T. Götsching</i>	
7.2	Tribological mechanisms of microstructured thermally sprayed surfaces ...	129
	<i>- Fr.-W. Bach, K. Möhwald, M. Erne, C. Hübsch, H. J. Maier</i>	
7.3	Tribological mechanisms of microstructured surfaces under dragged conditions	141
	<i>- G. Knoll, A. Rienäcker, S. Brandt, H. Fast</i>	
8	Test of cylinder liner under fired engine conditions	146
	<i>- F. Dinkelacker, H. Ulmer</i>	
8.1	Objective and approach.....	146
8.2	Engine test bench and cylinder liners	146
8.3	Methods to measure friction losses and oil emissions	149
8.4	Measurement uncertainty	150
8.5	Validation of the measuring method	151
8.6	Results: frictional losses	154
8.7	Results: oil emission.....	162
8.8	Conclusion.....	164
9	Own publications.....	167
10	Quoted literature	170

Formula symbols and abbreviations

Formula Symbols

Sign	Unit	Description
Δa_p	μm	depth of cut deviation
A	μm^2	cross section projection area
A_c	mm^2	cross-section of undeformed chip
A_E	μm^2	longitudinal section projection area
A_{MT}	mm^2	micro-dimple area
A_p	μm^2	plane projection area
a_p	μm	depth of cut
$a_{p,fit}$	μm	cut depth by circular fit
$A_{p,hist}$	-	threshold dimple depth
$a_{p,max}$	μm	maximum depth of cut
$A_{tot.}$	mm^2	total surface area
A_V	1	area of all pores divided by measured area
A_{WZ}	Mm^2	cross section tool
b	μm	length of cross section / micro-dimple width
b	mm	bore
$b_{a,d,(hist)}$	μm	width of ridges on side d(left, right) (histogram based)
b_{WZ}	mm	cutting tool width
D	mm	component diameter
D	-	damping matrix
$d(x,y)$	μm	Euclidian metric
D_{MT}	-	number of dimples for a rectangular elemental surface
f_0	Hz	natural frequency
$F_{a,tool}$	mm	axial feed rate
f_{ab}	-	relative cut volume
$F_{accurate,interp}$	μm	polynomial surface fit of $M_{2,interp}$
$F_{accurate,zero}$	μm	polynomial surface fit of $M_{2,zero}$
f_{ax}	mm	axial feed rate

F_{basic}	μm	basic polynomial surface fit
F_{c}	N	cutting force
f_{err}	Hz	excitation frequency
F_{i}	N	outer forces
F_{n}	N	normal force
F_{p}	N	passive force
F_{r}	N	friction force
G_{u}	-	upsetting rate
G_{s}	-	stretching rate
$h_{\text{a,l,hist}}$	μm	height of ridges on side d(left, right) (histogram based)
\bar{h}	μm	gap
K	-	stiffness matrix
k_{c}	N/mm^2	specific cutting force
k_{p}	N/mm^2	specific passive force
l_{E}	μm	length of cut by circular fit
l_{g}	mm	contact length
l_{s}	μm	length of longitudinal section / micro-dimple length
M	μm	measured surface data
m	g	mass
M	-	mass matrix
M_1	μm	basic form correction of surface M
$M_{2,\text{interp}}$	μm	M_1 with interpolated structure regions
$M_{2,\text{zero}}$	μm	M_1 with zeroed structure regions
$M_{3,\text{interp}}$	μm	form correction of $M_{2,\text{interp}}$
$M_{3,\text{zero}}$	μm	form correction of $M_{2,\text{zero}}$
$M_{4,\text{interp}}$	μm	final correction of surface M by interpolated structures
$M_{4,\text{zero}}$	μm	final correction of surface M by zeroed structures
M_{Fr}	Nm	friction torque
n	1/min	revolutions per minute
n_{comp}	min^{-1}	component revolution speed
n_{max}	min^{-1}	maximum revolution speed

n_{tool}	min^{-1}	tool revolution speed
p	Pa	pressure
p_{atm}	bar	atmospheric pressure
p_{cyl}	bar	cylinder pressure
p_{max}	bar	maximum cylinder pressure
p_n	bar	indicated pressure
$p_{\text{structure}}$	μm	height data of the bounding box of one micro cut
\bar{p}	Pa	average pressure in the lubricant film
R_a	μm	arithmetical deviation of the roughness profile
$R_{a,l}$	μm	mean longitudinal roughness
$R_{a,q}$	μm	mean cross roughness
r_i	mm	component inner diameter
R_{max}	μm	maximum roughness depth
R_{NaN}	-	R_{zero} (1 replaced by NaN)
R_{ridge}	-	ridge mask
r_{rot}	mm	rotational diameter
$R_{\text{structures}}$	-	structure mask
r_{tool}	mm	tool radius
r_{WZ}	mm	tool radius
R_z	μm	average surface roughness
R_{zero}	-	structure mask, calculated for M_1
r_β	μm	cutting edge radius
r_ϵ	μm	edge radius
s	mm	stroke
s_{ax}	mm	axial micro-dimple distance
S_{MT}	%	micro-dimple ratio
spf_X	-	quotient of parameter X for structure and tool
s_{rad}	mm	radial micro-dimple distance
s_{tan}	mm	tangential micro-dimple distance
$s_{v,\text{dyn}}$	μm	dynamic tool displacement
$s_{v,\text{min}}$	μm	minimum tool displacement

\vec{s}_c	μm	cross section
\vec{s}_i	μm	longitudinal section
\vec{s}_{tool}	μm	longitudinal section of cutting tool
t	s	cutting time
T_e	Nm	torque at the engines output
t_{ridge}	μm	threshold value for ridge identification
$t_{\text{structure}}$	μm	threshold value for micro cut identification
t_{tan}	°	tangential indexing
U_{BT}	mm	component's circumference
u_i	m/s	surface velocity
V	μm^3	structure volume
v	m/s	sliding speed
V_{burr}	μm^3	modelled burr volume
v_c	m/min	cutting speed
v_{comp}	m/min	component speed
V_G	μm^3	burr volume
V_H	cm ³	displacement
V_{MT}	μm^3	micro-dimple volume
v_{tool}	m/min	tool speed
V_v	%	pore volume percentage
$V_{v,\text{sp}}$	-	specific volume
w	μm	width of machined microstructures
x	Mm	Global deformation
x_i	mm	(film) coordinates
$x_{\text{scale}}, y_{\text{scale}}$	μm	resolution along x-/y-axis
$xy_{\text{scale}}(\phi)$	μm	mean resolution along an axis with angle ϕ to the x-axis

Symbols

Sign	Unit	Description
γ	°	angle of cut
ϕ	°	polar coordinate

$\Delta\mu$	-	friction coefficient deviation
σ	-	standard deviation
φ	°	alignment angle
φ_{tan}	°	parallel offset between two micro-dimples
2Θ	°	diffraction angle
α	°	clearance angle
α_{crit}	°	critical clearance angle
α_{eff}	°	effective clearance angle
ε	°	edge angle
ϕ	°	shear angle
γ	°	rake angle
γ_{eff}	°	effective rake angle
κ	°	flank angle
κ_{eff}	°	effective tool cutting edge angle
λ	-	chip compression ratio
λ_{limit}	-	revolution ratio limit
λ_n	-	revolution ratio
λ_s	°	tool cutting edge inclination
λ_v	-	speed ratio
μ	-	friction coefficient
μ_F	-	force ratio
μ_{min}	-	minimum friction coefficient
Φ^P	-	pressure flow tensor
Φ^S	-	shear flow tensor
η	m^2s^{-1}	dynamic viscosity

Abbreviations

Sign	Description
Al_2O_3	white alumina
AlSi17Cu4Mg	hypereutectic aluminum-silicon-alloy
APS	atmospheric plasma spray

BMEP	break mean effective pressure
BSE	back scattered electron
CCD	chip white light interferometer
CO ₂	carbon dioxide
CVD	chemical vapour deposition
EPMA	electron microprobe analyzer
Fe50Mo	iron and molybdenum mixture
FeCr13	chromium-based steel
FeCr13/Mo	chromium-based steel and molybdenum mixture
FeMo	iron and molybdenum mixture
FMEP	friction mean effective pressure
GJS400	spherulitic graphite cast iron
HV	Vickers hardness
IMEP	indicated mean effective pressure
Mo/NiCrBSi	molybdenum and nickel alloy mixture
NA	numerical aperture
NLPM	normal liters per minute
RRV	rotational friction wear tests
RT	room temperature
S235JR	steel
SEM	scanning electron microscope
WLI	white light interferometer
XRD	X-ray diffraction

1 Introduction

More than 51 million vehicles with an annual total mileage of about 699 billion kilometres are registered in Germany [DES12, UMW12]. Assuming an average consumption of 7.5 l per 100 km, a reduction in fuel consumption of 1% to 3% would lead to savings of 524 to 1,573 million litres of fuel [UMW12]. Efforts to reduce fuel consumption encompass a variety of measures, from reducing the vehicle weight to increasing its power density, nominal speed and maximum mean effective pressure. Power densities of contemporary diesel and gasoline engine designs range from 30 kW/dm³ to 105 kW/dm³ for charged gasoline engines [SCH11]. However, an increase in the specific power density is accompanied by an increase in the thermo-mechanical stress of the piston group (piston, piston rings and liner): Higher blow-by losses, wear as well as entry of oil into the combustion chamber are the undesirable side effects. In this connection, the piston group is responsible for up to 50% of the total mechanical losses of an engine, in particular for higher specific loads [DEU10]. As a reaction towards these continuously increasing thermo-mechanical stresses, various approaches to tribological optimisation of surfaces have already been pursued, especially in the area of cylinder liners. In addition to specific material systems and honing methods, micro-dimples cut into a surface have been providing, for some time now, a viable alternative approach to improve friction and wear properties as well as to reduce oil consumption.

The effect and the tribological potential of such microstructures were fundamentally investigated within the interdisciplinary DFG research group 576. Based on a wide range of experiences, the primary objective was to make the tribological behaviour of thermo-mechanically highly stressed surfaces far superior to conventional surfaces by a distinct creation of microstructures. During the six-year duration of the project (2006 to 2012), scientists at the Leibniz Universität Hannover and the Universität Kassel from the disciplines of tribology, production and measurement technology worked closely together (see [Figure 1-1](#)). Their collaboration provided fundamental insights concerning the simulation-based design of stochastically and deterministically structured surfaces (subproject 1). Stochastic surface structuring was realised by porous, thermally sprayed coatings, whereas deterministic surface structuring by the cutting of micro-dimples into a surface (subprojects 2 and 3). Innovative optical measuring strategies were developed to measure the produced microstructures (subproject 4). Based on extensive experiments, the tribological potential of microstructures for different contact conditions, load collectives, and demonstrators were investigated, and the tribological correlations were systematically elaborated (subprojects 1, 2 and 3). Furthermore, a transfer of the research results in an industrial application was realised by the microstructuring of industrially manufactured cylinder liners. The experimental investigation of those machined liners was carried out on a heavy duty diesel single cylinder test engine (subproject 5).

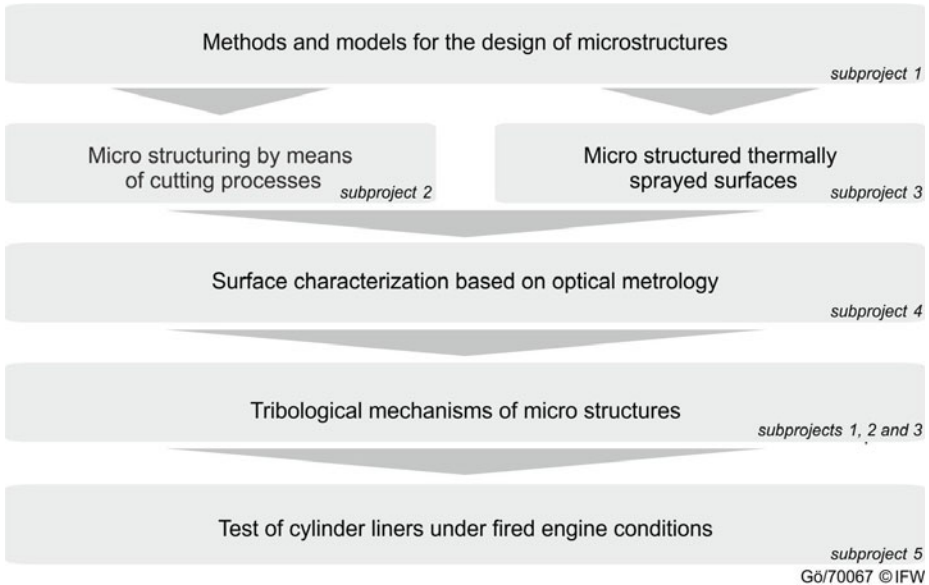


Figure 1-1: Subprojects of the research group

2 Project overview

2.1 Consortium

The interdisciplinary consortium in the fields design, manufacturing, characterisation and scientific testing of microstructured surfaces pursues the above-mentioned sub-projects. The coordinator and spokesman of this consortium as well as the participating institutions of the Leibniz Universität Hannover and the Universität Kassel are listed below:

Coordinator and spokesman of the research group:

Prof. Dr.-Ing. Berend Denkena
 Institut für Fertigungstechnik und Werkzeugmaschinen IFW
 (Production Engineering and Machine Tools)
 Leibniz Universität Hannover
 An der Universität 2
 30823 Garbsen

Subproject 1: Methods and models for the design of microstructures

Lehrstuhl für Maschinenelemente und Tribologie IMK
 (Machine Parts and Tribology)
 Universität Kassel
 Mönchebergstraße 3
 34125 Kassel

www.uni-kassel.de/maschinenbau/institute/imk

Senior scientists: Prof. Dr.-Ing. Adrian Rienäcker, Prof. Dr.-Ing. habil. Gunter Knoll

Scientists: Dr.-Ing. Sven Brandt, Dipl.-Ing. Herman Fast

Subproject 2: Microstructuring by means of cutting processes

Institut für Fertigungstechnik und Werkzeugmaschinen IFW

(Production Engineering and Machine Tools)

Leibniz Universität Hannover

An der Universität 2

30823 Garbsen

www.ifw.uni-hannover.de

Senior scientist: Prof. Dr.-Ing. Berend Denkena

Scientists: Dipl.-Ing. (FH) Jan Kästner, Dipl.-Ing. Tim Götttsching

Subproject 3: Microstructured thermally sprayed surfaces

Institut für Werkstoffkunde IW

(Materials Science)

Leibniz Universität Hannover

An der Universität 2

30823 Garbsen

www.iw.uni-hannover.de

Senior scientists: Prof. Dr.-Ing. Hans Jürgen Maier, Prof. Dr.-Ing. habil. Dr.-Ing. E.h.

Dr. h.c. Friedrich-Wilhelm Bach

Scientists: Dr.-Ing. habil. Kai Möhwald, Dipl.-Min. Martin Erne, Dipl.-Geow. Christoph

Hübsch

Subproject 4: Surface characterisation based on optical metrology

Institut für Mess- und Regelungstechnik IMR

(Measurement and Automatic Control)

Leibniz Universität Hannover

Nienburger Straße 17

30167 Hannover

www.imr.uni-hannover.de

Senior scientist: Prof. Dr.-Ing. Eduard Reithmeier

Scientists: Dr.-Ing. Dipl.-Phys. Markus Kästner, Dr.-Ing. Dipl.-Wirtsch.-Ing. Martin

Bretschneider, Dr.-Ing. Omar Abo-Namous, Dipl.-Phys. Florian Engelke

Subproject 5: Test of cylinder liners under fired engine conditions

Institut für Technische Verbrennung ITV

(Technical Combustion)

Leibniz Universität Hannover

Welfengarten 1A

30167 Hannover

www.itv.uni-hannover.de

Senior scientist: Prof. Dr. Friedrich Dinkelacker

Scientist: Dipl.-Ing. Hubertus Ulmer

2.2 Starting situation and need for action

Combustion engines are widely distributed in the world and, barring an unforeseen development, will maintain their dominant position in the near and middle future, as alternative mobility concepts like electric cars cannot compete with the power density of conventional combustion engines. In some fields of transport industry, as for example long-haul trucks or container ships, electrification does not seem feasible at all. When designing combustion engines, the main focus is laid on efficiency, since it is directly related to specific fuel consumption as well as to CO₂ emissions. This is reflected by continuously stricter exhaust-gas limits and taxation regulations, which take into consideration the amount of CO₂ emissions as well as the planned obligatory fleet consumption of 120 g CO₂ per km.

Since up to 50 % of the mechanical losses are related to the piston group depending on the operating point, their reduction represents one of the most effective means for reducing the total friction in combustion engines. The tribological functional properties of components sliding against each other are determined by load, relative speed, material combination, and to a significant extent, by their surface properties as well. Thus, performance and lifetime of such tribological systems can be improved by optimising the surface topography. For this reason, cylinder liners are generally honed which ensures not only their high shape accuracy but also the characteristic criss-crossing groove microstructure on the surface. As a result, oil retention volume and properties can be adjusted by means of the surface roughness and the crossing angle of the grinding grooves. In general, the aim is to achieve high load capacities and thus favourable sliding properties via low roughness and high contact ratios. Furthermore, a certain minimum roughness is required for the oil retention. However, the criss-crossing groove structure, developing on the surface, is a communicating system where the lubricant is not only evenly distributed but is also displaced by the sliding partner. This is a disadvantage especially for low sliding speeds, such as those typical for the dead centre area (top dead centre), with regard to the development and the maintenance of hydrodynamic lubrication conditions [FLO85].

Here, micro-dimples cut into cylinder liners have been providing, for some time now, a promising approach to improve friction and wear properties as well as to reduce oil consumption. [Figure 2-1](#) shows the friction force for one cycle for a normally honed as well as for a finely honed and additionally laser-structured cylinder liner as published by one of the partner institutes of this research group in 2004. It can be seen that friction forces can be significantly reduced by the creation of micro-dimples, especially in mixed friction areas [TOM08, GOL04, HEU07].

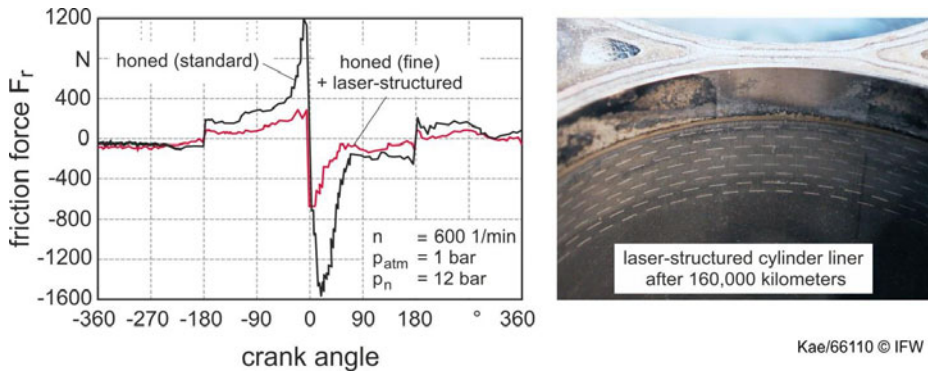


Figure 2-1: Reduction of the friction losses at the piston group by laser-structured cylinder liners [GOL04]

By combining a low basic roughness and the hydrodynamic pressure increasing effect of laser dimples, a reduced piston group friction of up to 53% during fired operation could already be reached. The simultaneous reduction in oil consumption of 70% to 85% can be explained by the lower basic roughness and the smaller oil retention volume of the cylinder liners [ABE06]. The creation of micro-dimples in piston rings can result in a reduction in fuel consumption of up to 4% [ETS09]. In the field of thrust bearing technology, surface structures and micro-dimples also show a great potential to minimise friction, as demonstrated by several research papers on analogue components [ETS99a, ETS99b, WAN03].

However, previous findings concerning the tribological functioning of microstructured surfaces are mostly based on particular test series, random tests and idealised contact geometries. As a consequence, only limited methods and tribological models for an application-oriented, and thus load-specific, design of such surfaces are available. Therefore, it is difficult to transfer existing knowledge and methods to other tribological contact and load conditions. To obtain essential knowledge of microstructures, which would allow their usage in a wide range of applications, fundamental experiences based on extensive, systematic theoretical as well as experimental test series have to be gained, thus ensuring perfect transferability.

In recent years, laser machining as a microstructuring method has been further developed [ETS05, SIE09]. When creating geometrically defined micro-dimples within minimum tolerances, the rather high productivity of this method decreases immensely due to low removal rates. Furthermore, laser-structured surfaces need refinishing in order to remove melt protrusions [ABE06]. In many fields, the high equipment costs pose a serious obstacle to the use of this technology. Additional methods, which could be used to create micro-dimples, are micro-spark erosion [GRU97, MAS89, UHL06], micro-forming [HIR07, KLO07, PET05] or electrochemical machining [COS09, STÖ08]. Nevertheless, small workpiece surfaces, necessary refinishing as well as difficult integration into the existing process chains remain a challenge for the large-scale industrial application of these methods onto cylinder liners.

Cutting processes already show a multitude of innovative approaches for microstructuring of surfaces. Common cutting processes, such as turning, milling or grinding, can be scaled down for the microstructuring process. Due to the high flexibility of these processes, various structures can be machined on the workpiece surface. The use of mono crystalline diamond tools, in particular, allows the creation of minuscule structure dimensions with high aspect ratios, geometry and surface qualities [BRE04, BRI07]. However, diamond cutting is primarily suited for the machining of non-ferrous materials [GLA04]. Thus, it cannot be used for cutting of micro-dimples into cylinder liners, which are generally made of ferrous materials. Furthermore, the small cutting thickness which results from the application of diamond cutting tools limits the surface capacity. Consequently, no cutting processes are suitable for cutting geometrically defined micro-dimples with high reliability and accuracy into large tribologically stressed surfaces.

Another effective approach to a tribological functionalisation of thermo-mechanically highly stressed surfaces is the coating with friction-reducing, wear-resistant coats. These coating systems are already used in the field of diesel engines, showing great tribological potential. It has been proposed that the possible elimination of cast iron cylinder liners could lead to a considerable reduction in weight, and thus reduce the "blow-by", because there would be no distortion of the cast iron liner and the aluminium motor engine [FLO11]. Thereby, the use of specifically produced porosities which exhibit positive effect on friction, wear and oil retention is of a special interest because they can act as micro-dimples [HOL11, BAR05]. Moreover, a major focus was put on the investigation of molybdenum spray materials since using molybdenum as a coating material has been shown to improve friction and wear properties [OVE79]. However, systematic knowledge concerning the load-specific tribological design and manufacturing of such coatings does not exist as of yet. [FLO03].

In order to evaluate the tribological functioning of microstructures, their arrangement and geometry must be known. For this purpose, parameters for their characterisation, but also methods to identify them quantitatively, are required. Small dimensions as well as highly-complex geometries of microstructures (pores, steep flank angles) and components (bores) pose a major challenge to measurement technology. Consequently, measuring methods for an extensive automated characterisation of structured surfaces are still in development. Furthermore, a certain lack of meaningful parameters which can be used for the evaluation of the changes of the tribological behaviour of structured surfaces has been identified [DON95].

The characterisation of surface roughness is currently based on tactile measurements [VOL05, WEI06, BIC12], but tactile measurements of large lateral dimensions require long measurement times and, by the nature of the technique, risk damaging the tested surface. Moreover, the accuracy of the measurements is limited for surfaces with high aspect ratios caused by morphological filtering of the stylus [STO93, KRY04]. Using optical measurement devices for point measurements, such as confocal chromatic sensors, provides a less time-consuming alternative without the risk of

inflicting damage to the workpiece [BRO04]. For this reason, optical measurement techniques are frequently used for the characterisation of surfaces in industrial projects [SCH07, OFE07]. Hence, norm texts, such as the EN ISO 25178, regulating the application of optical surface measurements are currently being designed and are to be published in the near future. Additionally, 3D surface data obtained by optical measurements can be analysed with methods of image processing to extract the surface structures relevant for the further research of their tribological effect [BOD98, STO93, WEI06]. Using chromatic sensors, for example, is suitable for large slopes, as it exhibits a lateral resolution of 1 μm and a vertical uncertainty of about 100 nm in a measuring range of 500 μm . By integrating a chromatic sensor within a coordinate measuring machine, it is possible to measure large surface fields with a minimised uncertainty.

2.3 Summary of main results

The wide-ranging expertise of the research group was reflected in the five subprojects. In the first subproject, numerical simulation tools (KORI3D / PRO) were enhanced in order to calculate the tribological properties of microstructures. Using a Lattice-Boltzmann model to describe the physical properties of the engine oil inside the microstructures, a new approach was developed. Through the novel simulation technique, it was possible to determine the ideal layout of the microstructures. This knowledge was used as an input for the manufacturing processes and for further layout developments within the tribological experiments (see chapter 3).

Two different approaches regarding the manufacturing of microstructures were utilised. In the first stage, a machining process that uses an axially parallel turn-milling strategy was developed. By adjusting the feed rate and the rotational frequencies, various micro-dimple arrangements could be machined continuously. Typical dimensions varied from 1 mm to 2 mm in length, 50 μm to 100 μm in width and 5 μm to 30 μm in depth. To investigate the basic correlations between process variables, quality characteristics and chip formation mechanisms, fly-cutting tests were carried out (see chapter 4). Subsequently, a thermal spray process that allows the manufacturing of coatings with a defined porosity was developed. The microstructures were formed by the porosity of non-molten and re-solidified spray particles (see chapter 5).

In the next sub-project, optical sensors were developed in order to characterize the technical surfaces. A white light interferometer was used to measure small surface excerpts with high resolution. A coordinate measuring machine was modified with a confocal chromatic sensor in order to allow in-cylinder-measurements. Furthermore, data processing methods and optimised image alignment techniques were developed to ensure high resolution images of the microstructures (see chapter 6).

The tribological mechanism of machined and thermally sprayed microstructures was analysed by means of tribometer testings and a test rig specially designed for the cylinder liners (see chapter 7). During the testing, the creation of machined micro-

dimples led to the reduction of the minimum friction coefficient by up to 79% as well as to its shift towards lower relative speeds by 77%. The identified effects indicate that machined micro-dimples support hydrodynamic pressure build-up between the friction partners under planar contact conditions (see chapter 7.1). When testing thermally sprayed microstructures, coated surfaces consistently exhibited enhanced frictional properties compared to those of uncoated steel or cast iron. In comparison with the reference samples, the coatings provide the potential of using the microstructures to build a hydrodynamic pressure and additionally use the microstructures as an oil retention capacity. Due to the lamellar structure of the coatings, a new microstructured surface with the same properties is exposed after wear (see chapter 0).

An experimental analysis of a microstructured cylinder liner was carried out on a single cylinder heavy-duty research engine under fired conditions. The friction, in terms of the friction mean effective pressure (FMEP), was determined using the "indication method". Additionally, oil consumption measurements were carried out using an advanced mass spectroscopy system. The surfaces of the investigated cylinder liner were plateau honed, fine honed with machined micro-dimples and coated by thermal spraying. Depending on the micro-dimple arrangement, cylinder liners with machined microstructures showed a decrease of FMEP by a maximum of 19 % and significantly less oil consumption at low and medium engine loads compared to an ordinary plateau honed liner (see chapter 8).

3 Methods and models for the design of microstructures

*Institut für Maschinenelemente und Konstruktionstechnik (IMK), Universität Kassel
G. Knoll, A. Rienäcker, S. Brandt, H. Fast*

3.1 Objective and approach

The objective of this sub-project was the development and validation of simulation methods for the tribological characterisation of the effect of hydrodynamic micro-dimples with respect to improved friction wear and oil consumption in the system piston ring/cylinder liner.

The influence of dimple cross section geometry, depth and placement of micro-dimples relative to each other as well as the influence of the ratio of lubricant gap to dimple depth on load capacity were investigated. In a first survey, a comparison between the solution of the Reynolds equation and a full solution of the Navier-Stokes equations is presented.

To transfer the insights gained from the model simulations onto the application piston ring – cylinder liner, the Patir and Cheng's average flow model was employed. For this purpose, the influence of the micro-dimples on pressure and friction was determined in a flow simulation with a solution of the Reynolds equation for a representative surface section.

The principal values of the (shear- and pressure) flow tensors were determined with the help of the simulation software FLOSIM, developed at IMK, and stored in lookup tables as a function of the average oil film thickness for use in piston ring/cylinder liner and oil consumption simulations.

Piston ring friction was determined using the software KOR3D, which calculates piston ring motion relative to ring groove and cylinder liner under inner and outer loading. Basis for this is a multibody system dynamics formulation for the ring pack coupled with relevant system interactions, which include gas dynamics, inertia forces, and traction forces in the lubricant, which reflect the flow tensors determined with FLOSIM.

Oil consumption was determined with the software PRO. In this simulation, oil evaporation is determined on the basis of wall temperatures from the solution of the unsteady Fourier equation in the domain between cooling water, cylinder liner and oil film. PRO builds on results which were previously determined with FLOSIM.

3.2 Comparison between Computational Fluid Dynamics and the Reynolds equation

This chapter aims to compare the results from the lubrication theory to those obtained with the full Navier-Stokes equations as well as to characterise the differences which were found. This comparison was conducted on a model problem with a single dimple with different dimple depths. The obtained insights served as a basis for the decisions necessary in order to modify the average flow model accordingly.

The Reynolds equation of lubrication theory is derived from the full set of Navier-Stokes equations under a number of simplifying assumptions. An important subtask of the project consisted in establishing a quantitative measure for the deviation between solutions to the Navier-Stokes equations and the Reynolds equation.

To this purpose, a 2-dimensional model with a constant gap between both sliding surfaces (constant gap length l and height h), dimple width b and bounding surface velocity v was applied to a number of different dimple depths which were used in the solutions of both sets of equations. Lubricant pressures at inlet and exit were set to zero (relative to the ambient pressure) as a boundary condition. The pressure equation could be solved under the Sommerfeld cavitation condition, which allows negative pressures

While the Sommerfeld cavitation condition is considered physically incorrect representation of cavitation itself, it is well suited for a relative comparison because cavitation models, which are different in the Reynolds equation (e.g., Kumar-Booker) and the Navier Stokes equation (e.g., Raleigh-Plesset), do not need to be fed with parameters.

Figure 3-1 shows exemplary results for the pressure distributions for shallow ($h/t=0,5$) and deep ($h/t=0,067$) dimples. It can be seen that the solution of the Reynolds equation for shallow dimples matches the solution of the Navier-Stokes equations well, justifying the assumptions behind the lubrication theory.

As the dimples become deeper, the difference between the solutions becomes increasingly prominent ($h/t=0,067$). Thus, in the transition zone between gap and dimple, the pressure calculated from the Reynolds equation is significantly smaller than the pressure calculated using the Navier-Stokes equations.

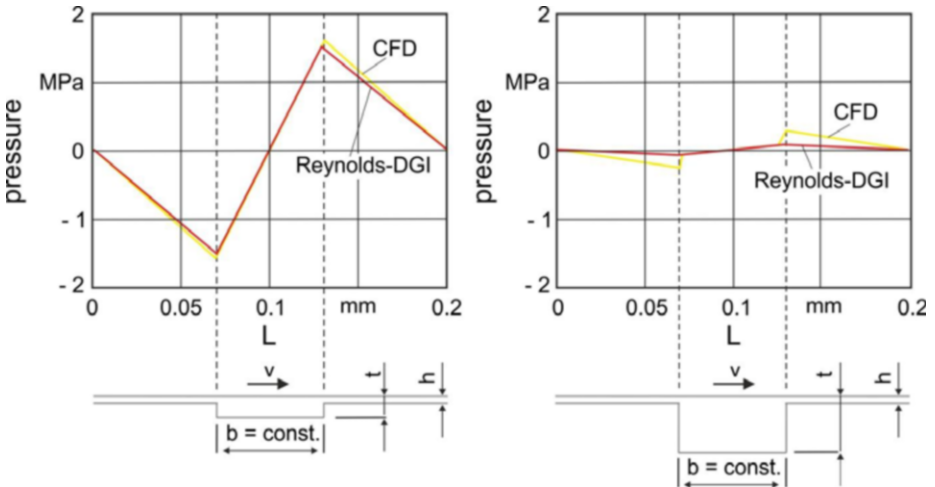


Figure 3-1: Comparison of results between Reynolds equation and CFD (Sommerfeld-BC)

This can be explained by two of the assumptions on which the derivation of the Reynolds equation is based: negligible velocity components and pressure differences in the gap height direction. In the following, Figure 3-2 shows the velocity profiles in the gap direction from the solution of the Navier-Stokes equations; these grow with increasing dimple depth and support pressure generation.

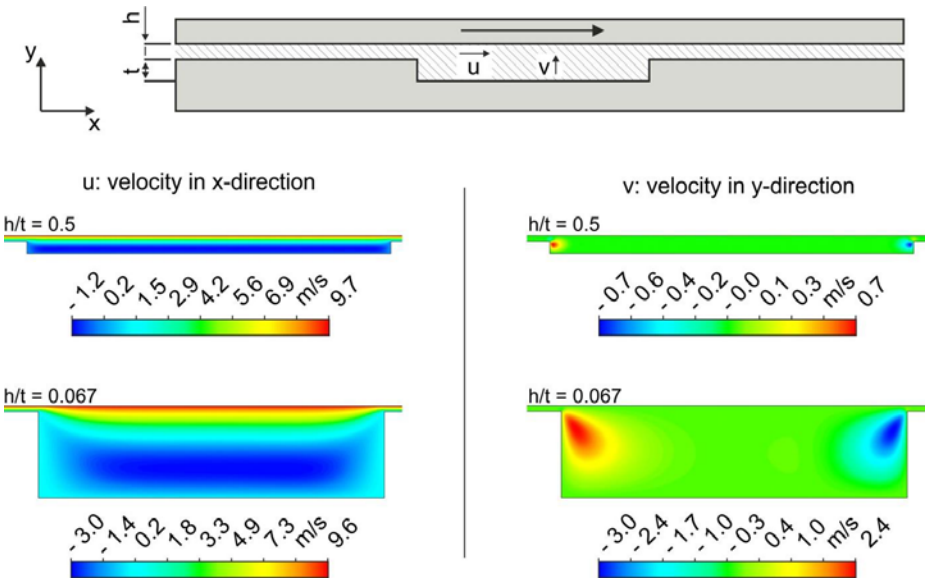


Figure 3-2: Velocity profiles in the dimple (Navier-Stokes solution)

3.3 Investigation of dimple geometry and arrangement

Cross section geometry

The influence of dimple cross section geometry on hydrodynamic pressure build up was investigated by means of a simulation. Calculations were performed with a commercial CFD code (CFX) under consideration of the cavitation model explained in chapter 3.2. In addition to dimple cross section geometry, the dimple depth was varied in such a way that the optimum range of gap height to dimple depth could be determined. Figure 3-3 summarises the computational model, including the quantities which were kept constant as well as the variables. The width of the dimples was held constant between all variants for a better comparison. In coordination with the Institute of Production Engineering and Machine Tools, henceforth IFW, it could be determined that the variants investigated in the simulation could actually be manufactured by means of cutting processes. Variants in dimple geometry were considered to fall into two distinct classes: symmetric (base, variants 1 and 2) and non-symmetric (variants 3 - 8). For practical purposes, the variant geometry is presented in a simplified manner.

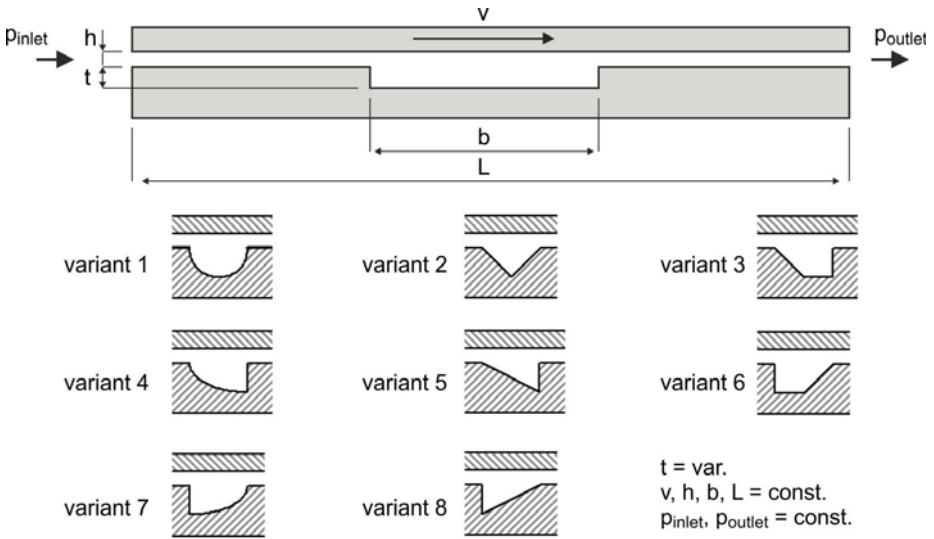


Figure 3-3: Variants for dimple cross section variation

Figure 3-4 shows the hydrodynamic pressure for the base configuration as a function of the dimple depth. It can be seen that the pressure distributions are very similar in the range of optimum dimple depths; a fact which does not allow for a significant conclusion to be drawn. It was therefore decided to compare the resultant forces rather than the pressure distributions.

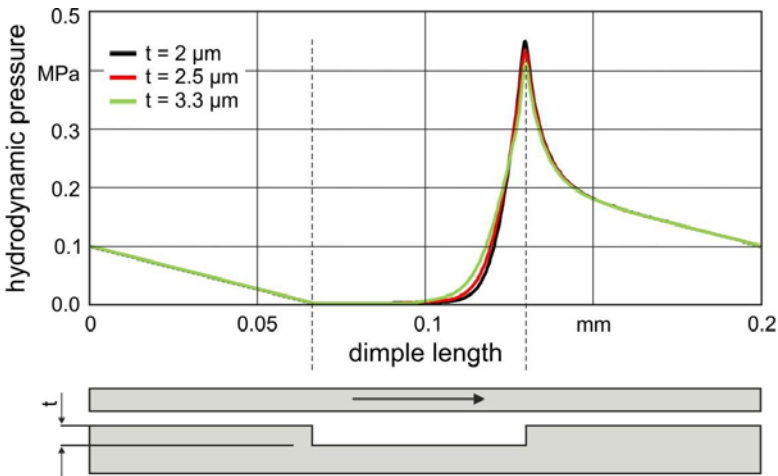


Figure 3-4: Pressure distributions of the base configuration (exemplary)

In the following, dimple cross section geometries are evaluated in contrast to the base configuration. For a better overview, variants are subdivided into symmetric and non-symmetric ones. Figure 3-5 presents symmetric geometries. It can be seen here

that, for low h/t relations, variants 1 and 2 show an improved load carrying capacity relative to the base configuration; this capacity reaches its optimum for h/t ratios close to 0.15. With an increasing h/t ratio, towards shallow dimples, the pressures even out among all variants.

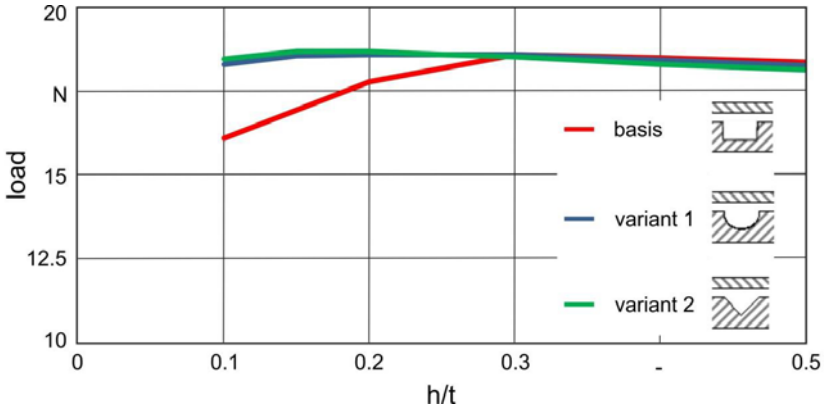


Figure 3-5: Symmetric dimple geometries

In Figure 3-6, variants 3 - 5 are compared to the base. Here, the generated pressures exceed those of the base variant. Compared to the symmetric dimple contours, the optimum ratio of gap to dimple depth (h/t) is increased, indicating a better performance of non-symmetric dimples for shallow dimple depths.

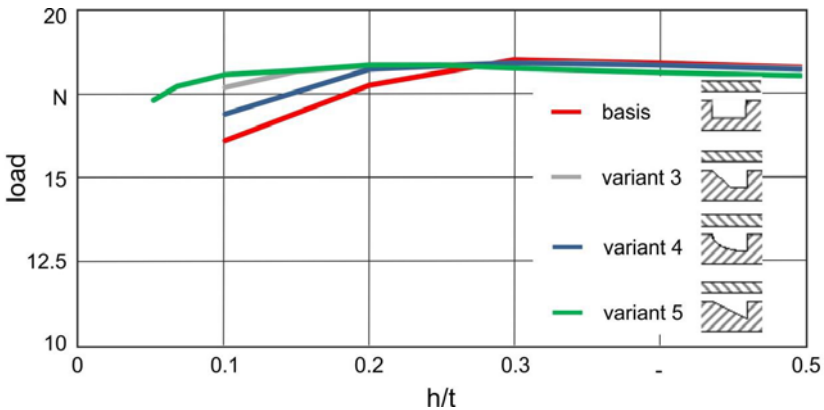


Figure 3-6: Non-symmetric dimple geometries

Figure 3-7 shows another comparison between non-symmetric and base configurations. Variants 6 - 8 are similar to variants 3-5; however, they are mirrored relative to the direction of motion. In this case, an improved load carrying capacity could be recorded for the non-symmetric contours relative to the base configuration, especially for gap-to-depth ratios (h/t) smaller than 0.25.

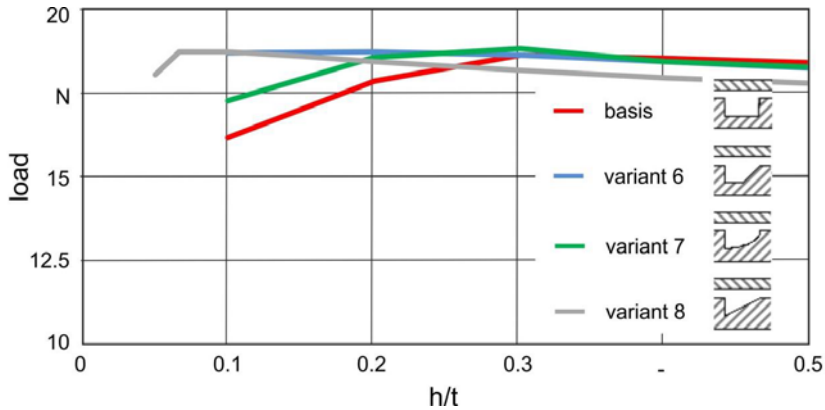


Figure 3-7: Non-symmetric dimple geometries (continued)

The results of this investigation indicate that the dimple cross section geometry influences the load carrying capacity minimally. A comparison with the base configuration shows that employing a rectangular cross section, as well as symmetric dimple cross sections with circular or triangular shape, results in an improved pressure generation. However, it appears prudent to suggest focusing further investigations on ellipsoidal dimple cross sections, as these are characterised by a comparatively uncomplicated fabrication process.

Investigating the influence of dimple geometry on load carrying capacity indicated that local geometry alterations had a minimal impact on the load carrying capacity of the system, and that the optimum ratio between gap height and dimple depth lies between 0.2 and 0.3.

Lateral dimple position

Taking the results presented in the previous chapter into consideration, the hydrodynamic load carrying capacity for a model with three dimples was investigated to identify the optimum dimple configuration. The inlet length L_1 , the dimple distance L_2 , held constant between the second and the third dimple, and the exit length L_3 were varied. The circular dimple geometry was chosen because earlier results indicated that it has superior load carrying capacity, at least in some instances. Another reason for this choice was the similarity of this geometry to the geometries manufactured by means of cutting edges at IFW (compare variant 1 in [Figure 3-5](#)). The ratio of gap width to dimple depth used in the models and calculations was chosen to be $h/t=0.2$: close to the higher end of the identified optimum between 0.1 and 0.2.

The following figure shows an exemplary pressure distribution for a study with respect to the exit length. All studies were conducted using the same boundary conditions (c.f. chapter 3.2) including ambient pressures (1 bar) at inlet and exit. The upper bounding surface was moved with a shear velocity of 10 m/s from left to right relative to the stationary dimpled lower bounding surface. For comparison purposes, the av-

verage load carrying pressure was computed and compared between different configurations.

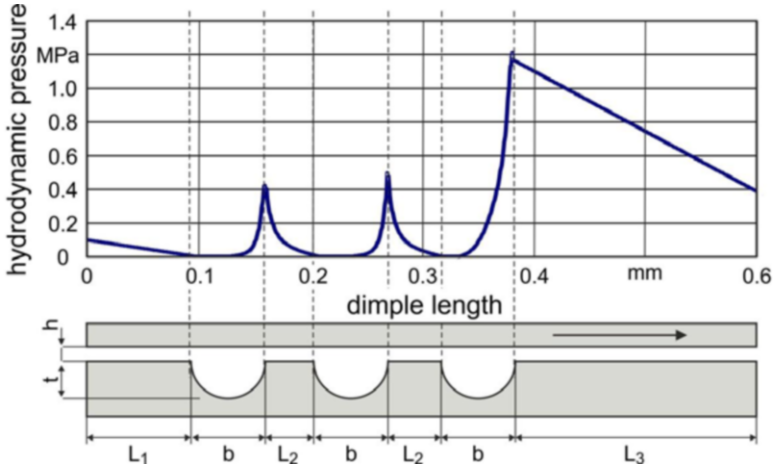


Figure 3-8: Exemplary pressure distribution for the 3 dimple model

Dimple distance L_2

For given and equal inlet and exit lengths $L_1=L_3$, the inter-dimple distance L_2 was varied between 20 μm and 100 μm . The results showed only an insignificant influence of the inter-dimple distance on the load carrying pressures. Although the investigations did not allow for a significant conclusion with regards to the dimple positioning, locating them closely to each other appears to be, by a small margin, the more beneficial option (Figure 3-9).

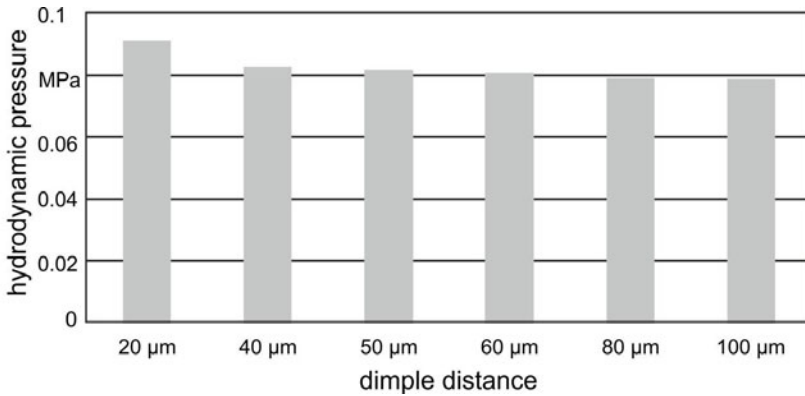


Figure 3-9: Variation of inter-dimple distance

Inlet length L_1 and exit length L_3

The variation of both inlet- and exit-length was conducted for a constant inter-dimple distance of 50 μm . For the inlet-length variation, an exit length of 100 μm was held constant. Vice versa, for the exit-length variation, an inlet length of 100 μm was held

constant. Figure 3-10 shows the effect of the length variation on the average load carrying pressure. When increasing the inlet length, the average bearing pressures decreases (red bars). A comparison between the pressure distribution and the base-line, Figure 3-10, indicates that cavitation, as a reason for the pressure, decreases along L_1 . An increased inlet length L_1 results in an increased cavitated region and can be therefore identified as the cause of loss in load carrying capacity.

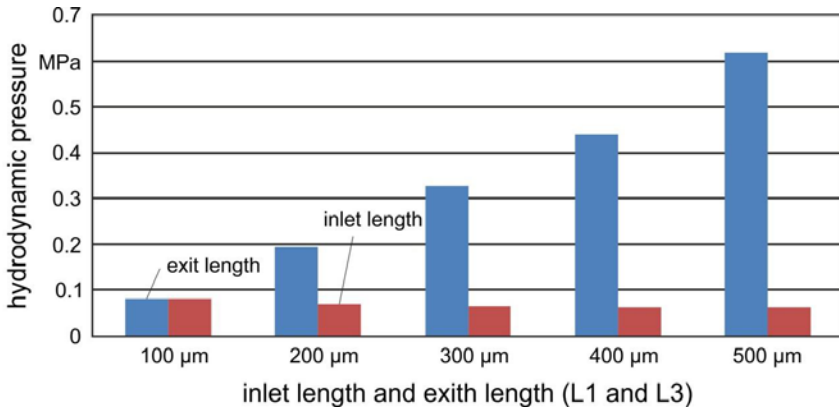


Figure 3-10: Variation of inlet and exit lengths

In contrast to the inlet length variation, the average load carrying pressure increases with increasing exit length L_3 . The throttle effect, which increases pressures and decreases the extent of the cavitated region, was identified as a reason for this phenomenon. Figure 3-11 shows hydrodynamic pressures on the left and volume fraction of gas and oil on the right for all three dimples. The gas fraction can be seen as an indicator for an occurring cavitation.

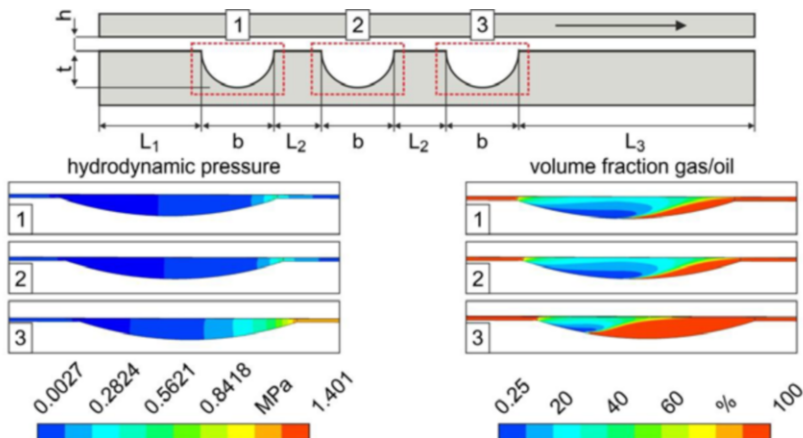


Figure 3-11: Hydrodynamic pressures and volume fraction gas in the fluid

All in all, the obtained results helped identify the exit length as the most significant parameter influencing the generation of load carrying pressures. Consequently, it

was concluded that placing non-dimpled areas with constant width downstream of the dimples would have a positive effect on the load carrying capacity.

Study of 3D dimple cross section geometry

An additional series of simulations was devoted to the study of the influence of dimple cross section lateral to the direction of the flow and upper surface velocity. When machining 'real' dimples, the dimple shape is created by a rotating cutting edge, which leads to a contour of a dimple with a width-variable depth while the cutter engages in the cylinder liner. The influence of the depth variation was studied for a model dimple with 5 μm maximum depth, subjected to the boundary conditions outlined in chapter 3.2. Moreover, a real variable width dimple contour was compared to a sharp edged constant depth contour.

The pressure distribution shown in Figure 3-12 was characterised by a pressure decrease in front of the dimple in its upstream section, relative to the direction of motion. Similarly to the observed two dimensional models, this was caused by cavitation. Downstream, behind the dimple, a steady decrease of pressures to the ambient boundary pressure could be observed.

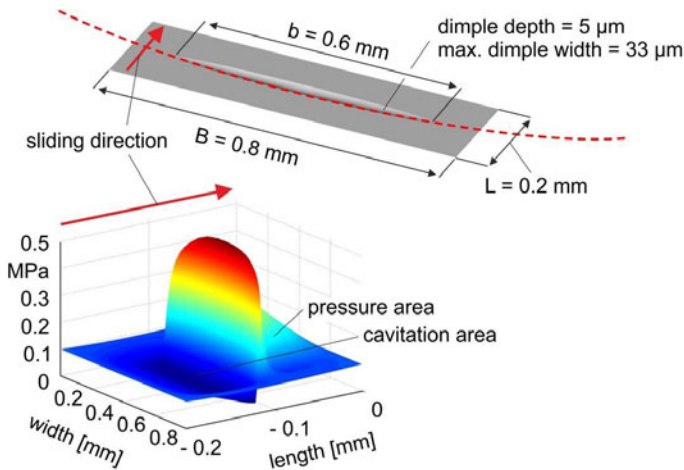


Figure 3-12: Overview 3D-Model geometry and pressure distribution

Figure 3-13 compares pressure distributions of both models in transverse (width) direction. The upper bounding surface and hence most of the flow move orthogonally in the longitudinal direction. The flanks of the pressure distributions show significant differences, e.g. the rounded contour is characterised by steeper flanks, leading to higher overall pressures and to an improved load carrying capacity.

A comparison of the two dimensional computations (Figure 3-5, Chapter 3.3) shows that the base and variation 1 exhibit similar trends even though the investigated contours were oriented longitudinally in flow direction. Furthermore, the rounded contour supports a stronger pressure generation.

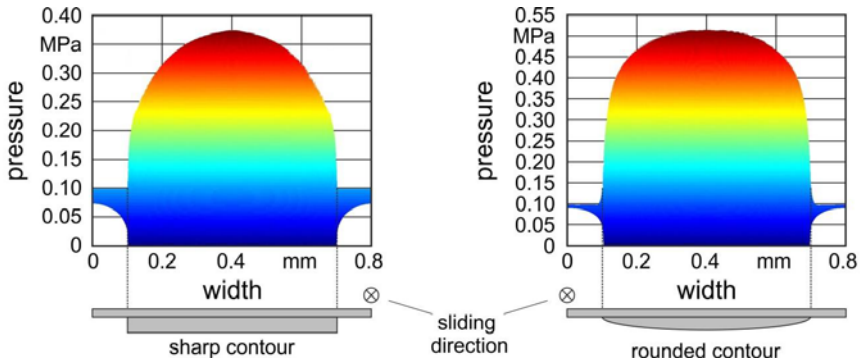


Figure 3-13: Influence of dimple flanks on pressure generation

3.4 Simulation model for piston ring friction coefficient test rig

A simulation model for the prediction of measurements, taken on the test rig for piston ring friction coefficients, was established with the simulation tool KOR13D.

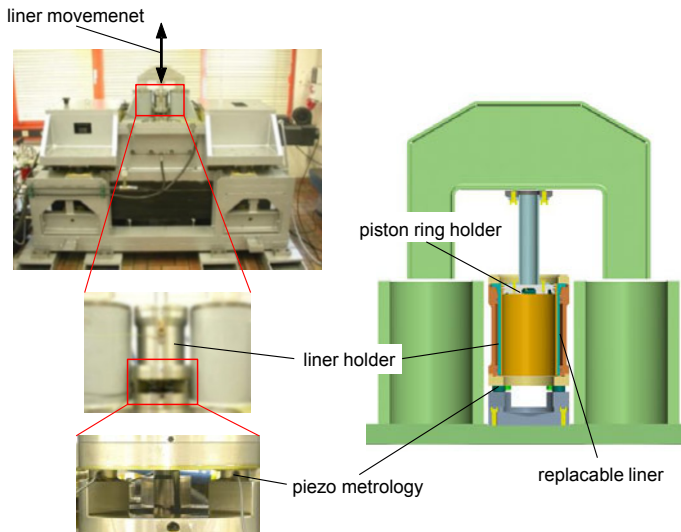


Figure 3-14: Piston ring friction coefficient test rig (SRV test rig)

Aside from the geometry and dynamic boundary conditions, the surface topographies of the ring and the liner were represented in the model with the help of Patir and Cheng's flow factors (see [Figure 3-15](#)).

The friction coefficients for metal-to-metal contact under boundary lubrication conditions had to be defined prior to the input for KOR13D. To accomplish this, dedicated tribometric tests for each ring were performed with the SRV test rig ([Figure 3-14](#)). Using this information, a full factorial simulation plan was set up, covering the range of

radial oil film heights and ring preloads, both being quantities which had not been fully known previously.

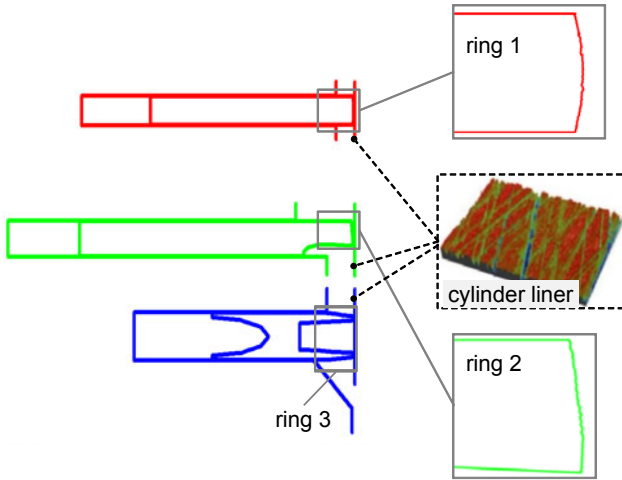


Figure 3-15: Surface roughness profiles piston rings and cylinder liner

Figure 3-16 shows the comparison between the measured and the simulated friction forces for the top ring. A good qualitative agreement between them can be observed. The discrepancies which characterise the locations where the direction of motion is reversed are assumed to be related to the use of piezo quartz force measurements. Under static loads, the signal from the force measurement system vanishes within 0.1 seconds. For the angular speed investigated, the time between reversal points is 0.16 seconds, which facilitates the assumption that some portion of the measured signal disappears before reaching the reversal point. For a more detailed discussion on how such a simulation model can be fine-tuned, see reference [KNO08].

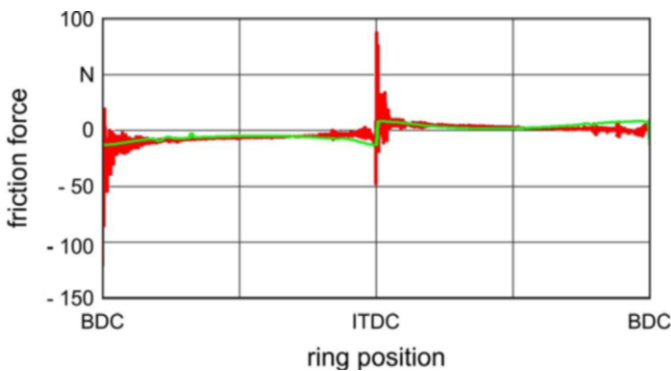


Figure 3-16: Comparison between measurements and simulation

Despite the differences between measurements and simulation close to the reversal points, both test rig and simulation appear to be suited to characterise the influence of cylinder liner surface topography on the friction.

Furthermore, tribometer tests showed that noise in the signal increases with angular speed. The reason for this is the presence of vibrations which increase when the speed increases. To counteract this undesired behaviour and to provide the ability to vary the ring preload, a new fixture for the piston rings was designed (see [Figure 3-17](#)).

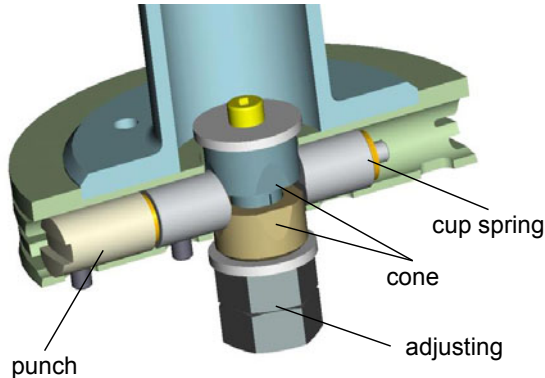


Figure 3-17: New piston ring fixture for variable ring preloads

The preload is generated by two cylinders with a conical wall; tightening a bolt moves the surfaces closer to each other and forces the rings to open. To maintain a constant preload during operation, the bolt is secured by a lock nut.

3.5 Design and validation of a test engine simulation model

A simulation model for the software KOR/PRO was designed to investigate the effects of structured surfaces on friction and oil consumption in the tribo-mechanical piston ring/cylinder liner system. This simulation reflected the one cylinder test engine run at the Institute for Technical Combustion (see chapter 8), henceforth ITV; it was used to compute piston ring motion, blow-by losses, and oil consumption and was validated using engine test data. In the following, the theoretical background of the software is explained.

Theoretical foundation

The effect of small-scale surface roughness, reflecting its micro-hydrodynamic properties, on the pressure generation in a macro-scale lubricated contact was determined by means of a flow simulation. In this flow simulation, executed on a small but representative area with 3D surface roughness, the Reynolds equation of lubrication theory was solved under simple boundary conditions, and the flow was compared to that of a smooth surface. The principal elements of the pressure and shear flow tensors were determined for two different situations: pure pressure and pure shear.

Based on Patir and Cheng’s original work [Pat78], research at IMK [Rie95], [Lag00] was focused on improving the numerical treatment and on the addition of a solid-to-solid contact pressure/deformation model, reflecting the individual surface roughness. In this effort, software modules for the generation of surface roughness (SIMOBF) as well as for the determination of flow factors (FLOSIM) were created. Numerical results obtained with FLOSIM were compared to two different analytical solutions, each representing slight differences in the roughness correlation functions, and a high level of agreement among them could be observed, validating the software. On the macro-scale of a real bearing global effects of surface roughness were reflected in the Reynolds equation modified by flow tensors as below.

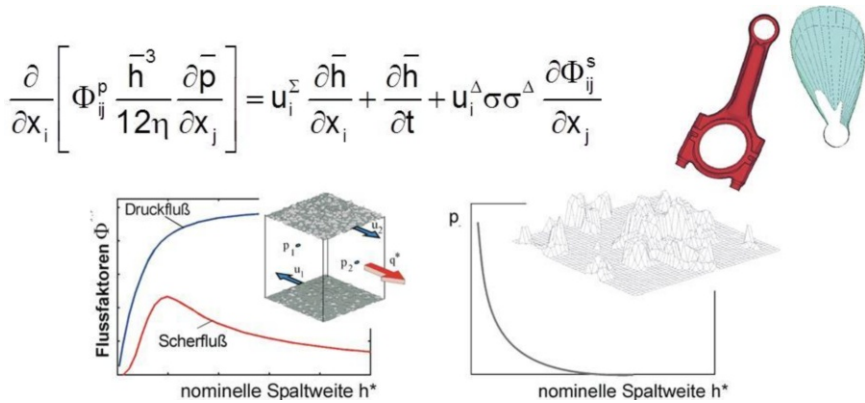


Figure 3-18: Modified Reynolds equation for rough surfaces

The simulation tool KOR3D, used for the analysis of piston ring friction and sealing, was developed during previous research projects, named “Piston Ring Friction I-II” [KNO92], [KNO94]. KOR3D determines piston ring motion relative to ring groove and liner resultant from inner and outer loading. It is based on a multibody type formulation for piston ring motion coupled with physical interdependencies related to gas-dynamics, inertia effects, and lubricant friction. It also includes surface roughness effects.

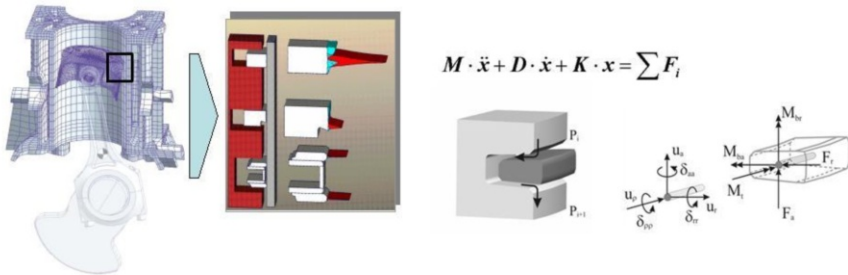


Figure 3-19: Simulation of piston ring dynamics

Main parameters considered by KOR3D simulations are:

- Geometry: Rings, piston and cylinder (including cylinder distortion, variable ring cross sections, ring wear, ring curvature, and ring surface structures and roughness);
- External boundary conditions: Piston secondary motion, transient cylinder pressures, and cylinder temperature distributions.

The program KOR3D computes the following results in a fully coupled approach:

- Piston ring motion (3D piston ring models based on the Finite Element Beam theory with distributed masses and stiffness as well as arbitrary cross sections);
- Hydrodynamic pressures (running surfaces and ring flanks) and related ring friction;
- Gas dynamics.

The following results are available:

- Minimum gaps per ring over time;
- Ring motion: Axial and radial;
- Ring friction;
- Blow-By and reverse blow-by, inter-ring-pressures.

The software PRO, also developed at IMK, is a simulation system used to compute engine oil-consumption related to the piston, piston rings, and liner system. PRO was developed within previous research projects and utilises results from the KOR3D simulations as its basis. Together with PRO, a matching procedure for the overall blow-by losses in KOR3D was developed; this procedure significantly enhanced the accuracy of the results.

A verification using experimental results, showed a high level of agreement between the measured and the simulated oil consumptions [KNO06] [KNO08].

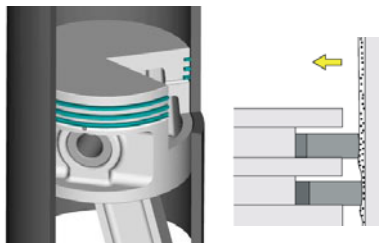


Figure 3-20: Simulation of oil consumption

In particular, the quantity of oil evaporations at the ring gap and on the free cylinder wall were determined based on wall temperatures computed from the transient solu-

tion of the Fourier heat conduction equation for the area between coolant and oil film on the liner.

Simulation model

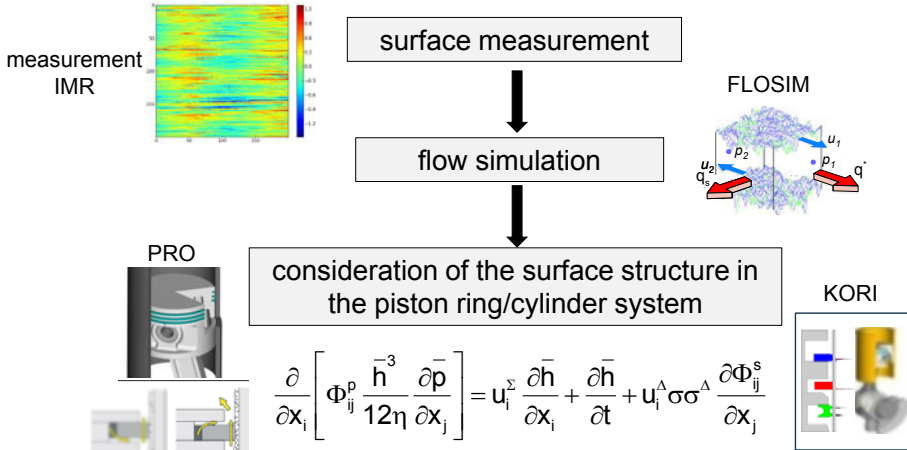


Figure 3-21: Modelling approach

While modelling the test engine, the following conditions were considered:

- Combustion pressures and –temperatures;
- Measured liner temperatures;
- Liner roughness structures;
- Piston ring geometry and related data;
- Oil film characteristics.

For the validation of the model, blow-by values taken from engine test data, which reflect the cylinder liner subjected to the fines honing process, were evaluated. Using these test data, the flow coefficients of the gas-flow model were calibrated for all speeds.

Figure 3-22 shows the levels of agreement between the measured and the simulated blow-by for all speeds.

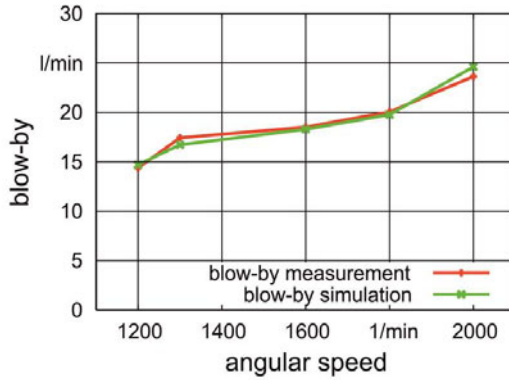


Figure 3-22: Blow-by matching for the test engine

Effect of liner roughness on piston ring dynamics

Using the calibrated simulation model, piston ring and oil consumption simulations were performed to evaluate the effects of manufactured liner surface roughness patterns on the piston ring friction and oil consumption under fired engine operation. Surface roughness patterns relate to:

- Serial honing;
- Very fine honing;
- Machined micro-patterns from a cutting process;
- Thermal coating.

Four engine conditions were selected from the engine map, as shown in [Figure 3-23](#). Related combustion chamber pressures and temperatures were supplied by ITV. [Figure 3-24](#) shows the friction losses over crank angle for all rings at a speed of 1600 rev/min and a mean effective pressure of 11.6 bar.

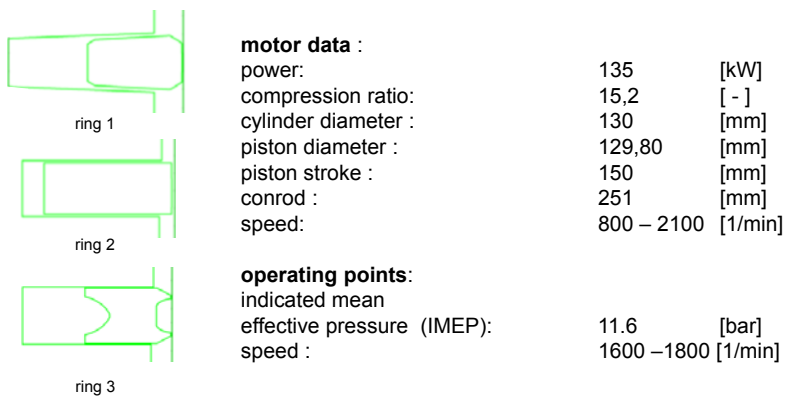


Figure 3-23: Test engine ring cross sections, load and speed variation

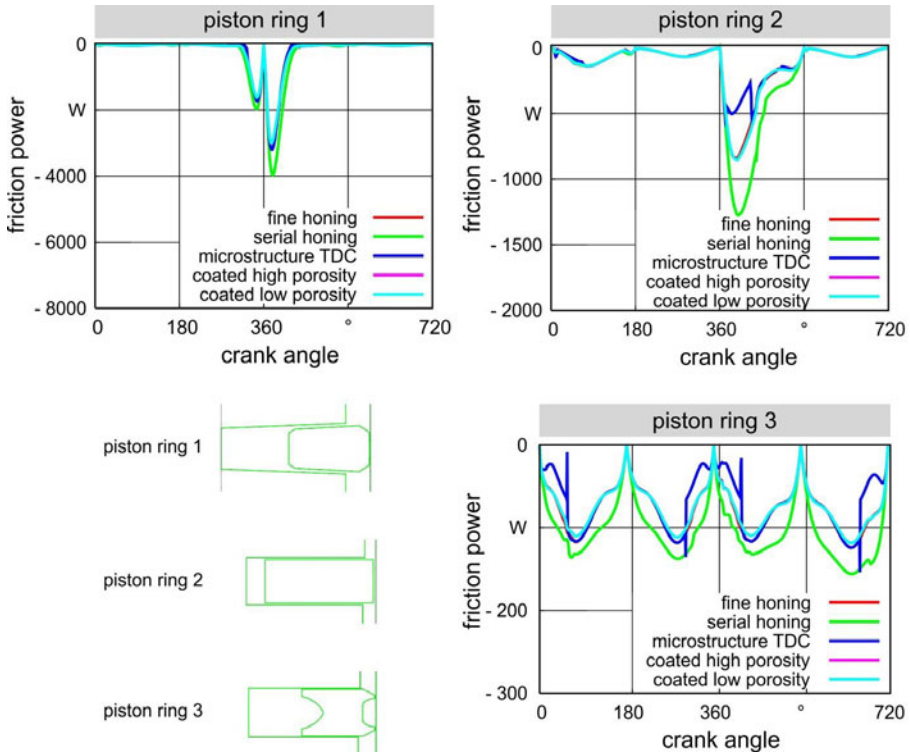


Figure 3-24: Friction losses piston rings

Mean pressure losses as a function of speed and load are presented in [Figure 3-25](#). Simulated and measured results were compared, showing a good qualitative agreement.

The causes of the existing deviations can be explained as follows:

- Cylinder liners distort during assembly due to the tightening of the bolts and during operation - due to the thermal expansion of the materials. Previous studies observe that higher order distortions, in particular, have critical influence when compared to computed results. However, cylinder liner distortions were an unknown variable in this project and hence could not be included in the simulation.
- Measured friction losses include piston rings, piston as well as the whole crank assembly, including connecting rods; the simulation, on the other hand, covers the piston rings only. Therefore, a quantitative agreement cannot be expected.

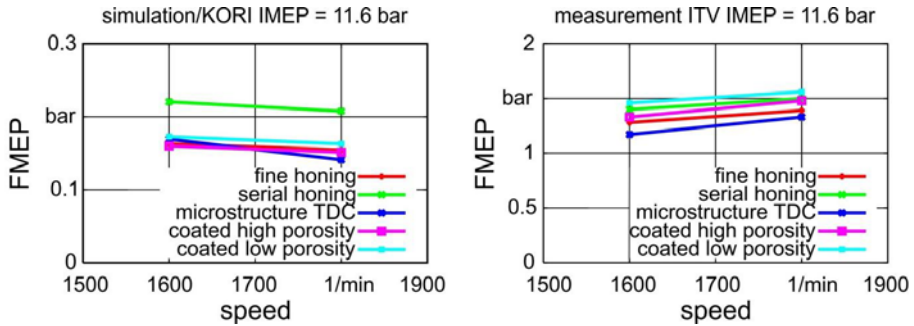


Figure 3-25: Friction mean effective pressures (FMEP) as a function of speed and load (measured vs. computed results)

Results show that structured cylinder liners exhibit the lowest friction losses near their top dead centres (TDC). Liners produced with other manufacturing processes show very similar friction losses as well. This indicates that friction losses depend more on engine speed than on engine load, regardless of the liner surface structure.

In contrast to other lubricated components (e.g., fluid film bearings), higher engine speeds result in reduced friction. This is due to a decrease in mixed friction: a consequence of higher surface speeds and related hydrodynamic pressures. In the measurements, the correlation between friction and speed increase can be explained by the journal bearings (main bearings and connecting rod bearings).

Surface topology effects on oil consumption

The assessment of the oil emissions in the investigated engine relied on the results obtained in the piston ring simulation. Further input, taking into consideration thermodynamic quantities, was directly determined by ITV, using the test engine, and consequently provided to IMK.

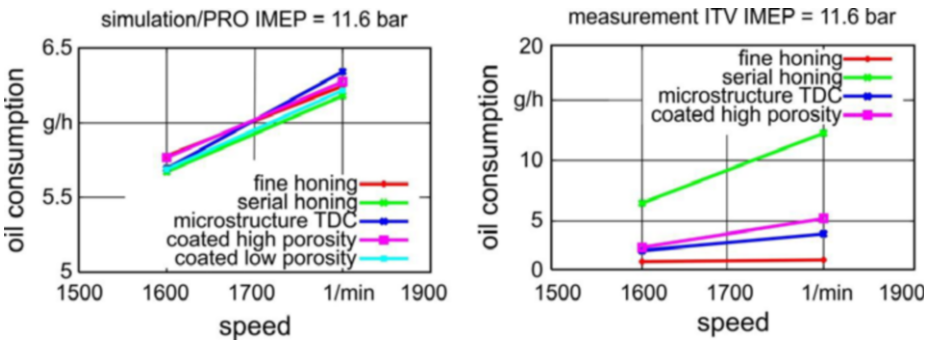


Figure 3-26: Oil consumption as a function of load and speed (measured vs. simulated)

As can be seen from Figure 3-26, measured oil consumptions correlate well with the simulated results as far as load and speed dependencies are concerned. Structured liners exhibit lower oil consumption behaviour compared to all other liners, especially at lower speeds. Deviations between measured and simulated results are very likely

related to the unknown liner distortions caused by assembly and thermal effects, as mentioned above.

3.6 Conclusion

The main objective of this subproject consisted in the development of simulation techniques for the tribological characterisation of deterministic and stochastic surface structures with regards to friction, wear and oil consumption in the piston ring-cylinder system.

Based on fluid dynamic computations, the influence of micro-dimple geometry on the load carrying capacity of lubricated contacts was investigated in the first phase. Results clearly show that micro-dimples can support an increased load carrying capacity, while details in the cross section geometry of the dimples exhibit only a minor influence on hydrodynamic loads. In addition, the effects of different dimple configurations were investigated. It was concluded that the exit length is the most relevant geometric feature for an increased hydrodynamic pressure.

In the second project phase, the concept of flow tensors was used to transfer the results of the first phase to the piston ring/cylinder liner system. Calculation of the principal values of the flow tensor (i.e., the flow factors), the friction factors, and the contact pressures was performed using the program FLOSIM. The obtained results were stored in lookup tables as a function of the gap height. Based on these tables, subsequent programs (KORI, PRO) were employed to compute piston ring motion, piston ring friction, and oil consumption.

Four different liner manufacturing techniques were compared: honing (series process), fine honing, machining and thermal coating. Results show that close to the top dead centre (TDC) position, structured (dimpled) liners exhibit their lowest friction rates. All other surfaces show very similar friction rates. Furthermore, surfaces with micro-dimples are characterised by low oil consumption, especially at low engine speeds.

Test results from the one cylinder test engine, provided by ITV, were used to validate the simulation. A comparison between test and simulation shows a high level of agreement between the measured and the simulated results.

4 Microstructuring by means of cutting processes

*Institut für Fertigungstechnik und Werkzeugmaschinen (IFW), Leibniz Universität Hannover
B. Denkena, J. Kästner, T. Götttsching*

4.1 Objective and approach

Goal of this subproject was to explore and develop a cutting process for the manufacturing of high-quality, friction-reducing micro-dimples. Prerequisite was the use of a single-edge cutting tool. To meet this challenge, the following subgoals were defined:

- Identification of the correlations between process and system variables and the geometry and quality of micro-dimples
- Development of strategies for machining the inner surfaces of cylindrical components

To this purpose, the correlations and interactions between the process variables and the geometry and quality of the micro-dimples to be machined had to be determined. This was necessary in order to define process limits as well as to determine process parameters and tool geometries for high-quality machining. To transfer these results to tribologically stressed components like cylinder liners, economically efficient strategies for the machining of inner walls of cylinder surfaces had to be developed.

To achieve these goals, the following approach was selected: The basics of a novel cutting technology for high-quality machining of geometrically defined micro-dimples with single-edge cutting tools were developed by means of fly-cutting experiments under variation of the system and control variables. Based on the experimental methods developed during the course of the project, the chip formation process was analysed for the present process kinematics. Consequently, material-, component- and tool-dependent as well as kinematic parameters influencing the quality characteristics of micro-dimples were identified and analysed. They were evaluated and classified with respect to the quality characteristics surface quality and burr dimensions. Using an analogue examination of the processes in the chip formation zone, basic correlations and interactions could be determined.

These basics were finally integrated in the elaboration and development of a process strategy suitable for the machining of the inner surfaces of cylinder components. The most important aspects were the correlations between geometry and kinematics, their influence on the arrangement and the geometry of micro-dimples, and the existing process limits. By transferring these results onto the demonstrator “Cylinder Liner” developed within the scope of this joint research project, the suitability and usability of this method could be validated. The integration of the microstructuring process within existing process chains as well as the tool systems required for this purpose were exemplarily illustrated for this demonstrator.

4.2 Experimental set-up – fly-cutting tests

To investigate the basic correlations between process variables, quality characteristics and chip formation mechanisms, fly-cutting tests were carried out on a Blohm Profimat 307 profile grinder, where the rotating cutting tool cuts through a plane surface (Figure 4-1). As the cutting tool oscillates around the peripheral surface of an aluminium disc and is simultaneously displaced in axial direction, the cutting edge of the tool describes a helical trajectory along the workpiece surface (Figure 4-1). The feed rate is negligible, as it is significantly lower than the cutting speed. The axial feed is larger than the highest expected micro-dimple width. Thus, a mutual interaction between adjacent micro-dimples can be excluded. By clamping the specimen with an inclination, micro-dimples with an increasing depth can be created. Due to the large rotational radius ($r_{rot} = 140 \text{ mm}$), the cutting edge enters and exits the workpiece surface at a very flat angle. In this way, the specific effects occurring at tool entry and exit can be examined.

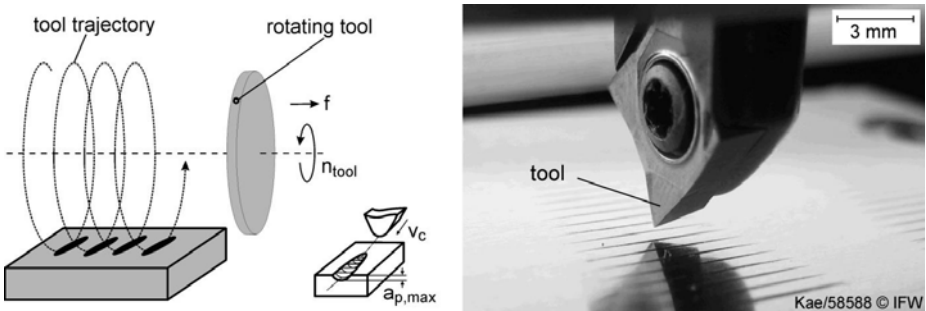


Figure 4-1: Fly-cutting test procedure

Test materials

Globular cast iron (GJS400), hypereutectic aluminum-silicon cast alloy (AlSi17-Cu4Mg) as well as a thermally sprayed high-density iron molybdenum coating (Fe50Mo) were used as test materials. These three materials are typically used in cylinder liners although they differ considerably in their non-homogenous structural texture. Figure 4-2 compares the microstructure of the materials used. Most tests were carried out using ferritic carbon steel (S235JR) with a finely grained homogenous structure.

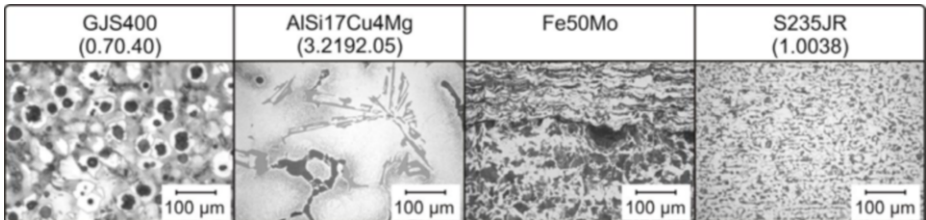
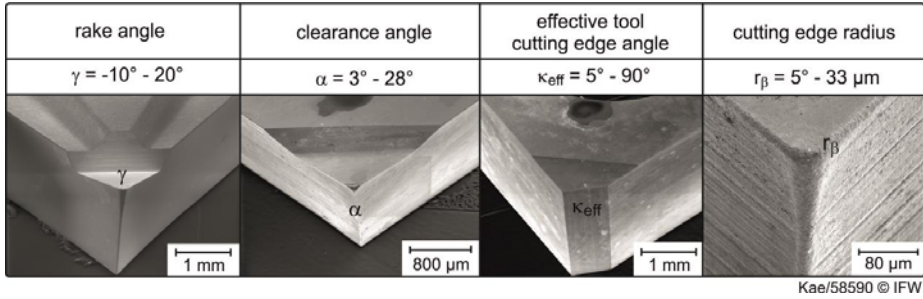


Figure 4-2: Test materials

Test tools

For the test series, CCGT0602 rhombic fine-grain indexable inserts for hard alloy were used. To ensure good comparability, only sharpened cutting edges were applied. Figure 4-3 shows the geometries varied at the cutting edge. Rake, clearance and effective tool cutting edge angles were achieved by grinding. Specific cutting edge radiuses of $r_\beta = 5 \mu\text{m}$ to $30 \mu\text{m}$ were realised via the Magnetfinish process.



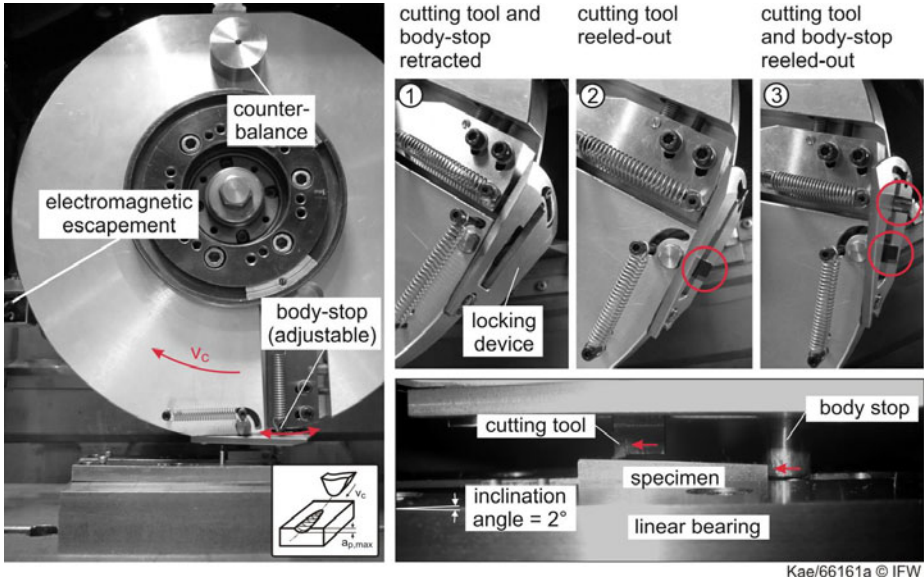
Kae/58590 © IFW

Figure 4-3: Tools with different geometries

The analytical methods introduced above proved insufficient for the identification of the correlations between process variables and the quality characteristics surface quality and burr dimensions. For this reason and taking the used kinematics into consideration, novel methods for the measuring of highly-dynamic cutting forces, as well as for the generation of chip roots, were developed.

Formation of chip roots by means of a quick-stop device

In the following, the design, structure and validation of the quick-stop device is shown for the kinematics used for microstructuring (Figure 4-4). The cutting tool as well as the body-stop can be moved into the aluminium disc by pivoting (cutting tool) or by linear displacement (body-stop). They can be locked by means of a special locking device. All guides have clearance fits with narrow tolerances. The distance between the cutting tool and the body-stop is adjustable, too. In this way, quick-stops along the cut are possible at different positions. During the test, the aluminium disc first rotates with a defined cutting speed above the specimen. By manual release of an inductive actuator, the locking device is actuated shortly after passing the specimen. After that the cutting tool and the body-stop are abruptly reeled out, supported by the spring and the centrifugal forces. In case of a repeated passing of the specimen, the cutting edge enters each time with a pre-defined depth of cut into the surface of the specimen. As soon as the desired quick-stop position is reached, the specimen is abruptly accelerated in cutting direction by the adjustable body-stop. The specimen is screwed to the slide of a spring-loaded dovetail guide and is held during the cut in its position by means of a slotted cylinder bolt, until the body-stop is retracted. Due to the slight inclination of the guide (inclination angle = 2°), the specimen moves minimally downwards, thus providing for an even quicker stop with an increased reproducibility.



Kae/66161a © IFW

Figure 4-4: Structure and functioning of the quick-stop device with adjustable body-stop

The quick-stop device was validated at cutting speeds v_c ranging between 30 and 300 m/min by means of SEM analysis of the chip roots. The SEM images in Figure 4-5, left, show four chip roots machined under identical conditions at a cutting speed of $v_c = 240$ m/min. The nearly identical quick-stop position as well as the shape of the chip roots (chip length, chip flow direction) suggest an appropriate reproducibility. In addition, no imperfections which would suggest kinematic errors or vibrations during the quick-stop can be seen in the chip area. Figure 4-5, bottom left, compares the chip roots for systematically varied cutting speeds in the range of $v_c = 30$ m/min to 300 m/min. Here, it is already possible to recognize cutting speed-dependent chip formation effects, such as a decreasing chip compression ratio with higher cutting speeds. Similarly, the dependence of the acceleration distance (difference between quick-stop position and desired quick-stop position) on the cutting speed is quite evident (Figure 4-5, right). The differing acceleration distances show a quasi-linear behaviour for the respective cutting speed range. This means that the acceleration distance increases by $1.66 \mu\text{m}$ per m/min. Despite the large acceleration distances compared to the depth of cut, comprehensive analyses prove no restrictions when determining the various impacts on chip formation.

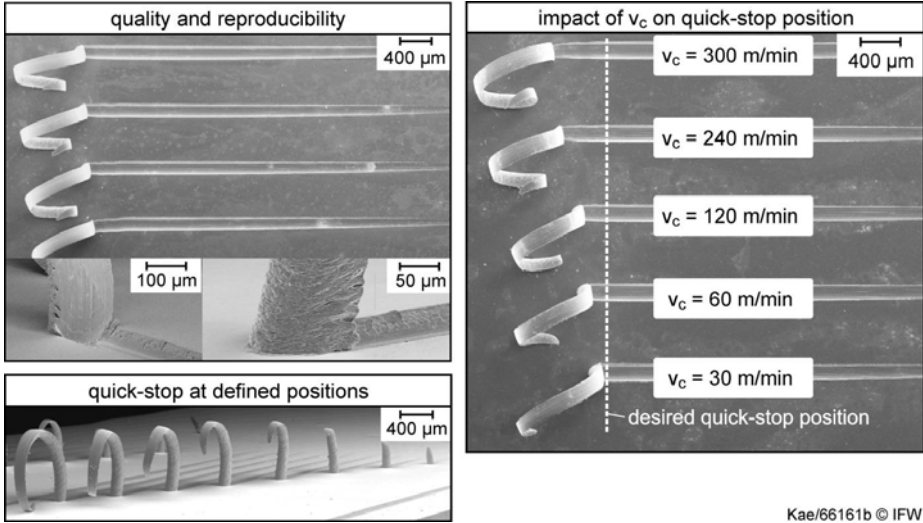


Figure 4-5: Validation of the quick-stop device at defined positions

Highly dynamic cutting force measuring method

In order to describe the mechanisms during the cut and with special consideration of the materials used when machining cylinder liners, a highly dynamic cutting force measuring method was developed and validated. For this purpose, KISTLER 9213 one-component piezo force sensors were applied. To measure the cutting force as well as the passive force at the same time, two sensors had to be used. The specimens were adhesively bonded to the sensor. Figure 4-6 shows the structure of the cutting force measuring system.

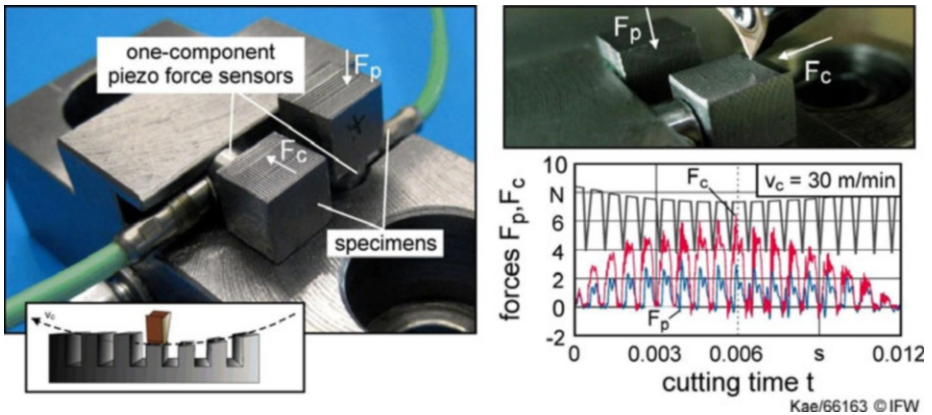


Figure 4-6: Highly dynamic cutting force measuring method

The natural frequency of the sensors used was $f_0 = 27$ kHz without and $f_0 = 22$ kHz with a specimen weighing 4 grams. To get exact results for subsequent tests with dif-

ferent materials, the force sensors were displaced along slotted specimens at cutting speeds ranging from $v_c = 30$ m/min to $v_c = 360$ m/min. Figure 4-6, bottom right, shows the cutting force and the passive force while machining at $v_c = 30$ m/min. The cutting force characteristics describe the slotted surface topography exactly. The validation of the test results proved that the sensors can be reliably used in processes characterized by an excitation frequency of $f_{err} = 5.2$ kHz. For higher excitation frequencies, the measured signal level is still significant, but the signal itself is already superimposed by harmonics.

4.3 High-quality cutting of micro-dimples

For the reliable application of machined micro-dimples in tribological systems, quality characteristics like cutting area topography, burr dimension, and contour accuracy have to be considered. In the following, all relevant cutting correlations as well as their influence on the resulting quality of micro-dimples are explained. In the first place, process-, tool- and material-specific parameters and interactions are examined.

Cutting edge: mechanisms

When cutting a micro-dimple, the cutting edge enters into the surface in a circular arc with a depth of cut of $a_p = 0$ μm , reaches a maximum depth of cut of $a_{p,max}$ and exits the surface with a depth of cut of $a_p = 0$ μm . No geometrical deviations from the desired contour and modifications depending on the depth of cut of the machined surface topography can be identified. According to the characteristics of the burr dimensions shown in Figure 4-7, the burr volume V_G follows a parabolic curve along the cut.

From the entry of the cutting edge up to the maximum depth of cut (1 - 2), the curve is characterised by a steep increase of the burr volume, reaching its maximum in the range of the maximum depth of cut (2). This increase of the burr volume is due to the quantity of the material that is plastically deformed by the cutting edge. The quantity increases exponentially along the depth and the cross-section of the cut. At the same time, there is an increased amount of material, overflowing the free edges and forming a burr. In the exit area of the cutting edge (3), the decrease of the burr dimensions is less than their previous increase in the entry area despite the decreasing depth of cut. The cross-section of the cut decreases exponentially, but not the cross-section of the chip, as seen in the SEM image shown in Figure 4-7, right. For the maximum depth of cut (2), the cross-section of the cut is maximal as well, going along with a high friction between the separated chip and the cutting surface. The friction forces are higher than the forces required for the chip compression ratio so that a decrease in the cross-section of the cut results in only a minimal decrease in the chip compression ratio. For the same depth of cut, the material quantity overflowing the free edges is consequently larger than in the entry area. The asymmetrical burr formation can be explained by the fact that the cutting speed vector enters into the surface in the entry area of the cutting edge and exits it in the exit area. The con-

siderably higher burr volume at the exit of the cutting edge is caused by the chip tear-off.

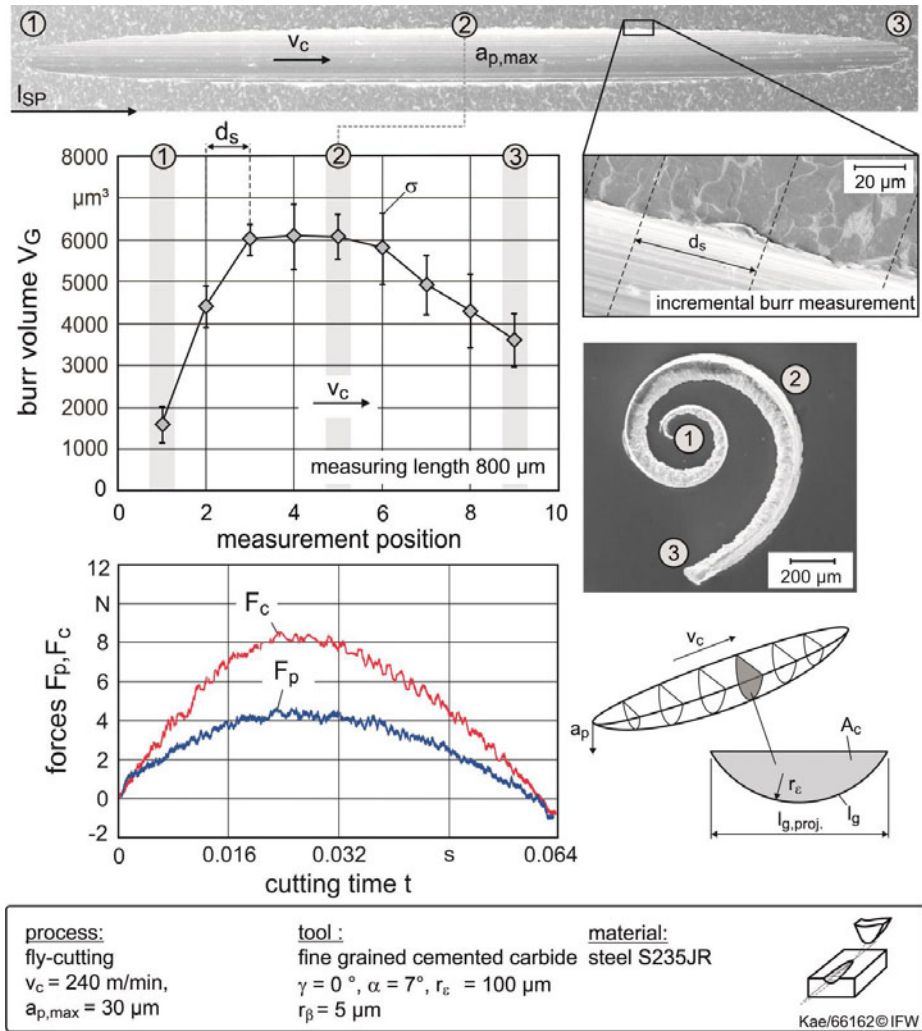


Figure 4-7: Formation of the burr volume and the chip along the cut

The dynamic change of the cutting conditions along the cut is accompanied by a dynamic change of the machining forces. As shown in Figure 4-7, bottom, the absolute cutting and passive forces describe a parabolic curve so that the maximum machining forces are in the range of the maximum depth of cut. The variation of the force signals, as can be seen in the SEM images, is caused by a discontinuous burr formation.

Influence of cutting speed on quality characteristics and chip formation

To identify cutting speed-dependent correlations for the presented fly-cutting process as well as the optimal cutting speed for high-quality machining of micro-dimples, the latter was varied in five steps from $v_c = 30$ m/min to $v_c = 480$ m/min. Consequently, the quality characteristics, i.e., machined surface topography, burr dimension, and component subsurface, were compared with the chip formation process (Figure 4-8).

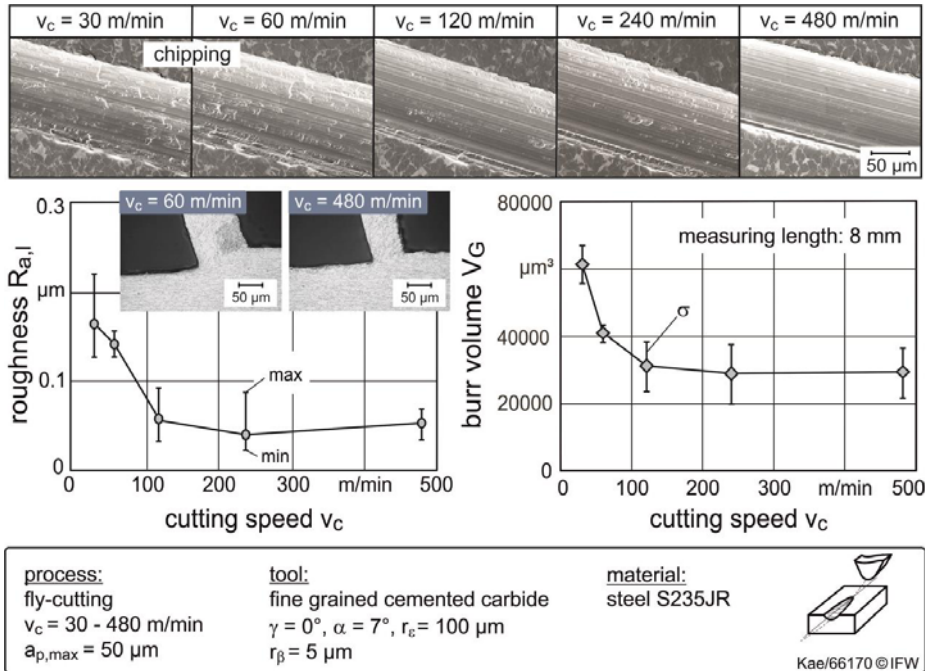


Figure 4-8: Influence of cutting speed on machined surface topography, burr dimensions and chip formation

At small cutting speeds (< 100 m/min), the surface exhibits distinct chipping in cutting direction. Micrographs show a plastically deformed zone of 2 μm to 3 μm thickness in the machined surface. At higher cutting speeds, the topography of the machined surface is comparatively flat, without distinct chipping and plastic deformations. This trend can also be observed for the longitudinal roughness (Figure 4-8, left). With increasing cutting speeds, the roughness decreases exponentially from $R_a = 0.17$ μm to $R_a = 0.04$ μm , whereas no further deviations can be observed in the cutting speed range from $v_c = 120$ m/min to 480 m/min. At cutting speeds below $v_c = 100$ m/min, the burr volume decreases exponentially from $V_G = 60,000$ μm^3 to $V_G = 30,000$ μm^3 . No significant deviations can be observed for cutting speeds from $v_c = 120$ m/min to 480 m/min either. As shown by the SEM images in Figure 4-8, the burrs increase and become more homogenous with increasing cutting speeds.

The decrease in chipping, in plastic deformation of the subsurface as well as in burr dimensions with increasing cutting speeds can be explained by the deformation processes in the chip formation zone. The polished micrograph sections of the chip roots in [Figure 4-8](#) show that the chip compression ratio and the chip thickness decrease when the cutting speeds are increased from $v_c = 60$ m/min up to $v_c = 480$ m/min. This results in a larger shear angle and a smaller shearing cross-section. The simultaneous decrease in the chip surface contact area results in a decreased coefficient of friction. In addition, the increasing strain rate and strain concentration zone are characterized by a stronger shear localisation. According to [BEN02] and [TOE11], this leads to a thermal softening of the material which counteracts the hardening occurring during the chip formation process. The lower deformation content in the chip formation zone is accompanied by a reduction in the 'ploughing' processes, causing chipping and plastically deformed subsurfaces. The energetically more favourable material separation is characterised by the specific cutting force, which declines by about 65 % for the respective cutting speed range.

As demonstrated by the presented results, higher cutting speeds are favourable for the manufacturing of high-quality micro-dimples. For this reason, cutting speeds above $v_c = 120$ m/min were selected for the further course of the process.

Tool-specific parameters influencing the quality of the micro-dimples and the chip formation process

In the following, tool-specific parameters which influence the quality characteristics and the chip formation are described. In a first step, wedge geometry and shape of the cutting edge are examined. In a second step, the cutting edge profile is considered.

Clearance angle

The examination showed that the clearance angle has no influence on the quality characteristics in the respective variation range of $\alpha = 3^\circ$ to 28° . However, it should be noted that the use of clearance angles above $\alpha = 15^\circ$ is not process-reliable due to unpredictable cutting edge breakouts.

Rake angle

The rake angle was varied in 10° -steps from $\gamma = -10^\circ$ to 20° at a constant clearance angle ($\alpha = 7^\circ$). Compared to large clearance angles, no cutting edge breakouts were identified for positive rake angles ($\gamma = 20^\circ$). Similarly to the preceding chapter, the changing of the quality characteristics is described here as well; furthermore, the most important correlations and interactions are exemplified on the basis of a chip formation analysis. As shown in [Figure 4-9](#), the rake angle affects burr dimensions and chip formation considerably. For the respective rake angle range, the burr volume V_G linearly decreases by about 70 %.

While the rake angle influences the specific cutting forces minimally, the specific passive forces significantly decrease with positive rake angles ([Figure 4-9](#), middle).

These differences diminish with the depth of cut but do exist throughout the complete range of the depth of cut. The force ratio increases progressively with the increase of the depth of cut, meaning that there is a direct correlation between the cutting force and the depth of cut. On the other hand, the force ratio level increases with a positive rake angle, which results from a decrease in the specific passive forces. This rake angle-dependent dominance of the passive force is also seen in the rotating experiments described by [DEN07], who explains it with the change of the direction of the resulting cutting force vectors in dependence on the rake angle.

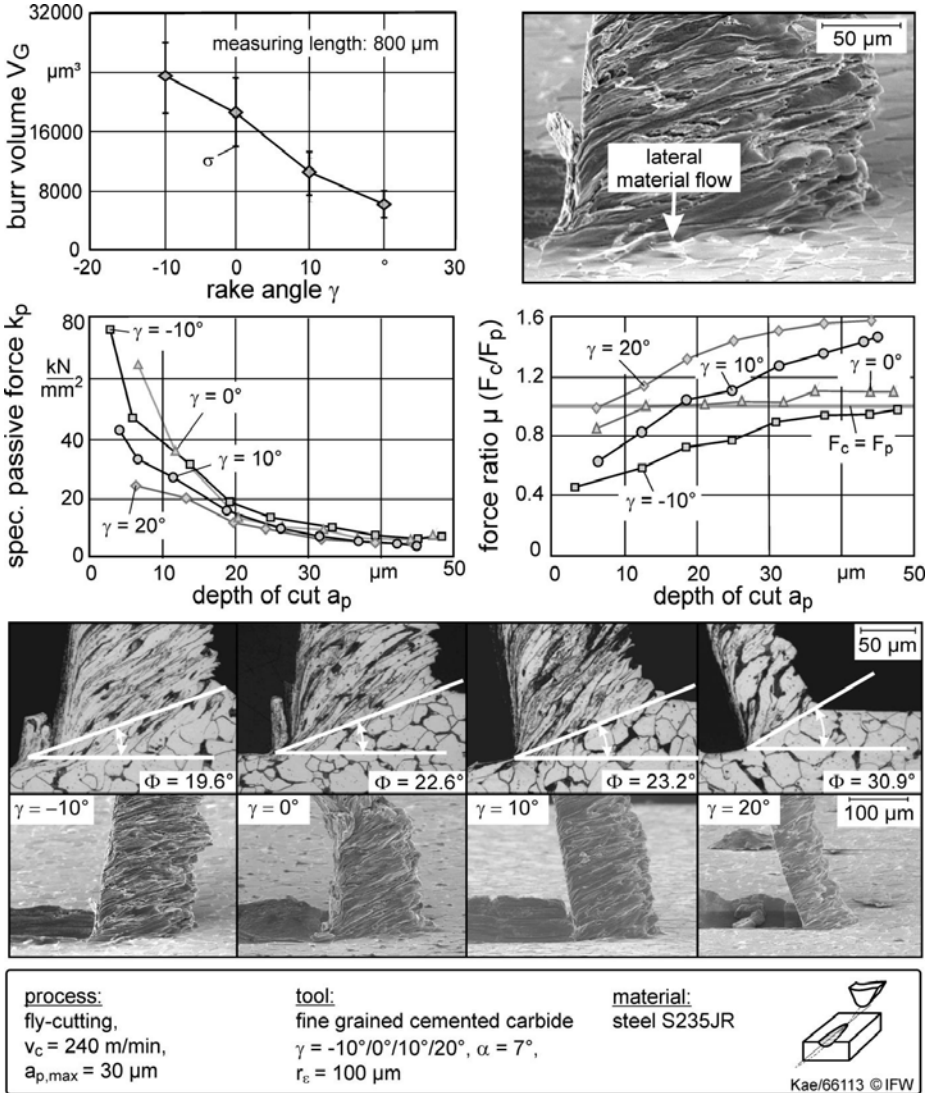


Figure 4-9: Influence of the rake angle on burr dimensions, forces and chip formation

The chip roots formed for different rake angles with identical process variables are compared in [Figure 4-9](#), bottom. The degree of deformation in the chip formation zone decreases with positive rake angles, resulting from a decrease in the chip compression ratio and the accompanying increase of the shear angle. At a rake angle of $\gamma = 20^\circ$, the compression level is very low ($\lambda \rightarrow 1$) so that the initial material texture can clearly be seen in the chip roots. According to [DEN07], this correlation can be explained by the fact that the chip flow on the chip surface is less likely to be diverted when the rake angles are positive, i.e., the chip flow on the chip surface is energetically more favourable. Thus, chip compression ratio, shear cross-section, and chip surface contact are reduced, resulting in an energetically more favourable separation process. Moreover, the SEM images show how the measured burr volumes increase with negative rake angles. Much more material is formed at the sides of the chip root, which indicates a distinct lateral flow in front of the cutting edge. Part of the material, which has been accumulated along the free edges at the sides of the chip root, remains in form of a burr.

Cutting edge radius

Due to the small depths of the cuts, the cutting edge radius r_β plays an important role when creating micro-dimples. The extent to which the cutting edge radius influences the quality characteristics of the micro-dimples as well as the processes taking place during the chip formation is explained in the following paragraphs. The tests were based on a variation of the cutting edge radius in five steps from $r_\beta = 5 \mu\text{m}$ to $30 \mu\text{m}$. A confocal microscope was used to take topographic images of the middle of a micro-dimple manufactured with different cutting edge radiuses and with a maximum depth of cut of $a_{p,\text{max}} = 30 \mu\text{m}$ ([Figure 4-10](#), top). The influence of the cutting edge radius on the chip formation as well as the longitudinal roughness profiles and burr dimensions is shown in [Figure 4-10](#) and discussed below.

For a cutting edge radius from $r_\beta = 5 \mu\text{m}$ to $15 \mu\text{m}$, the roughness first increased linearly from $R_z = 0.28 \mu\text{m}$ to $R_z = 0.49 \mu\text{m}$. According to [ALB60, SUB08], this increase is based on the 'ploughing effects', whereby the material sporadically flows below the cutting edge, leaving chipping on the generated surface. At $r_\beta = 15 \mu\text{m}$ to $30 \mu\text{m}$, the longitudinal roughness decreases to $R_z = 0.32 \mu\text{m}$ again. [BET71] explains this decrease with the roll-smoothing effects: On the one hand, due to larger cutting edge radiuses, more material flows out of the stagnant area below the cutting edge; on the other hand, due to more negative rake angles, this material is incorporated more evenly into the surface.

Similarly to the longitudinal roughness, the burr dimensions also show a contrary profile. First, they increase linearly from $r_\beta = 5 \mu\text{m}$ to $20 \mu\text{m}$ by nearly 400 %. According to [JIV08], this rise is due to the expanded stagnant area ahead of the cutting edge. The simultaneous increase in material gathered up ahead of the cutting edge is, on the other hand, accompanied by a considerably stronger lateral flow in the direction of the free edges. As the rounding along the edge radius and, thus, along the cutting edge zone is evenly formed, the effective rake angle in the area of the free edges

becomes extremely negative. It additionally contributes to the lateral material flow over the free edges. However, when the cutting edge radius increases to $r_\beta = 30 \mu\text{m}$, the burr dimensions decrease by nearly 30 % of the previous increase.

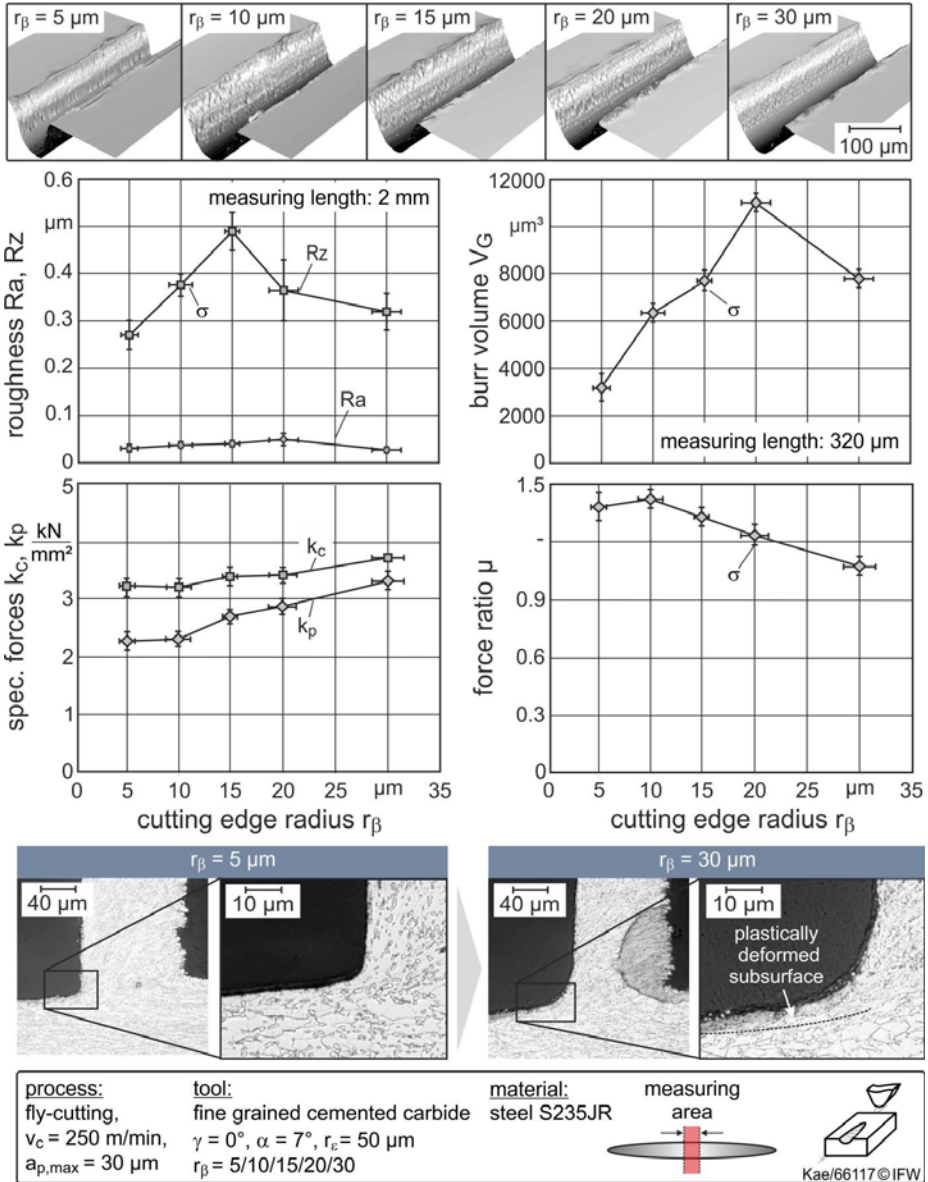


Figure 4-10: Influence of the cutting edge radius on longitudinal roughness, burr dimensions, forces and chip formation

A detailed analysis of the cutting edges rounded by the Magnetfinish technology shows that the cutting edge of an extremely rounded tool ($r_\beta = 30 \mu\text{m}$) is also recessed due to the long machining time, leading to a larger edge radius r_ε . In this way, the effective tool cutting edge angle κ_{eff} at the free edges is reduced, resulting in decreased burr dimensions (see subsequent chapter).

While the specific cutting force in the considered cutting edge area progressively increases by about 15 %, the specific passive forces progressively increase by about 45 %. The larger rising gradient indicates that the cutting edge radius has a considerable influence on the passive force component. The increasing prevalence of the passive force is consistent with the linearly decreasing force ratio. According to [JIV08], this shift is due to changed geometrical contact conditions: on the one hand, larger cutting edge radiuses lead to a larger contact surface. On the other hand, they result in a considerably more negative effective rake angle γ_{eff} and, thus, in a shift of the resulting cutting force vectors in direction of the passive force. Contrary to the findings of [JIV08], neither an increased chip compression ratio nor modified chip shapes or segmentation towards large cutting edge radiuses could be observed. As can be seen from the chip roots shown in Figure 4-10, bottom, the subsurface is plastically deformed for a cutting edge radius of $r_\beta = 30 \mu\text{m}$ up to a depth of 5 μm to 6 μm . The smooth transition from the stagnant area to the subsurface indicates that the material flows below the cutting edge and is then incorporated into the surface by ploughing and roll-smoothing processes, as already mentioned before.

Tool profile geometry

In cutting tool design, the tool profile geometry is of a paramount importance. Here, the effective tool cutting edge angle was identified as the most important parameter to influence the processes taking place on the free edges. To examine the correlations which result from a variation of the effective tool cutting edge angles, the angles were systematically modified in five steps from $\kappa_{\text{eff}} = 17^\circ$ to 79° . The tool cutting edge angle on the opposite side was kept constant at $\kappa_{\text{eff}} = 50^\circ$. Figure 4-11 shows the correlation between the development of the burr dimensions and the effective tool cutting edge angle as well as the processes taking place in the chip formation zone.

The burr volume exponentially increases by a factor of 24 for the range of the observed effective tool cutting edge angle. This trend can also be seen in the topographic images (Figure 4-11, top right). For very small effective tool cutting edge angles, the burr volume asymptotically approximates zero. In order to find out the reason for these significant differences, the chip formation process is analysed in the following. Figure 4-11, middle, compares chip roots and their micrographs created with effective tool cutting edge angles of $\kappa_{\text{eff}} = 17/50/66^\circ$. To illustrate the explanations, the bottom part of Figure 4.11 outlines the geometrical contact variables for a small and a large effective tool cutting edge angle. Based on the cross-sectional shape of the chip, which depends on the effective tool cutting edge angle, there are clear differences in chip formation. The micrographs of the chips show that the plastic defor-

mation degree at the free edges decreases with smaller effective tool cutting edge angles.

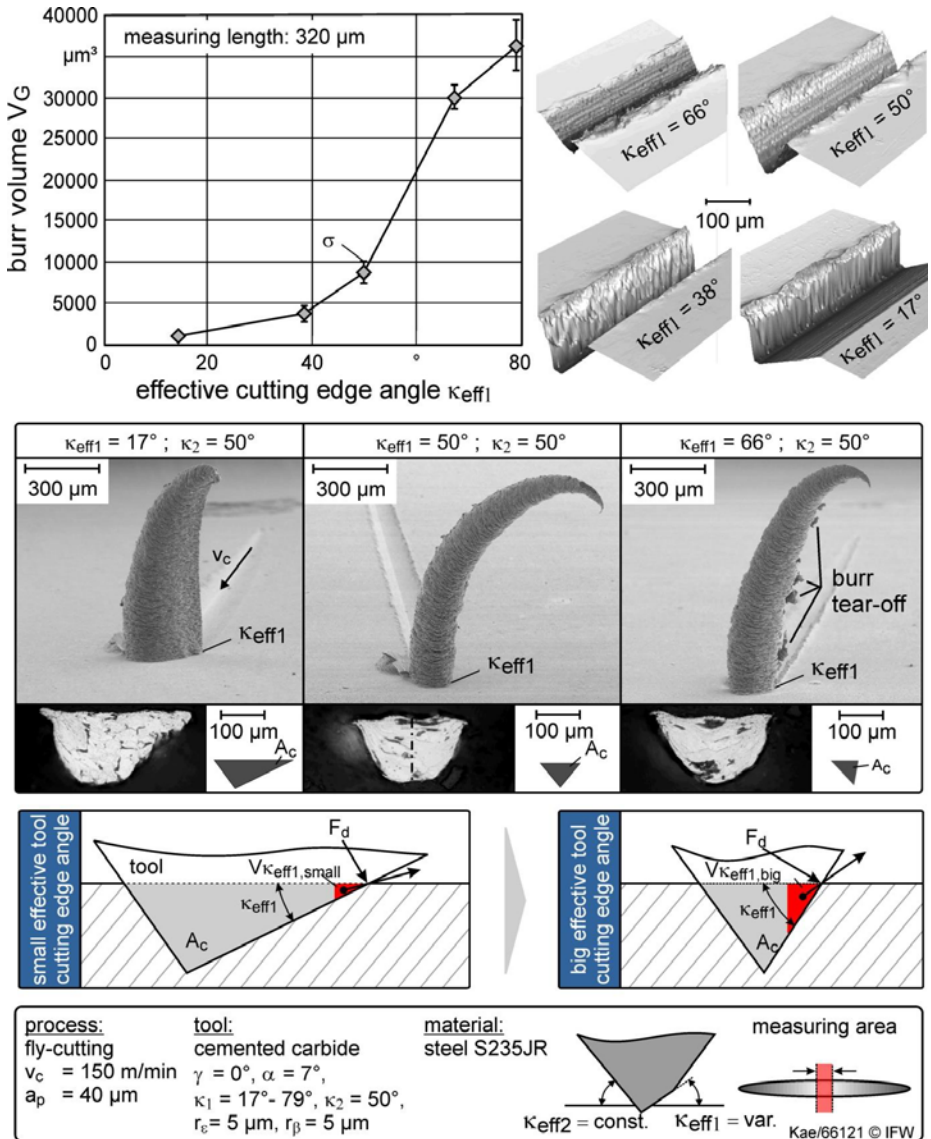


Figure 4-11: Influence of the effective tool cutting edge angle on burr dimensions and processes during chip formation

The exceedingly homogenous chip edge for an effective tool cutting edge angle of $\kappa_{\text{eff}} = 17^\circ$ is another evidence for the dominance of the shear component with smaller effective tool cutting edge angles. This can be explained by different factors. The red

triangles of equal width ($V_{K_{eff,small}}$ and $V_{K_{eff,big}}$) shown in Figure 4-11, bottom, correspond to the material volume accumulated in the area of the free edges ahead of the cutting edge. It can be seen that the material volume which is plastically deformed at the free edges during the separation and which works against the shear localisation increases with the effective tool cutting edge angle. Consequently, the decrease of the burr dimensions with smaller effective tool cutting edge angles can be explained by the fact that the material flow is redirected towards the free surfaces in both directions. In figure 4-11, bottom; this is represented by the arrows which begin at the centres of the surface areas of the red triangles and cut through the free edge. At the same time, the vector of the burr force F_d moves incrementally in the direction of the free edge.

Depending on which tribological parameters of a surface shall be realised by means of micro-dimples, cross-section profiles with small effective tool cutting edge angles at the free edges cannot always be applied, as seen in Figure 4-12.

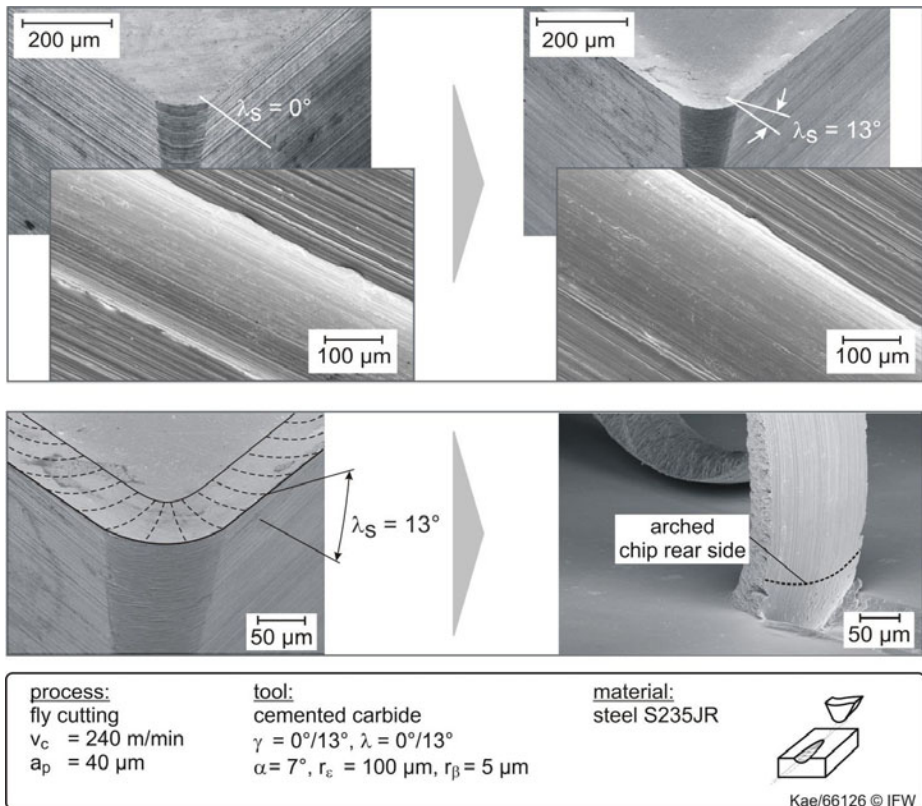


Figure 4-12: Reduction in burr dimensions by use of positive tool cutting edge inclinations

A positive tool cutting edge inclination λ_s counteracts the disadvantageous burr formation of large effective tool cutting edge angles. In this case, a cutting edge is used

whose positive rake angle of $\gamma = 13^\circ$ goes around the edge radius and then changes into a tool cutting edge inclination of the same size.

Along the edge radius, the constant contact conditions are placed orthogonally to the cutting edge. However, the positive rake angle changes into a positive tool cutting edge inclination of the same size. The reduced burr dimensions result from the fact that the positive tool cutting edge inclination as well as the positive rake angle favour shearing in the area of the free edges. Moreover, symmetrical positive tool cutting edge inclinations at the cutting edge lead the material away from the free edges before it reaches the cutting edge. They also concentrate it in the middle of the chip (see the arched chip rear side in [Figure 4-12](#), bottom right).

Material-specific separation mechanisms

It was examined to what extent the results obtained for S235JR steel were also valid for the materials GJS400 and Fe50Mo when applied (i.e., thermally sprayed) to the inner surface of cylinder liners. The processes taking place in the chip formation zone were of special interest here; consequently, these were correlated with quality characteristics, such as burr formation and machined surface topography. [Figure 4-13](#) compares the chip roots as well as the highly dynamic forces measured for the different materials.

Experimental evidence indicates that GJS400 cast iron exhibits a ductile material separation behaviour similar to the one of S235JR steel. Material separation is, however, locally interrupted by phase transitions and inclusions, which is also reflected in the measured highly dynamic forces. The machined surface topography shows open graphite pebbles partly bunching out of the machined surface. In micrographs, plastic deformations in the subsurface due to the separation process can be recognized. They are interrupted (i.e., partially separated from the surface) in the transition areas between graphite pores, ferrite seams, and basic pearlitic matrix due to different mechanical phase properties. The material is characterised by a distinct and uneven tendency to burr formation.

In thermally sprayed Fe50Mo coatings, no continuous chips were formed which can be explained by the fact that most of the material ahead of the cutting edge is separated by cohesive failure in the boundary areas of the sprayed lamella. This separation mechanism is also characterised by the highly dynamic forces measured. Supporting and ploughing effects below the cutting edge nevertheless result in relatively smooth machined surface topographies. Since the adhesiveness of thermally sprayed coating is in the first place based on mechanical clamping of partly fused particles, tear-offs at the free edges can be explained by lacking supporting effects of the surrounding material. The material does not tend to burr formation.

In general, the experiences made for steel can be transferred to the materials used here. Larger cutting edge radiuses result in increased burr dimensions for the ductile materials of S235JR steel and GJS400 cast iron. When machining thermally sprayed Fe50Mo coatings, large cutting edge radiuses have the advantage that they avoid

chipping at the free edges. Similar to S235JR steel, GJS400 cast iron tends to chip at low cutting speeds ($v_c < 80$ m/min). When machining Fe50Mo coatings, no influence on the quality characteristics caused by the cutting speed could be verified.

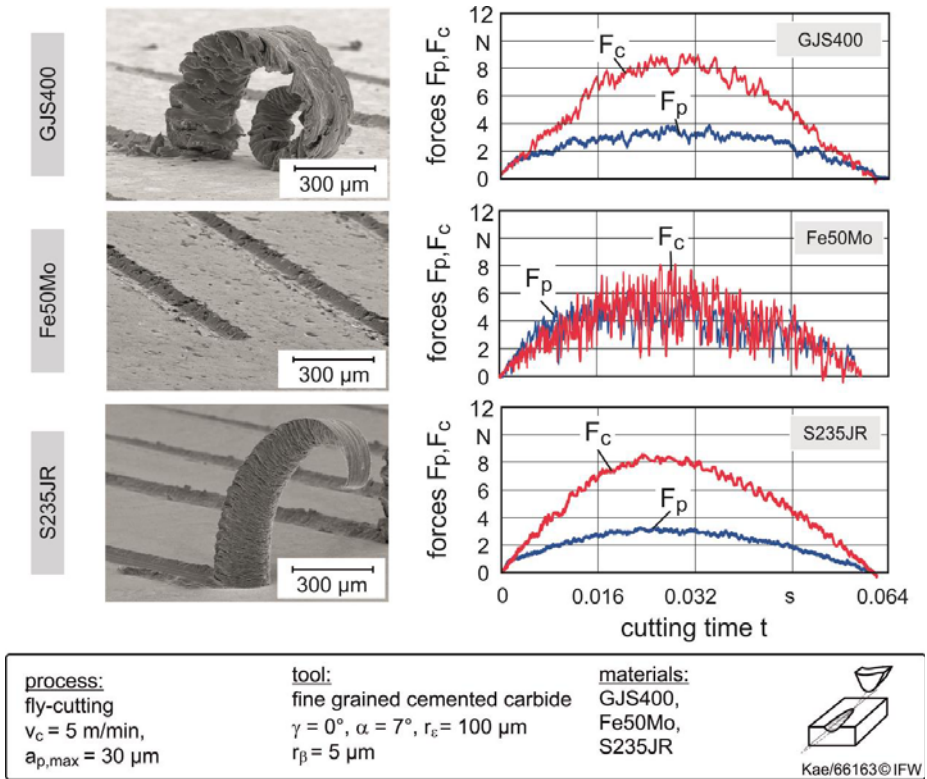



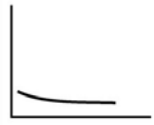
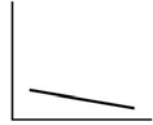
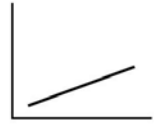
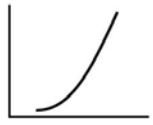
Figure 4-13: Material-specific separation mechanisms

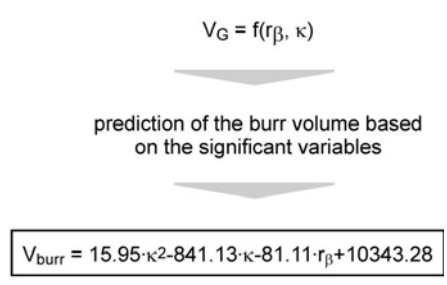
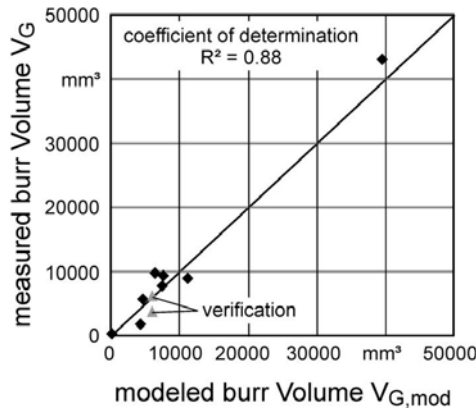
Model for the prediction of burr dimensions

As verified by the results presented above, burr dimensions at the free edges of machined micro-dimples are the most important quality characteristic. With respect to the tribological strain and to avoid subsequent finishing steps, burr formation must be avoided or is at least only tolerable for very small dimensions. The experiments carried out prove that burr dimensions can be influenced to a large extent by the tool geometry. To consider these interactions in the process design of machining micro-dimples, a model based on empirical data was developed to help predict burr dimensions. The burr volume V_G measured at the free edges serves as a basis for comparison. Based on the data determined in test series, the significant variables were identified. The variables cutting speed, depth of cut, rake angle, clearance angle, cutting edge radius, and effective tool cutting edge angle were considered in the significance analysis. For reasons of comparison, all test results, except for the variation of the

depth of cut itself, were compared at a depth of cut of $a_p = 30 \mu\text{m}$. When selecting a model approach, the results were implemented in a regression model where the qualitative characteristics of the burr volume were considered in dependence on the varied size.

The correlations between measured and modelled burr volume are qualitatively outlined in Figure 4-14. Moreover, the respective mathematical subfunctions are given below the single graphs. To determine the significant variables, the mean gradient is defined for each characteristic. Since the values of the gradient are still subject to the units of the respective variable, they have to be normalised. The significant variables are then determined via the ratio of the normalised gradient to the sum of all normalised gradients. The respective significant component of each variable is shown in Figure 4-14, bottom.

depth of cut	cutting speed	rake angle	cutting edge radius	cutting edge angle
				
$y = -4.76x^2 + 359.21x - 302.55$	$y = 21094x^{0.268}$	$y = -234.12x + 7019.5$	$y = 503.14x + 832$	$y = 10.9x^2 - 343x + 1972$
significance				
8.9 %	6.6%	12.6 %	15.1 %	58.4 %



Kae/66171© IFW

Figure 4-14: Correlations between measured and modelled burr volume

Variables whose normalised gradient is larger than 15 % of the sum of all normalised gradients were assumed to be significant. These are the cutting edge radius r_β with a normalised gradient component of 15.1 % and the effective tool cutting edge angle with a normalised gradient component of 58.4 %. By applying linear regression anal-

ysis and rounding off the determined coefficients up to the second decimal place, based on two significant variables, the model equation given in Figure 4-14, bottom right, is able to predict the burr volume. The verification of the model equation is given in Figure 4-14, bottom left. The modelled burr volumes map the measured burr volumes with a coefficient of determination of $R^2 = 0.88$. The model equation is also valid when the input variables are not the input variables of the model, as verified by the grey measuring points (verification).

4.4 Inner structuring of rotationally symmetrical components

Since tribologically stressed components like cylinder liners and thrust bearings generally have cylindrical surfaces, a process strategy was developed to cut micro-dimples into cylindrical surfaces with the help of single-edge cutting tools.

Process development for load-specific inner structuring of rotationally symmetrical surfaces

Based on axially parallel turn-milling, a machining strategy for cutting micro-dimples into the inner surfaces of cylindrical components was developed and analysed systematically. It was realised on a Gildemeister TWIN32 turning machine equipped with a tool holder driven at a maximum revolution speed of $n_{\max} = 4000$ 1/min. As shown in Figure 4-15, a rotating fly-cutting tool is moved with defined radial displacement under axial feed along the surface of a likewise rotating component, cutting non-overlapping micro-dimples below revolution ratio limit along the circumference of the component.

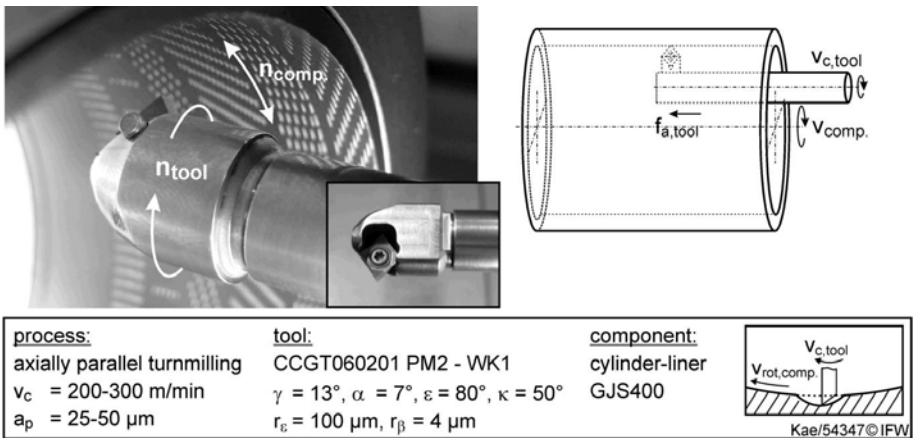


Figure 4-15: Process strategy for internal machining of cylindrical components

For an axially parallel internal machining of cylindrical components, the kinematic correlations and the influence of the process variables on the surface texture (i.e., arrangement of micro-dimples on the surface) as well as the micro dimple geometry and the existing process limits are described in the following. The geometrical and kinematic contact conditions between tool cutting edge and component were ana-

lysed in accordance with the mathematical basics given in [DER94, KRO69] and compared to those achieved by experiments.

Process / tool design and process limits

Kinematic parameters influencing micro dimple arrangement

The parameters which considerably influence the surface characteristics are the axial feed f_{ax} and the revolution ratio (Figure 4-16, top). The revolution ratio λ_n characterises the ratio between tool and component revolution speed. The axial feed f_{ax} defines the distance s_{ax} between two micro-dimples when the component runs parallel to its axis of symmetry. The tangential distance s_{tan} between two micro-dimples along the component's circumference is defined by the component's circumference U_{BT} and the tangential indexing t_{tan} , as follows:

$$s_{tan} = \frac{U_{BT}}{t_{tan}} \quad (4.1)$$

With the revolution ratio λ_n , the tangential indexing can be calculated as follows:

$$t_{tan} = \frac{360^\circ}{\lambda_n} \quad (4.2)$$

Based on the axial and tangential distance, the number of micro-dimples for a rectangular elemental surface D_{MT} with an axial length of edge x and a tangential length of edge y can be determined according to the following equation:

$$D_{MT} = \frac{x}{f_{ax}} \cdot \frac{\lambda_n \cdot y}{U_{BT}} \quad (4.3)$$

Depending on the tribological application, not only the distance between the micro-dimples but also their arrangement is of great importance. In this process, it is characterised by the parallel offset φ_{tan} of two micro-dimples (Figure 4-16, top). Compared to the revolution ratio λ_n , component diameter, surface curvature, and tool trajectory radius have no influence on the parallel offset. The diagram in Figure 4-16, left, shows the calculated curve of the parallel offset in dependence on the revolution ratio $\lambda_n = 10$ to 16; in the diagram on the right, the range is enhanced from $\lambda_n = 10$ to 11.5. In the upper part, optically measured topographic images of machined surfaces are compared. When the parallel offset is $\varphi_{tan} = 0^\circ$, the micro-dimples are arranged in an exact line (i.e. no offset), which is always the case at integral revolution ratios. In the case of half-integral revolution ratios, the overlapping micro-dimples are offset in axial direction by exactly half of their tangential distance (50 % offset). Between an integral and a half-integral revolution ratio, the micro-dimples are incrementally offset to the left (negative sign); between a half-integral and an integral revolution ratio, they are offset to the right (positive sign). With increasing revolution ratio, the tangential indexing t_{tan} and thus the tangential distance s_{tan} of the micro-dimples is reduced.

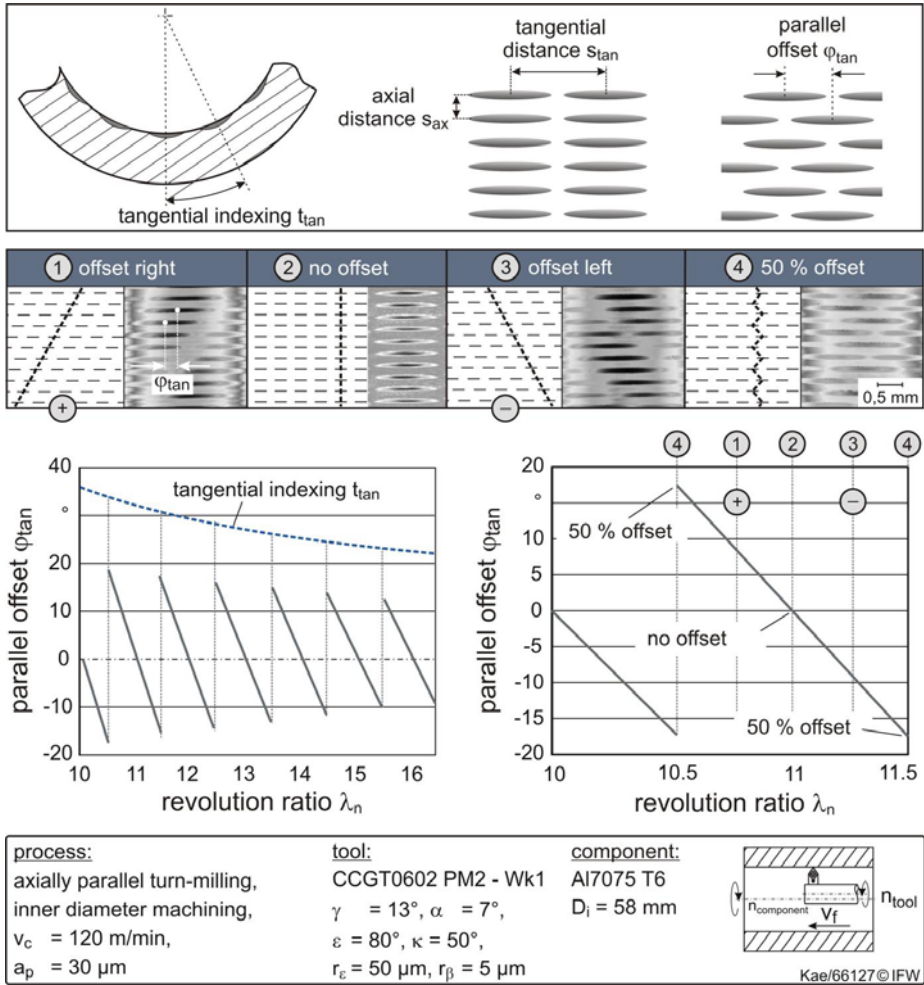


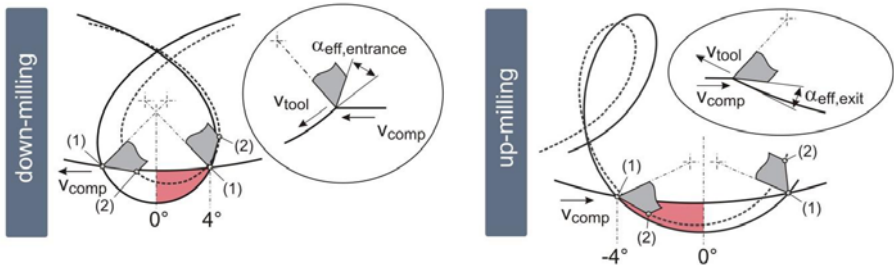
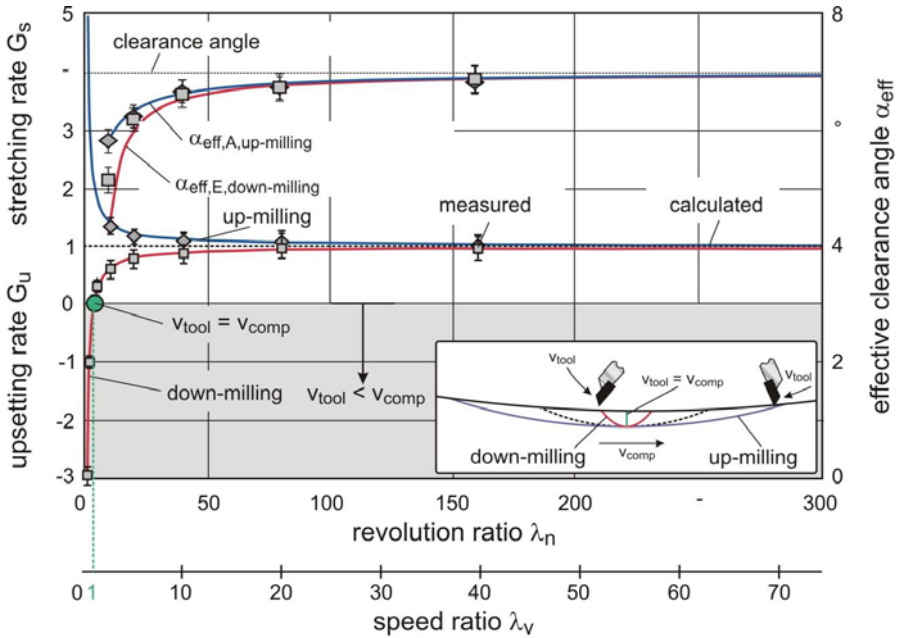
Figure 4-16: Surface characteristics and parallel offset in dependence on revolution ratio

Kinematic parameters influencing micro dimple geometry

In process design, it should be considered that the length of cut varies depending on the up- and down-milling as well as on the revolution ratio between tool and component. In Figure 4-17, the stretching rate G_c and the upsetting rate G_u , which characterise the ratio of the non-distorted length of cut to the distorted one, as well as the effective clearance angle α_{eff} are plotted against the revolution ratio for up- and down-milling. The measured values match the calculated ones very well.

During both up- and down-milling, small revolution ratios result in a severe distortion of the tool trajectory; thus, during up-milling the stretching rate G_s - and during down-milling, the upsetting rate G_u - increases exponentially. The effective clearance angle, plotted in Figure 4-17, has been calculated and determined experimentally in accord-

ance to [KRO69]. During up-milling, this angle is located in the entry area, whereas during down-milling, it can be found in the exit area of the cutting edge. In the case of smaller revolution ratios, the effective clearance angle decreases exponentially to $\alpha_{\text{eff}} = 4.4^\circ$ at $\lambda_n = 10$. The tool clearance angle $\alpha = 7^\circ$ is thus reduced by 2.6° max.



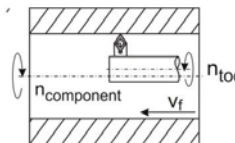
Prozess: axially parallel turn-milling inner diameter machining $a_p = 30 \mu\text{m}$, $\lambda_n = 0 - 300$ $n_{\text{component}} = 14 - 230 \text{ 1/min}$ $n_{\text{tool}} = 2300 \text{ 1/min}$	tool: CCGT0602 $r_{\text{tool}} = 10.15 \text{ mm}$ $\gamma = 13^\circ$, $\alpha = 7^\circ$, $r_e = 100 \mu\text{m}$, $r_\beta = 5 \mu\text{m}$	component: Al 7075 T6 $r_i = 41 \text{ mm}$	
---	--	--	--

Figure 4-17: Influence of the revolution ratio on stretching/compression of the cut and on a reduced clearance angle for up- and down-milling

During up-milling, cutting speeds and feed rates opposing each other result in a stretching of the cut. The trajectory is thus flatter in the exit area of the cutting edge.

As a consequence, the trajectory approaches the rear clearance surface edge of the cutting edge similarly accompanied by a reduced effective clearance angle. During down-milling, however, cutting speeds and feed rates of the same direction result in a compression of the cut. Indeed, the cutting edge enters into the component's surface at a steep angle, but here too, the trajectory of the rear clearance surface edge approaches the clearance surface of the cutting edge with increasing compression, reducing the effective clearance angle. The clearance angle, which is exponentially reduced with smaller revolution ratios, correlates with those of the stretching rate G_s and the upsetting rate G_u . Thus, based on this easily determined parameter, a prediction concerning the clearance angle reduction can be made.

For high-quality machining of micro-dimples, cutting speeds larger than 120 m/min are suitable (Figure 4-8). From tribological viewpoint, the tangential distance between two micro-dimples should be minimal. As a consequence, larger revolution ratios are required, thus, avoiding critical contact conditions between tool and component during the machining of cylinder liners. For the respective depth of cut in the range from $a_p = 0 \mu\text{m}$ to $40 \mu\text{m}$, the clearance angle is only reduced by 0.4° and is therefore not discussed in this context.

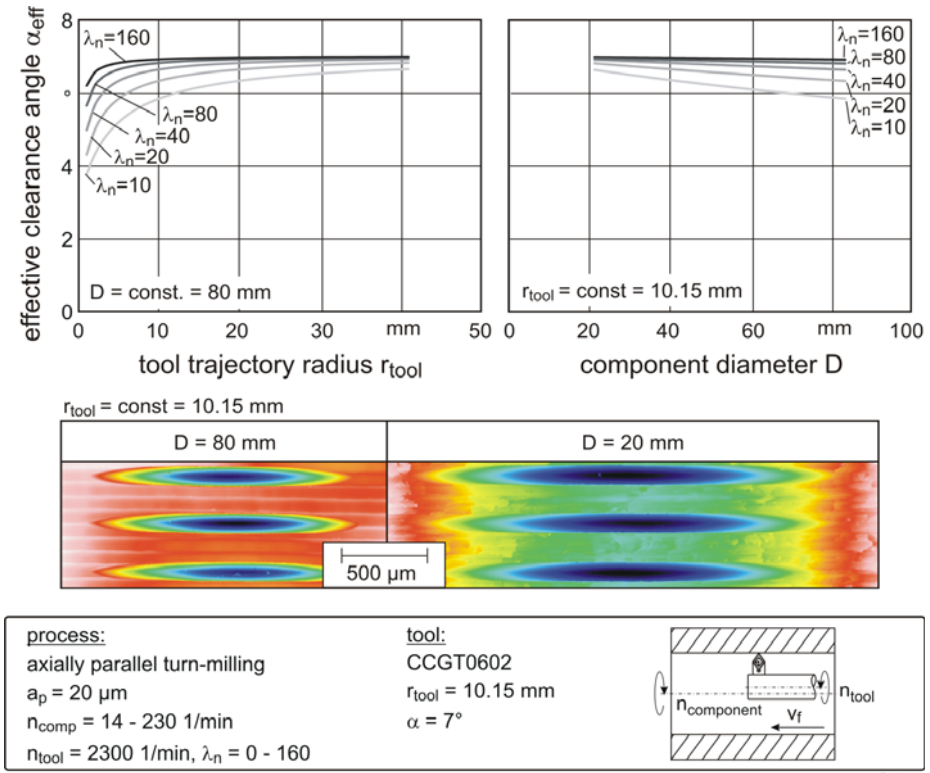
Geometrical kinematic parameters influencing micro dimple geometry

Besides the kinematic parameters, the tool trajectory radius r_{tool} and the component diameter D influence the effective clearance angle as well. Using the up-milling process as an example (Figure 4-18), the effective clearance angle calculated for revolution ratios from $\lambda_n = 10$ to 160 is plotted against the tool trajectory radius ($r_{\text{tool}} = 10.15 \text{ mm}$ to 41.00 mm) and the component diameter ($D = 20.3$ to 83.00 mm).

With smaller tool trajectory radii, an exponential non-negligible reduction of the effective clearance angle α_{eff} can be observed. This can be explained by the fact that for smaller tool trajectory radii, the tool cutting edge enters and exits the component at a steeper angle. Thus, when the cut is stretched or compressed, the generated surface approaches the rear clearance surface of the edge, accompanied by a reduced effective clearance angle. With smaller revolution ratios, the effective clearance angle is linearly more and more reduced, depending on the increasing component diameter. With constant revolution ratios, increasing diameters here result in larger tangential feeds, i.e., in a reduced revolution ratio (see Figure 4-17). If the revolution ratio is changed, and the tangential feed remains constant, the component diameter does not have any influence on the effective clearance angle.

To determine interactions with the component's macro geometry, in this case - the surface curvature, scratch tests were carried out at concave and convex components with diameters from $D = 10 \text{ mm}$ to 80 mm , and machining forces as well as burr and chip formation were analysed. The maximum forces which, according to Figure 4-7, can be found in the middle of a micro dimple are not affected by the component's curvature. In the entry and exit areas of the cutting edge, in particular, no differences can be identified between the machined surface topography and the burr dimensions.

The surface curvature merely affects the entrance and exit angle as well as the length of cut. This is shown in Figure 4-18, middle, where the measured topographic images of internally structured surfaces with diameters of $D = 80$ mm and $D = 20$ mm are compared. With smaller component diameters, tool trajectory radius and component radius approximate each other. As a result, the cutting edge enters the surface earlier and flatter and exits it later and flatter. When machining convex surfaces, this correlation is just the opposite. The flatter angles during the entry and the exit of the cutting edge are also reflected by the force signal and the chip formation along the cut; however, they have no influence on the micro dimple quality, as already mentioned above.



Kae/66169 © IFW

Figure 4-18: Clearance angle reduction in dependence on the tool trajectory radius and the component diameter for machining of inner surfaces

Load- and speed-specific structuring of cylinder liners

As the tribological stress (load, sliding speed) varies along the height of a cylinder liner, it is necessary to locally adjust the surface parameters by means of the micro-dimples. As summarised in Figure 4-19, the process developed for inner structuring of cylindrical components offers several adjustment possibilities.

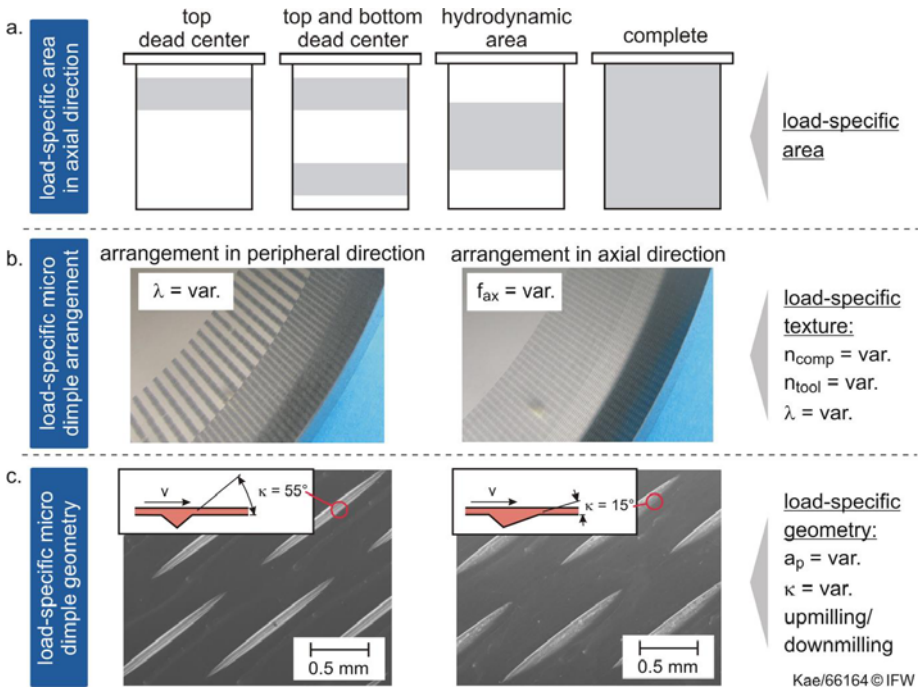


Figure 4-19: Variables for local load-specific cutting of micro-dimples

First, the area to be machined, e.g. the top and bottom dead centre area or the hydrodynamic area, can be flexibly specified (Figure 4-19 a). As already explained in the preceding chapter, the revolution ratio can be used to adjust the micro-dimple distance and arrangement in peripheral direction. Similarly, the axial feed f_{ax} can be used to adjust the micro-dimple distance in axial height direction (Figure 4-19 b). Micro-dimple geometry and dimensions (Figure 4-19 c) can however also be used to realise a local and variable functionalisation of the cylinder liner by selecting the respective process (down-milling/up-milling), the tool feed, and the cross-section geometry of the cutting edge. The tribological performance of load-specific structured surfaces is explained in detail in Chapter 7.

Microstructuring tools for machining of cylinder liners

When measuring the form of cylinder liners to be machined and honed for testing them on a test rig within the scope of the subprojects 1 (IMK) and 5 (ITV), out-of-roundness and deviations from their cylindrical form of up to $18 \mu\text{m}$ were measured. These resulted in considerable deviations of the depth of micro-dimples along the cylinder liner circumference. To compensate the deviations in form and position, the microstructuring tool presented in Figure 4-20 was developed.

The function principle is as follows: A rolling bearing (Pos. 2) placed into the tip of a rotating tool shank rests on the surface of a rotating component. Together with the bearing and located closely behind it, a cutting edge (Pos. 3) rotating with the tool

shank (Pos. 10) follows the surface contour. As a result, the specified depth of cut remains constant despite the form and position tolerances of the surface contour. The depth of cut can be continuously adjusted by an eccentric on the tool shank from $a_p = 0$ to $200 \mu\text{m}$ via a worm drive (Pos. 6+7).

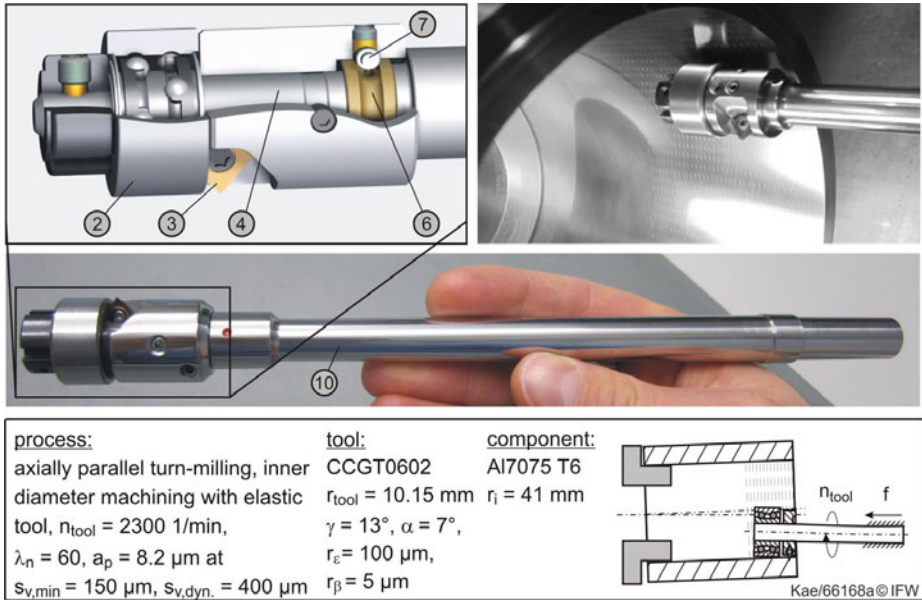


Figure 4-20: Structure and functioning of the tool concept developed for compensating deviations in form and position

To verify the potential of an elastic tool, its dynamic compensation quality when machining components whose form is not round was determined experimentally (Figure 4-21). In the following, the deflection varying along the component's circumference is called dynamic tool deflection $s_{v,\text{dyn}}$. To determine the compensation quality, the components clamped into a three-jaw chuck are machined with a defined eccentricity of $250 \mu\text{m}$ by means of the elastic tool after pre-turning. The component rotates with $n = 38 \text{ min}^{-1}$. With a minimum deflection of $150 \mu\text{m}$, a depth of cut of $a_p = 8.3 \mu\text{m}$ is set first. The maximum depth of cut is measured at three axial positions along the whole circumference of the component. Figure 4-21 compares the eccentricity measured along the component's circumference when clamped and the error of depth of cut measured along the component's circumference after structuring. Depending on the selected dynamic tool deflection $s_{v,\text{dyn}} = 250 \mu\text{m}$, the depth of cut varies from $a_p = 8.2 \mu\text{m}$ to $13.9 \mu\text{m}$. Compared to the dynamic tool deflection of the tool head, the dynamic error of depth of cut of $\Delta a_p = 5.7 \mu\text{m}$ is equal to a residual error of depth of cut of 2.3 %. The tool revolution speed which varies from $n_{\text{tool}} = 250 \text{ 1/min}$ to 6000 1/min has no influence on the specified depth of cut.

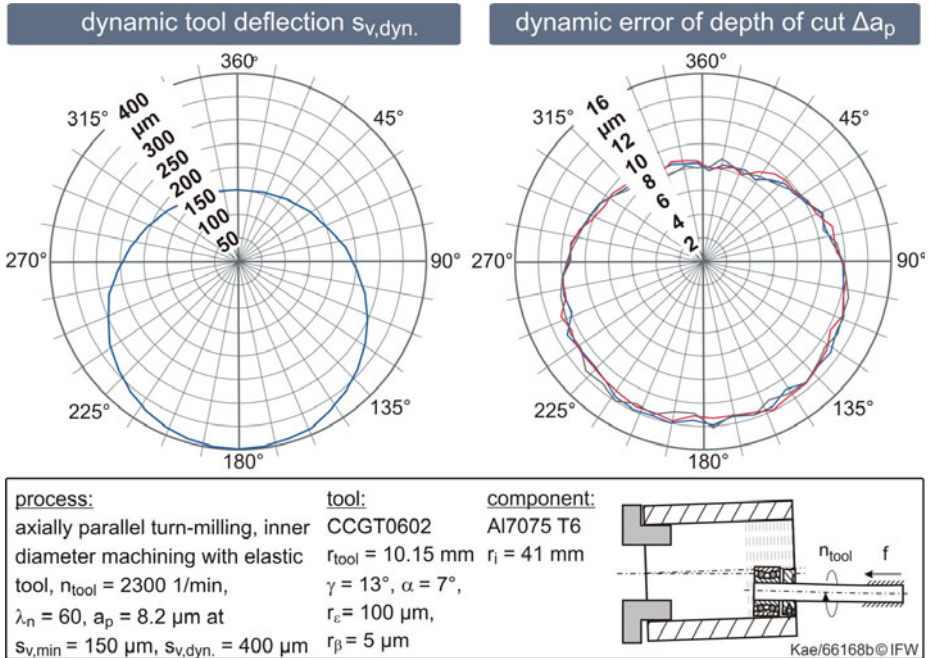


Figure 4-21: Compensation quality of the tool concept developed

Creation of hybrid cylinder liners

Apart from honing, a number of methods for machining cylinder liners were examined within the scope of this research project from a tribological viewpoint. Among others, these methods were also combined with machined micro-dimples, resulting in the creation of hybrid cylinder liners.

To gather basic experiences concerning the interactions between the pre-machined surfaces and the microstructuring process, an average surface roughness ranging from $R_z = 0,1$ μm to $5,2$ μm was provided by means of grinding and milling processes. Furthermore, micro-dimples were cut in parallel, diagonal and orthogonal arrangement into the surface texture. In the case of the surface roughness being similar to the micro-dimple depth, an overlapping of the microstructuring with the surface roughness and its arrangement becomes evident. This is in particular the case when considering the cutting force characteristics, since large surface roughness results in distinct local deviations of the machined cross-sectional area and the width of contact. However, no influence of the initial topography on the machined surface topography, the burr dimensions, or the component's subsurface could be observed. In this regard, there are no interactions between the microstructuring process and a pre-machined surface.

In order to determine the tribological interactions between the initial surface and the micro-dimples, cylinder liners to be tested on a driven single cylinder liner test rig

(see Chapter 7.3) were pre-machined by means of different mechanical methods. Moreover, micro-dimples with uniform parameters (U profile, $a_{p,max} = 7 \mu\text{m}$, $s_{ax} = 0.3 \text{ mm}$, $s_{tan} = 1.5 \text{ mm}$) were cut into their dead centre area along an axial height of 50 mm. All cylinder liners were made of GJL250 lamellar cast iron from one single material batch. Figure 4-22 compares the “hybrid” surfaces with regards to the surface roughness coefficients S_a as well as with regards to their SEM images. For this purpose, finely honed (a), normally honed (b), cylindrical ground (c) and turned (d, e) cylinder liners were structured. In addition, finely honed cylinder liners with thermally sprayed Fe50Mo coating were structured (f).

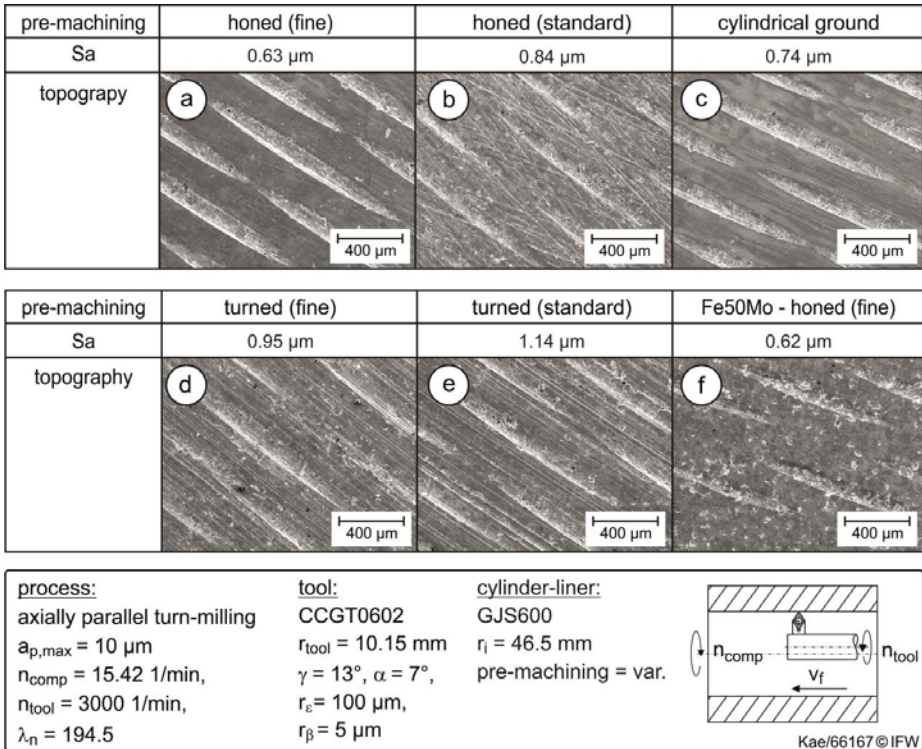


Figure 4-22: Hybrid cylinder liners

Similarly to GJS400 globular cast iron examined in Chapter 4.3, material separation was locally interrupted by phase transitions and inclusions when machining micro-dimples. The topography of machined surfaces shows open graphite lamellas. SEM images and micrographs show plastically deformed subsurface areas as well as open graphite lamellas. These are interrupted in the transition areas between graphite pores, ferrite seams and basic pearlitic matrix due to their different mechanical phase properties. Consequently, they are also partially separated from the surface in these areas. Depending on the pre-machining method, no influence on the subsurface

could be verified. Apart from their overlapping with the surface roughness, no interactions with the microstructuring could be observed.

The cylinder liners were tribologically examined on a single cylinder test rig before and after machining of micro-dimples; this is discussed in depth in Chapter 7.37.3.

4.5 Conclusion

In this report, parameters influencing the high quality machining of micro-dimples are presented. Small cutting speeds, negative rake angles as well as rounded cutting edges encourage ploughing effects which result in chipping and contour deviations. Due to a larger chip compression ratio, the lateral material flow ahead of the cutting edge towards the free edges is increased, leading to larger burr dimensions. Besides the material properties, a major parameter influencing the burr dimensions is the effective tool cutting edge angle. Due to a smaller material volume and a stronger material deflection, small tool cutting edge angles work against burr formation. If small effective tool cutting edge angles cannot be realised, burr formation can be avoided by use of positive inclination angles. Apart from S235JR steel, other materials used for cylinder liners, such as GJS400 and Fe50Mo were examined, and their interactions with microstructuring were analysed. The material GJS400 shows a ductile material separation which is comparable to the one of steel. For thermally sprayed Fe50Mo coatings, material separation is caused by cohesive failure in the boundary areas of the sprayed lamella.

Additionally, a process strategy for load-specific machining of micro-dimples into the inner surfaces of cylindrical components was developed and analysed. By systematic variation of the process variables, their influence on the arrangement and geometry of micro-dimples when machining inner surfaces of cylindrical components was described, and process limits could be identified. Tool geometries used so far when machining plane surfaces can be transferred to process strategies for machining cylindrical ones. In process design, it must however be considered that for up- and down-milling, certain process parameter combinations lead to a considerable distortion of the respective tool trajectory. Depending on the processing type, this can be accompanied by either stretching or compression of the cut. In both cases however, the effective clearance angle is considerably reduced which cannot be disregarded. Within the scope of this joint research project, the developed methods and gathered experiences made were applied to machining of a large number of cylinder liners whose tribological potential is described in Chapter 7. Besides load-specific microstructuring, hybrid cylinder liners were created as well. In this case, no interactions of the microstructuring process with the cylinder liners, which had been pre-machined by means of different manufacturing methods, could be observed.

In order to compensate deviations in form and position, an elastic microstructuring tool resting against the surface of the component to be machined was developed and characterised with regards to its performance characteristics. With the help of this tool system, deviations in form and position could be compensated up to 97 %. Con-

sequently, this allows for the microstructuring process with its narrow tolerances to be transferred to and integrated within the conventional machine tools and procedures.

5 Microstructured thermally sprayed surfaces

*Institut für Werkstoffkunde (IW), Leibniz Universität Hannover
Fr.-W. Bach, K. Möhwald, M. Erne, C. Hübsch, H. J. Maier*

5.1 Objective

The aim of this project was the development and research of thermally sprayed coatings with friction reducing micro-dimples. The basis for this approach was the systematic variation of the spray parameters. To achieve this objective, the following subtopics were studied:

- The relationship between the spray parameters and the layer structure
- Investigations of pore density and pore morphology
- Use of pores as dimples for reducing friction and oil consumption

For this purpose, the spray parameters which influence the degree of melting and acceleration of the spray particles, i.e., their kinetic energy on impacting the substrate, were varied. In particular, the hydrogen content in the process gas and the applied current show a strong influence as process variables. The spray distance has mainly effect on the kinetic energies during the impact of the particles on the substrate and the oxidation of particles in the process. To obtain insights into the relationship between surfaces and spray parameters, a detailed optical characterisation of the surface had to be carried out.

First, adequate materials suitable for applications with high frictions and wear had to be chosen as feedstock powders for spray coatings. Furthermore, each material had to be characterised in depth, and consequently, its influence on the spray parameters - investigated. Therefore, a close association with the Project 4 "Structure-based surface characterisation based on optical measurement technology" in terms of analysis of process parameters was necessary. The analysis of pore density, pore depth and average pore size provided essential knowledge concerning the evaluation of micro-dimples in thermal spray coatings.

Second, the previously used plasma-spray process had to be transferred to an internal coating process. It was particularly important to use the knowledge of the coating structure, which has been produced with a powerful torch to adapt to the reduced performance of an inner burner. Additionally, it was necessary to consider the lower heat dissipation because an insufficient cooling might influence the layer morphology. The coating of cylindrical components also had to be done on a nearly stress-free mounting on a rotary table so that the components had no distortion after spray.

5.2 Experimental

The aim of this study was the development of a novel procedure which allows control over the dimple-structures of thermal spray coatings (i.e., their distribution, geometry, and density). Special focus was put on the development of optimal dimple sizes for the layer structure of such coatings as a function of the hydrodynamic loads. The var-

ious possibilities to influence the dimple volumes by means of suitable process control were studied as well. Consequently, coatings of selected material systems were applied to the outer contours of rotationally symmetric components. To analyse the correlations between spray parameters and coating structure, cast iron substrates were coated differently with the conventional, powerful plasma torch F4 MB (Sulzer Metco, Wohlen/Switzerland). The material specific coatings were analysed in detail, and the factors which influence formation of pores were examined. In the second phase of the study, the experimental results were transferred to an internal coating process, and possible adjustments of the material system were investigated.

The formation of pores, in terms of microstructures, occurs when unmelted or resolidified spray particles are incorporated into lamellar composite particles. A variation of the current strength and a variation of the gas flow - in particular the hydrogen content - affects the input of heat to the spray particles. The heat input determines the degree of partial melting of the spray particles. If the particles are melted too strongly and accelerated too fast into the substrate, the drops nearly burst when impacting the substrate and form microporous layers with less cohesion. A too low particle temperature and acceleration result in a pasty character of the particles and a porous layer structure, since the slats cannot be applied directly above each other. Within a thermal coating, various areas can appear: areas, where the speed and the temperature of the particles have been either too high or too low; as well as areas, where the particles have had the optimum speed and temperature. However, not only the heat input but also the kinetics of the spray particles were influenced by the current and gas flow. The particles which were exposed to a low heat input tended to a low degree of melting, while particles which were exposed to low kinetic energies tended to solidify during the flight phase. The particles were incorporated as spherical particles in the coating (see [Figure 5-1](#)).

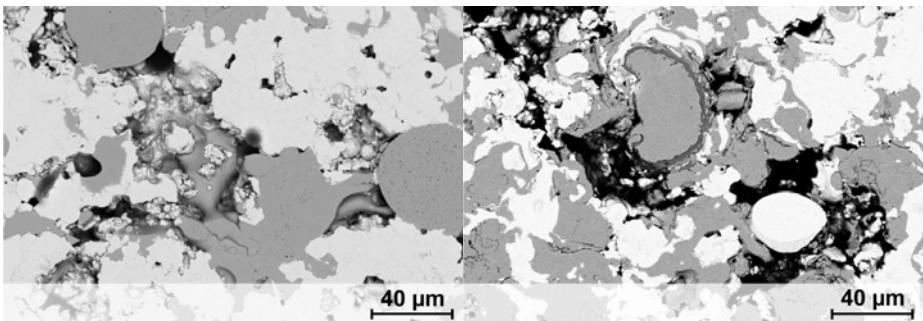


Figure 5-1: Scanning electron micrograph (SEM) of spray particles in a MoNiCrBSi coating (left) and in a FeCr13/Mo coating (right)

The unmelted coatings and the spray particles resolidified during the flight phase can be identified depending on the spray parameters. The powder feed also has an influence on the layer structure; namely, the powder feed has to be increased or decreased depending on the performance of the plasma particle flow in order to get

homogeneous dense layers. In this study, the powder feed was kept constant. [Figure 5-1](#) (left) shows scanning electron (SEM) micrographs of a MoNiCrBSi coating with unmelted spray particles. [Figure 5-1](#) (right) shows a FeCr13/Mo coating with resolidified spray particles, which are characterised by an oxide margin.

In general, the particles can consist of all the materials used; however, the melting and resolidification of particles depend on the melting temperature and the heat capacity. [Figure 5-2](#) shows schematically the setting of the atmospheric plasma spray process (APS) and its influencing factors. In this study, the parameters marked in red and their effects on the layer structure and the formation of microstructures in terms of pores were investigated.

Coating Process Atmospheric Plasma Spray (APS)

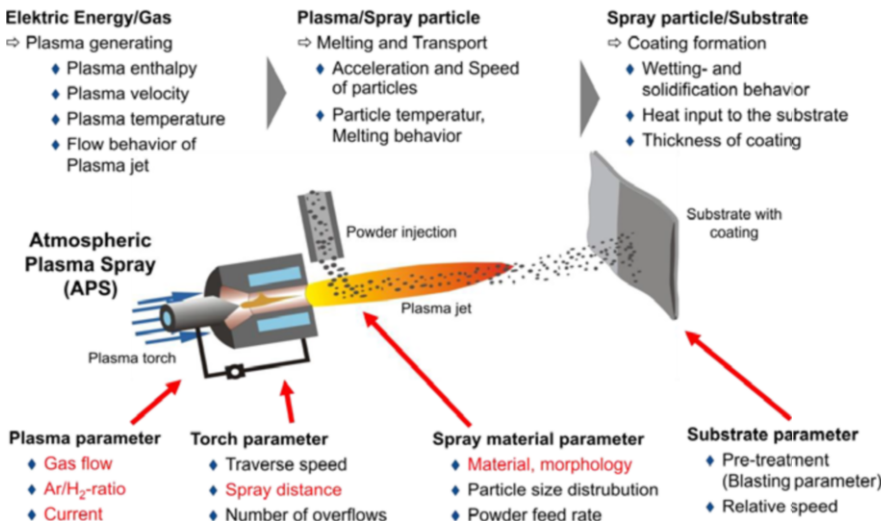


Figure 5-2: Schematic setting of the atmospheric plasma spray process (APS)

In the following, the consequences of varying the process parameters for each spray material are discussed.

5.3 Outer coating of rotationally symmetric components

Spray material Fe/Mo 50-50

As a potential spray material for the application of thermo-mechanically highly stressed surfaces, a pseudo-mixture of iron and molybdenum was used. Previously, molybdenum-containing coatings have shown promising friction reducing results when applied to coated cylinder bearing surfaces and piston rings [FLO03, SCO75]. Pure molybdenum powder shows high hardness which can be increased by means of thermal spray process at atmosphere. The formation of molybdenum oxides leads to a significant increase in hardness, which is required for the running properties of cylinder-piston bearing [OVE79, LEE90, NIR10]. However, machining (e.g. honing) of

pure molybdenum coatings is a complicated and expensive process. Mixing molybdenum with ductile phases facilitates the machining process and lowers its costs. Thus, in the first part of this study, molybdenum was mixed with iron which was intended to serve as a matrix for the hard phases of molybdenum. As an alloying element for steel, the addition of molybdenum increases the hardness and corrosion resistance. As a result, the sprayed coating exhibits not only pure phases of molybdenum and iron but also mixed phases, which lead to an increase of hardness and corrosion resistance. The iron tends to scale under high temperature conditions in oxygen atmosphere. At best, this can produce iron oxides such as wustite (Fe_{1-x}O), which is characterised by solid lubricant properties similar to those of graphite [BAR05, VEN09]. Molybdenum exhibits a higher melting point and a higher heat capacity than iron. Therefore, the proportion of non-melted and especially resolidified particles increased or decreased by varying the heat input through different current strengths and gas flows, which is accompanied with an increase or decrease of pores.

Table 5-1 below provides extensive material characterisation of the various iron-molybdenum coatings (Fe/Mo) used in the course of this study together with their spray parameters.

Table 5-1: Overview of used spray parameters

Sample	Spray distance (mm)	Current (A)	Hydrogen content (NLPM)
1-01	90	550	11
1-02	110	550	11
1-03	130	550	11
1-04	90	590	12
1-05	110	590	12
1-06	130	590	12
1-07	90	630	14
1-08	110	630	14
1-09	130	630	14

Figure 5-3 shows scanning electron micrographs of starting powders for Fe/Mo-sprayed coatings. Two powder mixtures containing 50 wt.-% iron and 50 wt.-% molybdenum in the fractions $-45+20\ \mu\text{m}$ and $-90+45\ \mu\text{m}$ can be seen. The large spherical particles shown in Figure 5-3, left, are agglomerated and sintered molybdenum particles. The morphology of the particles determines the melting properties of molybdenum. The agglomerated molybdenum particles provide a large surface/volume-ratio and can therefore melt well. The smaller irregular particles represent the iron powder.

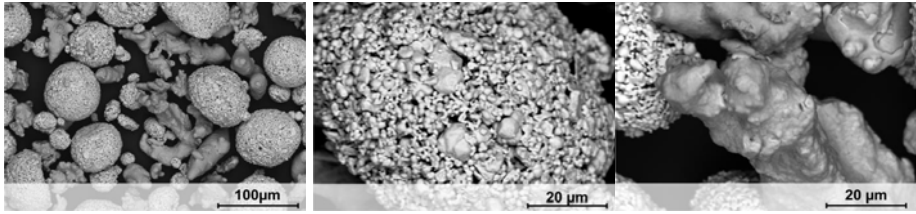


Figure 5-3: SEM micrographs of the Iron-molybdenum mixture (left), molybdenum particle (middle) and iron particle (right)

Figure 5-4 shows three polished cross-sections of Fe/Mo-coatings, which were sprayed with the conventional plasma torch SM F4 MB. Two different spray parameter sets were used to investigate the influence of a high or a low energy input on the formation of pores. Sample 1-09 (Figure 5-4, left) combines a high spray distance (130 mm) with a high energy input (630 A, 14 NLPM H₂). A homogeneous layered two-phase system can be seen, in which single macro-pores appear. The bright phase represents the molybdenum, and the dark phase - the iron. For the 1-03 sample (Figure 5-4, centre) a high spray distance was used (130 mm) in combination with a low energy input (550 A, 11 NLPM H₂). Similarly, a homogeneous structure of iron and molybdenum can be seen. Additionally, some particles often show substantially more pronounced oxide films. The proportion of spherical particles, which are characteristic of unmelted and resolidified particles, is comparatively higher. As a result, this sample exhibits a higher proportion of larger pores.

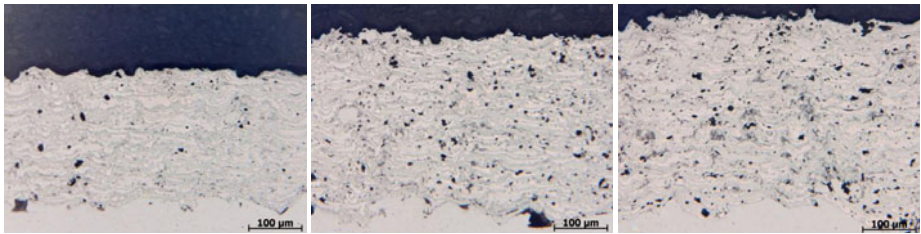


Figure 5-4: Polished cross-sections of Fe/Mo 1-09 (left), 1-03 (middle) and 1-01 (right)

Samples 1-03 and 1-01 represent a comparison between the same energy inputs used with different spray distances. Sample 1-01 (Figure 5-4, right) was sprayed from a spray distance of 90 mm and the sample 1-03 (Figure 5-4, centre) was sprayed from a distance of 130 mm. The development of the microstructure is similar for both samples; however, the layer application of the sample with the short spray distance is about 15 % higher.

Based on the cross-sections of Fe/Mo, initial conclusions about the material and its dependence on the varying spray distances can be made. Following, micro-sections of the top surface from Fe/Mo are shown, because this is the relevant surface for this research approach. The coatings differ in the morphology of their micro- and cross-sections due to the difference in their mechanical processing, i.e., grinding and polishing.

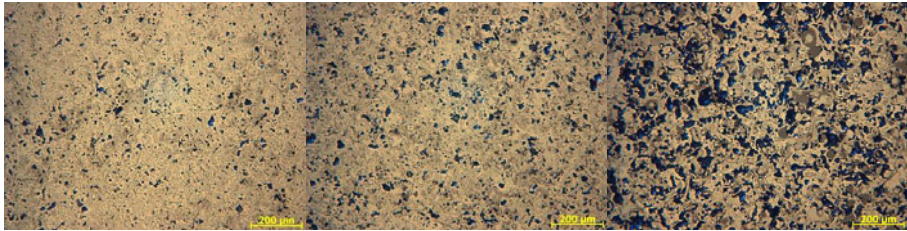


Figure 5-5: Polished micro-sections of different Fe/Mo coatings

The micro-sections support the conclusions which were gained from the cross-sections: namely, that the porosity in this coating material can be influenced by the energy input. Surface parameters such as porosity were investigated by subproject 4 “Structure-orientated surface characterisation based of optical measurement methods”. Table 5-2 shows the measured porosities of the different Fe/Mo coatings.

Table 5-2: Porosities from series 1 of Fe/Mo coatings

Sample	1-01	1-02	1-03	1-04	1-05	1-06	1-07	1-08	1-09
Porosity (%)	1	2	3	1	3	2	1	1	2

The measured porosities are within a narrow range of between 1 and 3%. This value is typical for thermally spray coatings as residual porosity. Despite reduced energy input, the F4 MB torch was too powerful which resulted in a higher porosity. Therefore, a strategy had to be developed to reduce the input of energy to the particles. In the first experimental setup, the current of the plasma torch was varied from 550 to 630 A. For the second series of experiments, a wider interval for the current rating and the gas flow was selected. The Taguchi L9 experimental design [TAG86] was used in order to obtain a manageable amount of samples and to vary the process parameters spray distance, current and process gas flow. This resulted in the following set of parameters:

Table 5-3: Taguchi-L9-Design of experiment

Sample	Spray distance (mm)	Current (A)	Hydrogen content (NLPM)	Argon content (NLPM)
2-01	90	400	8	30
2-02	90	500	10	35
2-03	90	600	12	40
2-04	120	400	12	35
2-05	120	500	8	40
2-06	120	600	10	30
2-07	150	400	10	40
2-08	150	500	12	30
2-09	150	600	8	35

SEM-micrographs (Figure 5-6) using backscattered electron (BSE) contrast allow for an exact assignment of the iron and molybdenum particles. Because of the higher atomic weight of molybdenum, it appears brighter in the micrograph than the lighter iron. In the following Figure 5-6, BSE images of the samples 2-01, 2-07, and 2-08 are shown. It can be seen that the coatings consist largely of a homogeneous mixture of the two phases, wherein in sample 2-01 the mixture of the lamellae is more homogeneous.

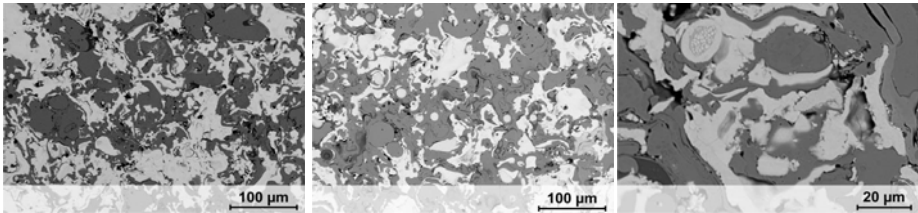


Figure 5-6: BSE-micrographs of Fe/Mo coatings. Sample 2-01 (left), 2-08 (Middle) and 2-07 (right)

Sample 2-08 (Figure 5-6 middle), which was coated from a greater spray distance, is characterised by a high content of spherical particles. These particles can be classified as molybdenum in many cases, which is an indication that the molybdenum particles are resolidified during the flight due to the high melting point. However, the particles are well embedded in the layered particles and do not form the starting point for pores. A micrograph of specimen 2-07 at higher magnification (Figure 5-6, right) shows that the molybdenum particles are often characterised by cracks and fractures. This reveals the brittle character of the sprayed molybdenum, especially of molybdenum oxide, which is responsible for the high hardness of the coatings. The cracks may occur, on the one hand, when the brittle molybdenum impacts the surface and, on the other, when the particles are cooled too rapidly on impacting the

surface. The measured porosities are in a range similar to the one seen in the first series of samples. It can be concluded that the energy input is still very high and the coatings are densely sprayed.

Table 5-4: Porosities from series 2 of Fe/Mo coatings

Sample	01	02	03	04	05	06	07	08	09
Porosity (%)	1.92	1.98	1.19	1.55	1.35	1.66	1.97	3.42	2.06

A comparison of the porosities from both series is shown in [Figure 5-7](#).

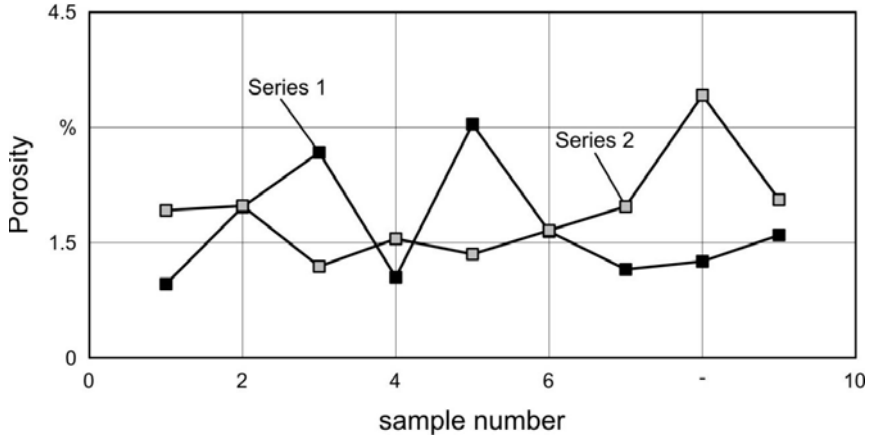


Figure 5-7: Comparison of porosity from series 1 and 2 of the Fe/Mo coatings

An element mapping was made by means of an electron microprobe (EPMA); once again, a clear separation of the two phases, which did not generate mixed phases even though they were mixed, could be observed. For each element, one mapping is shown, wherein the colour spectrum represents the accumulation of an element. A strong oxidation occurring mainly in the regions of the iron phase could be observed (cf. the oxygen mapping in the right field of [Figure 5-8](#)).

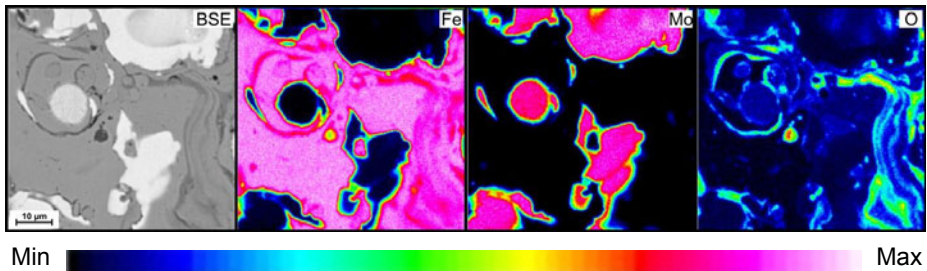


Figure 5-8: Element mapping of a Fe/Mo coating as recorded by the electron microprobe

The phase composition of the coatings was determined by means of X-ray diffraction (XRD). Diffractograms of two of the samples can be seen in [Figure 5-9](#), and within, phases of molybdenum and iron can be primarily determined. The characteristic peaks for the ferritic iron phase is 45° and 65° 2θ and the peaks of molybdenum

are at 40° , 59° and $74^\circ 2\Theta$. Furthermore, the iron oxide phase wustite ($\text{Fe}_{0.925}\text{O}$) can be detected. The content of wustite differs for the different Fe/Mo coatings. The highest content of wustite was found in the sample 2-08, which was sprayed from a high spray distance. A semi-quantitative phase analysis determined that the wustite content was approximately 5 wt.-% of the complete mixture; however, this analysis lacks accuracy due to the low intensities of the wustite peaks. In addition, the diffraction patterns show evidence of other iron oxides such as hematite (Fe_2O_3). The amount of these oxides could not be quantified because the peak positions were difficult to determine. Sample 2-01, which was sprayed from a short distance, also shows iron oxide phases similar to those in sample 2-08; these, however, cannot be determined as clearly as in sample 2-08. It can be assumed that the main phase of the iron oxides is also wustite, but other oxides such as hematite might also occur.

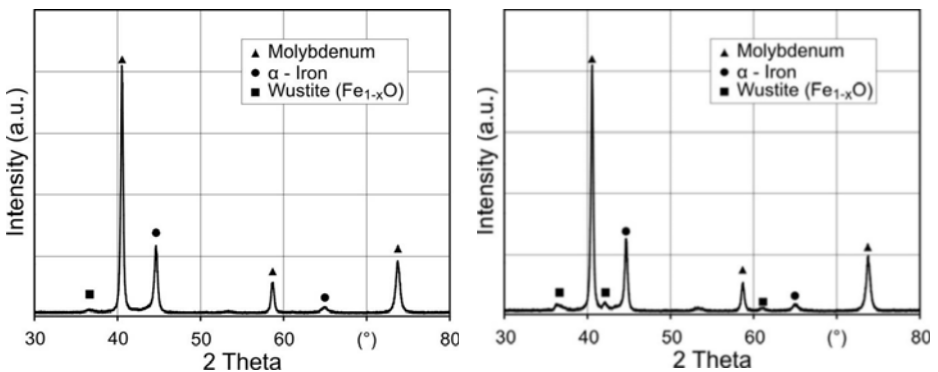


Figure 5-9: X-ray profiles of Fe/Mo coatings. Sample 2-01 (left) and sample 2-08 (right)

A dependence on the spray distance can be detected; it appears that prolonged flight time of the particles leads to a better mixing with oxygen. In contrast, XRD patterns of the starting powder do not show an evidence of oxides, which leads to the assumption that the low contents of individual oxides in the spray powder material cannot be detected by XRD.

Analysis with a confocal laser microscope indicates that the Fe/Mo coatings have significant relief differences. Figure 5-10 (middle) shows a height image of the sample 2-03. It can be seen that one of the two phases is set back after the grinding and polishing process. Secondary electron images (SE-image) with a scanning electron microscope show also reliefs between the two different phases. The material contrast from the SE images reveals that set-back phase is iron which exhibits lower hardness than molybdenum and is therefore eroded during the grinding process. Consequently, it can be concluded that during tribological load the bearing ratio of the layer is largely determined by the molybdenum phase.

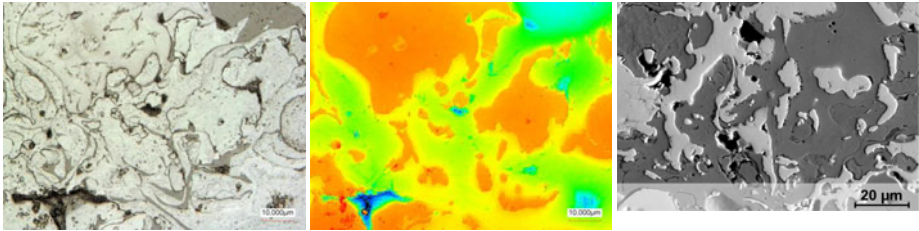


Figure 5-10: Confocal laser microscopy images of sample 2-03 (left und middle) und BSE-micrograph of sample 2-01 (right)

Micro-hardness testing was performed on cross-sections of some of the Fe/Mo coatings. Before testing the layers, measurement uncertainties were assessed by measuring a hardness test block. On each measured layer, 10 hardness impressions were set with a diamond pyramid (Vickers hardness). The results were processed by means of a statistical analysis and corrected. The results are shown in the following table.

Table 5-5: Vickers hardness of Fe/Mo coatings

	01	02	03	04	05	06	07	08	09
Hardness (HV 0.3)	-	-	-	-	-	442 ± 56	426 ± 83	-	459± 97

The tribological properties of the Fe/Mo samples were examined in “Pin-on-disc” experiments in heated synthetic oil (0W30). The coatings show improved performance in comparison to an uncoated reference sample made of steel, and especially at higher temperatures and higher contact pressures, the Fe/Mo coatings demonstrate a distinct advantage. The transition from mixing into the hydrodynamics friction occurs at lower velocities and the total friction is reduced. A detailed description of the tribological testings can be found in chapter 7 “Tribological mechanisms of microstructures”

Their advantageous tribological properties notwithstanding, the coatings are characterised by low corrosion stability. After a short time, they react with atmospheric oxygen and their iron phase is oxidised to hematite (see [Figure 5-11](#)). Consequently, molybdenum-containing coatings in combination with pure iron are limited for the application on cylinder liners only: Condensates such as formic acid and sulfuric acid may in the combustion chamber occur as a result from the combustion process and attack the layer system [FLO03]. Corrosion particles increase the friction between the liner surface and the piston.

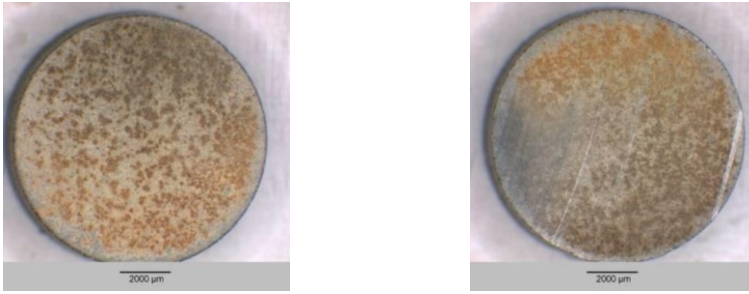


Figure 5-11: Optical microscopy images of tribometer pins with Fe/Mo coatings after storing under air conditions.

Spray material FeCr13

Another potential spray material investigated in the course of this study was a high-alloy ferritic steel material with a chromium content of about 13 wt.-% (henceforth abbreviated as FeCr13). In comparison to the Fe/Mo coatings, FeCr13 is characterised by its homogenous distribution in the coating, as the chromium is finely dispersed and the material consists of a single phase. Passivation of the chromium content is sufficiently high to ensure an adequate corrosion resistance to air and aqueous solutions and in applications under high temperature and oxygen presence. Similarly to molybdenum, chromium forms oxide during the spraying process, which can significantly increase the hardness of the sprayed material. The high corrosion stability strongly reduces the formation of abrasive iron oxides such as hematite (Fe_2O_3), but also the formation of the solid lubricant wustite (Fe_{1-x}O). The slightly lower hardness of FeCr13 and the uniform distribution of chromium allow good mechanical machining of the material. The control of the formation of pores based on the variation of the process parameters is more difficult in this material because the melting of the particles is more similar than between molybdenum and iron particles. As a result, the degree of melting and the kinetics of the particles can be determined only by the fraction interval of the powder.

The following paragraphs provide extensive material characterisation of the chromium based steel coatings (FeCr13).

Table 5-6: Overview of spray parameters used for the FeCr13 coatings

Sample	Spray distance (mm)	Current (A)	Hydrogen content (NLPM)
1-01	110	530	6
1-02	125	530	6
1-03	140	530	6
1-04	110	530	8
1-05	125	530	8
1-06	140	530	8
1-07	110	530	10
1-08	125	530	10
1-09	140	530	10

The starting powder for FeCr13 coatings is shown in [Figure 5-12](#). Two powder fractions were examined and one selected for the spray process. The powder fractions were $-20+45\ \mu\text{m}$ ([Figure 5-12](#), left) and $-25+5\ \mu\text{m}$ ([Figure 5-12](#), middle). The irregular shape of the spray particles resulted in a better melting of the chromium steel. It was therefore estimated that the process parameters would need lower energy inputs in comparison to the Fe/Mo-powder. Since the hydrogen content influences the energy input greatly, only the spray distance and the hydrogen flow rate were varied for the FeCr13 material. In comparison to the Fe/Mo coatings, the spray distance was increased to increase the number of resolidified particles and, consequently, the number of pores. The compositions of the two powder fractions are equal.

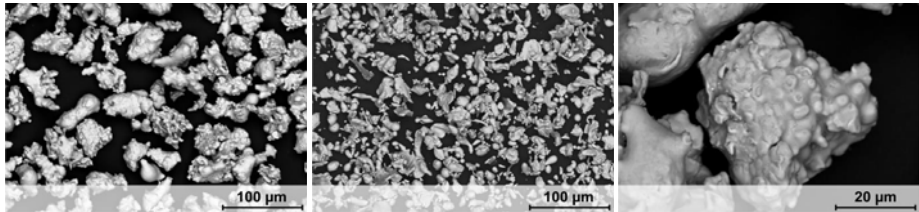


Figure 5-12: SEM micrographs of the chromium steel powders. Fraction $-20+45\ \mu\text{m}$ (left), fraction $-25+5\ \mu\text{m}$ (middle) and iron particle (right)

Polished cross-sections of FeCr13 coatings ([Figure 5-13](#)) show the same dependence on the heat input as for the Fe/Mo coatings. Sample 1-05 (125 mm and 8 NLPM) exhibits a dense lamellar structure with isolated macropores and strong oxidation ([Figure 5-13](#) left). Sample 1-02 (125 mm and 6 NLPM), which was sprayed with lower energy, is characterised by a higher percentage of pores ([Figure 5-13](#), centre). In addition, the coating is more strongly oxidised. Sample 1-02 (125 mm) and 1-03 (140 mm) were compared when investigating the properties of coatings the same energy input, but varied spray distances. The coating structure and the applica-

tion process was almost the same for both samples, but the sample with higher spray distance oxidised stronger.

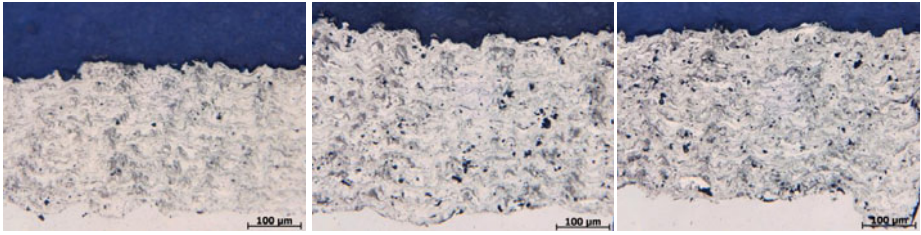


Figure 5-13: Polished cross-sections of FeCr13 1-05 (left), 1-02 (middle) and 1-03 (right)

For the analysis of the surface, micro-sections were also characterized with white light interferometry. The results show that the porosity interval is higher than the one of Fe/Mo coatings. The highest porosity was measured for sample 1-03, which was sprayed with low hydrogen flow and from a high spray distance. However, the sample shows a high standard deviation so that it must be assumed that the porosity interval of this series is similar to the Fe/Mo coatings.

Table 5-7: Porosities from series 1 of FeCr13 coatings

Sample	1-01	1-02	1-03	1-04	1-05	1-06	1-07	1-08	1-09
Porosity (%)	0.55	2.71	5.30	0.43	1.28	2.39	0.97	3.39	0.97

To allow for a comparison of the tribological characteristics of the FeCr13- and Fe/Mo coatings, a further series of FeCr13-samples were sprayed in accordance with the Taguchi L9 experimental design listed in [table 5-3](#).

Polished cross-sections were used to investigate the microstructure of the individual coatings. For this purpose, in addition to optical microscopy images, SEM micrographs recorded in BSE mode and height images obtained by confocal laser microscopy were analysed to obtain additional information on the phase composition and topography of the coating.

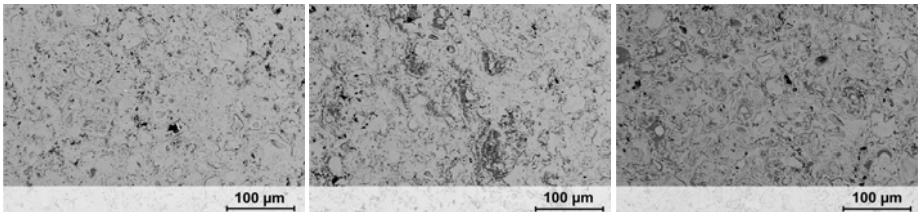


Figure 5-14: SEM micrographs of FeCr13 coatings 2-02 (left), 2-03 (middle) and 2-08 (right).

The SEM images ([Figure 5-14](#)) show three microstructures whose surfaces differ depending on the various process parameters with which the layers were sprayed. The two samples 2-02 and 2-03, which were sprayed from a distance of 90 mm, are characterised by nearly the same porosity and number of spherical particles. However, sample 2-03 shows a significantly higher oxidation: oxide films can be detected on

non-melted and re-solidified particles, in particular. Since this sample was sprayed with a higher heat input, it can be assumed that the particles were strongly melted and required a longer cooling time on the substrate; consequently, they were exposed to the oxidising atmosphere while in their melted state for a long time. In comparison, sample 2-08, which was sprayed from a distance of 150 mm, exhibits a higher proportion of resolidified particles as well as a higher porosity. This sample did not oxidise as much as sample 2-03; however, some particles show oxide rims with a thickness of up to 4 μm , which exhibit cracks indicating their brittle character.

Porosities of the individual coatings are summarised in the table below. The results reveals that the material FeCr13 tends to show lower material porosity. Due to the nearly homogeneous powder, the particles were molten in dependence on their size only. The location and time of contact between powder particles and plasma in the gas stream are important for different powder melting. Lower amounts of non-melted and re-solidified particles are the result.

Table 5-8: Porosities from series 2 of FeCr13 coatings

Sample	2-01	2-02	2-03	2-04	2-05	2-06	2-07	2-08	2-09
Porosity (%)	1.22	0.82	0.93	1.07	0.69	1.06	0.63	1.59	1.2

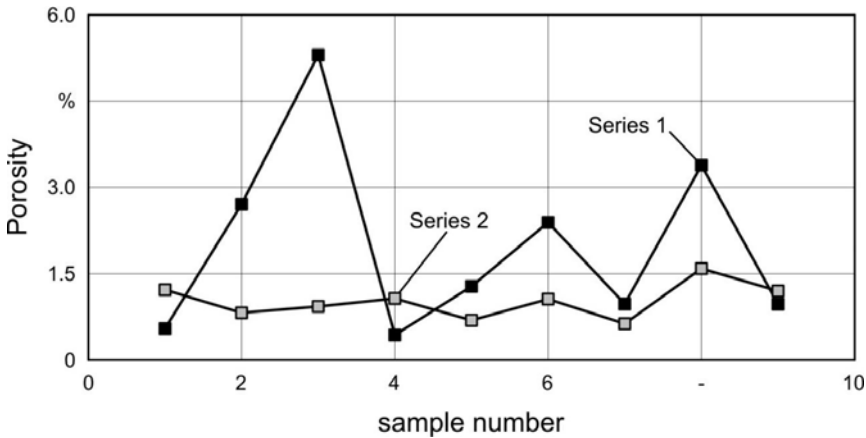


Figure 5-15: Comparison of series 1 and 2 of FeCr13 coatings

Analysis with the electron microprobe shows a homogeneous distribution of elements within the FeCr13-material (Figure 5-16). By and large, chromium is dissolved uniformly in the steel, but small precipitates of chromium are also found in the coating. The few grey areas in the BSE image represent the oxidised particles (cf. the elemental map for oxygen). In these areas, the chromium content is increased, too. This indicates that chromium precipitates were oxidised during the flight phase. The oxidised chromium provides for the high corrosion resistance and increased hardness.

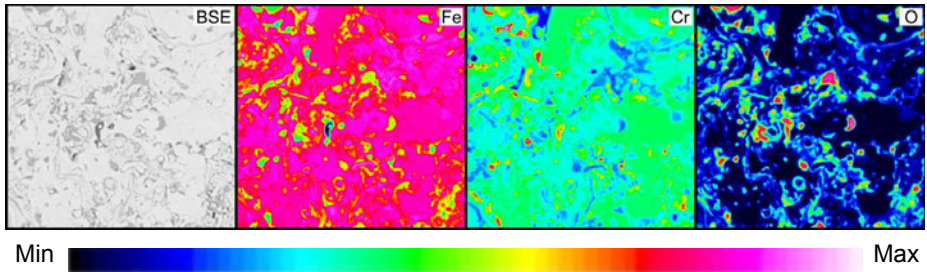


Figure 5-16: Element mapping of a FeCr13 coating by means of electron microprobe

The analysis of the phase composition shows mainly a single-phase ferritic stainless steel (Figure 5-17). Furthermore, the profiles also reveal iron oxides which were produced during the spray process. The strong oxidation of the material can be seen in the micrographs. The qualitative phase analysis concerning the peak positions at 30° , 35° , 57° and $63^\circ 2\theta$ indicate the presence of the iron oxide magnetite (Fe_3O_4); nonetheless, it is also possible that an iron-chromium oxide, namely chromite (FeCr_2O_4), is present as well. The appearance of chromium oxides is also supported by the oxygen distribution in the element mapping, which shows the accumulation of oxygen in the chromium rich areas. FeCr13 coatings, similar to Fe/Mo coatings, exhibit higher oxide content in samples which were coated from a longer spray distance than in those from a short spray distance.

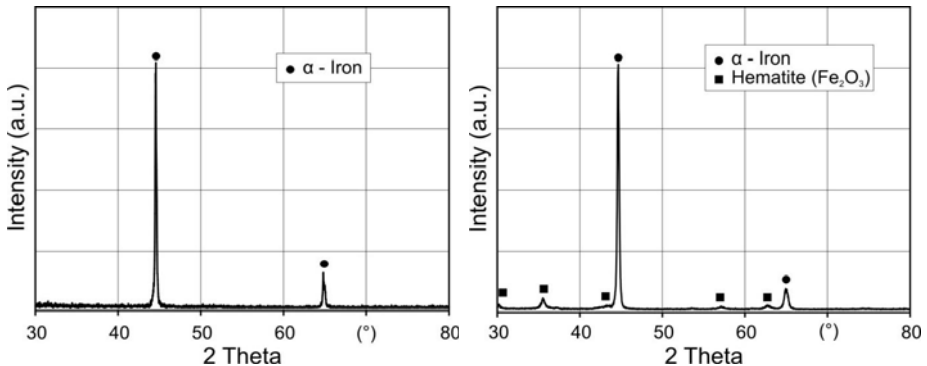


Figure 5-17: XRD profile of the FeCr13-powder (left) and the sample 2-08 (right)

The XRD profiles provide evidence of the presence of the iron oxide wustite; still, magnetite and chromite appear to be the prevalent oxide phases. Magnetite is attributed solid lubricant properties, which - though similar to those of wustite - are not as pronounced [Ven09]. The starting powder (Figure 5-17 left) shows no evidence of iron oxides.

Due to the single-phase composition of the FeCr13 material, there are no strong differences in hardness in between the coatings; thus, no relief formation can be observed during mechanical processing such as grinding. Figure 5-18 shows images of FeCr13-02 made with a confocal laser microscope. It can be seen that the coating

exhibits a flat surface without substantial differences in height between the individual spray lamellae.

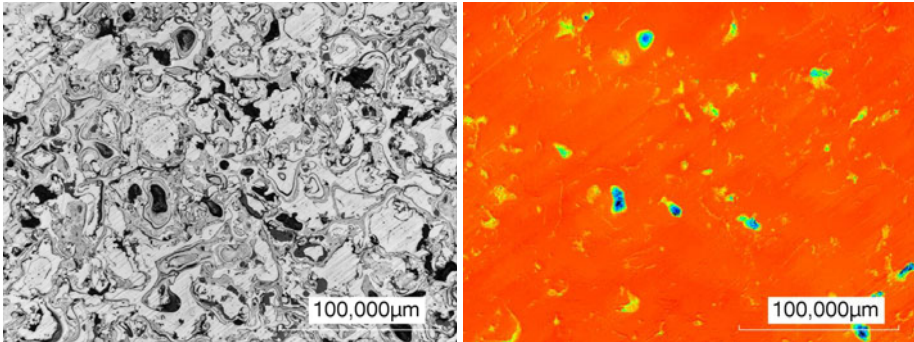


Figure 5-18: Confocal laser microscopy images of the sample 2-03

As with the Fe/Mo coatings, micro-hardness testing was also performed for the FeCr13 coatings. In each coating, 10 hardness indentations were set with a diamond pyramid (Vickers hardness). The values reveal that FeCr13- are characterised by higher hardness than the Fe/Mo coatings. This fact can be explained with the homogeneous structure of the single-phase FeCr13. The high proportions of iron in the Fe/Mo coatings lead not only to local hardness reduction but also to an increase of porosity. Moreover, FeCr13 coatings are partially strongly oxidised so that a high proportion of hard oxides increases the hardness.

Table 5-9: Vickers hardness of FeCr13 coatings

Samples	01	02	03	04	05	06	07	08	09
Hardness (HV 0.3)	544 ± 97	475 ± 55	502 ± 52	507 ± 55	-	-	-	-	-

The tribological properties were examined in “Pin-on-disc” experiments in heated synthetic oil (0W30). Similarly to the Fe/Mo coatings, the FeCr13 coatings show improved tribological properties when compared to an uncoated reference sample. However, the reference sample does show an equal or lower coefficient of friction in the hydrodynamic region for low contact pressures of 1.25 MPa and oil temperatures of 120 °C. A detailed description of the tribological testings can be found in chapter 7 “Tribological mechanisms of microstructures”. It should be noted that seizing effects might also have occurred in some cases. Examining the contact area of the two friction partners reveals friction welding due to the high chromium content. The "pin-on-disc" setup of the tribological tests cannot completely reproduce the running motion of the piston ring on the cylinder surface, as it is a point contact instead of a line contact. Nevertheless, the friction welding behaviour of the two friction partners in the cylinder could be similar to the results from the tribological tests.

Conversely, the FeCr13 material shows high corrosion stability due to its high chromium content, making it suitable for use in the combustion chamber.

5.4 Inner coating of rotationally symmetric components

For the internal coating by means of atmospheric plasma spraying, it was necessary to use a burner with a nozzle which operates at 90 ° to the burner shank.

In addition, due to the limited workspace, the coatings had to be applied with lower power and a smaller plasma jet. For this reason, the SM-F210 plasma torch from Sulzer Metco was used. The torch is designed for use on complex geometries and in boreholes. Since the output of this burner differs significantly from the output of the burner used for the outer contours, it was necessary to adjust the varying spray parameters during the first testing for the interior coatings. The Taguchi L9 experimental design was modified in the course of the first tests to study the influence of the process parameters. Most noteworthy is the spray distance which was limited due to the maximum diameter of the coated cylinders used as test specimens for the tribological tests. The test specimens for the rotational friction wear tests (RRV) were blanks with a final diameter of 83 mm after coating. Consequently, the maximum spray distance was chosen in such a way as to minimise the collision risk between the burner shank and the cylinder wall, whereas the minimum distance ensured that the plasma flame would not touch the cylinder wall. The current and the gas flow had to be adjusted so that the liner would not overheat, yet there would still be enough energy to melt the powder particles. As a result, the following test plan was formulated:

Table 5-10: Taguchi-L9-Design of experiments

Sample	Spray distance	Current (A)	Hydrogen content (NLPM)	Argon content (NLPM)
3-01	35	270	3	40
3-02	45	320	4	40
3-03	55	370	5	40
3-04	55	320	3	50
3-05	35	370	4	50
3-06	45	270	5	50
3-07	45	370	3	60
3-08	55	270	4	60
3-09	35	320	5	60

For the investigation of internally coated samples, initially flat samples were bound to a magnetic bearing (Figure 5-19). For an internal coating, either a special plasma torch or the component to be coated rotates, and the burner moves axially through the bore. In this case, the bearing rotated. The disadvantage of this experimental setup was the intermingling of powder particles after crossing the edge.

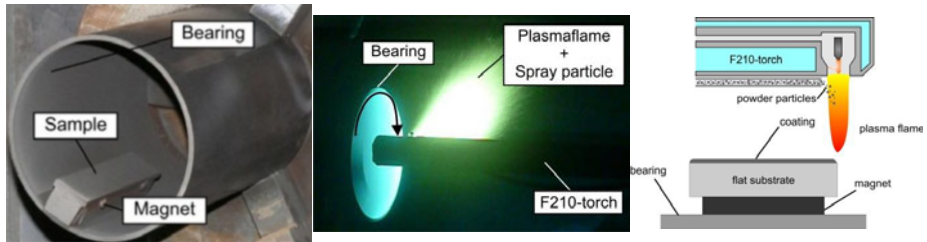


Figure 5-19: Experimental setup for internal coating of flat samples (left), plasma coating of a flat sample in a bearing (centre) and schematic coating process of a flat sample bound to magnet in a bearing (right).

Using the experimental setup shown above, two different spray materials were applied and tested afterwards. To produce application-near internal, coated flat samples, a sliding bearing structure was developed, and flat substrate and tribometer pins were integrated in its running surface (Figure 5-20). The advantage of this experimental setup was that the turbulence effects of the overspray near the edges were avoided. Moreover, the thermal evolution in the liner during the coating process was almost identical to the one in a real cylinder bore.

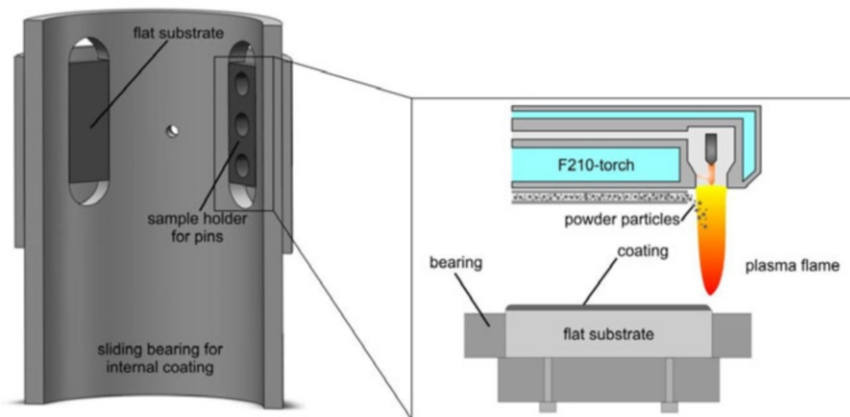


Figure 5-20: Scheme of a bearing with integrated sample holder (left) and schematic coating process of a flat testing sample (right)

Spray material FeCr13

The FeCr13 material, which had already been sprayed on outer contours and examined, was also used when investigating internally coated flat samples. For the purpose of this investigation, the Taguchi L9 experimental design and an F210-plasma torch were utilised as well.

The experiments on internally coated samples were primarily used for the transfer of the already received properties of this material. In comparison to the samples processed with the conventional plasma torch F4, the cross-sections of the samples

sprayed with the F210-plasma torch from the same spray distance, but with different currents and gas flows, exhibit a much higher porosity. Here, the individual coatings differ strongly not only in the number of the pores but also in their size. Furthermore, a larger number of unmelted or resolidified particles as well as a lower oxidation of chromium can be observed. Sample 3-08 (Figure 5-21 right), which was sprayed from 55 mm spray distance and with 270 A current, is characterised by the highest amount of non-melted or re-solidified particles. The 270 A current and the high spray distance are not sufficient to melt the particles completely and, as a result, many of the particles remain unmelted or are only partially melted. Sample 3-03, which was sprayed with a much higher current, shows a much denser microstructure and less spherical particles. The cross-sections, shown in Figure 5-21, reveal increasing porosity with decreasing current.

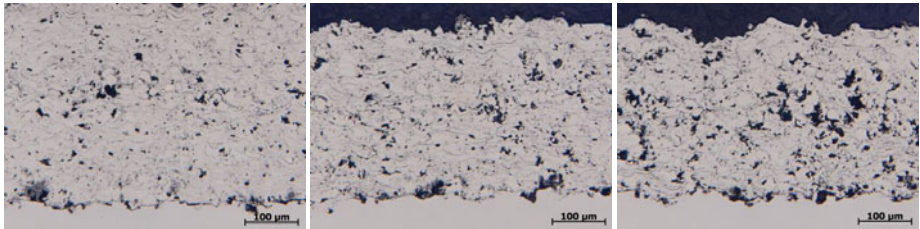


Figure 5-21: Polished cross-sections of FeCr13 3-03 (left), 3-04 (middle) and 3-08 (right)

The analysis of metallographic micro-sections (Figure 5-22) shows the microstructures of the tribologically active area. Samples 3-07, 3-02 and 3-06, which were sprayed from the same spray distance (45 mm), are used as examples. The porosity of the samples also decreases with increasing current.

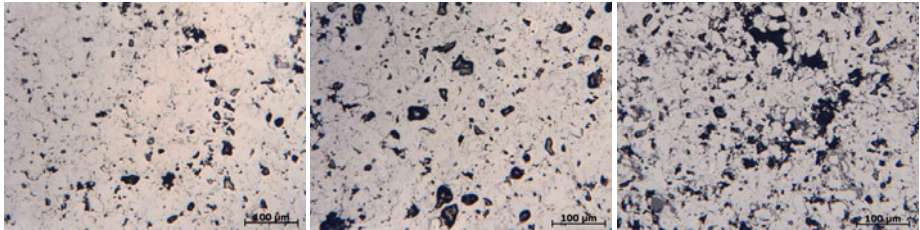


Figure 5-22: Polished micro-sections of FeCr13 3-07 (left), 3-02 (middle) and 3-06 (right)

A marked difference is observed in the surface formation of the internal FeCr13 coatings when compared with the surface formation of the external FeCr13 coatings. Thus, sample 3-06 is characterised by a strong degree of oxidisation, which is often associated with spherical particles. Furthermore, its pores are generally separated from each other and located in the immediate environment of oxidised or spherical particles. Sample 3-06, on the other hand, exhibits a higher porosity; its pores are partially connected, and partial pore clusters are observed as well. Overall, the coating cohesion seems less pronounced than in the FeCr13 outer contour coatings. For the analysis of the surface, pores were extracted and calculated from image files of

the micro-sections by means of digital image analysis. In comparison to the measurements made with the white light interferometer, this method is less reliable due to the possibility of oxides or foreign particles with dark areas being recognised as pores. The data obtained are summarized in Table 7-12.

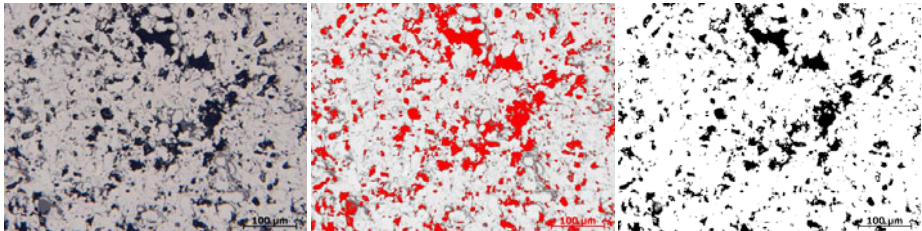


Figure 5-23: Extraction of pores by means of digital image analysis. Image of polished micro-sections (left), determination of a threshold value (middle) and extraction to a binary image (right)

Table 5-11: Porosities from series 3 of FeCr13 coatings

Sample	3-01	3-02	3-03	3-04	3-05	3-06	3-07	3-08	3-09
Porosity (%)	7	10	10	11	7	16	6	11	9

Hardness measurements on internally coated FeCr13-coating are significantly lower than those of externally sprayed coatings. These findings can be explained by the reduced adhesion of the particles due to the lower performance of the F210-torch. Nonetheless, the results of the hardness measurements also show a homogeneous hardness distribution, regardless of the porosity of the different FeCr13 coatings.

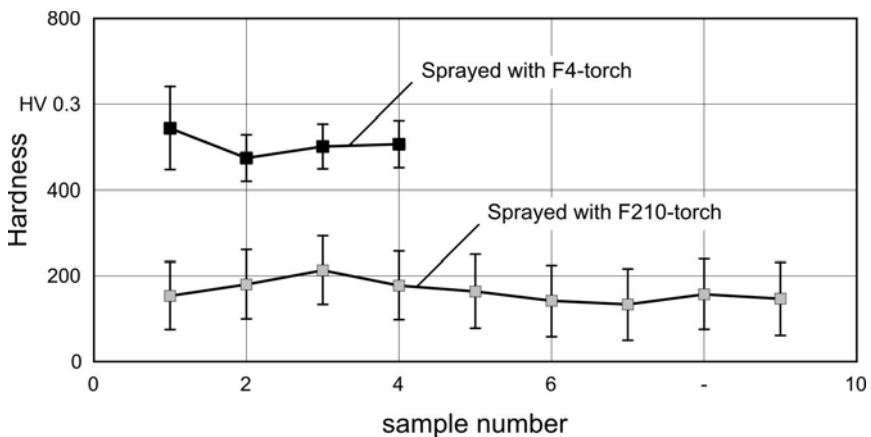


Figure 5-24: Comparison of series 2 and 3 of FeCr13 coatings

Due to its tendency to friction welding with subsequent scuffing as well as due to the high oxidation susceptibility of chromium during spraying, the pure FeCr13-material is not suitable for the coating of cylinder liners.

Spray material FeCr13/Mo 50-50

Applying Fe/Mo-compounds to thermo-mechanically highly stressed surfaces proved advantageous even though the iron phase with its high susceptibility to corrosion was a major limitation. Consequently, for the future approach, iron was replaced by the already well-studied chromium steel FeCr13. Thus, the positive properties of both materials were combined as the total content of chromium in the layer was reduced, and the corrodible iron was replaced.

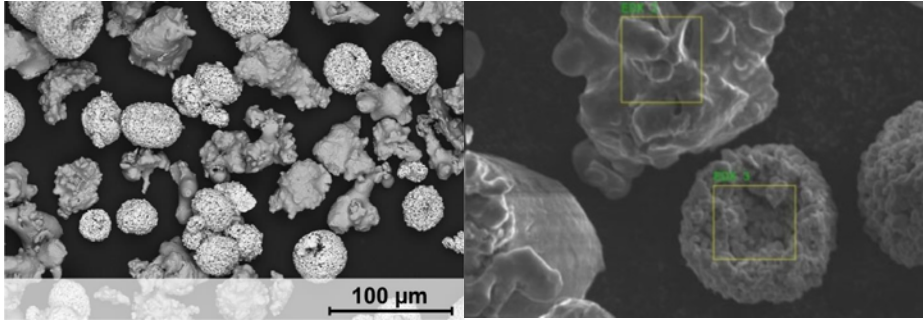


Figure 5-25: SEM micrographs of the chromium-based steel-molybdenum mixture (left); the boxes indicated the areas used for element analysis (right)

The powders used were similar to those of the first series of experiments. [Figure 5-25](#) provides SEM images (BSE mode) of FeCr13/Mo powder mixture whereby the bright spherical particles represent molybdenum, and the darker particles chromium steel, as confirmed by element analysis of the particles. Flat specimens were sprayed according to the Taguchi L9 experimental plan and prepared for metallographic sections. In the polished micro-sections, the coatings were formed as a function of the spray distance and the currents. Here, the layers differed not only in the number of the pores but also in the morphology. [Figure 5-26](#) shows three coatings which were sprayed with the same current but from different spray distances. Sample 4-08 ([Figure 5-26](#), right) is characterised by widely-dispersed pores, whereas sample 4-06 ([Figure 5-26](#), middle) exhibits a distinct narrow pore size distribution.

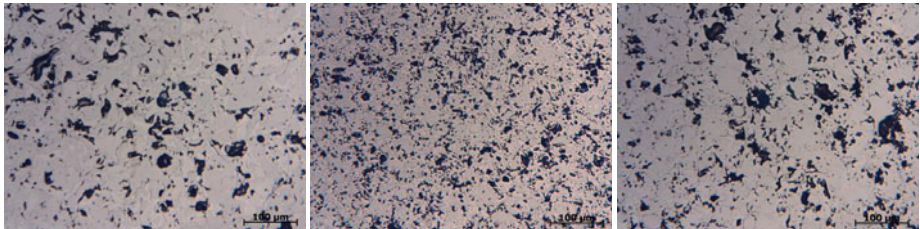


Figure 5-26: Polished micro-sections of FeCr13/Mo 4-01 (left), 4-06 (middle) and 4-08 (right)

The results from the pore extraction for FeCr13/Mo are summarised in the following table.

Table 5-12: Porosities from series 4 of FeCr13/Mo coatings

Sample	4-01	4-02	4-03	4-04	4-05	4-06	4-07	4-08	4-09
--------	------	------	------	------	------	------	------	------	------

Porosity (%)	11	10	8	10	9	14	11	14	7
--------------	----	----	---	----	---	----	----	----	---

In comparison to the Fe/Mo coatings, which were sprayed with the F4-torch, the FeCr13/Mo coatings also show significantly higher porosity level, which can be explained by the lower energy output of the F210-torch.

To investigate the suitability of FeCr13/Mo as a potential coating material, micro hardness testing (HV 0.3) were performed on the cross-sections of the samples. The hardness of the material varied depending on the area of the sample. Since molybdenum is harder than stainless steel, local differences in hardness played a significant role when determining the total hardness of the coating.

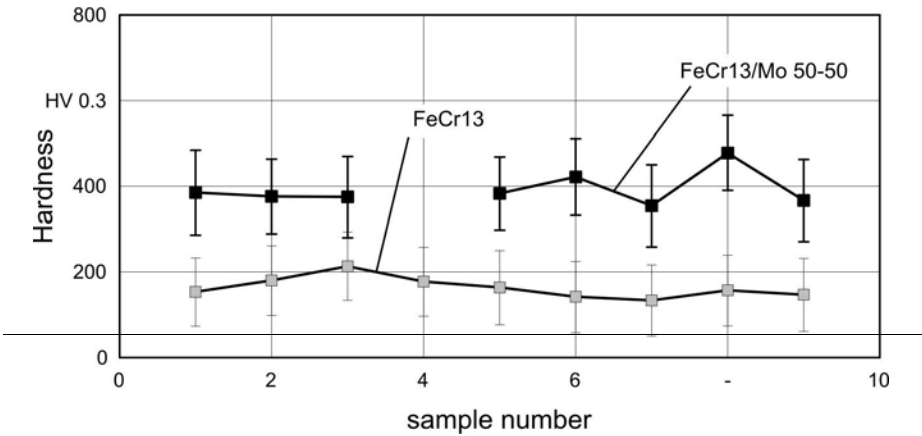


Figure 5-27: Comparison of Vickers hardness of FeCr13 and FeCr13/Mo

Figure 5-27 shows that the FeCr13/Mo 50-50 mixture is harder than the previously used pure stainless steel. The addition of molybdenum during thermal spraying process results in the formation of hard molybdenum oxides, which increases the hardness of the coatings. A mechanical treatment remains possible, but the parameters for the feed and cut forces must be customised when honing, for example.

A direct correlation between the spray parameters and the porosity could not be established. Therefore, a new full factorial experimental design was created, wherein the spray distance and the current were varied while the gas flow was kept constant. This resulted in the following experimental plan:

Table 5-13: Full factorial plan with varying spray distance and current

Sample	Spray distance (mm)	Current (A)	Gas flow (Ar/H) (NLPM)
4-01	35	270	50/4
4-02	35	320	50/4
4-03	35	370	50/4
4-04	45	270	50/4
4-05	45	320	50/4
4-06	45	370	50/4
4-07	55	270	50/4
4-08	55	320	50/4
4-09	55	370	50/4

An examination of the polished micro-sections revealed that the amount of resolidified particles increases with increased spray distance, and that the proportion of unmelted particles increases for low currents. Hence, the majority of non-melted or resolidified particles can be observed in samples which were coated from a high spray distance and at low currents. Subsequently, porosities can be identified primarily for these particles. The influence of the current on the pore formation of FeCr13/Mo layers is graphically represented in [Figure 5-28](#); furthermore, the samples which were sprayed from a short distance show a significantly higher oxidation level.

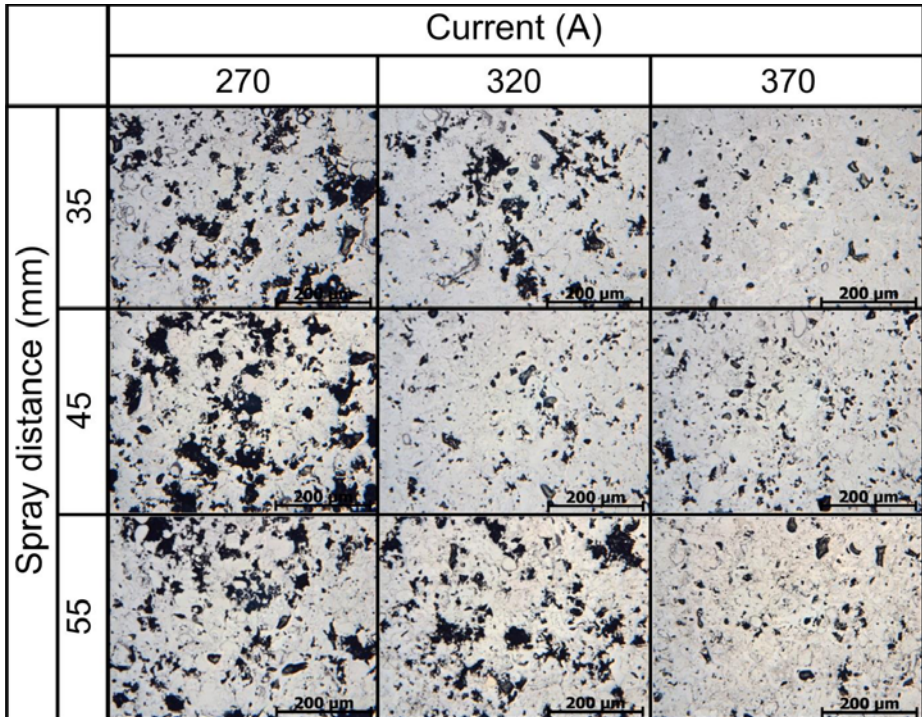


Figure 5-28: Overview of FeCr13/Mo coatings illustrating the dependence on spray distance and current.

Different surface parameters such as density and pore structure as a function of depth were also studied by means of white light interferometry. The measurements show different porosities and structure depths for each coating.

Table 5-14: Porosity of Series 4 of FeCr13/Mo coatings

Sample	4-01	4-02	4-03	4-04	4-05	4-06	4-07	4-08	4-09
Porosity (%)	4	3	3	8	3	2	6	6	2

The dependence of the porosity on the spray distance and current is shown in [Figure 5-29](#); only porosities covering an area larger than $200 \mu\text{m}^2$ were considered, since this has resulted in a reasonable threshold. The porosity of the FeCr13/Mo coatings depends primarily on the current: the coating material tends to form highly porous coatings at lower currents. Furthermore, the structure depth varies almost linearly with the porosity ([Figure 5-29](#), right).

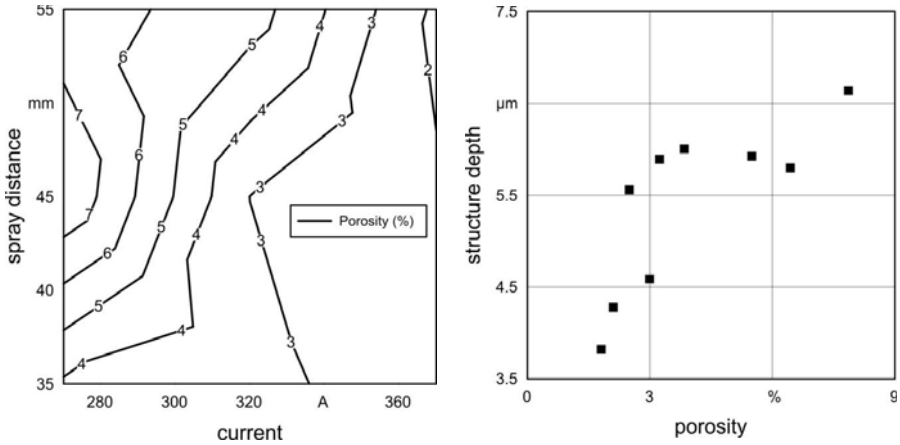


Figure 5-29: Correlation between spray parameters and porosity (left) and correlation between porosity and structure depth (right)

The coatings were also examined with respect to their element and phase compositions as well as their surface hardness. An element mapping of an electron microprobe (EPMA) in [Figure 5-30](#) shows results comparable to those of the Fe/Mo coatings. The mapping reveals a two-phased structure, wherein the molybdenum and chromium steel phases are clearly separated. Even though some areas of the chrome steel are characterised by a higher amount of chromium, the chromium phase itself exhibits a level of oxidation similar to the one of the iron phase in the Fe/Mo coatings. In general, the FeCr13/Mo coatings have lower oxygen concentrations, indicating higher corrosion stability.

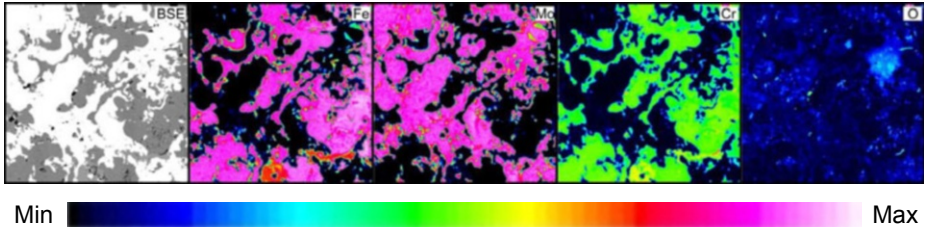


Figure 5-30: Element mapping of a FeCr13/Mo coating by means of electron microprobe

Additionally, the individual coatings were measured by means of EDX analysis to determine the element content and analyse whether the different spray parameters have an influence on the composition of the coatings. Three measurements were carried out at different points on each coating. The individual element contents of the coatings as well as their standard deviation are shown in [tables 5-15](#) and [5-16](#) on the following page.

Table 5-15: Element content of FeCr13/Mo coatings in wt.-%

Element	1	2	3	4	5	6	7	8	9
Si	0 (0.02)	0 (0.00)	0 (0.02)	0 (0.02)	0 (0.03)	0 (0.03)	0 (0.01)	0 (0.01)	0 (0.01)
Cr	7 (0.11)	7 (0.05)	7 (0.08)	7 (0.16)	7 (0.09)	7 (0.14)	8 (0.04)	6 (0.04)	7 (0.05)
Fe	40 (0.45)	39 (0.60)	42 (0.21)	42 (1.24)	41 (0.25)	43 (0.77)	47 (0.62)	36 (0.09)	43 (0.08)
Mo	53 (0.55)	54 (0.65)	50 (0.26)	51 (1.41)	51 (0.36)	49 (0.94)	45 (0.65)	57 (0.10)	50 (0.13)

No systematic relationship between the spraying parameters and the composition of the individual coatings could be observed. The composition of the FeCr13/Mo coatings is nearly constant between the individual coatings, meaning that selective evaporation of individual components could be excluded. Even though the level of oxygen in the coatings was also measured, the recorded values cannot be considered accurate since they might also include the level of residual oxygen at the surface. The XRD patterns of the samples show representative peaks of molybdenum and steel as well as NiCr phases. The FeCr13/Mo coatings also reveal peaks of the iron oxide wustite ($Fe_{1-x}O$) and molybdenum oxide (MO_2)

Micro-hardness tests (HV 0.3) of the cross-sections of the FeCr13/Mo coatings revealed high average hardness of about 400 HV 0.3. With regards to the hardness, the surface relevant for tribological applications was examined as well. For this purpose, a low-load hardness testing with a load of 29.42 N was used (HV 3). Experiments with a higher load were chosen to obtain an average over the biphasic character of the material revealed location-dependent hardness differences.

The values measured for the given micro-sections are listed in [table 5-16](#). The standard deviations of the measurements were, as expected, very low.

Table 5-16: Vickers hardness of polished FeCr13/Mo micro-sections

1	2	3	4	5	6	7	8	9
152 (11)	166 (12)	189 (12)	156 (12)	176 (4)	170 (10)	141 (6)	173 (18)	176 (8)

In comparison to the micro-hardness of the cross-sections, a decrease of hardness was observed ([Figure 5-31](#)).

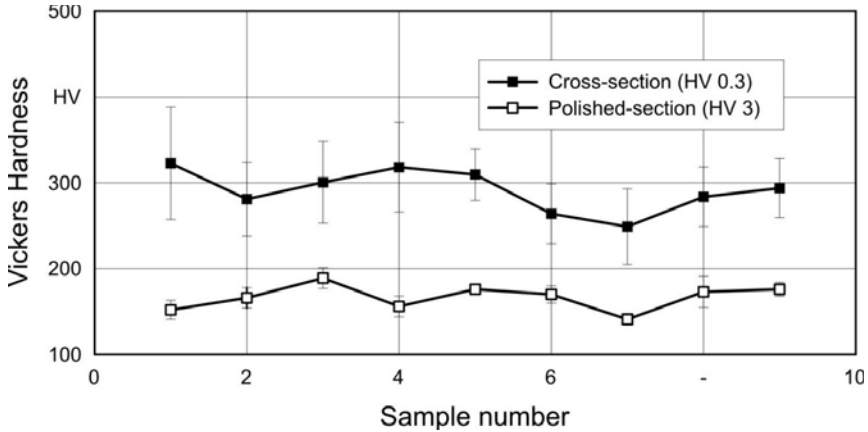


Figure 5-31: Comparison of the hardness of the cross- and micro-sections of the FeCr13/Mo coatings

Similar to the porosity, the hardness results measured on micro-sections show a dependence on the spray distance and amperage (Figure 5-32). For the hardness testing, the resistance of the surface against the indentation of a load from an indentation object was measured; surfaces with high porosity and accompanied low layer cohesion provided lower resistance to the indentation load.

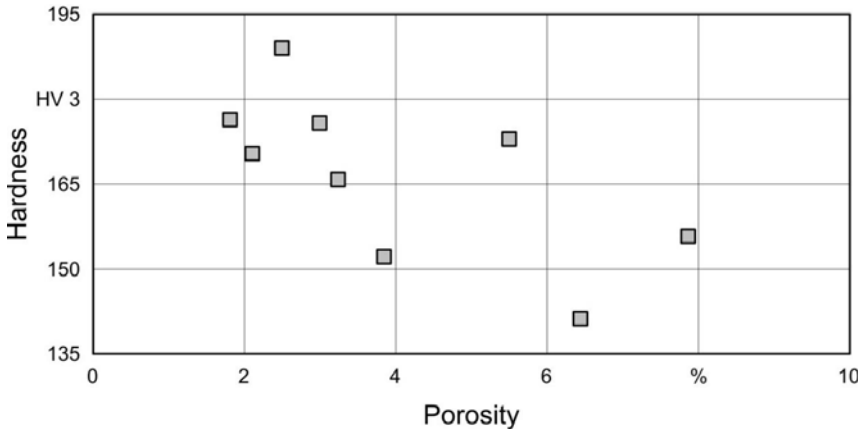


Figure 5-32: Correlation between hardness and porosity

The tribological properties were examined in “Pin-on-disc” experiments in heated synthetic oil (0W30). The coatings showed improved performance in comparison to an uncoated reference sample made of cast iron. The transition from mixing into the state of liquid friction occurs at lower velocities and at reduced total friction. A detailed description of the tribological testings can be found in chapter 7 “Tribological mechanisms of microstructures”

Spray material Mo/NiCrBSi 75-25

An additional material was investigated to validate the relationships between the spray parameters and the resulting surface formation. The selected material system was a self-fluxing nickel alloy with a high content of molybdenum. NiCrBSi coatings are often used in industrial applications where high wear resistance and high corrosion resistance are required. The single elements contribute their different properties to the coatings. Thermal spraying of nickel allows for an easy handling of the material; such coatings show moderate strength and corrosion resistance. The chromium phase increases the corrosion stability and can increase the hardness due to the formation of hard phases. Boron reduces the melting point, while the silicon phase promotes the self-fluxing properties. To use this material for surfaces with a high frictional load, the material was mixed with molybdenum, thus taking advantage of the previously described positive frictional properties of this element. In comparison with the iron and chromium-molybdenum steel mixtures, this mixture contained a higher amount of molybdenum. About 25 wt.-% of the mixture were comprised by the NiCrBSi-alloy, and the rest was molybdenum. The fraction of the powder mixture was 90+45 μm . SEM Micrographs of the powder are shown in [Figure 5-33](#).

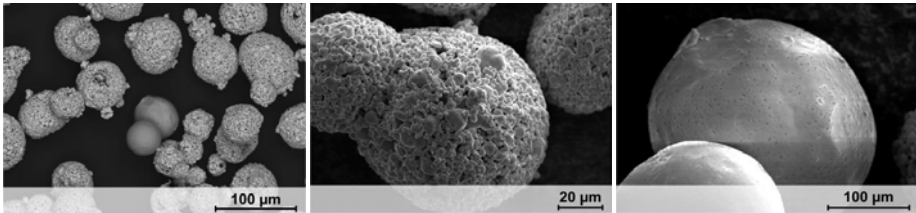


Figure 5-33: SEM micrographs of the NiCrBSi-molybdenum mixture (left), molybdenum particle (middle) and NiCrBSi-particle (right)

As with the other molybdenum-containing coating system, it can be seen that the molybdenum powder consists of agglomerated and sintered powder particles. The nickel alloy is characterised by gas-atomised powder particles. The elemental analysis of the nickel alloy detected all specified elements with the exception of boron which could not be detected due to its low atomic number.

The coatings were sprayed in accordance with the factorial plan, wherein the spray distance and the current were varied systematically. An overview of the polished micro-sections of the coatings is shown in [Figure 5-34](#).

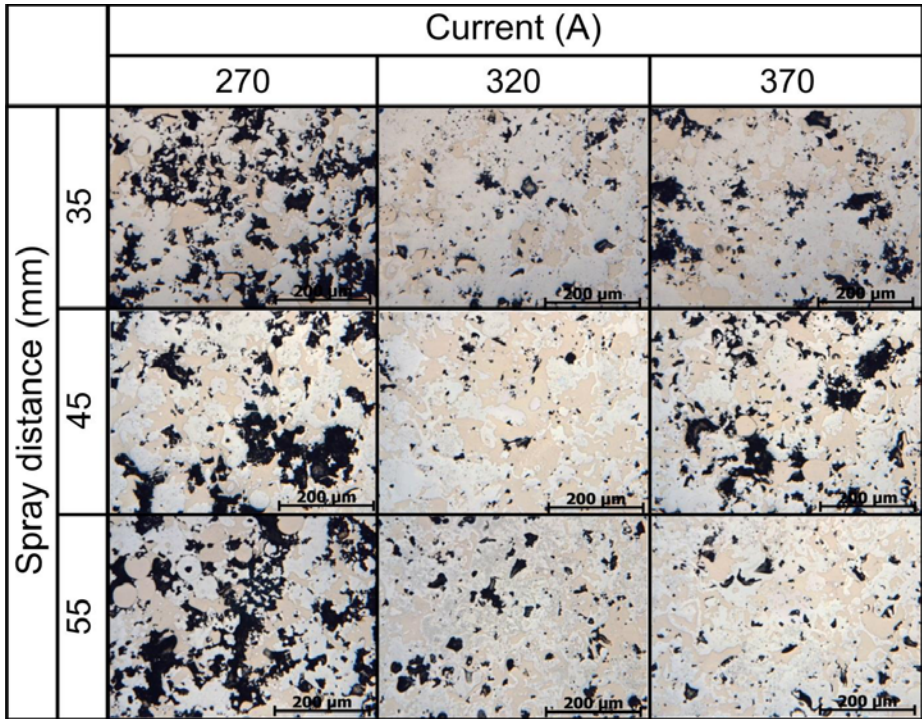


Figure 5-34: Overview of Mo/NiCrBSi coatings showing the dependence on the spray distance and current.

Similarly to the other investigated compounds, this material was significantly influenced by the current as well. The samples which were sprayed at 270 A current showed the highest porosity levels (Table 5-17). Sample 4-07, which was sprayed from a high spray distance (55 mm), also showed the highest number of spherical particles. The low energy input and the high spray distance resulted in many partially-melted and resolidified particles.

Table 5-17: Porosity of series 4 of Mo/NiCrBSi coatings

Sample	4-01	4-02	4-03	4-04	4-05	4-06	4-07	4-08	4-09
Porosity (%)	31	19	18	18	5	11	20	8	11

The correlation between the porosity and the process parameters is analogous to the one observed for the FeCr13/Mo coatings (Figure 5-35). Primarily, the formation of pores depends on the current. However, all the samples coated from 35 mm spray distance exhibit high porosities so that it must be assumed that the pore formation is also a function of the spray distance. The structure depth of the individual pores is almost linearly dependent on the number, or rather the area size of pores. This is similar to the FeCr13/Mo coatings. The micro-sections indicate that a high porosity

often results from the mechanical processing; it is furthermore associated with the connecting pores so that the size and depth of the micro-structure is also determined by the post-treatment process.

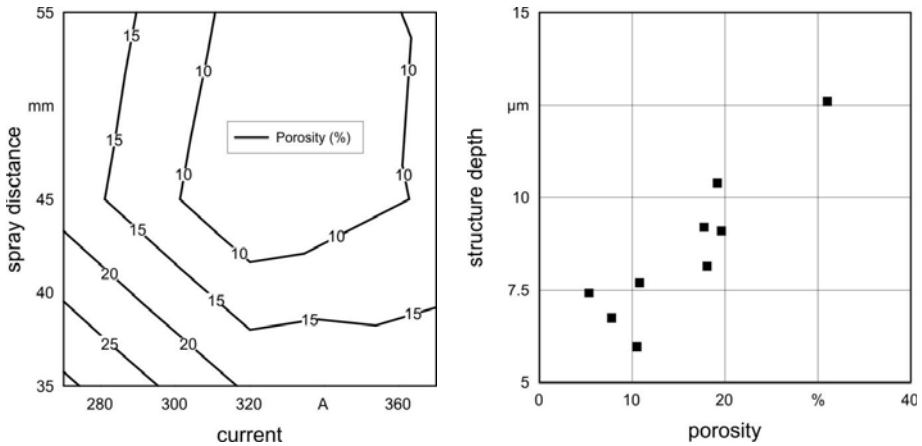


Figure 5-35: Correlation between spray parameters and porosity (left) and between porosity and structure depth (right)

After the surface analysis, the single coatings were examined regarding their element and phase content.

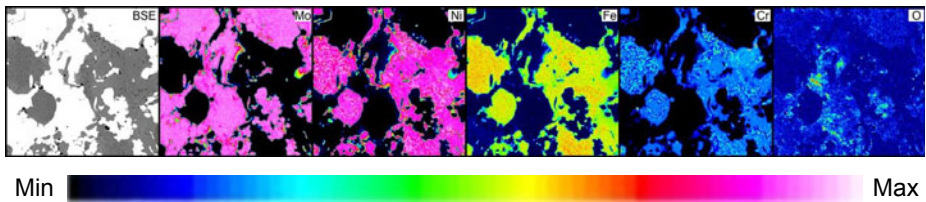


Figure 5-36: Element mapping of a MoNiCrBSi coating by means of electron microprobe

It can be seen that there is a separation of the molybdenum and the NiCr-phase. Additionally to nickel and chromium, iron can be detected. It is solved in the nickel-alloy. The oxygen distribution shows prevalent oxidation of the molybdenum phase. In order to determine whether the individual phases evaporate selectively, the process parameters were varied. The individual element contents with their standard deviation are listed in [Table 5-18](#) on the following page.

Table 5-18: Element content of Mo/NiCrBSi coatings in wt.-%

Element	1	2	3	4	5	6	7	8	9
Si	1 (0.07)	1 (0.03)	1 (0.03)	0 (0.03)	1 (0.12)	1 (0.03)	1 (0.04)	1 (0.02)	1 (0.02)
Cr	5 (0.32)	4 (0.17)	5 (0.16)	3 (0.22)	6 (0.58)	5 (0.12)	5 (0.16)	4 (0.20)	4 (0.03)
Fe	2 (0.23)	1 (0.05)	1 (0.03)	1 (0.06)	1 (0.16)	1 (0.04)	1 (0.01)	1 (0.07)	1 (0.02)
Ni	21 (1.27)	17 (0.83)	19 (0.68)	14 (0.88)	27 (2.91)	23 (0.47)	23 (0.47)	18 (0.86)	15 (0.14)
Mo	72 (1.89)	77 (1.05)	74 (0.89)	81 (1.20)	64 (3.75)	69 (0.65)	69 (0.65)	77 (1.17)	79 (0.20)

The phase analysis using X-ray diffraction reveals not only the main phases of molybdenum and nickel-chromium, but also small fractions of molybdenum oxide (MO_2). The MoNiCrBSi coatings show a maximum hardness of 327 HV3 and scatter over a wide range of hardness, while the FeCr13/Mo coatings are all located within a narrow range. All hardness values with standard deviations are given in the following table.

Table 5-19: Vickers hardness of polished Mo/NiCrBSi micros-sections

Probe	4-01	4-02	4-03	4-04	4-05	4-06	4-07	4-08	4-09
Hardness (HV 3)	205 ± 2	102 ± 15	211 ± 21	239 ± 39	327 ± 34	256 ± 39	290 ± 37	320 ± 40	299 ± 65

Analogous to the FeCr13/Mo coatings, the hardness of the Mo/NiCrBSi coatings correlate with their porosity.

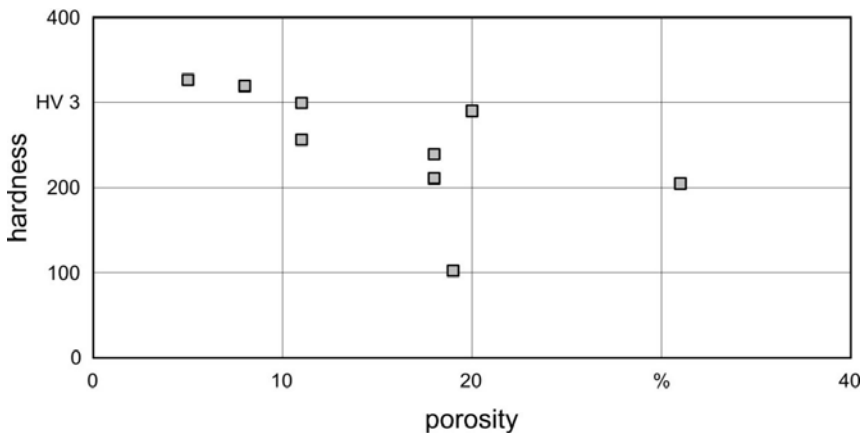


Figure 5-37: Correlation between hardness und porosity

The tribological tests show an improved behaviour of the layers in comparison to an uncoated steel surface. The individual Stribeck curves are in a narrow interval so that a direct correlation with the porosity cannot be observed.

The tribological properties were examined in "Pin-on-disc" experiments in heated synthetic oil (0W/30). The coatings show improved performance in comparison to an uncoated reference sample made of cast iron. The transition from mixing into the

state of liquid friction occurs at lower velocities and at reduced total friction. A detailed description of the tribological testings can be found in chapter 7 “Tribological mechanisms of microstructures”

5.5 Tribological testing of the inner coating of cylinder liners

The FeCr13/Mo 50/50 material was chosen as a suitable spray material for the coating of rotationally symmetrical specimens for use in tribological test rigs. Three liner geometries with different diameter and coating lengths were used. Figure 5-38 shows schematically the internal coating of a liner together with the plasma torch F210. In addition, the experimental setup for the fired testing is shown. The testing of the liners took place at the Institute of Technical Combustion (ITV).

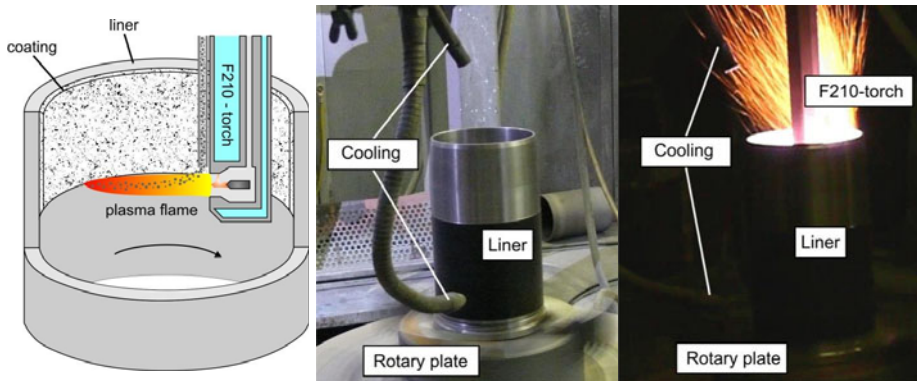


Figure 5-38: Schematic internal coating of a liner (left) based on [FLO03], experimental setup for coating liners for fire testing (ITV) (middle) and coating process with blow out of overspray particles (right)

The liners for the coating were mounted on a rotary plate and rotated at a speed of 200 rpm. During the coating the liner was cooled with dried air by two cooling nozzles. It was particularly important to cool the lower part of the liner, because the heat dissipation downwards is minimal. Furthermore, it was necessary to cool the insides of the liner, i.e., the applied coating, as well. Additionally, the powder particles which have not been incorporated into the layer, i.e., the so-called overspray, also had to be removed. In Figure 5-38 (right), the blow out of over-spray particles can be seen. The incorporation of the overspray in the coating may lead to the failure of the coating during the mechanical processing or to the formation of pore nests.

The liners for the RRV- (rotational friction measurement test rig) and shaker-testing were sprayed in accordance with the full factorial plan. The test specimens for the RRV-tests had a small inner diameter of 83 mm. Two of the liners could not withstand the honing process and were excluded from the test series. The coatings of liners 05 and 09 for the shaker-testing were also destroyed during the honing process. No connection with the coating properties is was obvious. When coating the liners for the fired testing, spray parameter variations 01 - 03 were omitted. Since these liners had

a diameter of 130 mm and a length of 253 mm, honing their thermally sprayed coatings was expected to be a major challenge; thus, some liners were chosen in advance as a backup for the specimens that would most probably be destroyed during the honing process.

The results from the flat samples showed that surface parameters, such as porosity and structural depth, but also characteristics, such as the hardness of coating materials, could be influenced by a specific variation of the spraying parameters. This study indicated that the layers depend primarily on the current used and less on the spray distance. The microstructure, the cohesion and the indentation hardness are largely determined by the variation of the spray parameters. Variables which determine the layer structure are the heat transfer to the particles and the impact velocity. The variation of the current represents the influence of the energy input. High currents lead to a higher energy input for the spray particles and, thus, determine the degree of partial melting and acceleration of the particles. If less energy is applied to the spray particles - for example, at low current - the amount of unmelted spherical particles increases; accompanied by a low coating cohesion, it results in a high porosity and low hardness. The properties of thermally sprayed coatings are strongly dependent on the coating cohesion and adhesion to the substrate. Since the adhesion of the coatings strongly depend on the mechanical interlocking of the particles among themselves and with the substrate, unmelted or resolidified particles play an important role. An increased number of such particles results in a bad adhesion, so that coatings having increasingly occurring round particles exhibit different properties than coatings which are mainly composed of splats. The porosity of the thermally sprayed coatings was generated near to unmelted or resolidified particles so that it could be used as a validation of adhesion. The MoNiCrBSi-01 coating, with its comparatively high porosity level (approximately 30%; highest among the investigated coatings), is characterised by its disadvantageous frictional behaviour. Nevertheless, all investigated molybdenum-containing coatings exhibited better friction behaviour than the one of an uncoated substrate. The hardness of the layers depends not only on the cohesion but also on the degree of oxidation of the molybdenum particles, as molybdenum can form very hard Mo-oxides. In order to ensure that the coatings can be machined, e.g., grinded or honed, ductile phases such as steel or nickel-based alloys were added, since increasing the amount of ductile phases resulted in lower hardness of the coatings. Thus, the FeCr13/Mo coatings have a lower hardness than the MoNiCrBSi coatings because their molybdenum content is higher.

In addition to the good wear and friction performance of the porous thermally sprayed coatings, the increased oil retention was another positive effect. For the use in light-weight engines, they can replace the previously used cast iron liners, thus saving weight. Additionally, no significant distortions occur between the aluminium cylinder and the coating so that the "blow-by" effect is minimised, and thus, the exhaust emissions are reduced [FLO11].

5.6 Conclusion

A number of coatings were applied to thermo-mechanically highly stressed surfaces by means of atmospheric plasma spraying in order to investigate the influence of the spray parameters on the formation of porosities, which can function as micro-dimples.

All materials showed similar tendencies: the lower the heat input, due to low current or low hydrogen gas flow, the higher the amount of non-melted and re-solidified particles, which form the starting point for porosities. Additionally, it was determined that an increase of the porosity of the coatings results in an increase of the individual pore depth. First, the coatings were prepared with a torch for coatings on outer contours, and then analysed and subsequently the information of coating these materials were transferred to an internal coating process. The coatings that were made with the torch F4 MB for outer contours exhibited a much lower porosity and a higher hardness than the coatings made with a torch for inner coatings. The melting rate of the powder particles was reduced by the lower energy input of the torch for internal coatings; thus, the amount of non-melted and re-solidified particles increased. The reduction of the coating cohesion and related hardness was associated with increased porosity. Due to the suitability of the individual materials for application on thermo-mechanically highly stressed surfaces, various mixtures containing iron, molybdenum, and chromium steel were used as coating materials. It was found that molybdenum-containing coatings provide a sufficiently high hardness due to the formation of brittle oxide phases. The high melting point of molybdenum also allows for its use for applications with high thermal stresses. Mixing ductile phases such as the iron to the molybdenum phase allowed for easier machining, e.g., grinding and polishing, of the coatings. As a function of the used spray parameters, the chromium phase in the steel-containing coatings was characterised by an oxidation level different from those of the other coatings. The chromium oxide also lead to an increase in hardness. In particular, the coatings which were sprayed with low heat input exhibited a high oxidation level of chromium particles because the particles were not strongly melted and accelerated, resulting in the formation of oxide films around the particles during their flight phase. The materials which were investigated at first were consequently further developed; iron was replaced with chromium steel in the molybdenum mixture. The purpose was both to increase the corrosion resistance of the coatings and provide the internal coatings with sufficient hardness. The Mo/FeCr13 mixture was investigated with respect to the possible control of the porosity and the pore depth. For this material, a full factorial plan with different spray distances and currents was used. It was revealed that, depending on the spray parameters, different amount of porosities and pore depths were created; thus, for example, the current controls the amount of pores. The lower the used current, and therefore the applied energy contribution, the higher amount of pores can be observed. A self-fluxing molybdenum/nickel alloy was chosen additionally for the inner coating. Similar to the FeCr13/Mo mixture, the ductile nickel phase was added to this material in order to ensure further processing of the coating. The nickel alloy also showed good corrosion characteristics and hard ox-

ide phases. This coating system was also studied with regards to the formation of porosity as a function of the spray distance and the current. It was shown that the porosity level depends strongly of the current and is less dependent on the spray distance. For the tribological experiments with cylinder liners of the other project partners, the FeCr13/Mo mixture was selected due to the good tribological behaviour. However, due to the differences in hardness between the molybdenum and steel particles, special attention should be paid to its post treatments, in this case, the honing process.

6 Surface characterisation based on optical metrology

Institut für Mess- und Regelungstechnik (IMR), Leibniz Universität Hannover, E. Reithmeier, M. Kästner, M. Bretschneider, O. Abo-Namous, F. Engelke

6.1 Objective and approach

Subproject 4, “Structure Oriented Surface Characterisation Based on Optical Measurement Technique”, focused on developing and researching methods which allow for a characterisation of the cylinder liners surfaces that have been micromachined in subprojects 2 and 3.

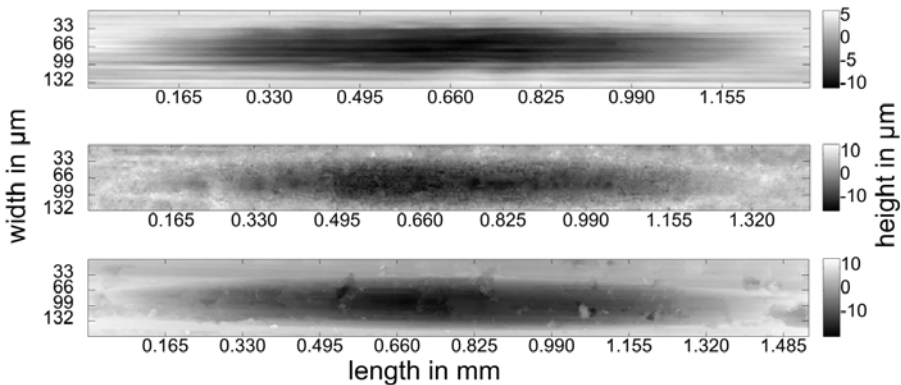


Figure 6-1: Measured micro-dimples on cylinder liner Shaker-2 using (top to bottom) a chromatic sensor, a confocal laser microscope (NA (numerical aperture) = 0.46), and a white light interferometer (NA = 0.55)

For the complex task of measuring the insides of a cylinder liner using optical sensors, new methods had to be developed. Since optical sensors for areal measurements, such as white light interferometers and confocal microscopes, require too much space and have a limited measuring range, a confocal chromatic white light sensor was used. The chromatic sensor is a point sensor that allows for precise positioning inside of cylinder liners, as only a small part of the apparatus has to be brought inside the cylinder while the signal is transported to the controller by optical fibre. This sensor was incorporated into a coordinate measuring machine that is able to position the sensor inside the cylinder with sub micro meter uncertainty. This measurement system was modified further to conduct measurements with different surface-to-sensor angles to identify undercuts in micro-dimples, which would increase oil retention in the surface. Structured flat surfaces and small cylinder segments were measured using a white light interferometer and a confocal laser microscope in order to develop and compare data processing and measurement techniques.

For the characterisation of the structured surfaces, new parameters as well as methods for calculating these parameters automatically from the measured data had to be developed. Moreover, algorithms for the subtraction of the form of the cylinder and

the waviness that take the micro-dimples into account had to be formulated. The research into the exact form of the micro-dimples necessitated the development of a new stitching technique so that high resolution data of the single dimples could be acquired. Watershed- and threshold-based methods were used for the automatic identification of microstructures. For the identification of undercuts, methods of data fusion and image processing were implemented, among them morphological 3D thinning.

6.2 Measurement techniques

White light interferometer

A white light interferometer (see Figure 6-2) was used for preliminary measurements of flat test surfaces as well as cylindrical test segments for the development of data processing techniques. As in a Michelson interferometer, the light emitted by the source is split into two separate beams. One is directed at the surface of the test subject while the other is led along a reference path at the end of which both beams are superimposed. If the optical path difference between the two is below the coherence length, both beams can interfere with one another, and the signal changes in accord with the z-position of the microscope. The signal is recorded by a CCD-chip at the end of the optical path. The microscope steps along the z-direction, and a stack of intensity values is recorded for each pixel of the field of view. By evaluation of the image stack, the height corresponding to each pixel can be identified and an areal height measurement is achieved.

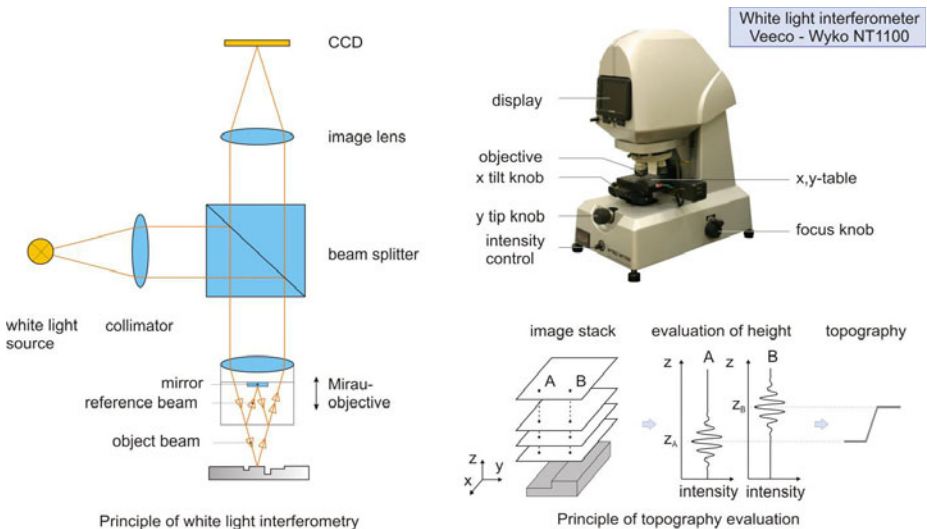


Figure 6-2: White light interferometer (WLI) and WLI principles

Chromatic sensor

In a chromatic sensor, dispersion is used to identify the distance between the sensor and the sample. The light originating from the sensor is reflected by the surface of the sample and guided back to the controller by an optical fiber, where a pinhole is used for evaluation. In order to acquire the height information, a spectrometer in the controller measures the central wavelength of the reflected intensity, which varies according to the sensor to surface distance due to the chromatic objective lens (see Figure 6-3). The controller of the chromatic sensor is operated by a PC-workstation via EIA-232 port, formerly known as RS-232. The height data is measured as a 15-bit-integer number that is scaled by the maximum range of the sensor, which is 429 μm resulting in a vertical resolution of 13 nm.

The chromatic sensor was integrated into a multisensor-coordinate-measuring machine, the MarVision OMS 553 HA (Figure 6-3) by Mahr Multi-sensor GmbH. This machine is equipped with four separate axes, three translational and one rotational axis. The translational axes move the sensor head, whereas the rotational axis rotates the sample. The translational axes are equipped with glass scales which allow for a position certainty of up to 0.1 μm with a translational uncertainty of $0.5 + L / 900$ μm for a translation of length L.

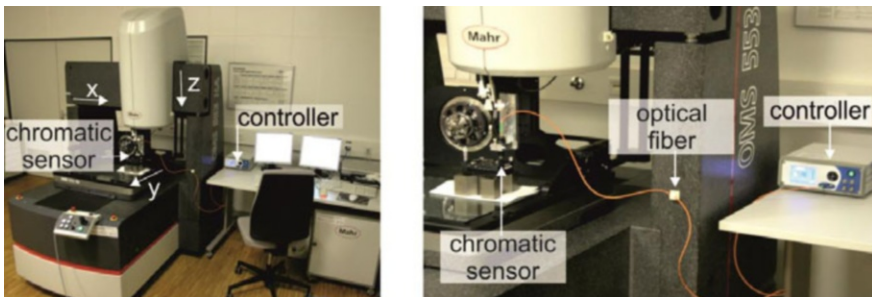


Figure 6-3: Coordinate measuring machine Mahr OMS 553 with chromatic sensor

Communication with the machine is achieved via the Ethernet protocol *mahr*talk to acquire information, such as the actual position and target coordinates, directly. An aluminium adapter was constructed to integrate the chromatic sensor RB-400.2 by Digital Surf into the vertical axis of the coordinate-measuring machine. The chromatic sensor is connected to the white light source of the Nobis XT controller by means of an optical fiber.

Software was developed using MATLAB and Python to synchronise and save the measured sensor data with the positioning data of the coordinate-measuring machine. Before the beginning of the measurement, the initial coordinates of the axis are calibrated by a homing run; following, the sensor is moved to the actual measuring coordinates. Having reached the measuring coordinates, the sensor is moved, with a constant speed, along the x-axis; alternatively, the sample is rotated with a constant angular velocity around the y-axis by the rotational axis. When a line meas-

urement is complete, the sensor moves along the y-axis to the next line. As the sensor moves over the sample, a three dimensional image of the sample surface is recorded. In order not to overload the program memory and therefore the measurement process, the measurement data are saved in temporary files to be processed later. After completing the measurement, the temporary data recording of the surface to sensor height information and the position of the cylinder liner are saved based on their timestamps. The lateral resolution of the measurement is equivalent to the step width along each scanning axis, which in turn is based on the translation between profiles and angular or regular velocity and measurement frequency of the sensor.

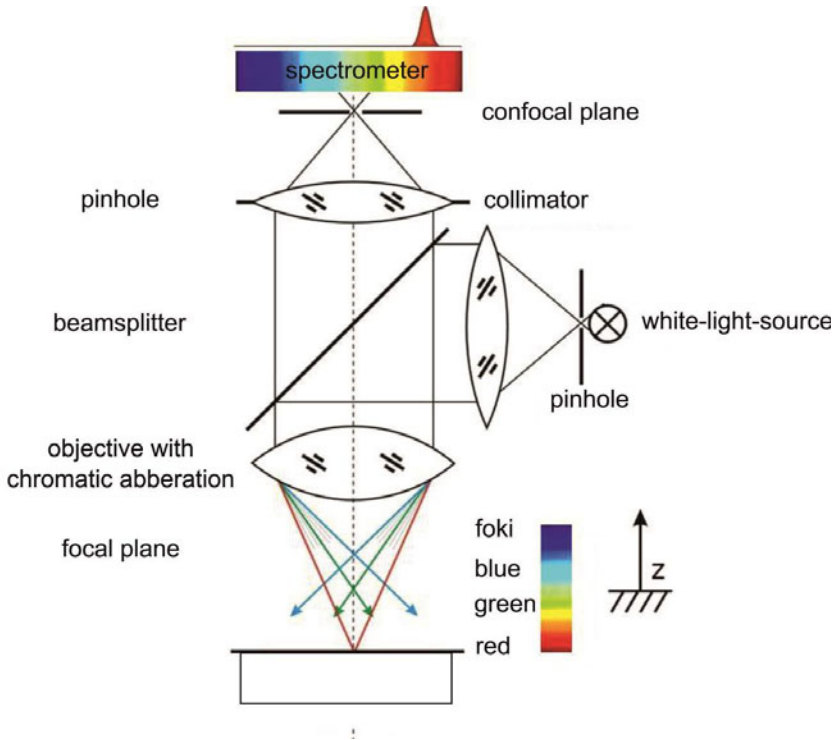


Figure 6-4: Physical principle of a chromatic sensor

To allow for a measurement from multiple angles while still maintaining the ability to measure the insides of cylinder liners, a modification of the chromatic sensor head was devised. A linear axis was used in conjunction with a hinge joint to change the angle between the work piece and the sensor along one axis as seen in [Figure 6-5](#).

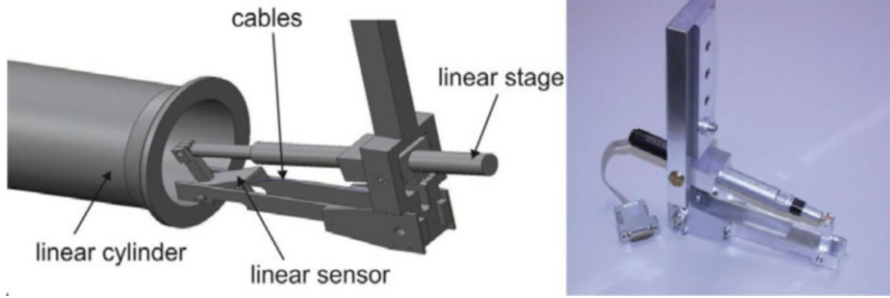


Figure 6-5: Modification of the chromatic sensor for measurement of undercuts

6.3 Measurement of machined micro-dimples

Data preprocessing - stitching

The form evaluation of the micro-dimples necessitated measurements with a high resolution; however, such measurements could not be obtained in a single measurement due to restrictions of the field of view of the white light interferometer. To address this problem, multiple overlapping measurements were performed and fused, to form a larger field of view. In stitching, measurements or images of scenes related to one another by translational transformation are spatially aligned and the data of these images is combined into a larger array of height or intensity values.

Because usual registration techniques like cross correlation for the spatial alignment of the measurements are computationally expensive and are not robust against translationally invariant image features ([Sze06]), a new method relying on the geometrical information of the dimple was devised. An example of the overlapping high resolution measurements can be seen in [Figure 6-6](#).

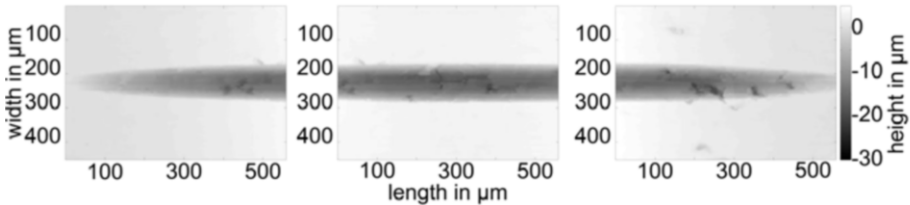


Figure 6-6: High resolution images of a micro dimple by white light interferometry

The dimple feature used for alignment of the measurements is the cross-sectional area (see page 105) which is a function of the position on the cross section line of the dimple representing the area below the reference surface height. The cross-sectional area functions of the measurements of [Figure 6-6](#) can be seen in [Figure 6-7](#).

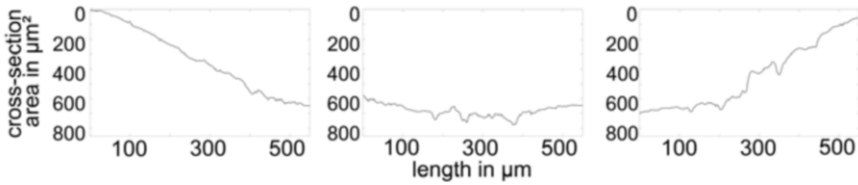


Figure 6-7: Characteristic cross-section area of [Figure 6-6](#)

When comparing the cross-section areas of two adjacent measurements, the shift between them is identified by means of an optimisation of a least squares algorithm. The relative coordinates of the measurements are then used to align the measurements as seen in [Figure 6-8](#).

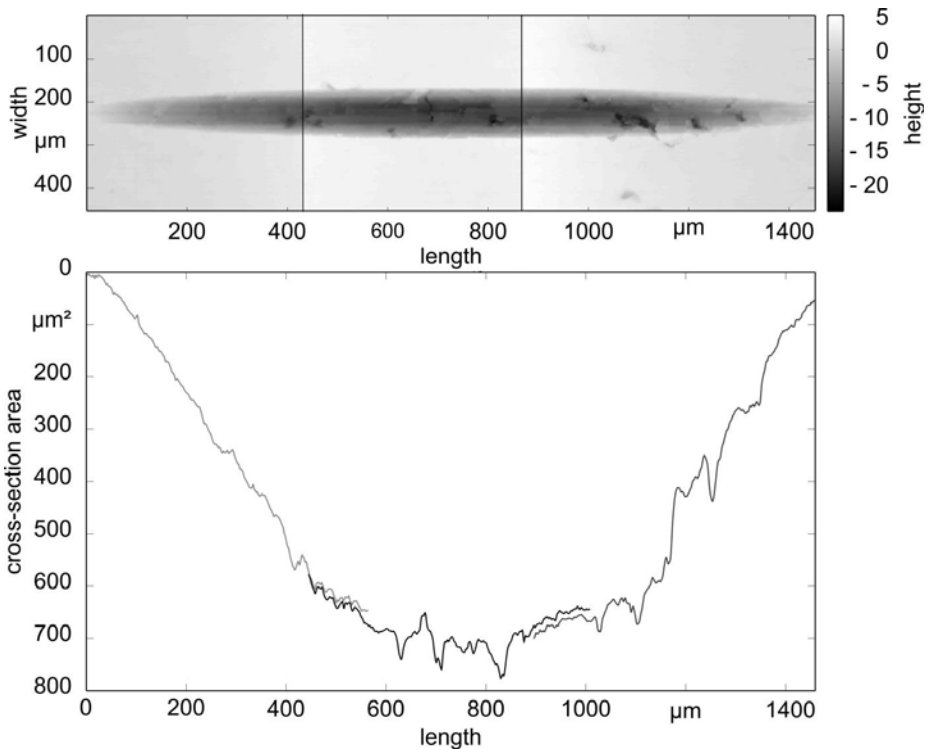


Figure 6-8: Stitching using the shift information

Data preprocessing - form and waviness

In subproject 2, the insides of cylinder liners were structured using fly-cutting process, thermal plasma spraying, and honing. To investigate the resulting structures, the cylindrical form due to areal measurement using the white light interferometer had to be removed for a robust characterisation of the micro-dimples, which does occur due to the simultaneous measurement of a high number of surface points, as op-

posed to the point measurements using the chromatic sensor which remove the cylinder form via the measurement principle.

The cylindrical shape of the measured surface causes height differences in the measurements of up to 20 μm, depending on the cylinder radius. An example of an unprocessed measurement and a height profile undisturbed by the dimple can be seen in Figure 6-9.

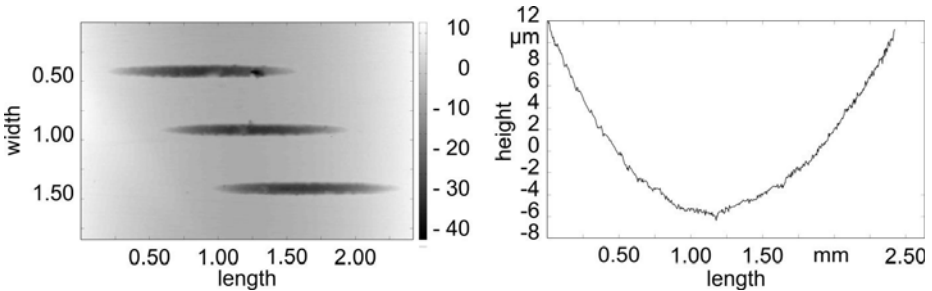


Figure 6-9: Unprocessed measurement with form

Use of a polynomial surface fit of the 4th order (F_{basic}) removes the cylindrical form; however, the surface fit overcompensates due to the influence of the dimple. This results in a data processing artifact in the measurement data M_1 .

$$\min(M - F_{basic}) \Rightarrow M_1$$

The resulting height data bends downwards at the edges of the field of view as seen in Figure 6-10. The differences in height introduced by the basic fit have a typical amplitude of a few micrometers.

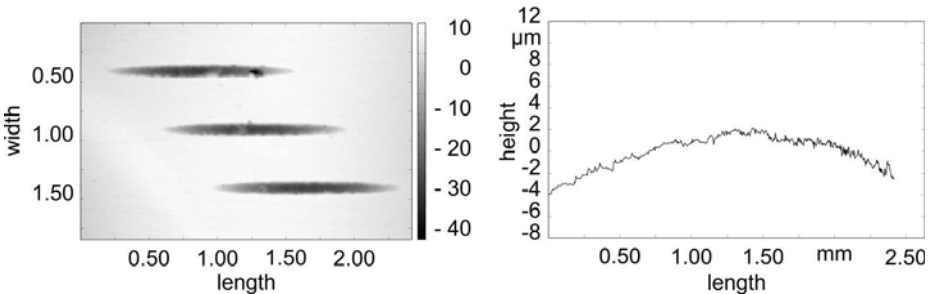


Figure 6-10: Measurement after basic fit (left), profile showing overcompensation

Segmentation methods for the identification of micro-dimples

Using segmentation algorithms, such as watershed and threshold methods, allows to identify the area of the cavities as well as to consequently remove it from the measurement data by replacing the cavities with NaN-values. These are either replaced by the mean height value of the plane of reference or interpolated to form the basis for a more accurate fit. The new measurement data sets $M_{2,zero}$ and $M_{2,interp}$ are formed as follows:

$$M_{2,zero} = M_1 \cdot R_{zero}$$

Replacing the measurement data of the micro-dimples with an interpolation of the neighbourhood results in the following:

$$M_{2,interp} = \text{interpolate}(M_1 \cdot R_{NaN})$$

The resulting measurement data sets $M_{2,zero}$ and $M_{2,interp}$ can be seen in [Figure 6-11](#). Since the interpolated data has a smoother surface, it fits more closely to a polynomial than the constant value set $M_{2,zero}$.

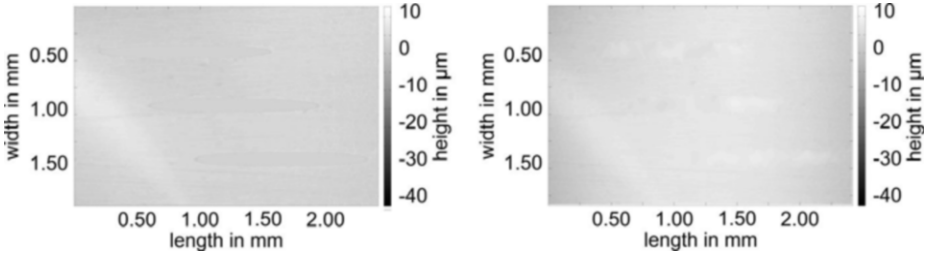


Figure 6-11: Micro-dimples replaced by zeros (left) and interpolation (right)

Both data sets are subjected to a secondary polynomial fit using a least squares algorithm.

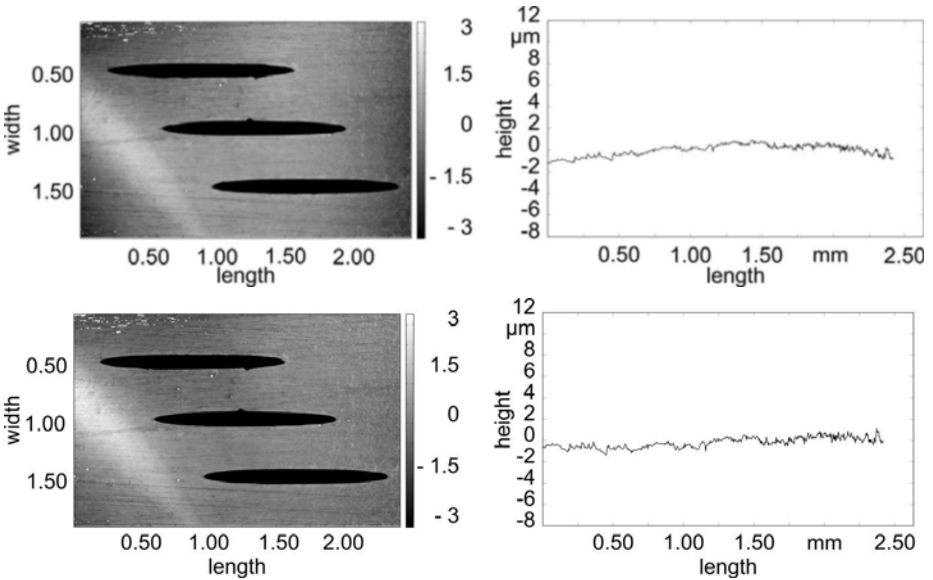


Figure 6-12: Measurement after accurate fit with zero replacement (top) / interpolation (bottom)

[Figure 6-12](#) shows the combed surface fit subtractions when replaced by zeros and interpolation.

$$1. \min(M_{2,zero} - F_{\text{accurate},zero}) \Rightarrow M_{3,zero}$$

$$2. \min(M_{2,interp} - F_{accurate,interp}) \Rightarrow M_{3,interp}$$

The final surface is created by subtracting both the basic and the accurate fit from the original measurement data.

1. $M_{4,zero} = M - F_{basic} - F_{accurate,zero}$
2. $M_{4,interp} = M - F_{basic} - F_{accurate,interp}$

When using a constant replacement, the final surface still retains a slope of ca. $1\mu\text{m}$ amplitude; in contrast, the profile of the surface obtained by interpolation shows no geometrical deviation.

Data processing - region detection

The measured height-data is saved in a two dimensional matrix (see [Figure 6-13](#)). The next step is the identification of the structured surface parts in the height-map by means of segmentation.

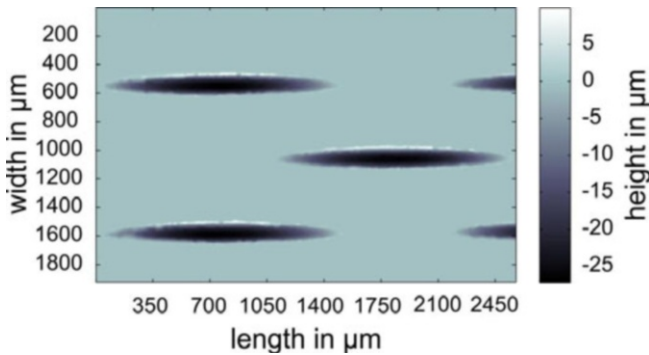


Figure 6-13: Measurement data of a micro machined surface, measured by a chromatic sensor

The first segmentation step is executed by means of watershed transformation, i.e., by flooding the lowest part of the surface with virtual water. As the level of the water rises it meets the basin boundaries. The watershed regions are the boundaries of the water basin at the time of overspill. This way, the data is successively segmented by height. Since the structures have height values below the plane of reference, these are segmented first. The material heaped around the structures (ridges), by the cutting process, ([Figure 6-14](#)) is segmented as a region which lies between the structures. These regions belong to the surface and are therefore falsely segmented as a structure.

In the lower part of [Figure 6-15](#), a more successful method for structure identification is presented. This method works by defining a threshold on the surface at $t_{structure} = 0,2\ \mu\text{m}$. This is an empirically measured value that gave the best results for segmentation of micro-dimples and ridges. So the structure mask $R_{structures}$ is given by:

$$R_{structures}(x,y) = \begin{cases} 1 & \text{for } p(x,y) \leq t_{structure} \\ 0 & \text{for } p(x,y) > t_{structure} \end{cases}$$

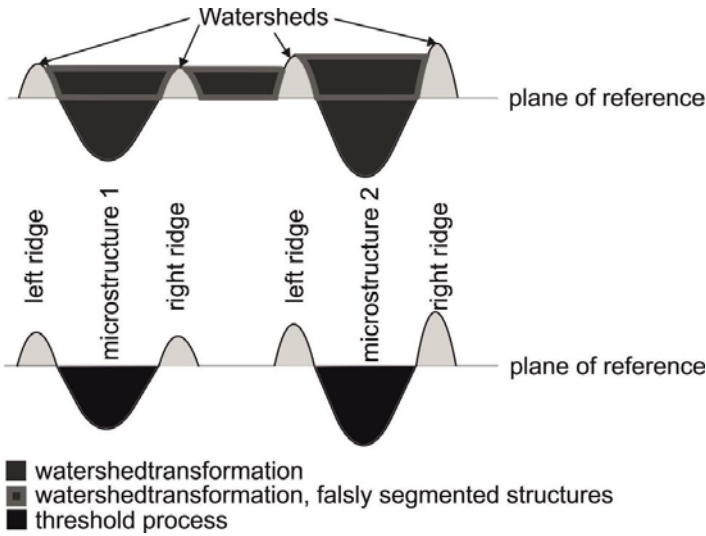


Figure 6-14: Watershed transformation, false structure detection

Figure 6-15 presents the structure mask identified by the threshold process. Since, in general, a number of structures can be found in a single structure mask $R_{structures}$, these have to be registered as separate regions. To this end, the structure mask is divided by assigning each true pixel a regional index based on its neighbourhood [VIN91]. After the regional assignment, regions that have fewer pixels than the threshold value are discarded, as these are either false regions or micro-dimples that were incompletely measured. As a result, only completely measured micro-dimples remain for evaluation (Figure 6-15). By only accessing height information $p_{structure}(x,y)$ of one of the identified regions via a specific region mask, the measured structures are separated from the rest of the measured data.

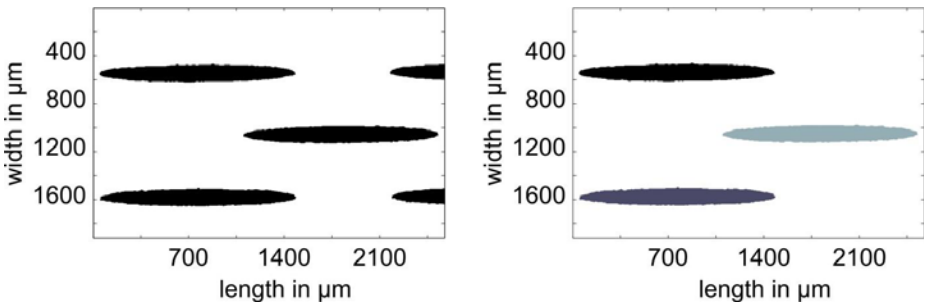


Figure 6-15: Structure mask of Figure 6-13 (left), labelled regions (right)

Next to the microstructures, the cutting process creates hills of surface material that are not a part of the structures and have to be described separately. The search for these ridges is restricted to an extended bounding box around the primary structure. The original bounding box is extended by a factor 1.4.

Figure 6-16 shows the detected ridges and the extended bounding boxes. A mask for these ridges, R_{ridge} is generated by:

$$R_{\text{ridge}}(x,y) = \begin{cases} 1 & \text{for } p(x,y) \geq t_{\text{ridge}} \\ 0 & \text{for } p(x,y) < t_{\text{ridge}} \end{cases} \text{ with } p(x,y) \text{ in vicinity to } R_{\text{Region}}$$

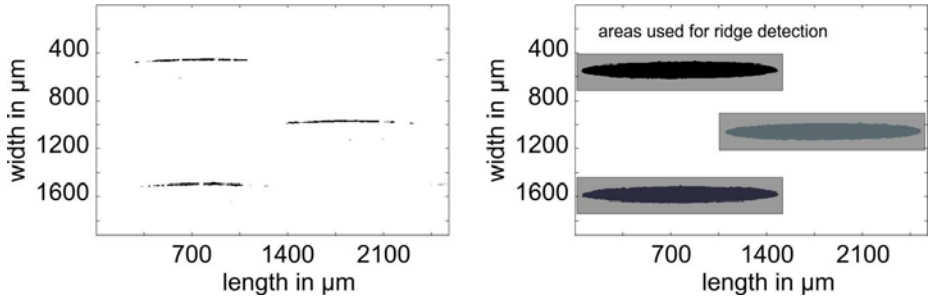


Figure 6-16: Ridges (left) and extended bounding boxes for ridge detection (right)

Data processing – micro-dimple characteristics

In cooperation with subproject 2 new descriptive parameters were developed to characterise the micro-dimples. The parameters and their calculation will be explained in the following chapter. Using common fabrication parameters, the micro-dimples have two axes of symmetry: the longitudinal section \vec{s}_l and the cross section \vec{s}_c . These are vectors in the measuring plane (see Figure 6-17). They can be obtained by fitting two lines to the height data of each structure whereby the first one gives the longitudinal section, and the second is fitted perpendicular to the first one and gives the cross section.

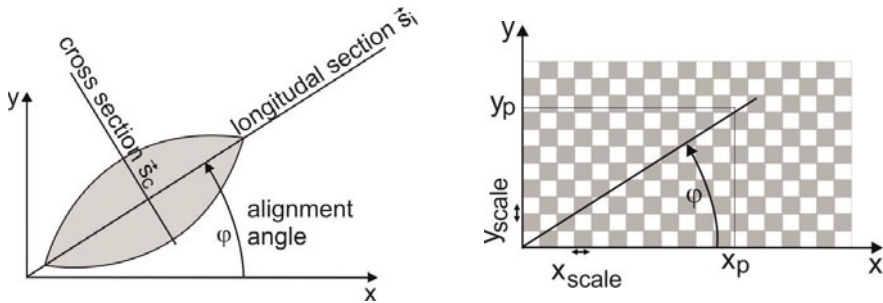


Figure 6-17: Longitudinal and cross section of micro-dimples (left), scale along alternate axes (right)

The measured height data is formatted as a two dimensional array that represents an equidistant grid. By identifying the angle between the x-axis and the axis of the longitudinal section the orientation angle of the structure can be found and the measurement data rotated.

The resolution along the x-axis is given by $x_{\text{scale}} = d(x_n, x_{n+1})$, where $d(a,b)$ is the Euclidean distance measure for the points a and b and is a parameter that describes

the measurement. The resolution along the y axis is defined in a similar way. After rotating the measurement data to correct the orientation of the dimples the mean resolution along an axis with an angle of ϕ to the x axis in the image plane (Figure 6-17), is given by:

$$xy_{\text{scale}}(\phi) = x_{\text{scale}} \cdot \cos(\phi) + y_{\text{scale}} \cdot \sin(\phi).$$

Dimple-length l_s and dimple width b

Both parameters dimple length l_s and dimple width b are calculated on the basis of \vec{s}_i and \vec{s}_c . The dimple length is the length of the longitudinal section; the dimple width is the length of the cross section.

$$l_s = xy_{\text{scale}} \cdot \sum R_{\text{structures}}(x,y) \forall R_{\text{structures}}(x,y) \in \vec{s}_i$$

$$b = xy_{\text{scale}} \cdot \sum R_{\text{structures}}(x,y) \forall R_{\text{structures}}(x,y) \in \vec{s}_c$$

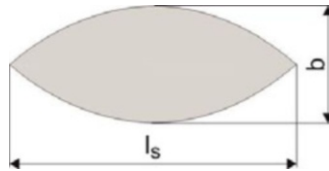


Figure 6-18: Dimple length and dimple width

Maximum dimple depth $a_{p,max}$ and histogram based threshold dimple depth $a_{p,hist}$

The maximum dimple depth a_p is the depth of the deepest point in the dimple, and the minimum value of the height map in the structure region is used for this parameter.

$$a_{p,max} = \min (p_{\text{structure}}(x,y))$$

As this parameter is only based on a single pixel value, it is extremely susceptible to noise and measurement artefacts.

A more robust parameter can be calculated by plotting a histogram of the height values of the structure region. Figure 6-19 shows that the pixel numbers decrease rapidly for high depth values, but this descent still takes place over a few micrometers. A threshold which ignores the 4 deepest percent of the height values is used. Experiments have confirmed this to be a robust threshold value. In the following, only the histogram-based dimple depths are used, and therefore, simply called dimple depth.

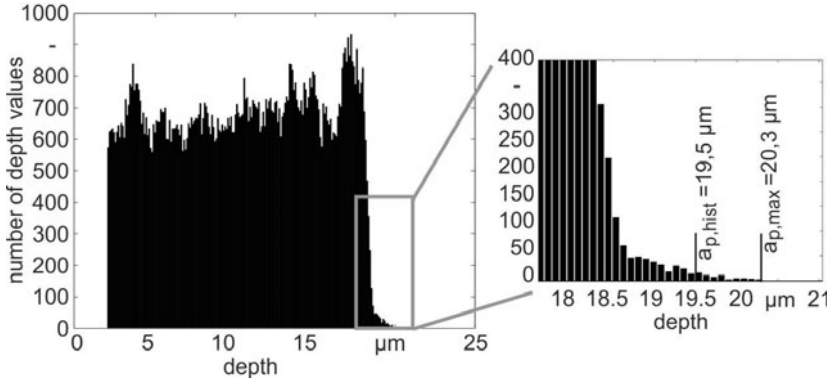


Figure 6-19: Histogram of height values

Ridgewidths $b_{a,l,hist}$, $b_{a,l}$, $b_{a,r,hist}$, $b_{a,r}$ and ridgeheights $h_{a,l,hist}$, $h_{a,l}$, $h_{a,r,hist}$, $h_{a,r}$

The ridges originating from the cutting process need to be analysed separately, as the orientation of the blade affects their form. Similar to the parameters for dimple depths, parameters based on single values and histogram-based parameters were defined. The calculation of these parameters follows the same steps as those described for the dimple depths (above).

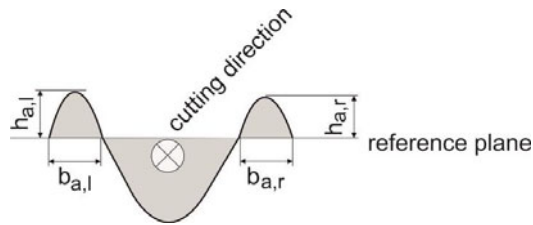


Figure 6-20: Ridge widths and ridge heights

Dimple volume V

The dimple volume V is calculated from the height map of the dimple in the following way:

$$V = \sum_{x,y} |p(x,y)| \times x_{scale} \times y_{scale} \quad \forall x,y: R_{structure}(x,y) = 1.$$

The volume of the structures can be used as a parameter to describe the oil retention capacity.

Areas A , A_p , A_E

The areal parameters are based on the longitudinal section and the cross section. These parameters are calculated as follows:

$$A = \sum_{(x,y) \in \bar{s}_q} |p(x,y)| \cdot xy_{scale}(\phi)$$

$$A_E = \sum_{x,y \in S_i} |p(x,y)| \cdot xy_{scale}(\phi)$$

$A_p = \sum_{x,y: R_{structures}(x,y)=1} x_{scale} \cdot y_{scale}$. A is the dimple crosssection area, A_p is the projected area, and A_E is the area of structured surface.

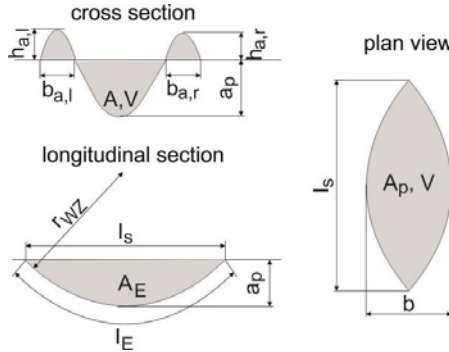


Figure 6-21: Areal parameters of projections of micro-dimples

Tool radius r_{WZ} , dimple depth by circular fit $a_{p,fit}$

In the cutting process, the blade moves along a circular path. By fitting a circle to the height data along the longitudinal section, the radius of this path can be estimated. This radius is called tool radius. By applying the same method, the dimple depth can be calculated as well. By using the centre of the fitted circle as a reference point, the dimple depth can be calculated as follows: $a_{p,fit} = r_{WZ} - z_{circle}$

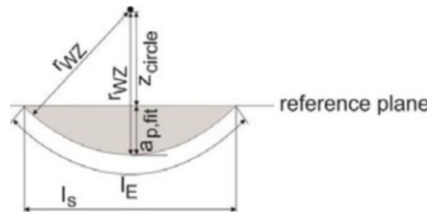


Figure 6-22: Tool radius and tool radius based depth

Dimple length l_E

The dimple length is this part of the circumference of the circular movement which the blade had made inside the material. It is calculated using $a_{p,hist}$ and l_s in the following way:

$$l_E = \frac{\arctan\left(\frac{2a_{p,hist}}{l_s}\right) \times (4a_{p,hist}^2 + l_s^2)}{2a_{p,hist}}$$

Relative dimple volume f_{ab}

The relative dimple volume is a measure that sets the volume of the ridges and the volume of the dimples in relation [GAH81]. Only the areas, and not the volumes, are used for calculation in the cross section:

$$f_{ab} = \frac{A_{\text{dimple}} - (A_{\text{ridge}_{\text{left}}} + A_{\text{ridge}_{\text{right}}})}{A_{\text{dimple}}} \text{ at } a_{p,\text{hist}}, 0 < f_{ab}.$$

Thus, for small ridges $f_{ab} \approx 1$, while for more pronounced hills f_{ab} is small. A case of ideal micro cutting would be $f_{ab} = 1$, whereas $f_{ab} = 0$ would be an example of ideal micro ploughing (see subproject 2). A more in depth description of the ridge / dimple volumes is achieved by evaluating f_{ab} not only at the point $a_{p,\text{hist}}$ but also across the length of the dimple at different cross sections. This way, a parameter vector \vec{f}_{ab} can be formed from the f_{ab} . For a more robust calculation, the mean over all of these cross sections is used.

$$f_{ab,\text{total}} = \frac{\vec{f}_{ab}(1) + \vec{f}_{ab}(2) + \dots + \vec{f}_{ab}(n)}{n}$$

$$f_{ab,\text{total}} = \frac{\sum A_{\text{dimple}} - (\sum A_{\text{ridge}_{\text{left}}} + \sum A_{\text{ridge}_{\text{right}}})}{\sum A_{\text{dimple}}} = \frac{V_{\text{dimple}} - (V_{\text{ridge}_{\text{left}}} + V_{\text{ridge}_{\text{right}}})}{V_{\text{dimple}}}$$

Roughness

The mean roughness values $R_{a,i}$ and $R_{a,q}$ are calculated for the dimple as follows:

$$R_{a,i} = \frac{1}{n} \sum_{i=1}^n \left(\left| \bar{s}_i(i) - \frac{1}{n} \sum \bar{s}_i \right| \right), R_{a,q} = \frac{1}{n} \sum_{i=1}^n \left(\left| \bar{s}_q(i) - \frac{1}{n} \sum \bar{s}_q \right| \right).$$

The longitudinal roughness $R_{a,i}$ is a measure for the areal dimple quality, and the cross roughness $R_{a,c}$ measures the quality of the blade.

Edge angle ε and Edge radius r_ε

The blade used in the cutting process is the negative of the dimple (see Figure 6-24). The tip of the blade can be described by a circle with radius r_ε up to a certain height. If the blade cuts in deeper than the tip radius r_ε the upper, triangular form of the blade is also found in the resulting dimple and can be identified via the angle ε (see Figure 6-23).

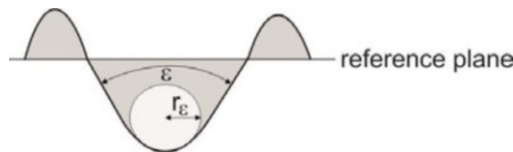


Figure 6-23: Edge - angle and radius

These parameters are obtained by fitting a circle to the height data of the cross section and lines to the outlying regions using a least-square-procedure (see Figure 6-24).

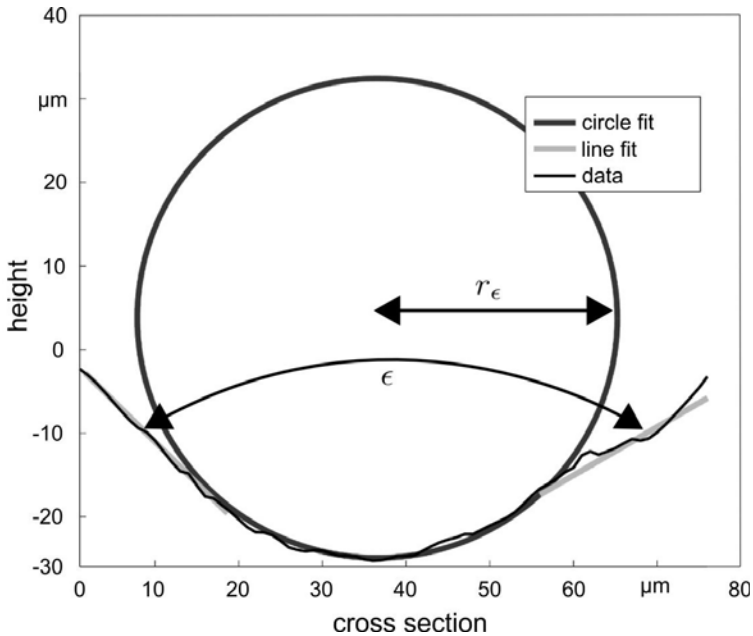


Figure 6-24: Circular fit to micro-dimple, surface ifw0030

A geometric difference analysis between the blade and the resulting dimples was conducted on blades used in the cutting process. The blades and dimples were measured using a white light interferometer to compare the cross sections of blade and dimple. The measurement data of the blade was used to create a binary image of the blade profile in which artifacts were repaired by the morphological operation of dilation followed by erosion. Using a gradient algorithm, the contour of the blade was determined (see Figure 6-25). The cross sections of blade $\bar{s}_{tool}(x)$ and dimple \bar{s}_q were fitted together by a least square algorithm.

A starting position for the fitting algorithm is found by searching for the global minima of both functions and removing the offset:

$$\bar{s}_{tool,fit,min} = \bar{s}_{tool}(x - x_{tool,fit,min}) - (\min \bar{s}_{tool} - \min \bar{s}_c).$$

The optimisation of the fit is performed as follows:

$$\min_{x,z} \sqrt{\bar{s}_{w,fit,min}(x) - \bar{s}_q + z + e \cdot c^2}.$$

The optimisation is performed by variation of the x position of the functions in respect to one another as well as the height offset between the two. The cost function penal-

ises big translations along the x-axis by the parameter c and the number of data points outside of the dimple cross section e .

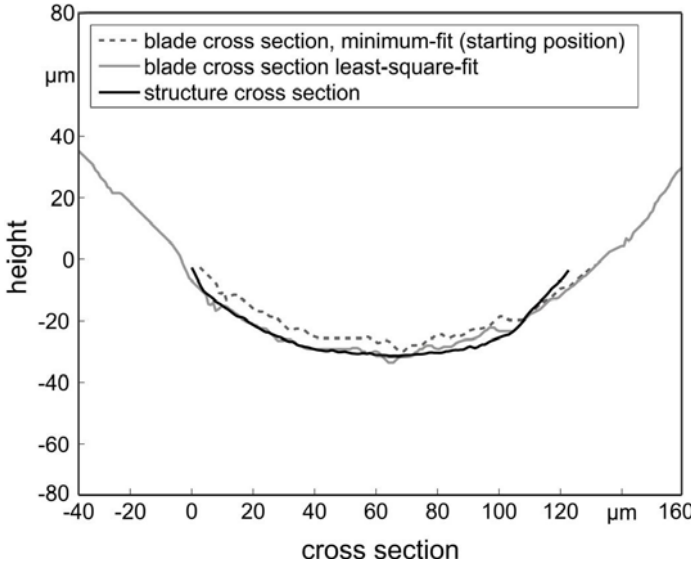


Figure 6-25: Least-square fit of tool and micro-dimple, surface ifw0110-19

Once the datasets are fitted together, a number of parameter quotients are calculated:

$$spf_b = \frac{b}{b_{WZ}}, spf_A = \frac{A}{A_{WZ}}, spf_{r_\epsilon} = \frac{r_\epsilon}{r_{\epsilon, WZ}}, spf_{a_{p, hist}} = \frac{a_{p, hist}}{a_{p, hist, WZ}}.$$

In an ideal cutting process, these parameters are close to one; any difference indicates discrepancies between blade and dimple.

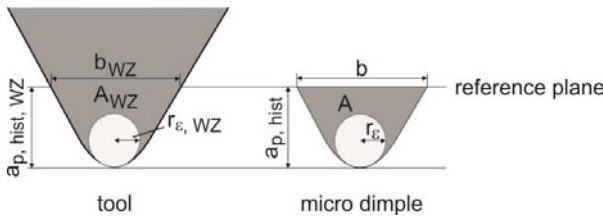


Figure 6-26: Cutting tool in comparison to the micro-dimple

6.4 Measurement of thermal sprayed surfaces

Data processing – micro pore characteristics

The stochastic structures created by thermal plasma spraying were characterised by statistical evaluation of a number of surface images. This option was chosen over the stitching of multiple images because the errors introduced by the stitching exceeded

the information gained and because the pore structures have small dimensions compared to the area of the measurement.

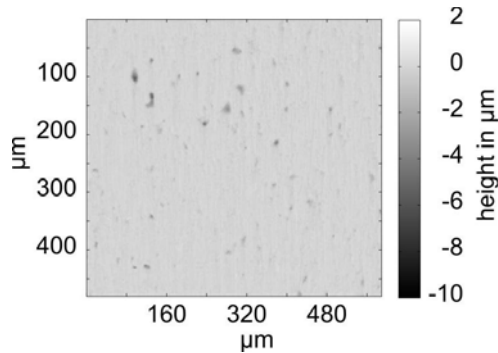


Figure 6-27: Measurement of stochastic structures, surface CA2

Defects that appear at the edges of the structures were interpolated. The surfaces were aligned by a planar fit to the height data, and the plane of reference was determined by a histogram based analysis. Figure 6-28 shows the histograms of two height maps of the test subject CA2. The reference plane was determined by the maximum value of the histogram, and the new height map was calculated by $p(x,y) - h_{\max, \text{hist}}$.

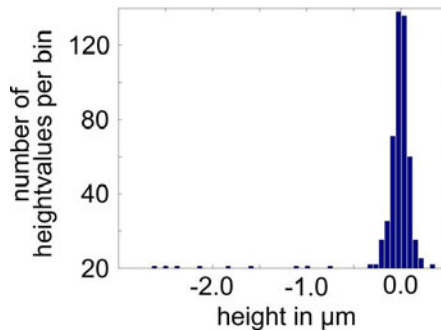


Figure 6-28: Histogram of the height distribution of Figure 6-27

The stochastic structures caused by thermal plasma spraying had no symmetry but had a statistical height and width distribution; therefore, a more general approach was used to accurately describe their properties. The area of all pores was divided by the area of measurement to form the quotient A_V .

$$A_V = \frac{\sum_{i=1}^n A_i}{x_{\text{scale}} \cdot x_{\text{length}} \cdot y_{\text{scale}} \cdot y_{\text{length}}}$$

A similar approach was used to relate the volumina of the pores to the volume of the material. The volume of all pores $\sum_{i=1}^n V_i$ was divided by the area of measurement and the maximum depth of all pores $\max(t_i)$.

$$V_V = \frac{\sum_{i=1}^n V_i}{x_{\text{scale}} \cdot x_{\text{length}} \cdot y_{\text{scale}} \cdot y_{\text{length}} \cdot \max(t_i)}$$

Another parameter was the specific volume relation $V_{V,\text{sp}}$:

$$V_{V,\text{sp}} = \frac{\sum_{i=1}^n V_i}{x_{\text{scale}} \cdot x_{\text{length}} \cdot y_{\text{scale}} \cdot y_{\text{length}}}, [V_{V,\text{sp}}] = \mu\text{m}.$$

The watershed transformation, described earlier, was used for segmentation of the pores. In addition to the areal and volumetric parameters described above, parameters analogous to those described for the characterisation of deterministic structures were formulated for the areas, volumes and depths of single structures.

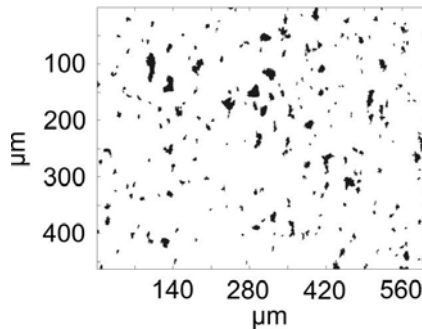


Figure 6-29: Structures found in the left part of [Figure 6-27](#).

6.5 Multi-measurement methods

Undercut detection

Simulations were used to check whether the data fusion algorithms can fuse the different data to a 3D dataset of the surface. While varying the angle between the surface and the sensor, a virtual undercut normal was created, and a simulated measurement was conducted. Afterwards, the resulting individual measurements were fused based on the positioning data. Consequently, the surface of the material was reconstructed from the data. The measurement process can be seen in [Figure 6-30](#) a) to c) with the result in [Figure 6-30](#) d). The reconstruction of the surface (grey line in [Figure 6-30](#) d) from the different fused height data was achieved stepwise while taking the measurement direction into consideration.

Data processing – undercut detection

Areal microscopic- and optical point sensor methods only allow measurements of functions of two lateral coordinates; in case of translations, for each pair of coordinates x and y only one value $z(x,y)$ will be measured. Surfaces including undercuts as seen in [Figure 6-31](#) are functions of three coordinates. The measurement data are angle dependent projections of the true surface, so measurements under varying sur-

face to sensor angle and data fusion are needed to reconstruct surfaces with undercuts.

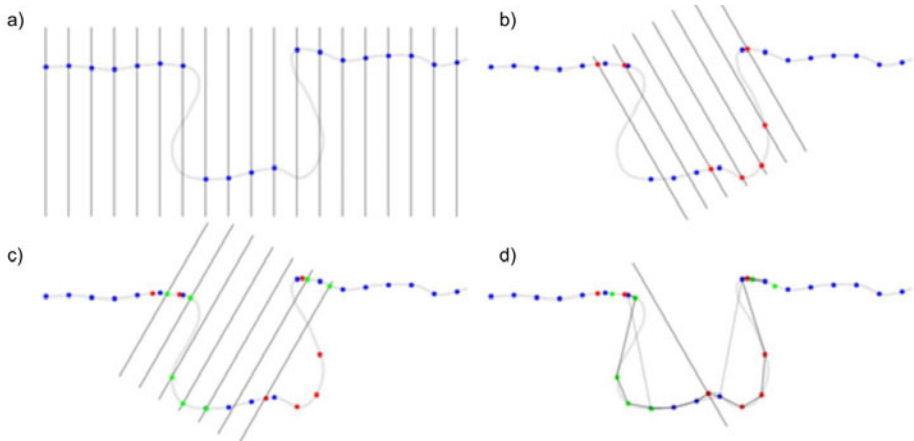


Figure 6-30: a)-c) scanning process of a microstructure with undercuts, d) resulting surface estimation

A method was devised to reconstruct full 3D data of surfaces from multiple measurements with optical surface sensors by varying the measurement angle.

In the first step, the different measurements were converted from matrices with height values to point clouds which were then rotated into equal positions by means of a least square optimisation method. The point clouds were constructed from the coordinates and the original indices of each point of measurement in the height matrix. This was necessary to obtain connectivity information which was needed in the reconstruction of 3D bulk data.

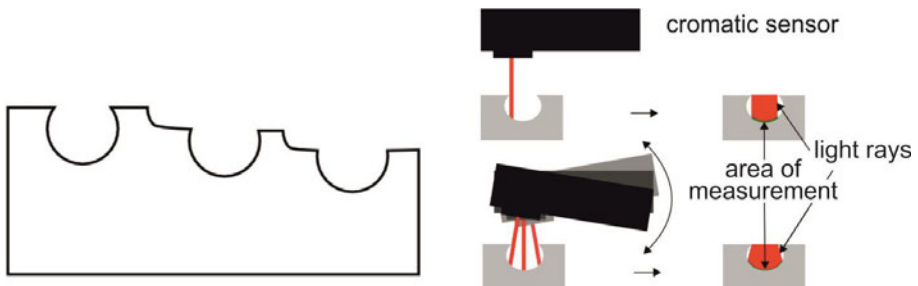


Figure 6-31: Porous surface including undercuts (left) and comparison of measurement areas for fixed and turnable chromatic sensor (right)

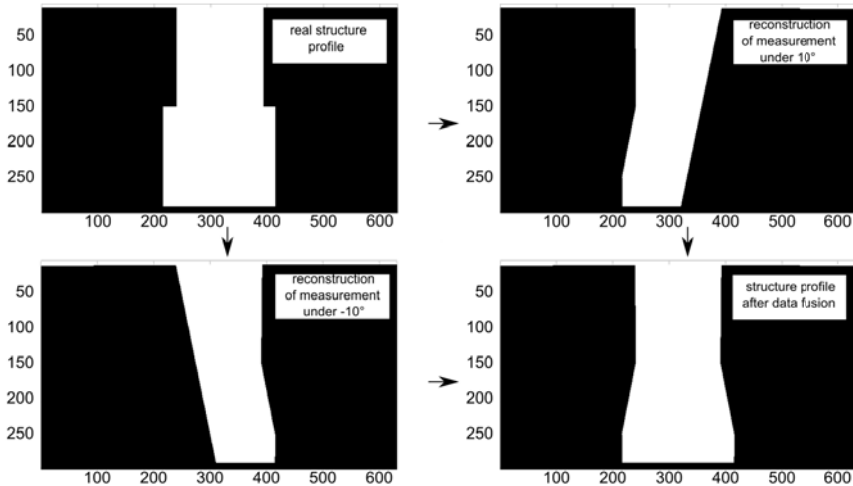


Figure 6-32: Profile of surface with structure and undercuts (top left), height information by measurements under varying surface to sensor angle (top right and bottom left), result of fusion by logical “or” (bottom right)

In the next step, the rotationally aligned point clouds were interpolated into height matrices for spatial alignment. The alignment was performed using image registration techniques developed at our institute. The alignment coordinates were then used to transform the point clouds into the same coordinate system. Consequently, the aligned data was used to construct 3D bulk data for each measurement by linear interpolation and morphological filling. The bulk data consisted of binary 3D matrixes whereby 0 represented the workpiece material and 1 - the outside of the workpiece (Figure 6-32). The fusion necessary for the reconstruction of the 3D object was performed by using a logical “or” operator.

Figure 6-33 indicates the presence of undercuts in the micro-dimples, which widen roughly below the surface by $0.3 \mu\text{m}$ with cavity openings of a few micrometers and depths of 2 to $3 \mu\text{m}$. As the spot size of the chromatic sensor is about $1 \mu\text{m}$, such cavities could only be represented by a very small number of pixels which, in combination with the difficulties of image registration and rotational correction, complicated the actual reconstruction of these microstructures by chromatic measurements.

Even the higher resolution of the white light interferometer was insufficient to successfully reconstruct undercut cavities. Future work should focus on improving the rotational correction and image registration so that smaller structures can be reconstructed better.

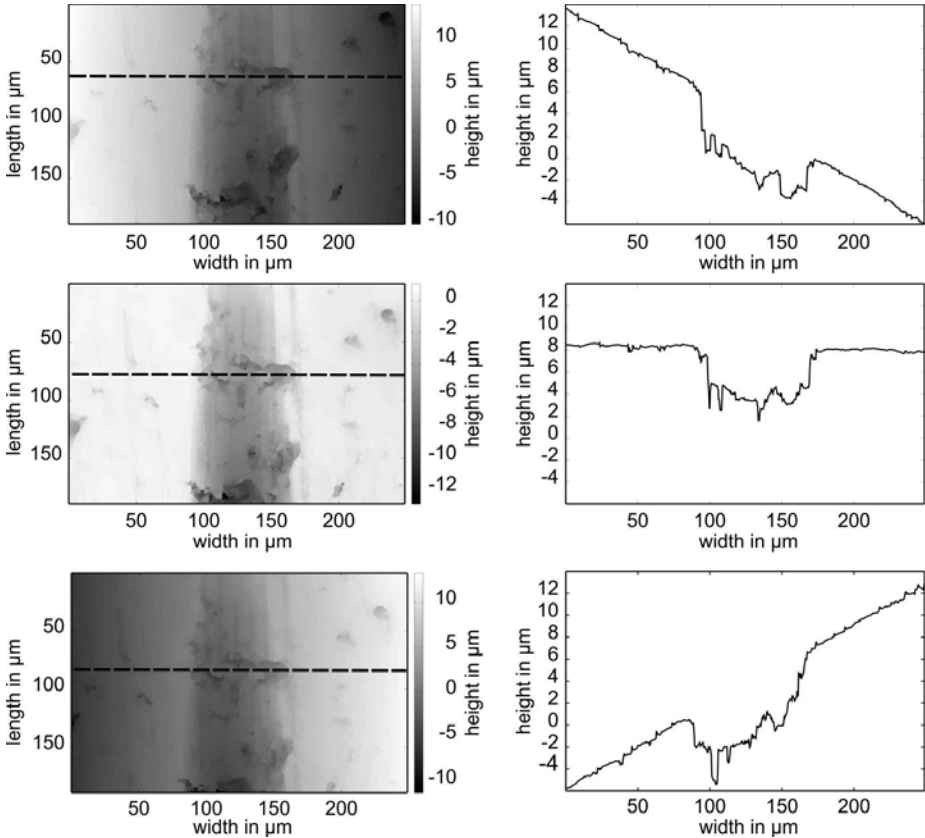


Figure 6-33: Multiple measurements of micro-dimples using WLI with surface to sensor angles $+4^\circ / 0^\circ / -4^\circ$ (top to bottom); profiles indicate the existence of undercuts with depth of up to $0.3 \mu\text{m}$

3D morphological-thinning

A new approach for the characterisation of surfaces by morphological thinning was investigated. To successfully identify structures, a method for the detection of hills and valleys was developed using morphological 3D thinning. Thinning is a method that extracts the topology of binary data. In 2D, topologic features consist of connected areas, junctions, endpoints and holes (Figure 6-34). In 3D, additional features like through holes that connect two not-set areas can also be taken into consideration.

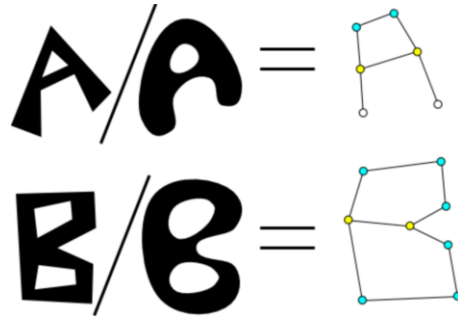


Figure 6-34: 2D morphological thinning

In 1.5D, the method functions as follows: The line/height space is transformed into a pixel space, and the measured data is used to form 'true' pixels against the 'false' pixels of the background. Following, the space above (below) the data is filled with 'true' pixels to find valleys (hills). These data are then thinned morphologically until only a skeleton of the 'true' values remains. Once the skeletisation is completed, the endpoints of the skeleton are evaluated as positions of valleys (hills) (see [Figure 6-35 a](#)). [Figure 6-35 b](#)) exemplified the method which was proposed for the finding of the undercuts. To identify the undercuts, it is necessary to build the 'true' space in a more sophisticated way, with the function of measurement used as a dividing line between the 'true' and 'false' pixels.

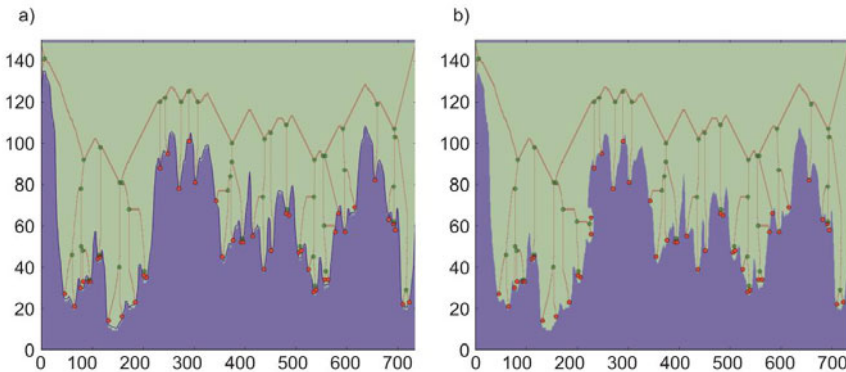


Figure 6-35: 1.5D thinning (left), 2D thinning (right)

For use in 2.5D images, the pixel space is extended into a voxel space with all voxels above (below) the surface being 'true'. Subsequently, a sophisticated algorithm is used for fast morphological thinning which does not change the Euler-characteristic of the 'true' space. The devised thinning method uses a generalisation of the 4-color-scheme generally utilised in 2D thinning to avoid accidental thinning. This 8-color-scheme is used in conjunction with parallel computing on a GPU to minimise the computation time. Using measurement data collected by variation of surface to sen-

sor angle as described above, a 3D surface model could be constructed. This model is sufficient for the undercut detection by means of thinning as described in the 1.5D case. Figure 6-36 presents a method for pore detection. First, an image taken using a white light interferometer is used to generate a height map; then, the space above the surface is filled with 'true' pixels which were thinned until only a few arms stretched into the pores. This method showed great potential and should be investigated further in future research.

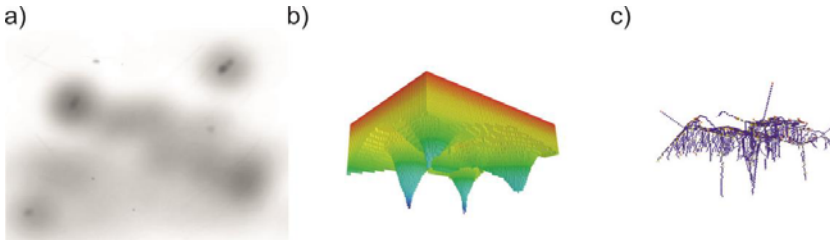


Figure 6-36: a) height map of surface with pores, b) true voxels above surface, c) skeletisation of surface with arms extending into pores

6.6 Conclusion

Optical measurement techniques allow for a fast and non-destructive evaluation of surface roughness. To adapt optical sensors to the challenge of surface characterisation of microstructured cylinder liners, new measurement and data processing methods were developed and implemented. The complex geometry of the microstructures to be characterised necessitated new approaches for structure identification and form removal.

The optical sensors used for measurement of the microstructured surfaces were a confocal chromatic sensor, a point sensor using chromatic aberration for distance measurement, and a white light interferometer, which uses incoherent light and image stacks for areal height measurements.

Optical measurements inside of intact cylinder liners were complicated due to the small size of the cylinder opening compared to the size of the sensor. To overcome this problem, a sensor setup was constructed using a coordinate measuring machine (CMM) as well as a specially tailored sensor head with a chromatic point sensor and an optical fiber. The CMM was used to position the sensor head inside the cylinder liner at close to ideal measuring distance and orientation. The point sensor measured the distance between the sensor and the object while the CMM rotated the cylinder liner. The synchronous positioning information provided by the CMM and by the chromatic sensor were fused to obtain 3D coordinates of the cylinder liner surface. The main merit of this technique was that the cylinder form was removed by the measurement setup.

To analyse the form of micro-dimples, high resolution measurements using a white light interferometer were made. Due to a small field of view with respect to the dimples, these measurements had to be aligned among each other to form a larger

measurement data set. The proper alignment was achieved by identifying the relative shift between two images when evaluating the area cross-section with respect to the lateral position. Using a least square fit, the area cross-sections of each single measurements data sets were aligned with their respective neighbours. Based on this, the single measurement data sets were fused to form a large scale, high resolution image of the micro-dimples. These measurements allowed for an analysis of smaller features of the dimples than the measurements using the chromatic sensor.

The measurements using a white light interferometer were carried out on samples with underlying cylinder form, which had to be removed for proper evaluation of the dimples. Simple form removal by polynomial fit to the surface results in flawed findings due to the influences of the microstructures. Thus, a new method which removes the form regardless of the structured surface parts had to be designed. In a first step, the form was removed by a polynomial fit; consequently, the structures were segmented and replaced with other height values which fit the plane of reference better. Following, a second polynomial fit was used on the remaining data. Both surface fits were then removed from the original measurement, and the relevant surface microstructure was evaluated.

Investigation of a large number of structured surface samples necessitated automated segmentation algorithms. Microstructures in the measurement data were identified by segmentation using watershed and threshold methods. The bounding box surrounding the structures was extended and used to search for ridges at the edges of the structures by means of threshold methods.

To find correlations between the form of the microstructures on the surface samples and their respective tribological behaviour, the identified structures were characterised by parameters describing their individual form as well as more statistical parameters such as areal and volumetric ones. Micro-dimples were also compared to the blade used in the cutting process by fitting an idealised blade to the structure or to the actual measurement data of the used blades.

To analyse microstructures for possible undercuts, which would increase the value of a number of areal and volumetric parameters used for surface evaluation, methods that allow for undercut detection were developed. The sensor head of a chromatic sensor was modified to allow for an adaptation of the surface to sensor angle, which allows for the measurement of undercuts. The undercuts could then be identified by evaluation of large measurement data sets obtained by 3D data fusion of several smaller data sets. Another method was developed for the recognition of undercuts using a white light interferometer; this method involved the automatic measurement of overlapping high resolution fields of view and merging them to form a larger field of view. The process was repeated for different surface to sensor angles; the resulting measurements were then aligned and transformed into 3D binary data and merged.

With the aim of identifying undercuts automatically, a new method was developed to skeletonise 3D binary data. This method is based on the thinning of 2D binary data,

which removes morphologically irrelevant pixels. This was generalised to a 3D binary voxel space. This algorithm showed great potential for the analysis of 3D surface data for hills and valleys as well as undercuts, which can be identified by the endpoints of the 3D surface skeleton.

7 Tribological mechanisms of microstructures

7.1 Tribological mechanisms of machined micro-dimples under planar contact conditions

*Institut für Fertigungstechnik und Werkzeugmaschinen (IFW), Leibniz Universität Hannover
B. Denkena, J. Kästner, T. Göttching*

In order to verify the friction-minimising potential of machined micro-dimples, they were cut into thrust bearing rings; consequently, their functional properties were determined on a ring-on-disc tribometer setup for planar contact with large surface coverage. Furthermore the tribology results of the machined micro-dimples were consequently compared with experimental testing results of micro-dimples that were fabricated with other manufacturing methods. This was done, in order to emphasize the potential of the new innovative micro structuring method by means of cutting, which was developed within this research (see chapter 4).

Ring-on-disc tribometer tests

The tribological performance of the micro-dimples was characterised by means of a ring-on-disc setup on a Wazau TRM 5000 tribometer. Lapped ($R_a = 0.05 \mu\text{m}$ to $0.1 \mu\text{m}$) starting discs structured by machining and made of aluminium bronze Cu-Si10Ni5Fe4 alloy were combined with a rotating axial cylinder roller bearing disc (steel, tempered and lapped) (Figure 7-1).

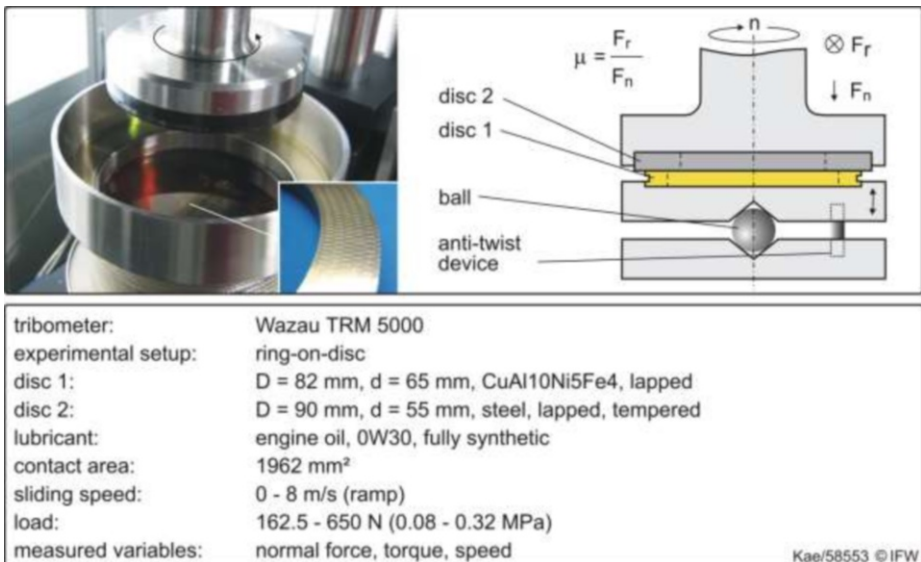


Figure 7-1: Ring-on-disc tribometer setup and boundary conditions of the test

In order to ensure the planar contact with the disc, the disc - which is fixed against rotation - floats on a ball. The fully-lubricated tests are carried out using an entirely synthetic engine oil of 0W30 viscosity. A 2-component dynamometer, integrated in

the flow of force below the fixed disc, measures the normal force F_n and the friction torque M_{Fr} with a measuring frequency of 100 Hz. Taking the mean ring diameter into consideration, the friction coefficient is calculated based on the variables listed above. In order to detect speed-dependent effects, the disc is accelerated up to a relative speed of 9 m/s. From this point on, a linear deceleration of the speed until standstill takes place within a preset time interval of 3 min; as a result, the entire Stribeck curve can be continuously depicted for this range.

For these ring-on-disc tribometer tests, micro-dimples were cut in a radial arrangement into the bronze rings via an orthogonal turn-milling kinematics (Figure 7-2, left). In Figure 7-2, right, the parameters relevant for the surface characterisation in this chapter are outlined.

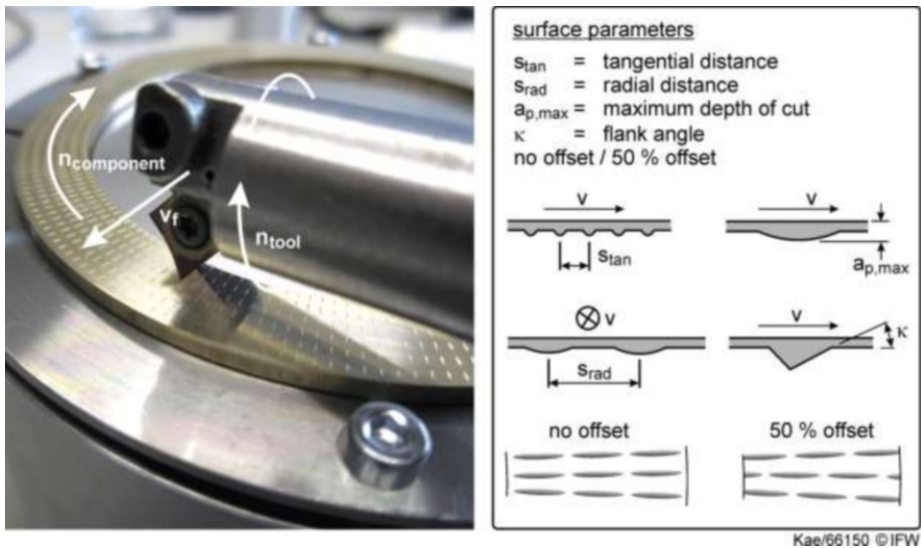


Figure 7-2: Machining strategy for the axial bearing rings and surface parameters relevant for the ring-on-disc tribometer tests

In the context of these tribometer tests, only micro-dimples with a U-shaped cross-section profile were considered. First, only the micro-dimple ratio was varied ($S_{MT} = 11\%$ to 45%), depending on the tangential micro-dimple distance ($S_{tan} = 0.25\text{ mm}$ to 1 mm). The micro-dimple ratio S_{MT} was defined as the percentage ratio of the projected micro-dimple area A_{MT} to the total surface area A_{tot} , as follows:

$$S_{MT} = \frac{\sum A_{MT}}{A_{tot}} \cdot 100\% \quad (7.1)$$

Furthermore, the arrangement of the micro-dimples (no offset and 50% offset) as well as the micro-dimple dimension were varied via the maximum depth of cut ($a_{p,max} = 10\text{ }\mu\text{m}$ to $50\text{ }\mu\text{m}$). For V-shaped cross section profiles, the geometry of the cross sections of the individual micro-dimples was also varied via the tool cutting

edge angle ($\kappa = 15^\circ$ to 55°). In all test series, the radial micro-dimple distance remained constant at $s_{rad} = 1.5$ mm.

Only those Stribeck curves where the surfaces of the employed rings and discs showed even contact patterns after the test runs were used in the evaluation. This was necessary in order to identify the influence of the individual present surface parameters in a reproducible way. During the test series, the oil temperature was monitored and kept constant at 60° C by means of a continuous readjustment. This was necessitated by the previously identified dependence of the friction coefficient on the oil temperature and, thus, on the oil viscosity.

Functioning of machined micro-dimples

Prior to focusing on the individual influence of the varied surface parameters, it had to be clarified if, to what extent, and in which speed range the machined micro-dimples have a friction-minimising effect for the ring-disc-contact investigated in this research. Figure 7-3 illustrates the functioning of micro-dimples. The Stribeck curves of a slide ring with micro-dimples ($a_{p,max} = 20 \mu\text{m}$, $s_{tan} = 0.5$ mm, $S_{MT} = 15\%$, 50% offset) as well as of a slide ring without micro-dimples are compared, each for the two test loads 325 N and 650 N. Both slide rings have a comparable fundamental roughness. Both Stribeck curves show the mean values of three test runs.

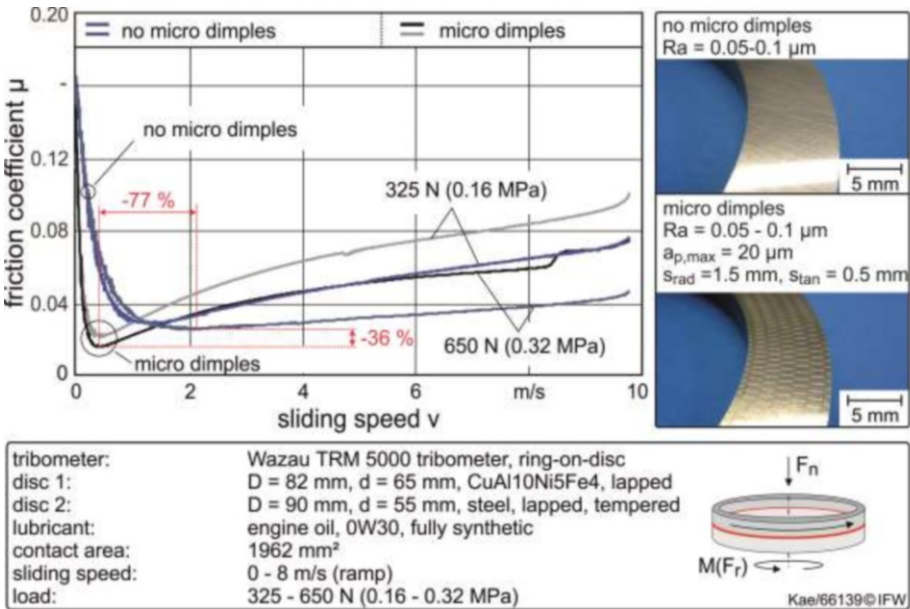


Figure 7-3: Functioning of micro-dimples at different test loads and speeds

Regardless of whether micro-dimples were created on the rings or not, the Stribeck curves first showed load-specific differences in their levels. In the hydrodynamic range, in particular, the level of the Stribeck curve rises when the test load decreases-

es. Etsion et al., who investigated structured and non-structured rings in the ring-on-disc contact, explains this load-dependent tendency with the lubrication gap height [ETS04]. With decreasing load, the height of the lubrication gap increases, leading to energetically unfavourable turbulences and shear effects becoming predominant in the gap itself. In the hydrodynamic range, a similar effect is based on the increase of the friction coefficient. The lubrication gap height increases as well due to the increasing of the relative speed between the friction partners. The shearing losses in the lubricant also increase as a function of the relative speed.

At low relative speeds, the friction-minimising potential of machined micro-dimples is independent of test load and relative speed in the range of limited and mixed friction of the Stribeck curve. Micro-dimples can reduce the respective minimum friction coefficient of the Stribeck curves by 24% to 36%, depending on the respective test load. Another tribological effect of micro-dimples is a considerable shifting of the minimum friction coefficient towards lower relative speeds. While the minimum friction coefficients without micro-dimples are in a speed range of $v = 1.36$ m/s to 2.04 m/s, the minimum friction coefficients with micro-dimples are in a speed range of $v = 0.38$ m/s to 0.46 m/s. When using micro-dimples, the minimum friction coefficients can thus be shifted between 72% and 77% towards lower relative speeds. This shifting can also be seen from the steeper decline of the Stribeck curves. When using micro-dimples, the tribological system changes much faster from the mixed friction range to the hydrodynamic range; this is especially profitable in the case of starting or oscillating tribological systems. The shifting of the minimum friction coefficients towards lower values and speeds corresponds to the results of [ETS99a, ETS99b, ETS09, WAN04].

In the hydrodynamic range, some test series show higher friction coefficient levels when micro-dimples are cut into the surface. This is explained by the fact that micro-dimples represent an additional surface roughness which can lead to additional energetically unfavourable turbulence in the lubricant film, particularly in case of high relative speeds between the friction partners.

Influence of micro-dimple ratio on friction coefficient and minimum friction coefficient

In the following, the tangential micro-dimple distance was varied between $S_{\text{tan}} = 0.25$ mm and 1 mm by means of the speed ratio during the turn-milling process. The variation of this surface parameter was combined with a variation of the micro-dimple ratio in a range of $S_{\text{MT}} = 11\%$ and 45% . In [Figure 7-4](#), top, the Stribeck curves for the different micro-dimple ratios are shown, and the corresponding minimum friction coefficients are explicitly given. The results show that the friction coefficient decreases with an increasing micro-dimple ratio. At the same time, the minimum friction coefficient declines continuously. Compared with a non-structured surface, the minimum friction coefficient can be reduced up to 50% by means of a micro-dimple ratio of 45%. A clear tendency whether the minimum friction coefficient is shifting with the micro-dimple ratio towards lower speeds cannot be observed.

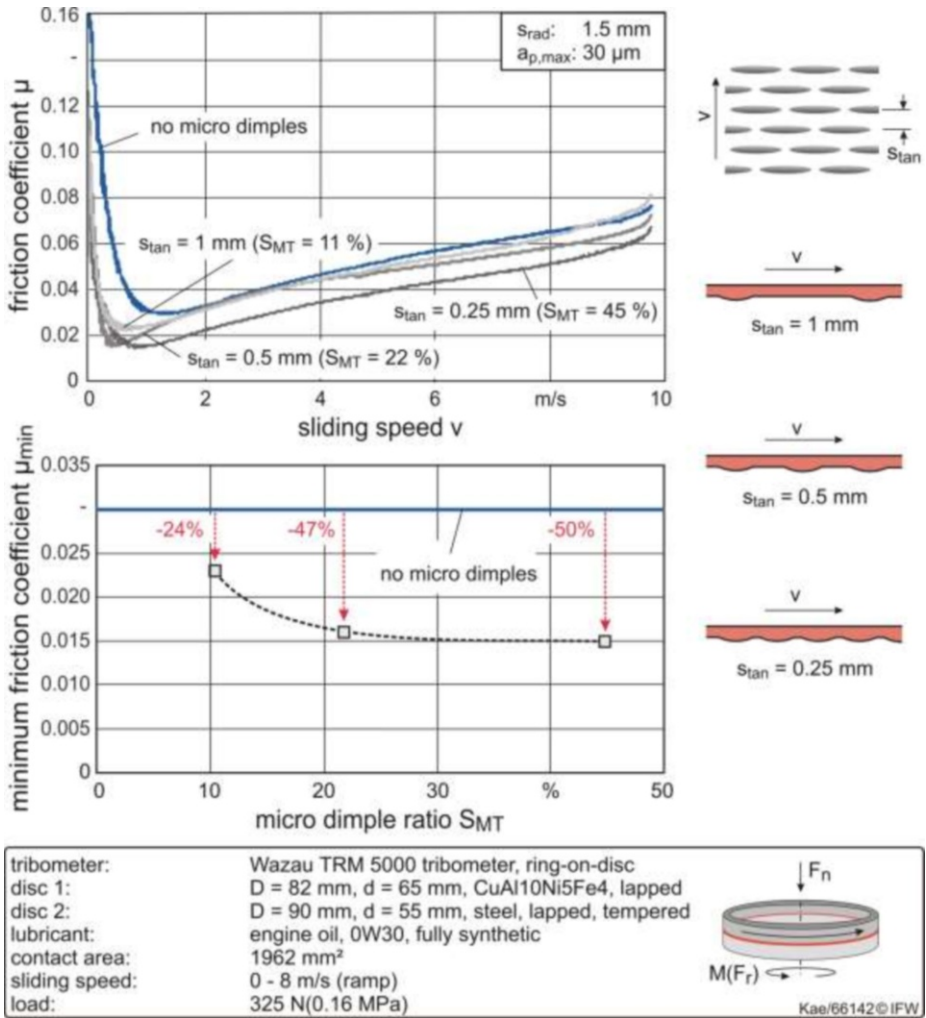


Figure 7-4: Influence of the micro-dimple ratio on the characteristic of the friction coefficient and the minimum friction coefficient

Reducing the friction coefficient in dependence on the micro-dimple ratio corresponds to the work of [LAG00, SCH05, WOE06]. The reduction is explained by the fact that the number of micro pressure peaks in the contact area increases simultaneously with the number of micro-dimples and, thus, with the total contact pressure. Uehara and Wakuda also found out that the friction coefficient increases again when micro-dimple ratios rise extremely [UEH03, WAK03]. In their opinion, this tendency can be explained by the fact that the decrease of the micro-dimple ratio leads to a decrease of the contact ratio of the examined surface. This decreasing contact ratio leads to a higher surface pressure which results in reduced lubrication gap heights and, consequently, in increased mixed friction ratios. However, the tendency of the friction coef-

ficient to rise again with the micro-dimple ratio could not be verified for the variation range of this research work.

Influence of micro-dimple arrangement on friction coefficient and minimum friction coefficient

The tribological examinations also focused on the arrangement of micro-dimples, distinguishing between no offset and 50% offset (Figure 7-5, right). Both types of structures had identical tangential and radial micro-dimple distances and dimensions and, as a result, the same micro-dimple ratios.

The tribological differences between these two structure variations are shown in Figure 7-5. Despite identical micro-dimple densities and dimensions, structures without offset show a continuously lower friction coefficient level throughout the complete speed range when compared to those with 50% offset. The Stribeck curve is shifted almost in parallel by an average of $\Delta\mu = 0.006$ towards the lower friction coefficients. Considering the minimum friction coefficient, micro-dimples arranged with no offset lead to reduced friction coefficients of 63%, whereas the 50% offset structure shows a reduced friction coefficient of 20%. Both structure variations exhibit a comparable shifting of the minimum friction coefficient towards lower speeds.

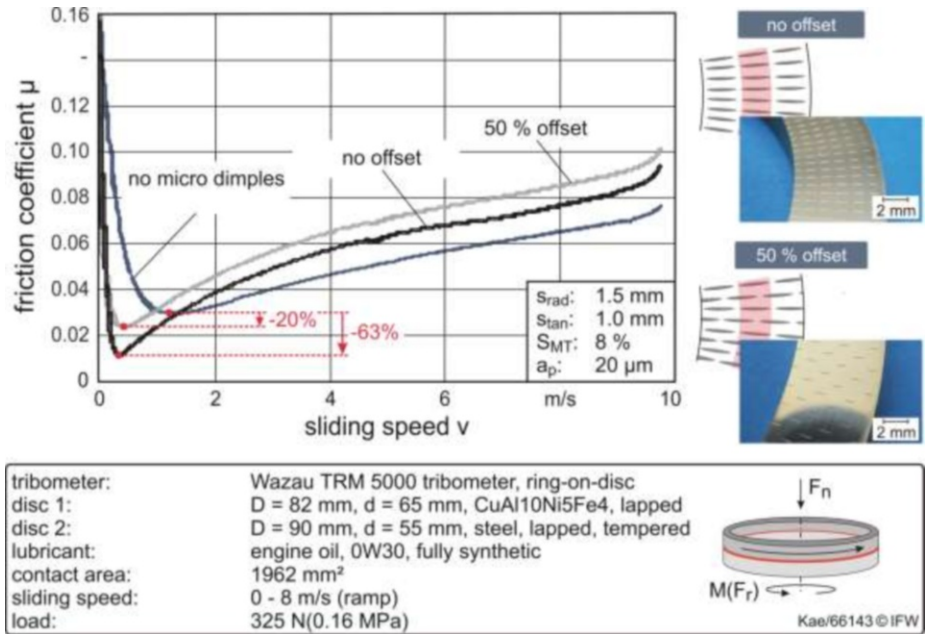


Figure 7-5: Influence of the micro-dimple arrangement (no offset/50% offset) on the characteristic of the friction coefficient)

The different levels of the Stribeck curves for the two structure variations are due to the radial coverage of successive micro-dimples. If there is no offset, an exact radial coverage of successive micro-dimples arranged with a tangential distance of s_{tan} is

reached. In case of 50% offset, successive micro-dimples are radially offset by half of the radial distance, in the present case by 0.75 mm, so that an exact coverage can only be reached with the next but one micro-dimple. Thus, compared to the structures without offset, the distance between two micro-dimples is doubled. In the range of the minimum friction coefficient, in particular, a similar tribological effect seems to exist when using a structure without offset. This effect was observed when increasing the micro-dimple density. It can be concluded that both the number of micro-dimples on a surface element and their arrangement on the element affect the pressure build-up and the resulting friction properties.

Influence of micro-dimple dimensions on friction coefficient and minimum friction coefficient

Prior to the experimental phase of this project, it was deliberated that apart from the number and the arrangement of micro-dimples, their dimensions would influence the friction properties as well. Thus, the micro-dimple dimensions were varied by means of the maximum depth of cut $a_{p,max}$. Figure 7-6 compares the Stribeck curves for U-profile geometries with maximum micro-dimple depths between $a_{p,max} = 10 \mu\text{m}$ and $50 \mu\text{m}$. Moreover, in Figure 7-6, middle, the minimum friction coefficients as well as the micro-dimple volumes are plotted depending on the micro-dimple depth.

Depending on the micro-dimple dimensions, the friction coefficient level decreases over the complete speed range almost in parallel to the reduced micro-dimple dimensions. Compared to a non-structured surface, the lowest micro-dimple depth of $a_{p,max} = 10 \mu\text{m}$ allows a reduced minimum friction coefficient of 85%. Furthermore, the minimum friction coefficient shifts with decreasing micro-dimple dimensions towards lower relative speeds. In Figure 7-6, the minimum friction coefficients as well as the corresponding micro-dimple volumes are plotted depending on the micro-dimple depth. It can be seen that both variables follow a similar exponential growth, indicating that differing minimum friction coefficients are primarily caused by the volume of the micro-dimples.

In the hydrodynamic range, micro-dimple dimensions show an influence on the friction coefficient level. On average, this level decreases with smaller micro-dimple dimensions. This tendency can be explained by the fact that due to their smaller dimensions (depth, area, volume) as well as their smaller effective tool cutting edge angle, smaller micro-dimples produce less turbulence in the lubrication gap. However, there are also limits in dependence on the micro-dimple dimensions. If the micro-dimples are too large, as is the case with a maximum micro-dimple depth of $a_{p,max} = 50$, the friction coefficient level clearly exceeds the one of a non-structured surface (in this case by 66%). At this point, micro-dimples cause an increase in friction. The reason for such an increase in the minimum friction coefficient towards larger micro-dimple dimensions can be seen in the reduced pressure build-up. [UEH04] proved as well that increased micro-dimple dimensions lead to a decrease in their friction-minimising potential. In his opinion, this is because larger micro-dimple dimensions allow an easier oil transport from the dimples to the lubrication gap, coun-

teracting the pressure build-up in the micro-dimple. [GAH09] postulates that excessively deep surface structures can even lead to a collapse of the lubricant film; he identifies this as the reason for the noticeably high friction coefficient level at a micro-dimple depth of $a_{p,max} = 50 \mu\text{m}$.

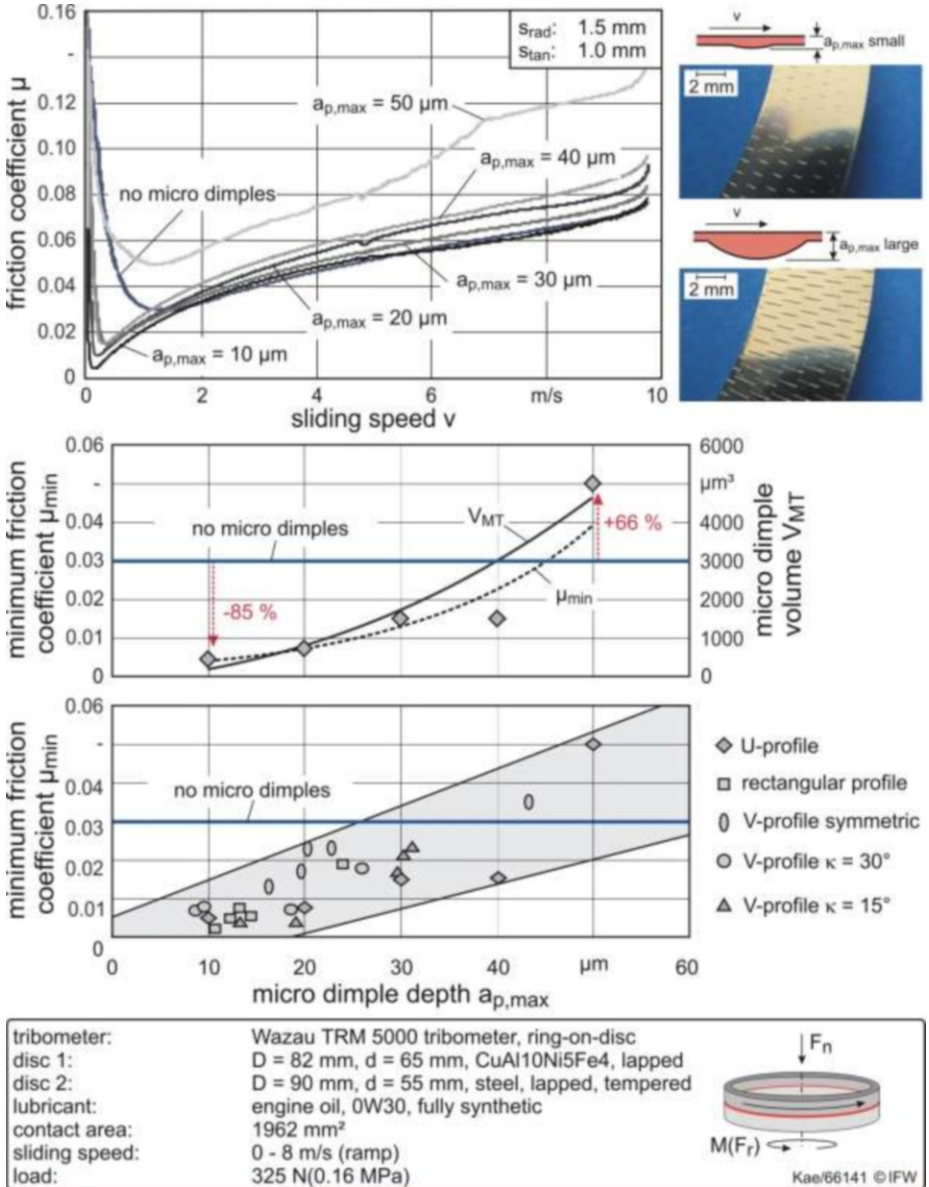


Figure 7-6: Influence of the micro-dimple depth on the characteristic of the friction coefficient and the minimum friction coefficient

The described effect of depth could be observed for all examined micro-dimple cross section geometries. In Figure 7-6, bottom, the minimum friction coefficients are plotted depending on the micro-dimple depth for U profiles, rectangular profiles, symmetrical and asymmetrical V profiles. It can be seen that, on average, the minimum friction coefficients rise almost linearly, depending on the micro-dimple depth. The values measured for the different micro-dimple cross section geometries are overlapping; thus, at this point, no general statement can be made concerning the geometry flow. However, the used V-profile geometries clearly show level differences, which are examined in the following parts of this paper.

Influence of micro-dimple geometry on friction coefficient and minimum friction coefficient

The systematic variation of the micro-dimple cross section geometry was carried out by means of the flank angle between $\kappa = 15^\circ$ and 55° (Figure 7-7).

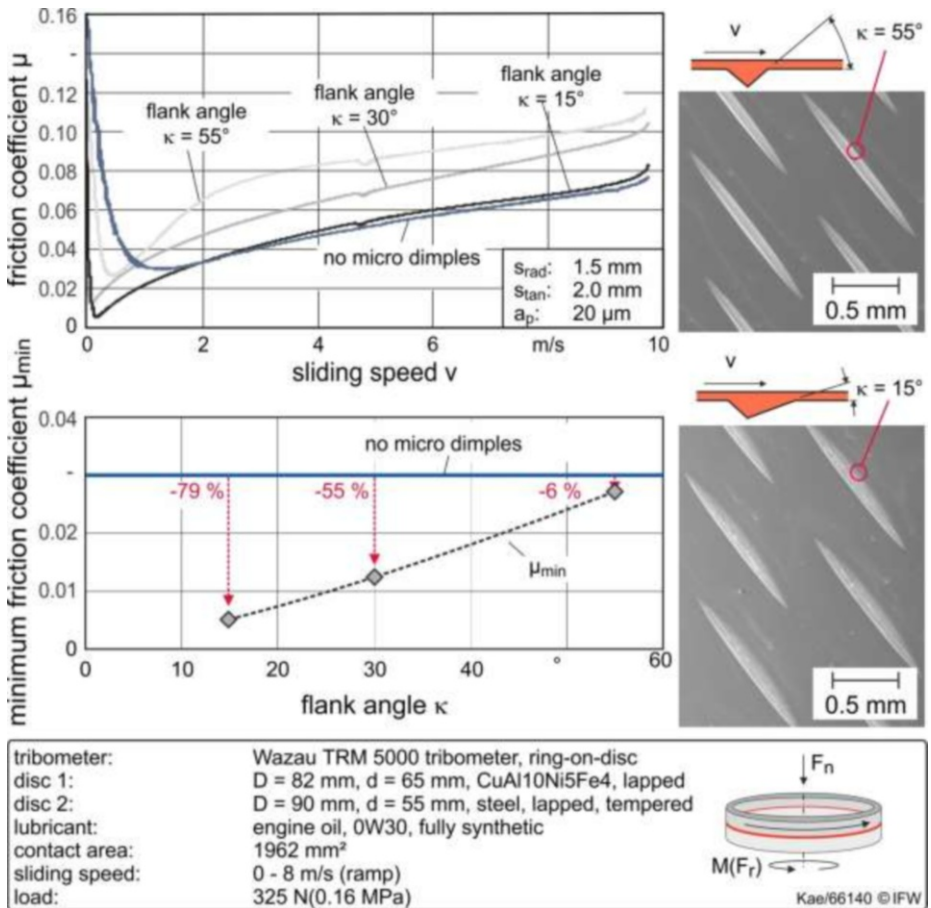


Figure 7-7: Influence of the flank angle on the characteristic of the friction coefficient and the minimum friction coefficient

All other geometry parameters, including the opposite tool cutting edge angle, were kept at a constant level. When creating micro-dimples, the flank angle was set by means of the angle κ .

The friction coefficient level decreases towards smaller flank angles over the complete speed range. At a flank angle of $\kappa = 15^\circ$, the friction coefficient level of the non-structured disc is slightly lower compared to the microstructured disc for the hydrodynamic range. This is due to the fact that micro-dimples with smaller flank angles produce less turbulence in the lubricant.

In the range of limited and mixed friction, a clear tendency can be observed as well. In [Figure 7-7](#), bottom, the minimum friction coefficient is plotted depending on the flank angle declines continuously towards smaller flank angles. At a flank angle of $\kappa = 15^\circ$, the minimum friction coefficient can be reduced by up to 79% compared to the non-structured surface. This tendency is due to the fact that micro-dimples with smooth flanks favour pressure build-up since, due to their geometry, they provide a tapered lubrication gap. This supports the hydrodynamic contact pressure build-up. No clear tendency that the minimum friction coefficient shifts with smaller flank angles towards lower relative speeds can be observed.

Conclusion

In this chapter, the friction-minimising potential of machined micro-dimples as well as the influence of the micro-dimple arrangement, dimension and geometry on friction characteristics under planar contact conditions was systematically evaluated. At low relative speeds, the friction-minimising potential of machined micro-dimples is independent of test load and relative speed in the range of limited and mixed friction of the Stribeck curve. Apart from reduced minimum friction coefficients, micro-dimples also lead to a significant shift of the coefficient towards lower relative speeds. These tendencies are additionally amplified by the high micro-dimple ratio characteristic of the no offset arrangement, by small micro-dimple dimensions as well as by a flank angle tapered in the speed direction of the sliding partner. During testing, with the creation of micro-dimples, the minimum friction coefficient could be reduced by up to 79% and shifted by 77% towards lower relative speeds. The effects which were identified indicate that machined micro-dimples support hydrodynamic pressure build-up between the friction partners under planar contact conditions, which is in accordance with the findings of the contemporary state-of-the-art research.

The friction-minimising effect of micro-dimples in the range of low sliding speeds can be used especially efficiently for starting plain bearing systems. Plain bearings in a combustion engine as for example crankshaft, camshaft and big end bearings are potential fields of application for micro-dimples. Since automatic start-stop systems have gained popularity, tribological stressed components in combustion engines pass through the mixed friction range much more often than before, thus, offering an enormous application potential for friction-minimising microstructures.

7.2 Tribological mechanisms of microstructured thermally sprayed surfaces

*Institut für Werkstoffkunde (IW), Leibniz Universität Hannover
Fr.-W. Bach, K. Möhwald, M. Erne, C. Hübsch, H. J. Maier*

The potential friction-reducing properties of thermally sprayed coatings were examined on a pin-on-disc tribometer. For these experiments, the pins were coated and tested against a cast iron and a hardened-steel disc, respectively. The contact is comparable with the pairing piston ring/liner surface [LAN87].

Pin-on-disc experiments

The tribological behaviour of various coatings with different porosity was investigated by means of a pin-on-disc testing machine on the tribometer TRM 5000 (Wazau GmbH, Berlin). The specimens were coated on steel substrates and ground and electrochemically polished for the experiments. The pins were floats on a ball and locked to prevent rotation so that a complete surface contact was ensured (Figure 7-8). The samples were tested against a counter disc of cast iron (test series Fe/Mo 50-50 and FeCr13) or hardened steel (test series FeCr13/Mo 50-50 and Mo/NiCrBSi 75-25) in a motor oil bath.

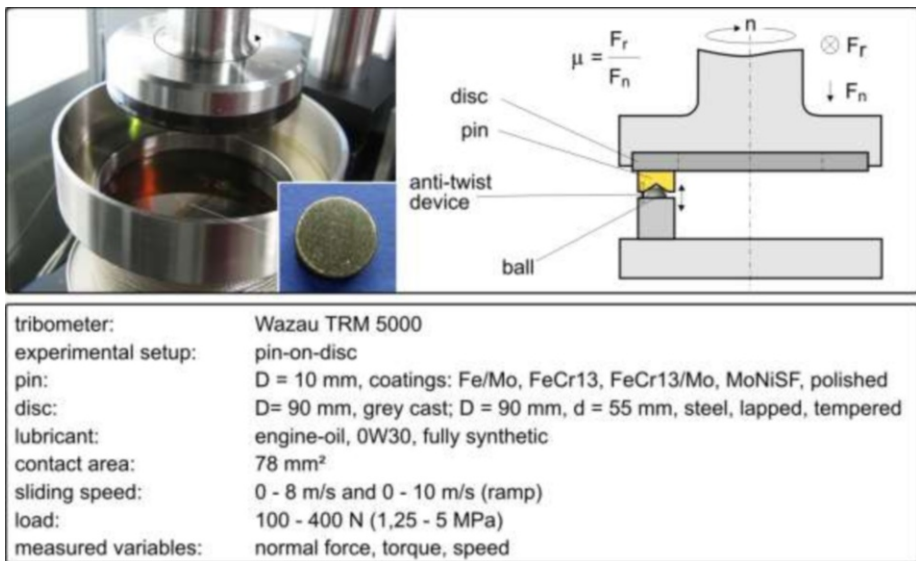
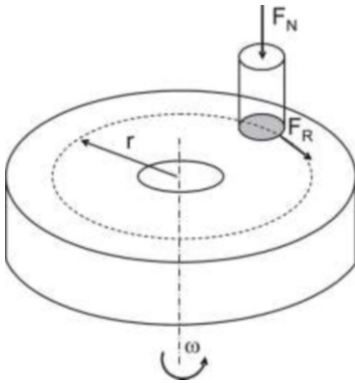


Figure 7-8: Pin-on-disc tribometer setup and boundary conditions of the test

In contrast to the tribological tests of the machined micro-dimples, the pin-on-disc setup was selected for the experiments with the thermal spray coatings. Ring-on-disc experiments with the FeCr13/Mo-coatings showed that plane-parallel contact surfaces of the specimen could not be easily manufactured: The coating of the rings lead to thermally induced distortions and, thus, a uniform surface contact could not be ensured. All experiments took place under full lubrication with fully synthetic motor oil with a viscosity of 0W30. In the first experiments with the Fe/Mo 50-50 and the

FeCr13 coatings, the influence of the normal force and the engine oil temperature were investigated. The samples were tested with forces of 100 N, 200 N, 300 N, and 400 N - which correspond to loading pressures of 1.25 MPa, 2.5 MPa, 3.75 MPa, and 5 MPa - and with oil at room temperature (RT), 60 °C, 90 °C, and 120 °C. For the studies on the FeCr13/Mo and Mo/NiCrBSi coatings, a force of 300 N and an oil temperature of 60 °C were chosen. A 2-component dynamometer, integrated below the fixed disc, was used to measure the normal force F_N and the friction torque M_{Fr} with a measuring frequency of 100 Hz. The friction coefficient was calculated based on these variables, considering the mean ring diameter (Figure 7-9).



Friction force at rotation:

$$F_R = \frac{M_{Fr}}{r}$$

Friction coefficient at rotation:

$$\mu = \frac{F_R}{F_N}$$

loading pressure:

$$p = \frac{F_N}{A_0}$$

Figure 7-9: Schematic illustrating the pin-on-disc setup with relevant variables

For the experiments, various test speeds were chosen to detect speed-dependent effects and to determine the behaviour of the coating in the three states of friction (contact, mixing, and liquid friction). The counter disc was quickly accelerated to 8 m/s and 10 m/s, and within 5 min, decelerated to 0 m/s. As a result, a Stribeck curve which shows the measured friction coefficient as a function the relative speeds could be created. The speed represents the lubricating gap height between the friction partners that result from the different speeds, oil viscosity, and pressures [CZ110].

The pins were placed into the specially prepared bearing with sample holders for pins (see Figure 5-20) for the coating in order to obtain results that are relevant for actual applications of internal coatings. For the Fe/Mo 50-50 and FeCr13 coatings, the Taguchi L9-plan (see Table 5-3) was used so that for each spray material, nine different coatings were applied. For the FeCr13/Mo 50-50 and Mo/NiCrBSi 75-25 coatings, the full factorial spray plan was used, wherein the spray distance and the current rating were varied (see Table 5-13).

Tribological properties of the Fe/Mo 50-50 coatings

Overall, the individual Stribeck curves of the Fe/Mo 50-50 coatings lie in a very narrow friction-coefficient interval. The following figure shows the Fe/Mo 50-50 - coatings at room temperature and a load of 100 N. In the field of hydrodynamic friction, the curves are positioned close to each other because in this region, the two sliding partners are separated by a lubricant film.

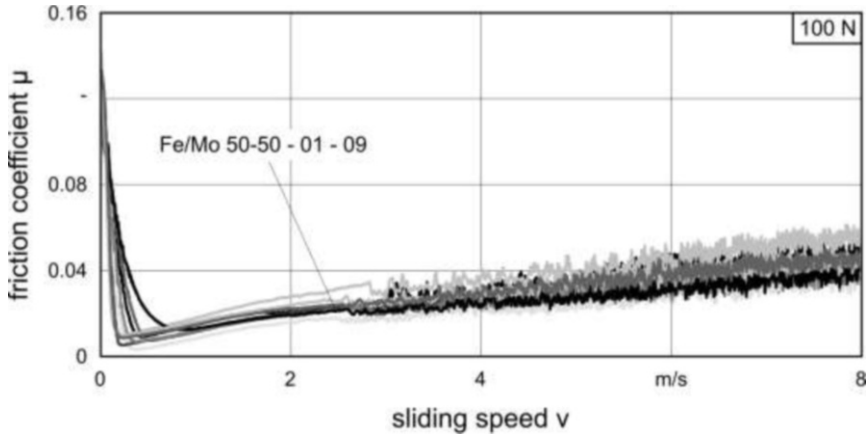


Figure 7-10: Stribeck curves of the Fe/Mo 50-50 coatings at room temperature and a load of 100 N.

As a comparison to the Fe/Mo 50-50 coatings, a steel substrate (X153CrMoV12) was tested with the same diameter. At nearly all loads and temperatures, the predominating effect is that the coatings provide better friction behaviour. In particular, the range of mixed friction, which occurs at low speeds, is relevant to the evaluation of wear. An early change of mixed friction in the hydrodynamic state of the liquid friction is desirable since, in this state, the two friction partners are separated by a sliding lubricating gap. This means that the occurring friction as well as the associated wear is minimal [CZI10]. At low loads (100 N), the differences between the steel specimen and the coatings are not very pronounced, but the coatings exhibit less friction at the individual speeds even if the reference changes at slightly lower speeds than the average value of the coatings in the hydrodynamic region. First, if the load increases, an improvement of the coatings can be detected. The coatings exhibit different frictional properties as a function of various loads and temperatures. Figure 7-11 and 7-12 show the friction properties of the coatings in comparison to the steel reference sample. The coatings are represented by three curves; each of the curves corresponds to the average, minimum, and maximum friction coefficient, respectively. The improvement of friction in comparison to the reference sample can be promoted by several factors. The porosity of the coatings possesses an oil retention capacity that favours a hydrodynamic pressure at low speeds by separating the two sliding partners faster [BAR05]. Additionally, secondary phases, such as magnetite or wustite, which were detected in Fe/Mo 50-50 coatings offer further potential for decreasing friction: they act as a solid lubricant and exhibit friction-reducing properties [VEN09, BAR05].

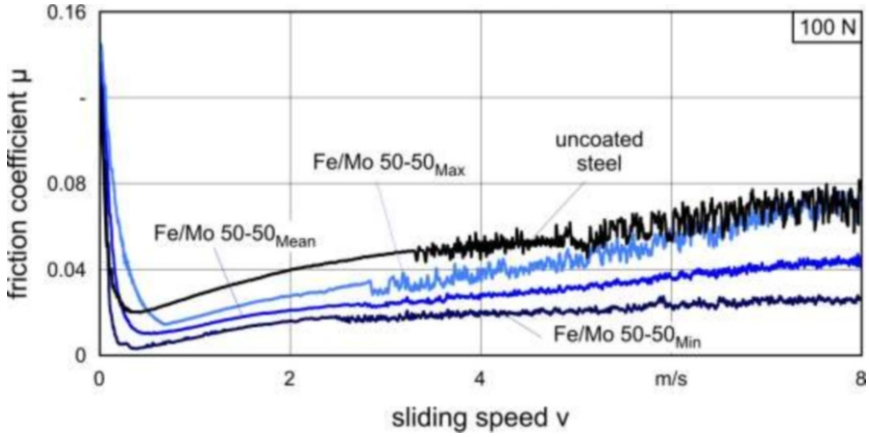


Figure 7-11: Stribeck curves of Fe/Mo 50-50 coatings and a steel reference sample (RT, 100 N)

The influence of the load on the tribological properties is graphically presented in Figure 7-12. At a load of 400 N (5 MPa), the friction coefficients of the coatings are closer together than at lower loads. Furthermore, there is a significant improvement of the tribological properties compared to the uncoated steel reference. The transition from the mixed friction to the liquid friction occurs at lower speeds and lower friction coefficients.

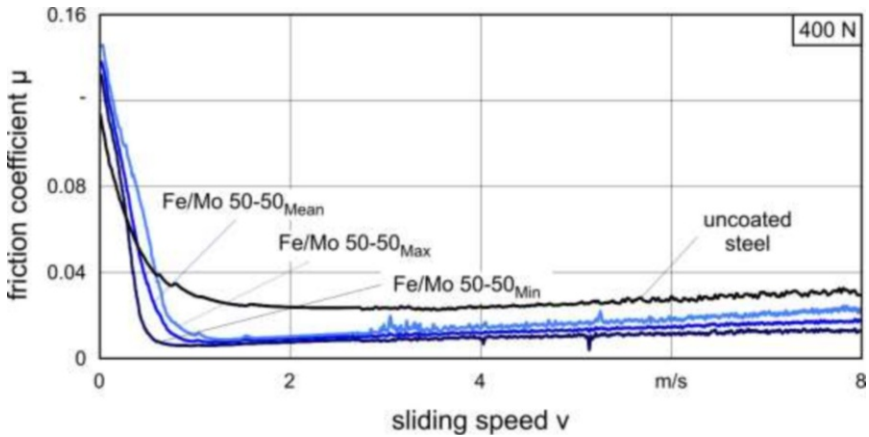


Figure 7-12: Stribeck curves of Fe/Mo 50-50 coatings and a steel reference sample (RT, 400 N).

In contrast to the machined micro-dimples, no direct correlation between the friction and the porosity or structure depth could be recognised over all loads and oil temperature ranges studied. However, the porosity, in the sense of microstructures, exhibits much smaller micro-dimples and the structures with large volumes are proportionally smaller so that the machined micro-dimples have a significantly higher total volume of cavities. In these investigations, other factors - such as surface roughness, wear patterns, and thermal properties of the materials used - have not been consid-

ered, but the samples were prepared identically and were assumed to have equal surface conditions.

Tribological properties of the FeCr13 coatings

The FeCr13 coatings were made analogously to the Fe/Mo 50-50 coatings and were identically prepared and tested. The run of the individual Stribeck curves of the FeCr13 coatings also lies within a narrow interval (figure 7-13).

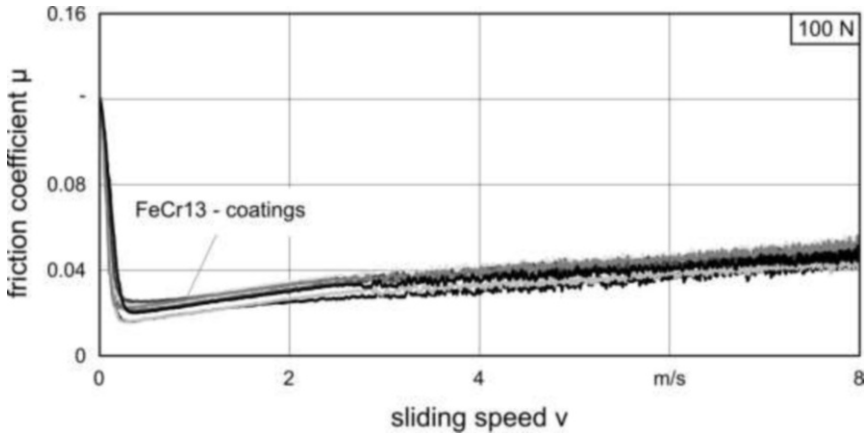


Figure 7-13: Stribeck curves of the FeCr13 coatings at 60 °C oil temperature and a load of 100 N

No direct correlation between the friction behaviour and the porosity or structure depth could be discerned. Nonetheless, surface analysis of the subproject 4 "Surface characterisation based on optical metrology" in connection with the friction coefficients of FeCr13 coatings reveal that there is, indeed, a friction dependency on the porosity - if a porosity threshold of about 200 μm^2 is set, i.e., if pores having a smaller area are hidden. At almost any speed, low friction coefficients are obtained at a high pore volume [HUE11]. However, other parameters - such as roughness and loading pressure - are not considered in this context. Nevertheless, the tendency that an increase of the micro-dimples proportion may favour the development of the hydrodynamic pressure corresponds to the results of the machined micro-dimples.

Figure 7-14 shows that, in comparison to the Fe/Mo 50-50 coatings, the reference sample exhibits lower friction coefficients than some of the FeCr13 coatings, especially at lower loads. Similarly, the FeCr13 coatings switch to the state of the mixed friction into the hydrodynamic state at lower speeds. At higher loads and higher oil temperatures, the coatings show lower friction coefficients than the uncoated steel sample, independently of the speed. The following figure shows the tribological behaviour of FeCr13 coatings compared to steel sample with an oil temperature of 60 °C and a load of 100 N.

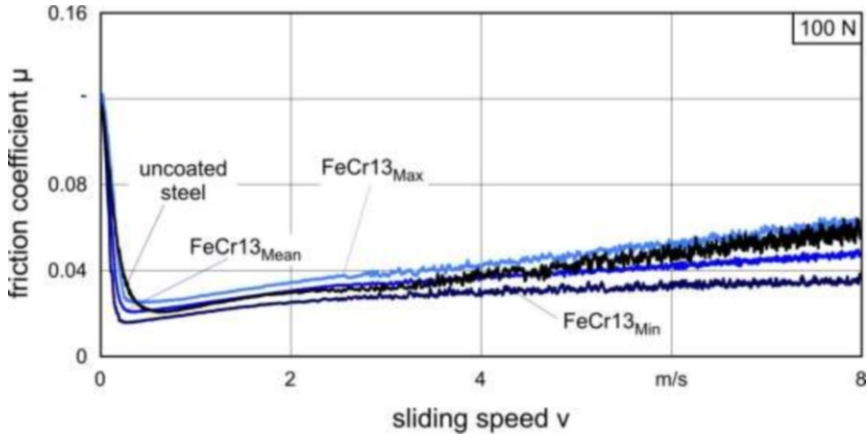


Figure 7-14: Stribeck curves of FeCr13 coatings and a steel reference sample (60 °C oil temperature, 100 N).

The tribological tests at 60 °C oil temperature show that, with increasing load, the steel sample reveals a higher friction coefficient in comparison to the coatings.

Overall, the FeCr13 coatings exhibit slightly higher friction coefficients than the Fe/Mo 50-50 coatings. The differences may be due to the secondary phases, which are assumed to act as solid lubricants. In fact, in the FeCr13 coatings, the detected iron oxide magnetite exhibits positive tribological characteristics which are almost equal to those of wustite.

Tribological properties of the FeCr13/Mo 50-50 coatings

In the studies of the FeCr13/Mo 50-50 coatings, which were also used for the other tribological tests, several aspects that can have an effect on the tribological behaviour of the pin specimens were studied. Therefore, round specimens with a diameter of 10 mm were made of S235 and coated afterwards. Before and after the experiments, the surfaces of the pin specimens were measured using a confocal optical microscope VHX-1000 (Keyence, Neu-Isenburg). These measurements aimed to determine whether, during the experiments, the entire pin surface or only some of its areas were in contact with the counter disc. Different areas can result in different surface pressures, and thus, cause different behaviour. Before the experiments were carried out, three roughness profiles were measured on each pin by an optical roughness instrument and averaged. The values are listed in [Table 7-1](#).

Table 7-1: Roughness values of the FeCr13/Mo 50-50 coatings

	Ra in μm	Rz in μm	Rmax in μm
FeCr13/Mo-01	0.32	3.58	7.40
FeCr13/Mo-02	0.38	11.82	4.52
FeCr13/Mo-03	0.27	2.49	4.86
FeCr13/Mo-04	0.31	2.74	4.55
FeCr13/Mo-05	0.43	3.40	5.32
FeCr13/Mo-06	0.34	3.27	5.66
FeCr13/Mo-07	0.36	2.90	4.79
FeCr13/Mo-08	0.54	4.12	5.77
FeCr13/Mo-09	0.45	2.46	3.99
GJS-400	0.35	2.39	4.13

In general, the roughness values of the coatings and the cast iron sample are similar; however, the coatings exhibit slightly higher values due to their porosity. Moreover, in these experiments, the Stribeck curves of the coatings are within a narrow interval. Figure 7-15 shows that, in the case of the Fe/Mo 50-50 experiments, the coated samples generally comprise the turning point of the mixed friction in the hydrodynamic friction samples at lower speeds. In addition, the minimal friction coefficient is lower than for the cast iron reference. The following figure also shows the mean (sample FeCr13/Mo-01 was excluded) as well as minimum and maximum friction coefficients.

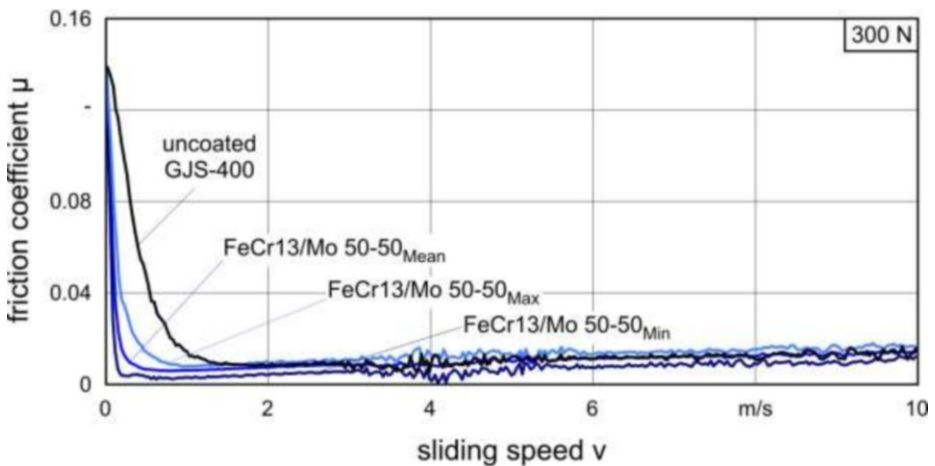


Figure 7-15: Stribeck curves of FeCr13/Mo 50-50 coatings and a cast iron reference sample (60 °C oil temperature, 300 N)

Moreover, with this coating system, no significant differences between the individual coatings could be observed. However, sample 1 is characterised by a curve which differs from those of the other samples (Figure 7-16). The friction coefficients for each speed are much higher than those for the rest of the coatings and the reference sample. In addition, the Stribeck curve of the coating FeCr13/Mo-01 exhibits an atypical course in the hydrodynamic friction state, as its friction coefficient does not increase again at higher speeds. Normally, the increase at higher velocities is caused by high shear forces in the engine oil [CZ110].

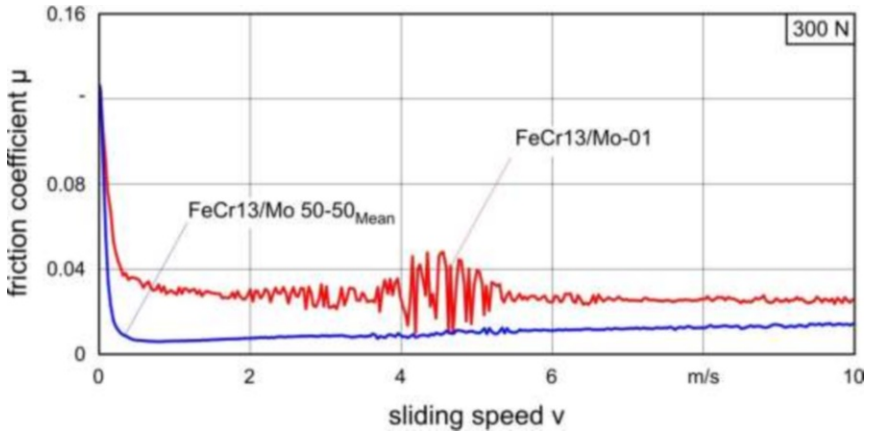


Figure 7-16: Comparison between sample FeCr13/Mo 50-50 and the mean friction coefficient of the coatings

A comparison of the pin surfaces after the tribological tests reveals that the contact area of the sample FeCr13/Mo-01 is considerably smaller than the contact areas of the other samples. Figure 7-17 provides a comparison between the contact areas of the FeCr13/Mo-01 and the FeCr13/Mo-03 samples. In the latter, the contact surface (red dotted line) comprises almost the entire pin surface; only the edge region does not show hints of wear, which indicates crowning of the pins due to the preparation process.

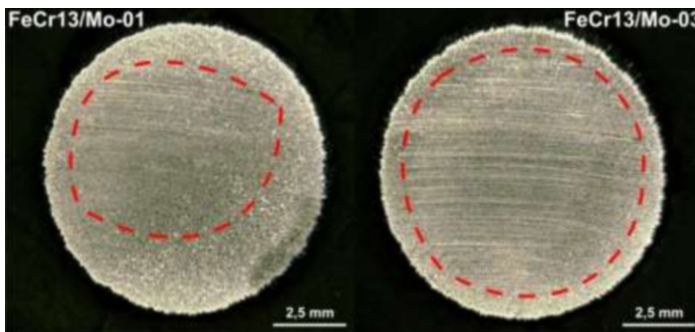


Figure 7-17: Comparison of the wear tracks of the FeCr13/Mo-01 and the FeCr13/Mo-03 samples after tribological testing

In this series of samples, the major factors influencing the friction were examined. Using three selected samples, the different friction coefficients of the coatings are discussed. Figure 7-18 shows three FeCr13/Mo 50-50 coatings compared to the cast iron reference. In this case, the sample with the lowest porosity (FeCr13/Mo-05) has the best frictional properties, whereas the sample with the highest porosity (FeCr13/Mo-04) provides the turning point into the hydrodynamic friction state at higher speeds.

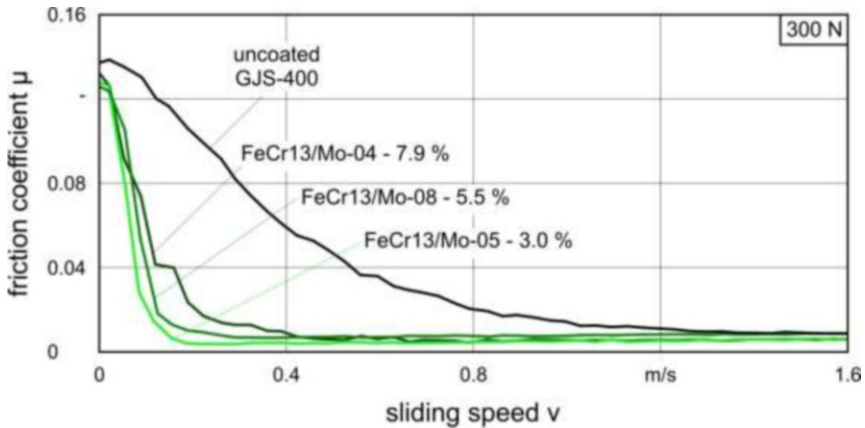


Figure 7-18: Selected Stribeck curves of the FeCr13/Mo 50-50 coatings

However, the sample FeCr13/Mo-04 exhibits the lowest roughness of all three coatings. Thus, the sample FeCr13/Mo-04 combines the two conflicting factors high porosity and low roughness, so there are other factors that have a decisive influence on the friction coefficient. When considering the wear marks on the surface, it can be seen that, after the experiments, all three layers are characterised by different contact surfaces (Figure 7-19). The sample with the best frictional properties has the largest contact surface, while the sample with the smallest contact surface has a highest friction coefficient.

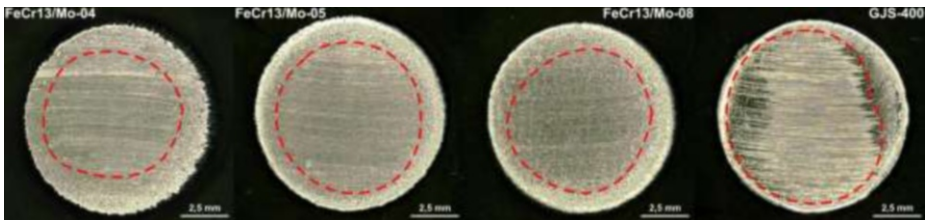


Figure 7-19: Comparison of the wear tracks of sample FeCr13/Mo-04, -05, -08 and the GJS-400 sample after the tribological experiments

Tribological properties of Mo/NiCrBSi:

The tribometer pins of the Mo/NiCrBSi 75-25 coatings were measured by means of confocal light microscopy before and after the experiments, similar to the FeCr13/Mo 50-50 samples, in order to examine the real surface during the tribological loading. For this purpose, three roughness profiles were recorded and averaged for each sample (Table 7-2).

Table 7-2: Roughness values of the Mo/NiCrBSi 75-25 coatings

	Ra in μm	Rz in μm	Rmax in μm
Mo/NiCrBSi-01	0.47	4.63	8.55
Mo/NiCrBSi-02	0.47	4.21	8.77
Mo/NiCrBSi-03	0.61	5.86	11.38
Mo/NiCrBSi-04	0.57	4.83	10.32
Mo/NiCrBSi-05	0.33	3.20	5.23
Mo/NiCrBSi-06	0.27	2.46	3.94
Mo/NiCrBSi-07	0.37	3.36	6.58
Mo/NiCrBSi-08	0.66	5.36	8.43
Mo/NiCrBSi-09	0.37	3.17	6.87
GJS-400	0.35	2.39	4.13

Overall, the curves exhibit a tribological behaviour similar to that of the other coating materials. The comparison between the Mo/NiCrBSi 75-25 coatings and the cast iron reference also shows an improvement of the frictional properties of the coatings. In the field of hydrodynamic friction, the reference and coating system have almost the same friction coefficient. Nonetheless, the turning point from the mixed friction to the state of hydrodynamic friction occurs at lower speeds, as is the case with the other coating systems. The mean, as well as the minimum and maximum, friction coefficients are shown in Figure 7-20.

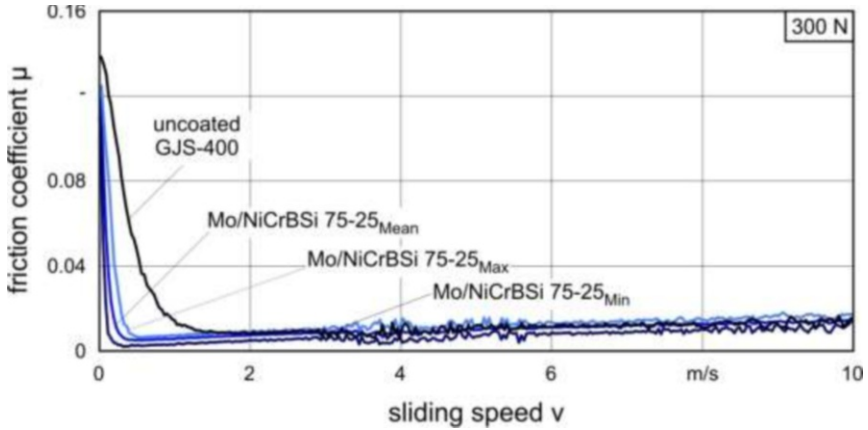


Figure 7-20: Stribeck curves of Mo/NiCrBSi 75-25 coatings and a cast iron reference sample (60 °C oil temperature, 300 N).

In the case of this coating material, no direct correlation between the porosity and the friction could be discerned directly. Thus, three curves were selected as an example, and their impact factors - analysed. Figure 7-21 shows three curves with different porosities. The sample with the highest porosity, Mo/NiCrBSi-03, has the lowest friction coefficient, whereas the sample with the lowest porosity, Mo/NiCrBSi-09, has a higher friction coefficient at a low speed and changes into the state of liquid friction at a higher speed. By comparison, sample Mo/NiCrBSi-06, which has nearly the same porosity as Mo/NiCrBSi-09, exhibits improved friction properties. Therefore, it can be assumed that, even in this coating system, the porosity plays a subordinate role.

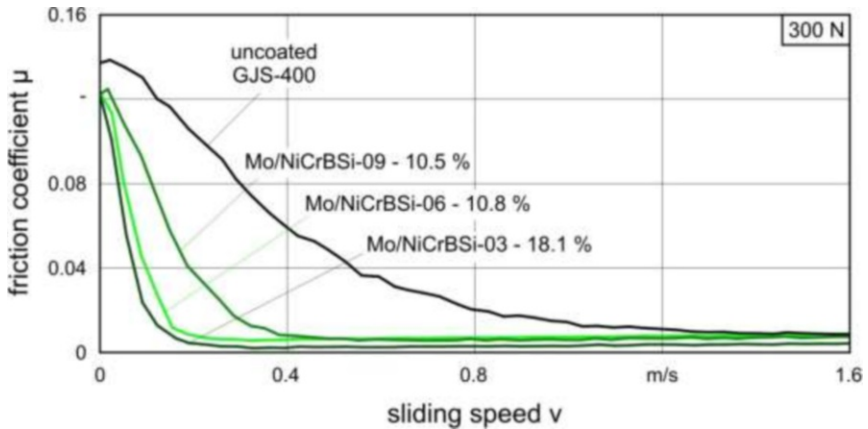


Figure 7-21: Selected Stribeck curves of the Mo/NiCrBSi 75-25 coatings

When compared to the FeCr13/Mo 50-50 coatings, the contact surface of the pins in this sample series has an important influence on the friction behaviour. Figure 7-22 shows the pin surfaces of the three samples. Once again, the sample with the lowest contact surface, Mo/NiCrBSi-09, is characterised by the highest friction coefficients,

and the sample with the largest contact area, Mo/NiCrBSi-03, shows the lowest friction coefficients.

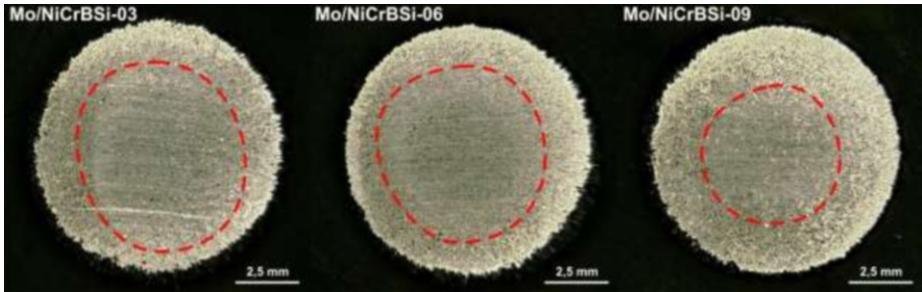


Figure 7-22: Comparison of the wear tracks of sample Mo/NiCrBSi-03, -06, and -09 sample after the tribological experiments

Conclusion

Through all experiments, the coatings exhibit enhanced frictional properties as compared to uncoated steel or cast iron surfaces. Both molybdenum and chromium oxides cause a significant increase in hardness. This can also lead to a positive effect regarding the frictional properties [MOK82]. In addition, secondary phases, such as magnetite and wustite, improve the friction characteristics as these can act as solid lubricants [VEN09]. In comparison to the reference samples, the potential for using the microstructures to build up a hydrodynamic pressure and additionally use the microstructures as an oil retention capacity can be exploited by thermal spray coatings [BAR05]. Due to the lamellar structure of the coatings, a new microstructured surface with the same properties is exposed after wear. After the experiments in the motor oil bath, which were followed by a cleaning, oil residue remained in the cavities while the reference samples could be cleaned completely. Experiments at different loads and oil temperatures showed that, at low loads, the differences between the friction coefficients of the uncoated steel sample, the iron-molybdenum mixture, and the chromium steel coatings are minimal. Due to the coatings, significant improvements can be observed at increasing loads only. The coatings which were made by an internal coating process also showed enhanced properties in comparison to an uncoated cast iron sample. This is due to their switch in the range of the liquid friction at a lower speed. This can also lead to a positive effect regarding the frictional properties [MOK82]. No significant differences between the single coatings of a material, which exhibit different porosities, could be discerned. Therefore, it can be assumed that the amount of porosity does not influence the reduction of friction directly. Micrographs of the pins, which were taken after the tribological experiments, reveal that sometimes different frictional behaviour can be explained by the different sizes of the contact surfaces during the experiments. With decreasing contact surfaces, the surface pressure increases. Brush marks after the experiments reveal the abrasive wear character of the coatings.

7.3 Tribological mechanisms of microstructured surfaces under dragged conditions

*Institut für Maschinenelemente und Konstruktionstechnik (IMK), Universität Kassel
G. Knoll, A. Rienäcker, S. Brandt, H. Fast*

Piston ring friction results for hybrid cylinder liners

Within this subproject, hybrid surface topographies were experimentally investigated with the piston ring friction test rig, which was first used within the scope of subproject 1 “Methods and models for the design of microstructures”. Hybrid surface structures are structures which exhibit deterministic and stochastic patterns at the same time. The fundamental idea in identifying the tribological properties of hybrid structures is to characterise deterministic and stochastic effects separately. For this purpose, two liners were friction-tested on the piston friction test rig. In a first step, both liners were coated at IW and then friction tested. In a second step, both liners were structured at IFW and then friction tested a second time.

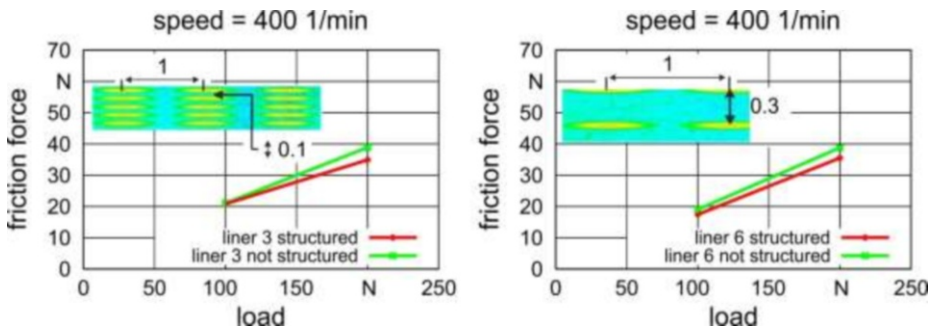


Figure 7-23: Friction force measurements of hybrid surface structures at the piston-ring friction test rig

Figure 7-23 shows speed and load dependent friction force values for hybrid surface structures. It is apparent that structured surfaces exhibit small advantages with respect to friction; however, no significant friction reduction can be discerned from the measurements shown.

Tribological test results for structured and coated cylinder liners

To determine the friction properties of coated surfaces at high speeds, the rotational friction measurement test rig (RRV) was used. In this test facility, the tested liner rotates around a piston ring carrier pressing three ring segments, each 120° apart, with a known force to the liner surface. The rig was designed to maintain high constant speeds over long periods of time; for this purpose, the axial motion of the piston ring was transformed into a rotational motion. To ensure realistic material combinations and contact conditions, specially designed ring segments and liners were used.

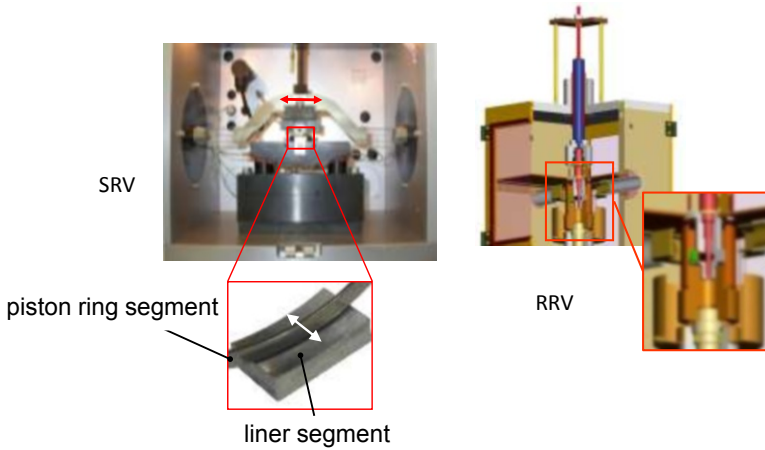


Figure 7-24: Design of the SRV and RRV tribometric test rig

The influence of the porosity of the coated surfaces on the friction behaviour was determined by means of the RRV rig. Cylinder liners were coated with variable porosities by IW (see [Figure 7-25](#)).

Porosity :	Porosity with the honing grooves :
dfg_2: approximately 6.3 [%]	dfg_2: approximately 30.8 [%]
dfg_3: approximately 3.7 [%]	dfg_3: approximately 15.5 [%]
dfg_4: approximately 2.5 [%]	dfg_4: approximately 12.3 [%]
dfg_5: approximately 1.5 [%]	dfg_5: approximately 8.1 [%]
dfg_6: approximately 1.6 [%]	dfg_6: approximately 11.7 [%]
dfg_7: approximately 1.6 [%]	dfg_7: approximately 11.4 [%]
dfg_9: approximately 2.3 [%]	dfg_9: approximately 19.3 [%]

Figure 7-25: Porosity values for cylinder liners (Coating by IW)

[Figure 7-26](#) shows the friction coefficient in relation to the sliding speed for different cylinder liners. The presented friction values are similar to each other even though, compared to the other liners, liners dfg_2 and dfg_9 show significantly lower friction values. The results shown here, however, are not conclusive because grooves from honing are considered to overlay the test results.

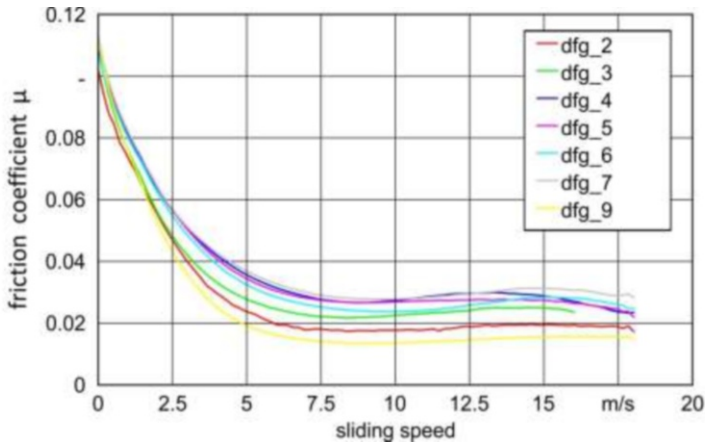


Figure 7-26: RRV-test results for variable porosities (coating by IW)

Wear investigations

This work aimed to determine the influence of the microstructures on the wear. SRV-tribometer tests were conducted on stochastic and deterministic micro patterns and compared to a reference probe. The test conditions - kept constant for all tests - were as follows.

Test Conditions:

- Normal Force = 100 N
- Frequency = 50 Hz
- Temperature = 100 °C
- Stroke = 1 mm
- Oil grade = 5W30

Precise measurements of the surface topography were essential for the success of the investigations. Thus, after a predetermined time period, the test specimen had to be dismantled from the test rig, measured, re-mounted, and tested once again. [Figure 7-27](#) compares the test results for deterministically structured surfaces to that for a reference specimen without micro-dimples. All probes were fabricated from the same material, and their surfaces were structured at IFW. The results for the structured surfaces remain similar to each other but differ significantly from the wear results of the reference probe. This means that the wear increases when the number of micro-dimples increases.

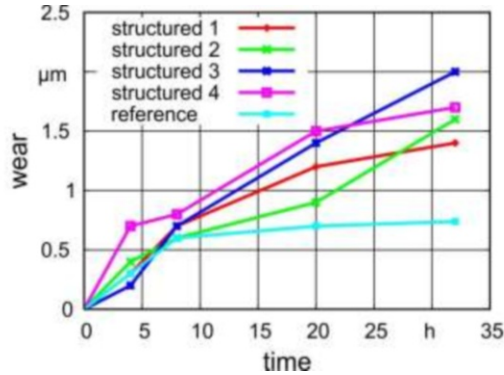


Figure 7-27: SRV-wear results for structured surfaces

Figure 7-28 shows the wear measurements for coated surfaces relative to the reference probe. When compared to the reference, coated samples exhibit very good wear resistance. This result can be used in further work on the combination of surface micro-structuring and coating so that both friction and wear can be optimised.

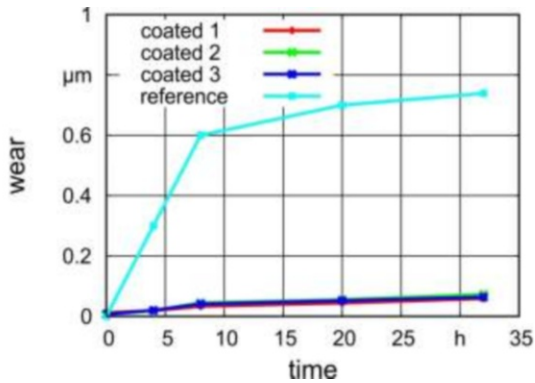


Figure 7-28: SRV-wear results for coated surfaces

Derivation of a wear model

The derivation of a theoretical wear model was a major objective of this work. A non-linear regression was used to derive a functional relationship between wear depth and test time for structured surfaces as an optimum fit to test results. The model function chosen, a hyperbolic tangent, is capable of capturing the increased wear during initial running-in, along with a subsequently decreased wear rate as present in the test data. For long wear tests, this function would need to be complemented by a linear function in time to cover the constant slope wear behaviour, typically seen after the running in phase is completed.

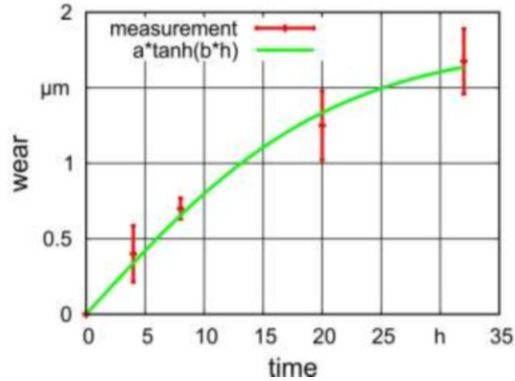


Figure 7-29: Theoretical wear model

Conclusion

To quantify the potential for lower friction of hybrid surface structures, tests were conducted on a piston ring friction test rig. The test results indicate that structured surfaces are characterised by lower friction coefficients.

The influence of porosity on friction was tested by means of the RRV test rig; however, the test results could not identify a significant difference between the friction behaviour of honed and structured surfaces.

Tests were carried out to determine the influence of the surface structuring and coating on the wear characteristics. The test results indicate a significant increase in wear for structured surfaces relative to the surface of the reference and the coated samples. In addition, a regression analysis was employed to develop a theoretical wear model that can be refined in future work.

8 Test of cylinder liner under fired engine conditions

Institut für Technische Verbrennung (ITV), Leibniz Universität Hannover
F. Dinkelacker, H. Ulmer

8.1 Objective and approach

After joining the research group in 2009, the Institute of Technical Combustion built up and evaluated an engine test bench for testing microstructured cylinder liners under realistic engine conditions. The entire test bench - including peripherals such as supply facilities, measurement data acquisition devices, and automatic control technique - was specifically built for this project.

8.2 Engine test bench and cylinder liners

The engine test bench consists of a single cylinder, heavy-duty research engine (diesel) based on the Mercedes-Benz series 500. Until recently, this engine type was used as a V8 in heavy trucks. The single cylinder engine with its test bench peripherals, the technical data of the engine, and the engine map can be seen in Figure 8-1.

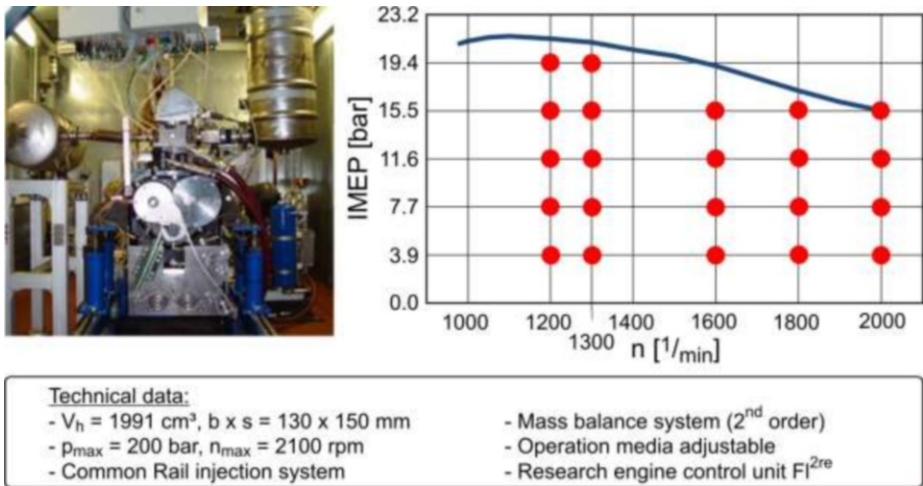


Figure 8-1: Single cylinder test bench and engine map

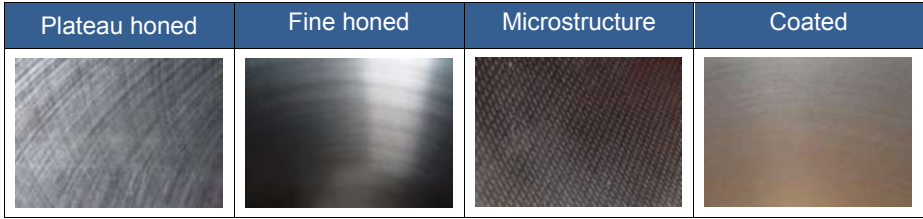
Compared to the original model, the single cylinder engine was modified and equipped with a mass balancing system up to the 2nd order to guarantee smooth running. In order to run the engine with a state-of-the-art combustion process, a modern Common-Rail high-pressure fuel system was adopted to the engine. In order to minimise the influence of interferences, it is necessary to remove the auxiliary devices from the engine. Thus, peripheral devices - such as a high pressure fuel system and conditioning systems for oil and coolant - were designed and built. In addition, these devices ensured defined operation conditions due to accurate control and monitoring of the engine's fluids. A research engine control unit (FI^{2RE} IAV GmbH) was used for

control and monitoring of the test bench as well as for data acquisition. Moreover, with its control algorithms for the Indicated Mean Effective Pressure (IMEP) and combustion burn rates, the FI^{2RE} provides stable and constant engine operation points.

During the measurement campaign, the same piston from a MTU series 2000 engine was used. It is equipped with two compression rings (keystone and rectangular) and one oil control ring (bevelled edge) with a coil spring. The so called “wet cylinder liners” of the Mercedes-Benz series engine were used. To provide constant boundary conditions, new piston rings and new engine oil were used for every test run. All other engine parts remained the same. A run-in program of 7 hours was carried out with every cylinder liner. After that, the friction of the engine was determined for the operation points shown in [Figure 8-1](#). The following types of cylinder liner surfaces were investigated during the project:

- plateau honed (original Mercedes-Benz liner, reference #1),
- fine honed (reference #2),
- covered with machined microstructures and
- covered with coated microstructures.

The friction reducing properties of microstructured cylinder liners were evaluated on the basis of both the plateau honed liner and the fine honed liner. Every microstructured liner has fine honed base surface. The machined structures were manufactured on pre fine honed liners and the coated ones were fine honed after the thermal spray process. [Figure 8-2](#) shows the investigated liners in an overview.



#	1	2	3	4	5	6
Symbol						
Details	plateau honed (reference)	fine honed (reference)	microstructure TDC $s_{axial} = 0.3 \text{ mm}$	microstructure hydrodynamic $s_{axial} = 0.2 \text{ mm}$	microstructure entirely $s_{axial} = 1 \text{ mm}$	microstructure entirely $s_{axial} = 0.5 \text{ mm}$

#	7	8	9	10	11
Symbol					
Details	microstructure TDC and BDC $s_{axial} = 0.5 \text{ mm}$	coated fine honed porosity=9.4%	coated fine honed porosity=3.1%	coated fine honed porosity=6.4%	coated honed porosity=1.8%

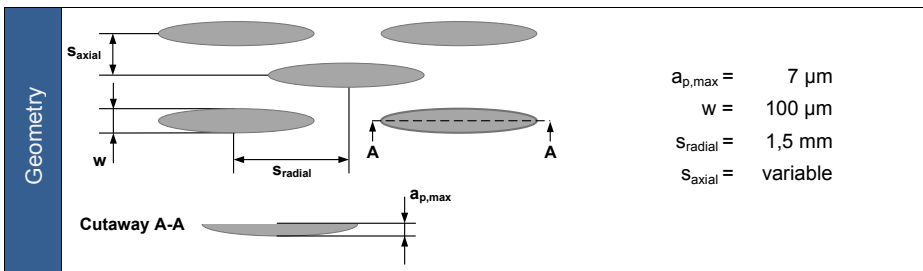


Figure 8-2: Overview of the tested cylinder liner

In order to guarantee constant boundary conditions during the complete testing-period, the following parameters remained constant at all times:

1. Temperature

For the measurement of the friction, the exact conditioning of the oil and of the cooling water is of significant importance. This is due to the strong tempera-

ture dependency of the oil viscosity and to the cooling water depending heat transfer to the cylinder wall. Both temperatures were controlled to be constantly $80^{\circ}\text{C} \pm 1 \text{ K}$ at the inlet of the engine.

2. Pressure (relative)

The oil pressure of all oil circuits was controlled to be constantly at $4 \text{ bar} \pm 0.05 \text{ bar}$. The air pressure was adjusted from 1.25 bar (at an IMEP of 3.8 bar) to 2.05 bar (at an IMEP of 15.5 bar). The exhaust gas back pressure was adjusted to be always 200 mbar above the intake pressure.

3. Operating fluids

Commercial Diesel fuel (EN 590) and oil from type SAE 10W-40 (Avia TURBOSYNTH HT-E) were used.

4. Further boundary conditions

Each operation point was held until all parameters reached a constant state. The load (IMEP) was adjusted by the research engine control unit in such a way that the 50% mass fraction burnt point (α_{Q50}) was stable at 10° crank angle (CA) after Top Dead Centre (TDC). All measurements were averaged over 200 cycles to reduce the influence of stochastic fluctuations.

8.3 Methods to measure friction losses and oil emissions

In order to measure the friction losses, the indication method was applied. Here, the measurement of the CA resolved cylinder pressure p_{cyl} and the integration over one whole engine cycle results in the Indicated Mean Effective Pressure IMEP. The measurement of the torque T_e at the engine output allows determining the Break Mean Effective Pressure BMEP. The difference of both values is the Friction Mean Effective Pressure FMEP, being a measure of the mechanical losses of the engine:

$$\text{IMEP} = \frac{1}{V_H} \int p_{\text{cyl}} dV \quad \text{FMEP} = \text{IMEP} - \text{BMEP}$$

$$\text{BMEP} = \frac{1}{V_H} 2\pi T_e$$

In engine technology, these given mean pressures are commonly used to describe the corresponding power:

Indicated Power (inside the engine)	$P_i = \text{IMEP} * V_H * \frac{n}{2}$
Effective Power (output of the engine)	$P_e = \text{BMEP} * V_H * \frac{n}{2}$
Friction Power	$P_r = P_i - P_e = \text{BMEP} * V_H * \frac{n}{2}$

The measurement of the cylinder pressure was carried out with a water cooled Kistler sensor (7061B), which is characterised by its high resistance against thermal shock. In order to increase the accuracy, the sensor was calibrated on a high precision pressure compensator (accuracy 0.01%). The torque T_e at the engine's output was measured with a highly accurate measurement flange type T40 from HBM (class of

accuracy 0.05). Due to a significant impact on the IMEP, the geometrical TDC was determined using an AVL TDC Sensor type 428.

For one set of experiments, the blowby of the piston system was determined with the blowby-meter AVL 442. These data were used for the validation of the simulation tools of subproject 1 “Methods and models to design micro structures”.

The measurements of the oil emissions were performed in cooperation with the “Institut für Messtechnik” of the Technical University of Hamburg-Harburg. Unburned oil, and thus unburned hydrocarbons, are limited by emission laws. As structured liners may lead to an enhanced amount of oil on the liner surface, it is necessary to control the lubricant oil emissions. Thus, apart from friction and wear, oil emissions are another important factor to be taken into consideration when regarding the tribological optimisation of cylinder liner systems. For the measurement of the oil emissions, a mass spectrometer - which had been developed in earlier projects [FVV03, FVV07] and which had been adapted for the application on test engines - was used. The separation of the unburned hydrocarbons from the lubricant oil from those of the diesel fuel was done with a quadrupole filter. The system allows the direct evaluation of the measurement signal. The reproducibility of the measurements depends on the oil concentration. The statistical deviation, indicated by the standard deviation, ranges from 2 to 12 % depending on the concentration level [KRA09]. Figure 8-3 shows the experimental setup.

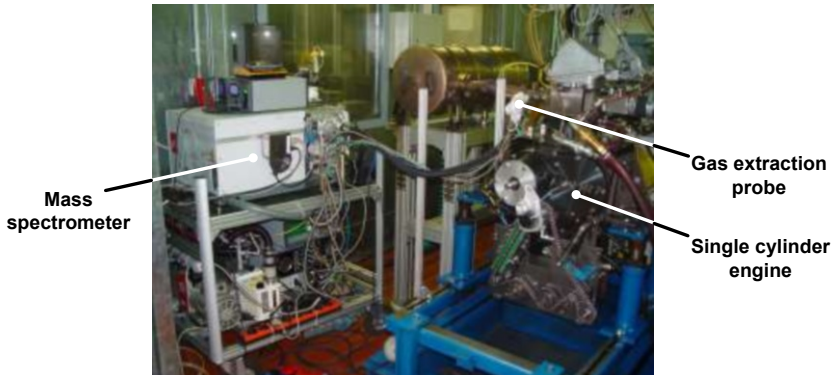


Figure 8-3: Oil emission measurement system in the test bench

8.4 Measurement uncertainty

A measurement model was developed in order to determine the measurement uncertainty of the discussed indication method as well as the error influence of the in-cylinder indication and of the torque measurement (Figure 8-4). The measurement uncertainties were determined according to the regulations of the “Deutsche Akkreditierungsstelle”. The maximum mean absolute error for the determination of the Friction Mean Pressure FMEP was determined from the geometrical addition of the individual errors to be ± 0.03 bar (2σ).

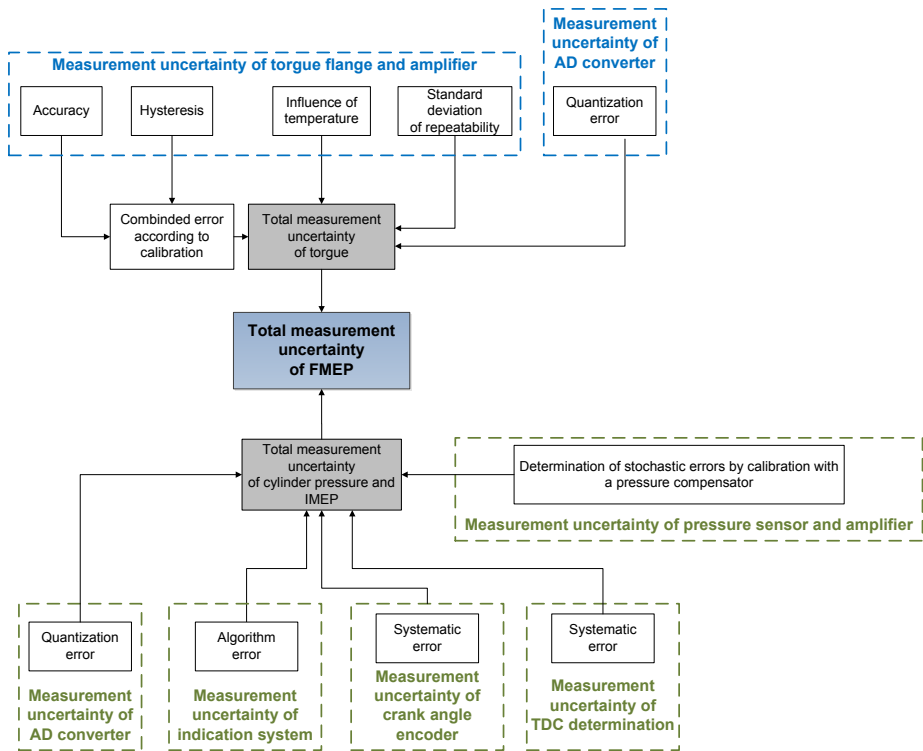


Figure 8-4: Measurement model

8.5 Validation of the measuring method

The following aspects were investigated by validating the method of determining the frictional losses:

- deviation,
- reproducibility and
- influence of the engine assembly on the FEMP determination.

Deviation

The deviation of the FEMP determination was investigated by testing 6 cylinder liners under the same conditions. For this purpose, 3 original liners with a plateau honed surface and 3 fine honed liners were used. Compared to the rest of the investigated liners, two of them (one original and one fine honed liner) showed higher deviations regarding FMEP than the expected measurement uncertainty. These liners were regarded as outliers and were not included the following investigation. [Figure 8-5](#) shows the determined FMEP values in the engine map without the outliers.

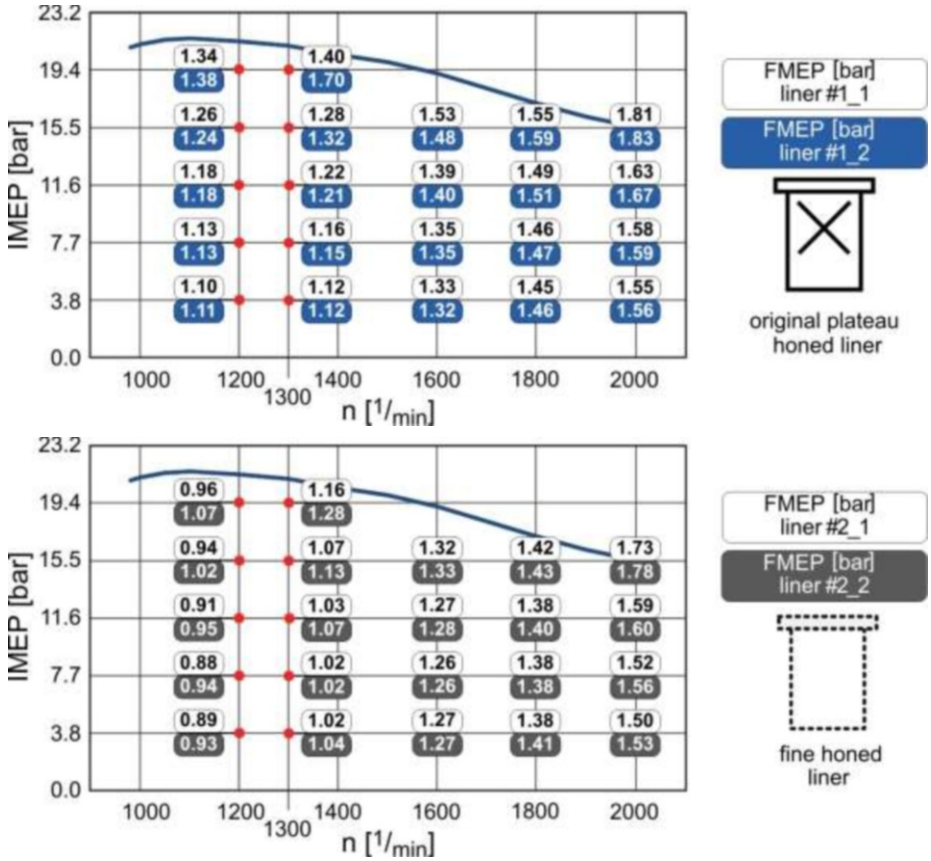


Figure 8-5: Deviation of FMEP

Regarding the original liners, the deviations were less than the expected measurement uncertainty in almost every engine operation point. An increase of the load correlates with an increase of the deviation, whereas the high deviation at 1300 $1/min$ and 19.4 bar IMEP can be regarded as an outlier because of a not swung-in engine state. The maximum deviation of 0.05 bar FMEP was determined for 1600 $1/min$ and 15.5 bar IMEP. In 16 of 22 engine operation points, the fine honed liners showed deviations smaller the measurement uncertainty. In the remaining points, the deviation ranges between 0.04 and 0.12 bar FEMP. The slightly higher deviations might be caused by differing surface characteristics due to the hone process which was carried out by a contractor company.

Reproducibility

The reproducibility of the FMEP determination was investigated by means of a repeated start of the engine. For that purpose, the engine was operated under fired conditions at 1300 $1/min$ and 11.6 bar IMEP with a fine honed liner. The FMEP was determined after the start of the engine and a swing-in period. Following, the engine

and its peripherals were stopped for a defined short period in order to cool down and subsequently restarted. Figure 8-6 shows the determined FMEP values for the several test runs. It can be noticed that the reproducibility is excellent.

Test run #	FMEP [bar] at 1300 1/min, IMEP=11.6 bar
1	1.03
2	1.04
3	1.03
4	1.03

Figure 8-6: Repeatability of FMEP determination

Influence of engine assembling

In order to investigate the influence of the assembling of the engine on the friction, a test run was carried out using a microstructured cylinder liner. After a run-in program and a preliminary FMEP determination, the liner –together with the liner housing and the piston assembly– was completely disassembled and put back together again. All screws and engine parts were tightened as per instructions. In this regard, the tightening of the cylinder head bolts is of significant importance, as it causes a deformation of the cylinder liner and its housing. This, in turn, can lead to increased out-of-roundness. Therefore, keeping the boundary conditions regarding the engine assembly constant was mandatory in order to ensure a precise FMEP determination. Figure 8-7 shows the FMEP values of the first and the second test run.

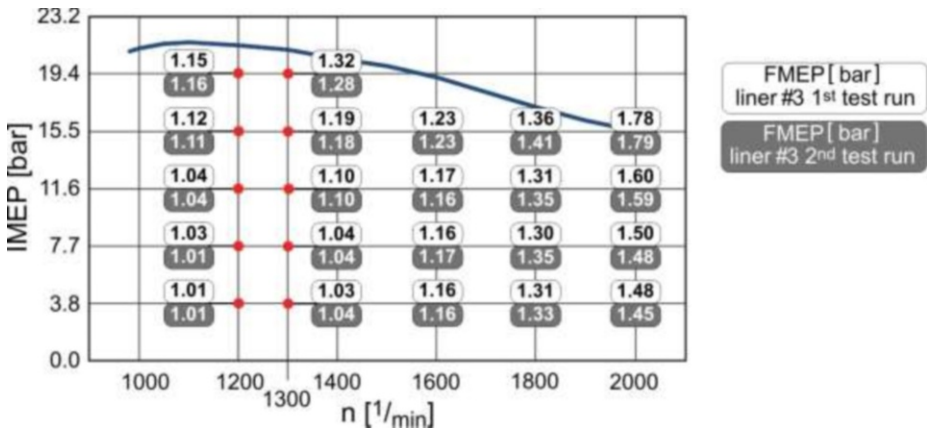


Figure 8-7: Influence of engine assembly on friction (FMEP) determination

The discrepancies between the two test runs are obvious only at 1800 1/min. In most of the operation points, the differences in FMEP range from ±0.01 – 0.02 bar and are therefore within the measurement uncertainty. It can be noticed that, with regard to the assembling instructions, assembling and reassembling of the liner does not influence the FMEP.

8.6 Results: frictional losses

This section presents and discusses the results regarding the frictional losses of the microstructured and coated cylinder liners. The friction (in terms of FMEP) was investigated for constant load in dependency on the engine speed. Even though test runs with microstructured liners were successfully completed, test runs involving the coated cylinder liners caused significant difficulties.

In the course of the project, several liners which –on closer inspection– exhibited surface damages were purchased from the executing honing company. Thus, liner #9, for example, showed surface damages in form of scratches in the middle part of the liner, most probably caused by the honing process. Consequently, another honing company was selected for the renewed purchase of cylinder liners. However, the quality of the provided liners, though to some extent better, did not differ significantly. Coated cylinder liners for heavy-duty engines with correspondingly bigger bore sizes are not common in series application. It can be thus concluded that more detailed processing experience is needed to ensure the production of high-quality, durable coated liners. Consequently, the development of a modified honing process with an adapted mechanical load for coated cylinder liners with big bore sizes is of particular interest.

Another problem concerning the coated liners occurred in the course of this investigation. The test of liner #11 caused a piston seizure during the run-in program. Liner #10 caused a piston seizure during the oil emission measurement. Thus, the seized piston rings had to be examined. Figure 8-8 shows SEM images of an unused top ring and an element line scan of the seized ring used with liner #10 using the energy-dispersive X-ray spectroscopy (EDX).

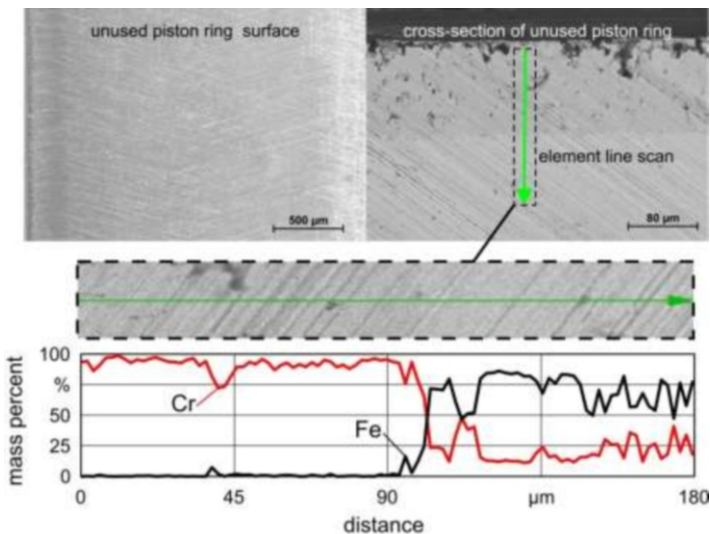


Figure 8-8: SEM images of the ring surface and element analysis

The surface of the ring provides a uniform smooth surface with traces of the surface treatment. On the basis of a cross-section, it can be seen that the ring is coated. An element line scan through the ring, from its edges towards its centre, indicates that the coating consists of chromium. Chrome plating is a method commonly used to increase the hardness and scuff resistance of piston rings [SCO75]. The following illustration shows the used top ring after scuffing of liner #10.

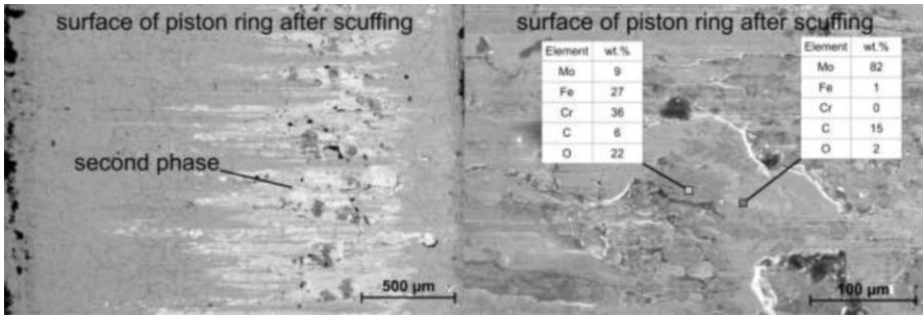


Figure 8-9: SEM images of a top ring after scuffing with elemental analysis

Even at low magnification, a second phase with a higher atomic mass can be seen on the ring surface. At higher magnifications, it can be seen that the second phase builds an irregular 'reef' on the piston ring. Element analysis of this reef shows that it is composed of the coating material FeCr13/Mo 50/50, which was applied to the liner. Presumably, this is the result of a friction weld between the chromium-containing friction partners. Under certain friction and hot-gas conditions, chromium can soften and therefore tends to scuff [SCO75]. In this case, the scuffing of the liners occurred on two sockets, which were honed by different manufacturers and with different surface quality; this leads to the conclusion that the surface quality is another factor which can influence the scuffing liability.

Due to this problem, an alternative to the chromium-plated rings was needed. Unfortunately, suitable piston rings matching the geometry of the piston grooves could not be found. Therefore, only three coated cylinder liners can be presented in this report.

Comparison between the reference liners: plateau and fine honed

Two types of reference liners were investigated: an original Mercedes-Benz liner with a rough, plateau honed surface ($R_z = 6 \mu\text{m}$) and a fine honed liner with a surface roughness less than $1 \mu\text{m}$ R_z . Figure 8-10 shows the determined friction loss (in terms of FMEP values) as the arithmetic mean of two samples for each liner type.

The higher surface roughness of the original liner leads to increased mixed friction areas, whereas - due to the smoother surface - the fine honed liner shows significantly less friction losses. When comparing the mean frictional benefit over all engine operation points, the fine honed liner shows about 8 % less FMEP compared to the original liner. In particular at low engine speeds, the frictional losses are reduced by 13 – 14 %. Because of the fine honed surface, lower oil retention properties and,

therefore, increased wear or possibly a piston seizure can be expected. However, no damages of the fine honed liners were observed during the entire project. The wear of the fine honed and microstructured liners could not be assessed by the engine tests. Nonetheless, the specific microstructuring of the fine honed surface was expected to provide increased oil retention properties and therefore less wear and tear even during longer testing periods.

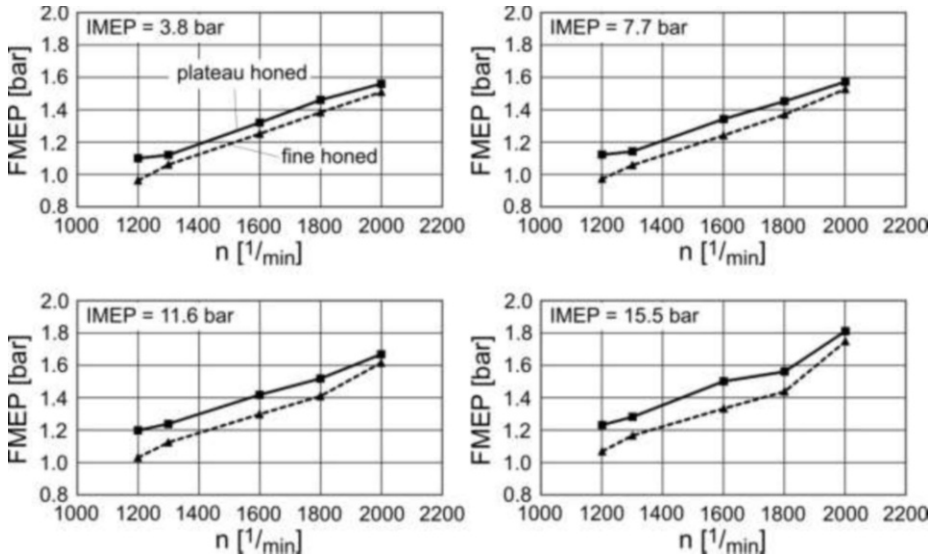


Figure 8-10: Friction loss (FEMP) of plateau honed compared to fine honed liner

Microstructures in dead centre areas

The piston dead centres and especially the Top Dead Centre (TDC) are the most stressed areas along the cylinder liner surface. There, the piston velocity is equal to zero, and consequently, the hydrodynamic pressure built-up collapses. Therefore, the piston rings cannot be completely separated from the liner surface by the lubricant, which leads to increased mixed friction effects. Due to the load of the cylinder pressure and the high temperatures from the burnt gases, the thermo-mechanical stress is considerably higher in TDC than in Bottom Dead Centre (BDC). On diesel engines, in particular, this leads to an increased liner wear at TDC.

Therefore, cylinder liners were manufactured with microstructures in TDC (liner #3) and in both dead centre areas (liner #7). It was expected that the microstructures would increase the oil retention capacity on the liner surface, leading to an increased hydrodynamic pressure built-up and, thus, to lower friction. The determined FMEP values, as shown in Figure 8-11, confirmed this theory. The liner with microstructures in the TDC area, in particular, showed the lowest frictional losses throughout the whole investigation. Compared to an original liner, the FMEP was up to 19 % lower at 1600 $1/min$ and 15.5 bar IMEP. FMEP also showed dependency on the engine speed:

the operation points with the lowest friction were at 1600 – 1800 $1/min$. There, the frictional losses were considerably lower even compared to the fine honed reference.

Compared to an original liner, cylinder liner #7, which was microstructured in both dead centre areas, showed reduced frictional losses as well. However, the benefit is lower than those of liner #3. At engine speeds ranging from 1600 – 2000 $1/min$, the determined FMEP values were on a similar level as the fine honed reference. At lower engine speeds, the frictional losses showed a slight increase.

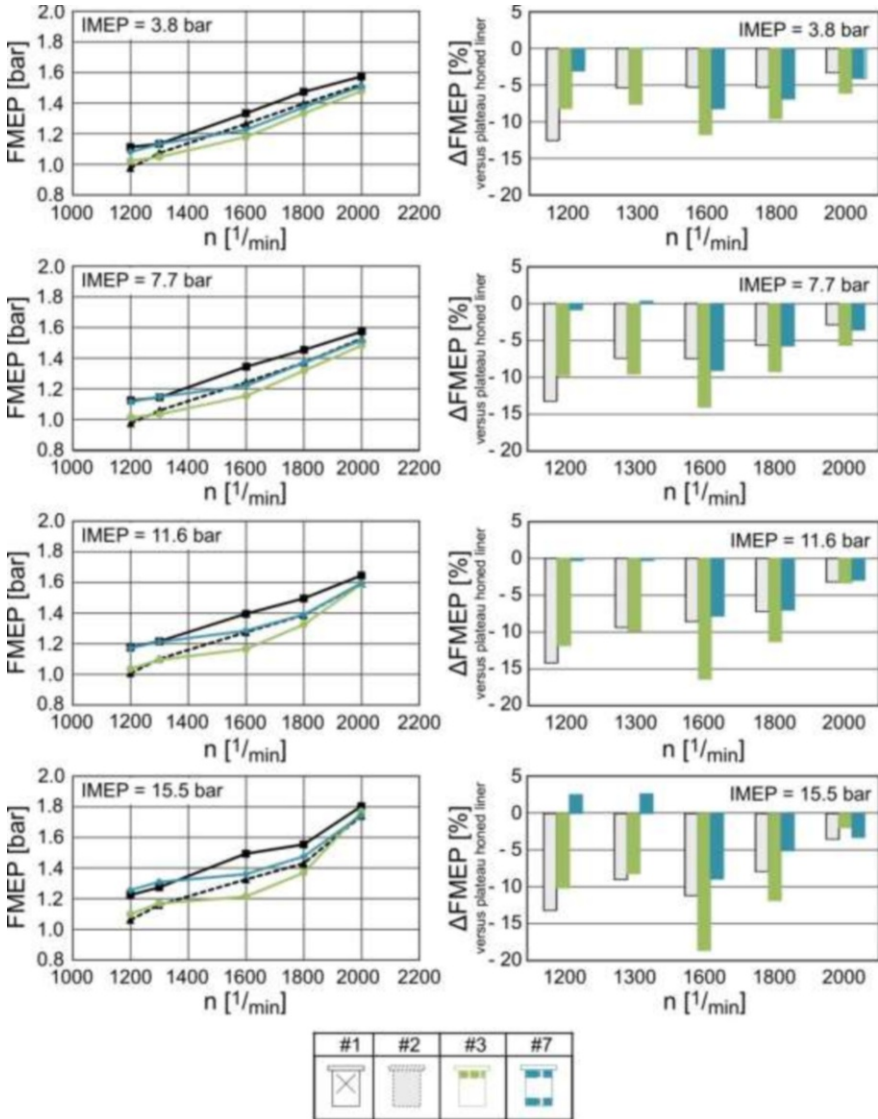


Figure 8-11: Effect of microstructures in TDC and BDC

The performed investigation shows that –as expected– microstructures in the dead centre areas of the cylinder liner lead to considerably lower frictional losses compared to those of an original liner. The frictional differences of the two liner types can be explained with the density of microstructures per area unit. The microstructures of liner #3 were manufactured with an axial distance $f = 0.3$ mm; their density is 40 % higher when compared to the one of liner #7. As a result, the oil retention capacity of the thermo-mechanical highly stressed TDC area is higher, which leads to lower frictional losses. Due to the fact that the microstructures act as a lubricant reservoir, it seems possible that the oil transport on the liner surface is also affected. However, if and to what extent this fact can be an explanation for the measured FMEP dependence on the engine speed could not be revealed during this project.

Microstructures in areas of hydrodynamic lubrication

Derived from the fundamentals of tribology, the Stribeck curve describes the coefficient of friction as a function of the relative velocity of two friction partners and the normal force. According to the Stribeck curve, an increase in relative velocity leads to a higher friction coefficient due to fluid friction. Regarding the tribology of the piston cylinder sleeve group, the piston velocity reaches its maximum in the middle part of the piston stroke. Thus, predominantly fluid friction can be expected in the middle part of the cylinder liner.

Experiments using a tribometer (see chapter 7.1) examined the above presented circumstances for cold boundary conditions. In order to investigate whether the same results can be achieved in a fired engine, a cylinder liner with microstructures in the hydrodynamic area was manufactured. In comparison to the reference liners, an increase in friction was expected due to the increasing engine speed, and therefore, due to the higher piston velocities.

The microstructures were manufactured with a very low axial distance of $f = 0.2$ mm in order to enhance the density of the microstructures per area unit, and thus, to increase the oil retention capacity of the surface. Figure 8-12 shows the determined FMEP values. As expected, the frictional losses show a significant dependency on the engine speed. At lower engine speed, the frictional losses are lower than those characteristic of the original liner. With an increase of the engine speed, the friction rises considerably. This effect can be noticed in all diagrams.

Moreover, in all engine operation points, liner #4 exhibits FMEP values higher than those of the fine honed reference. The investigation showed that –apart from a decrease– an increase of friction due to an enhancement of fluid friction is also possible.

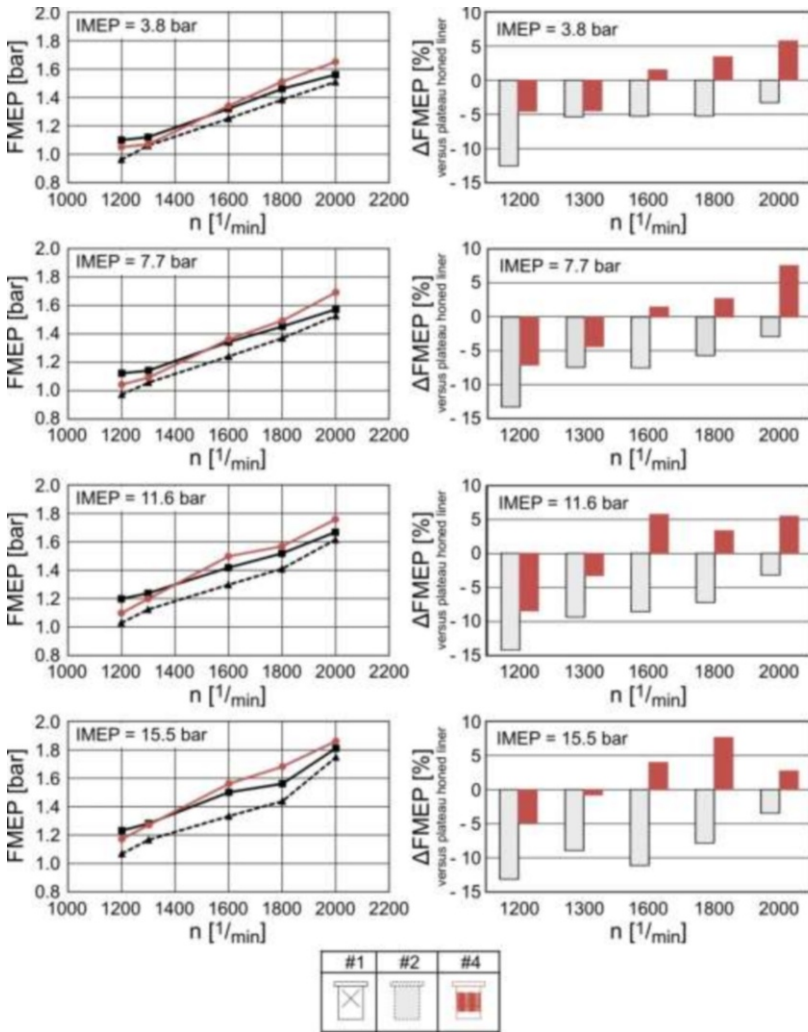


Figure 8-12: Effect of microstructures on hydrodynamic lubrication

Influence of the structure density on friction

It was expected that increasing the density of the microstructures would result in an increase of the friction loss due to the higher oil retention capacity in the hydrodynamic area of the line surface. Basically, liner #5 and #6 can be regarded as a combination of both variants “dead centre areas” and “hydrodynamic area”. Following the measurements described above, it was expected that increasing the density of the microstructures would increase the friction loss in the hydrodynamic range where the piston velocity is high. However, the measured values do not confirm this theory. Despite the increased density of its microstructures, liner #6 showed lower friction losses. Unfortunately it was not possible to carry out more tests in order to find satisfacto-

ry explanations for the measured trends during this project. Investigating this issue by means of additional tests would be a challenging further project.

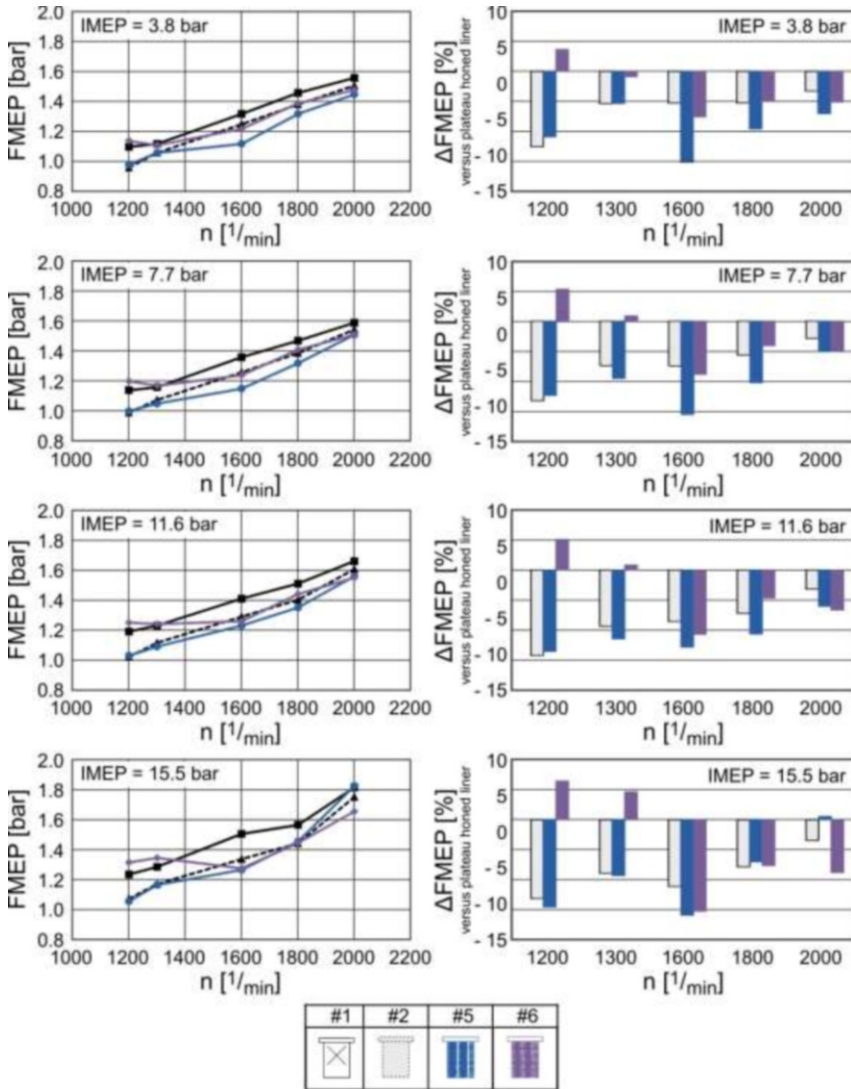


Figure 8-13: Influence of the structure density on friction

Thermal spray coatings

Figure 8-14 shows the results of the measured friction for five liners; three out of those five had coated surfaces (#8, #9, #10). Compared to the reference liner #1, the coated liner #8 shows reduced friction for low load and for lower engine speeds. The other two coated liners, #9 and #10, exhibit a similar trend as well. However, for higher load and speed, their friction is higher than that of reference #1. In some cas-

es, the friction of liner #9 was up to 10 % higher than that of the reference liner. It should be noted here that even before the engine tests, liner #9 showed some minor damage in form of radial grooves, possibly caused by the honing process which was carried out after the coating. It is likely that this damage induced the higher friction. The fine honed liner #2 was characterised by the lowest friction in nearly all measurement points.

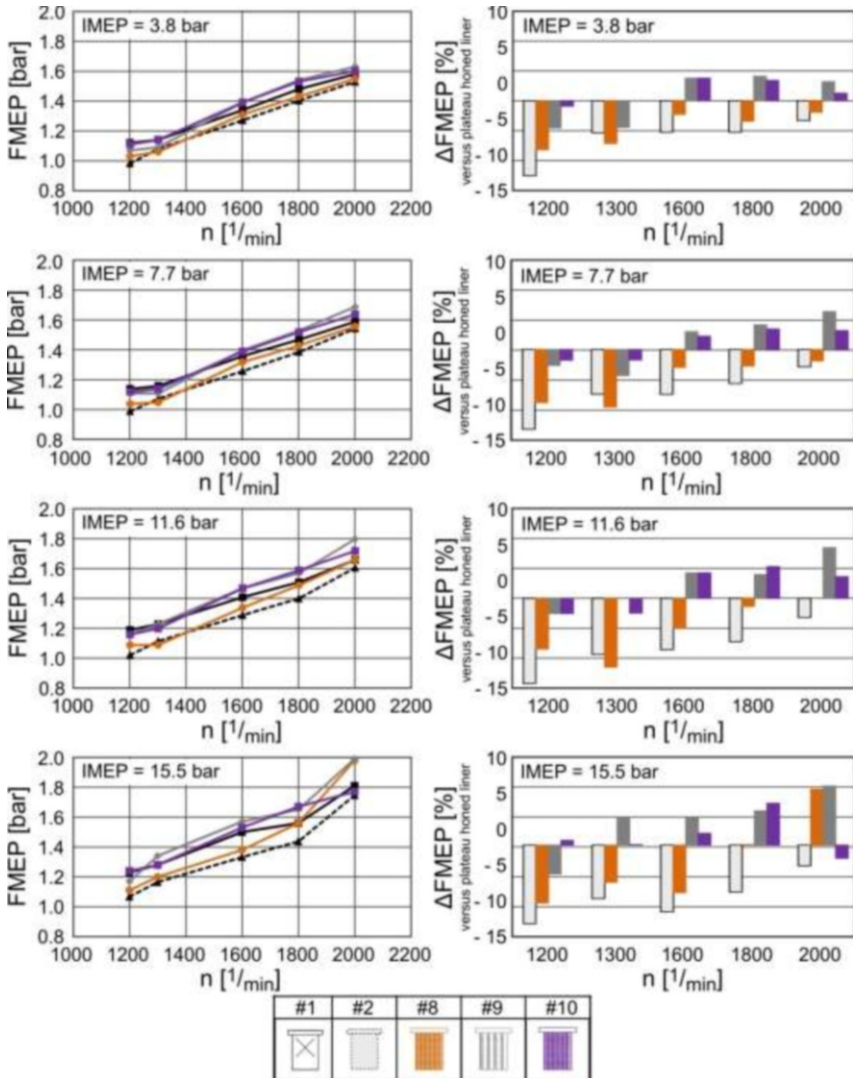


Figure 8-14: Friction of coated cylinder liner

A definite conclusion regarding the influence of the coating on the friction of liners #9 and #10 could not be made. On the one hand, the coated liners often showed dam-

ages: liner #9 was damaged even before the start of the engine tests, whereas liner #10 showed strong seizure problems during the later experiments (oil emission measurements). On the other hand, the coatings were applied to the whole surface of the liner. The above-described experiments with the microstructured liners show that the location of the structured surface can have both positive and negative effects on friction. Due to the high effort needed for the coating process and the difficulties experienced in the final honing stages, further –more detailed– experiments with the coated liners could not be conducted in course of this project.

The influence of the porosity could not be investigated due to the same reasons. Nonetheless, it can be expected that higher porosity of the liner surface, and correspondingly, increased amount of oil would lead to reduced friction, at least in the regions near the dead centres.

8.7 Results: oil emission

Additionally to the measurement of friction, a series of experiments was conducted to investigate the emissions resulting from the lubricating oil. Since microstructuring the surface results in an enhanced amount of oil in the structured part of the liner, it had to be investigated whether this would lead to an increased amount of unburned oil which results in hydrocarbons (HC) and particles (soot). As these emissions are limited by law, an investigation of the dependency of the liner surface on oil emissions is of high importance. A mass spectrometer as described above was used. Hereafter, the oil emissions are discussed for the liner shown in [Figure 8-15](#). No results can be shown for liner #10, as this liner experienced seizure problems during the measurements.

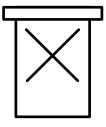
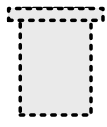

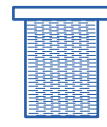


#	1	2	3	5	8	10
Symbol						
Details	plateau honed (reference)	fine honed (reference)	microstructure TDC $S_{axial} = 0.3 \text{ mm}$	microstructure entirely $S_{axial} = 1 \text{ mm}$	coated fine honed porosity=9.4%	coated fine honed porosity=6.4%

Figure 8-15: Overview of the tested liners regarding oil emissions

[Figure 8-16](#) shows the oil emission measurement results for the lower load conditions. The highest oil emission values are found for the plateau honed series production liner (#1). The oil emissions of this liner depend strongly on the engine speed as well. The fine honed liner (as a second reference) shows significantly lower oil emission, with a reduction factor up to 9. This may be attributed to its surface which is much smoother than that of the plateau honed liner. The microstructured liners show a somewhat higher oil emission than the fine honed liner. However, even their oil emissions are much lower than those of the series production liner.

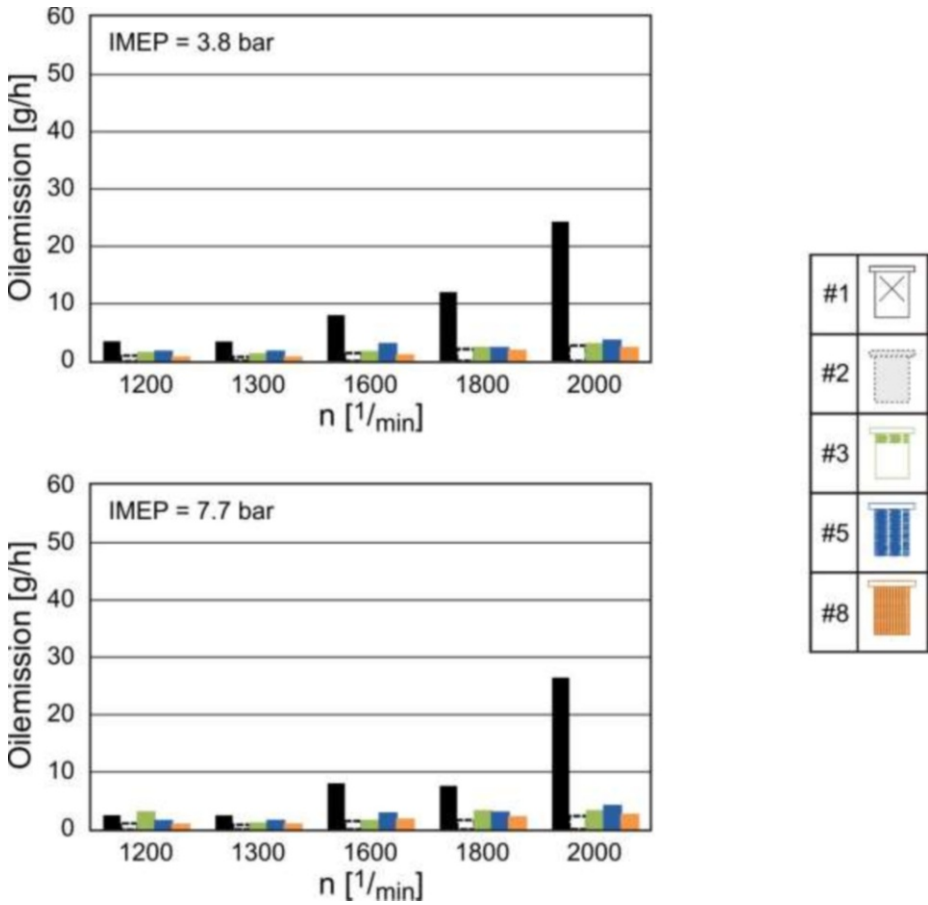


Figure 8-16: Oil emission in relation of liner surface at low engine load

Figure 8-17 shows oil emissions measured for higher load. Here, the oil emissions of the microstructured liners were partly higher compared to the plateau honed series liner. The completely structured liner (#5) exhibits higher oil emission at low engine speeds; consequently, the amount of oil on the liner structure is even higher and leads to enhanced oil emissions. The same applies to the partly structured liner (#3) for high engine speed. No measurement values are available for liners #5 and #8 for the operation points with 2000 1/min, as the measurement system failed to measure here.

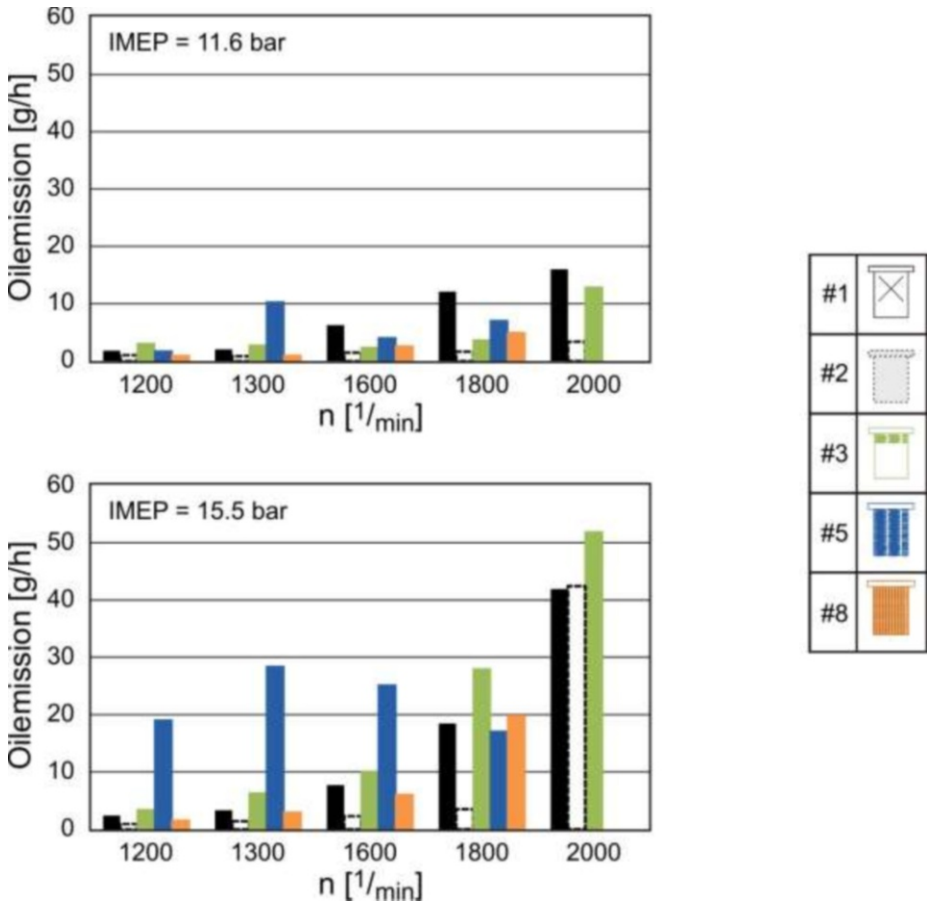


Figure 8-17: Oil emission in relation of liner surface at high engine load

In summary, the oil consumption level is still in the range of the series production liner and not far outside of it. The measurements suggest that oil emissions are not significantly enhanced by the microstructures. For lower loads, emissions are significantly reduced; for high loads, the emissions are to some extent higher than the reference values, but the amount is not outstanding. So far, compared to the series production liner, the oil emission does not seem to be influenced the microstructured liner systems significantly.

8.8 Conclusion

During the course of this project, microstructured cylinder liners were investigated under fired conditions within a single cylinder research engine. To measure the mechanical friction loss, the indication method was applied. Thus, the difference of the Indicated Mean Effective Pressure inside the cylinder and the Brake Mean Effective Pressure at the output shaft was determined. In extensive pilot tests, the measure-

ment technique was validated. It was shown that the discrepancies between different similarly produced liners and the influence of mounting were negligibly low and that the repeatability for the same operation conditions was good. With the help of a measurement model, the maximum measurement error was estimated at ± 0.03 bar (2σ) FEMP. All measurements in the fired engine were performed within a wide range of the engine operation map. The cooling water as well as the oil circuit of the engine was conditioned to hold defined temperatures on a constant level in order to provide constant boundary conditions. The engine oil and the piston rings were changed before each measurement of a new liner. Each liner was operated according to the same defined operation program (7 h running-in program and 3 h measurement).

As a reference, liner from series production (with rather rough plateau honed surface and a R_z -value of $6 \mu\text{m}$) was used. Additionally, a fine honed liner (R_z -value $< 1 \mu\text{m}$) was taken as second reference, as the microstructured liners were based on such fine honed surfaces. For both types of reference, three liners were compared. Two of each gave consistently repeatable results concerning the friction losses while one of each reference liner showed significant deviations. These liners were marked as outliers and not taken into consideration during the further investigation. The fine honed liner showed 8 % less friction than the liner from series production.

Two types of micro structures were investigated: machined microstructures and coated surfaces with microstructuring through a defined porosity of the surface.

In the case of the machined microstructured liners, a variation of the structures was investigated; previous measurements on a tribometer as well as numerical simulations found this variation most promising. Here, a relatively small depth of the microstructures of typically $7 \mu\text{m}$ and distances between the structure lines in the range of 0.2 and 1 mm was selected. A variation of this distance on liners with microstructures along the whole liner surface could not provide a clear answer to the question which distance gives the best results. Possibly, different concurrent tribological effects overlap in this case, as both mixed friction and hydrodynamic friction regimes are concerned. Furthermore, liners where the microstructures were applied only to the dead centre areas where investigated. It can be noticed that structures in the region of the Top Dead Centre of the piston resulted in a significant reduction of the friction losses for a wide range of operation points. Compared to liner from series production, the Friction Mean Effective Pressure could be reduced by a maximum of 19 %. The microstructures provide potentially the retention of the lubricant oil, which is an important parameter influencing the practical application. Microstructures near the dead centre seem suited for the tribological conditions characteristic of this area, e.g., low speed of the piston and mixed friction due to displacement of the oil film. The found improvement of the tribological friction properties was so far in agreement with expectation. For further validation of the hypothesis, microstructures were also arranged in the middle part of the liner where the piston velocity is higher and where the hydrodynamic friction exhibits correspondingly greater significance. Based on the

Stribeck curves, it was expected here that, analogous to the cold tribological experiments, the friction would increase if the amount of oil situated in this region increased. Indeed, the experiments validated this expectation.

For the coated microstructured surface of cylinder liners (produced by IW), the friction measurement was only partly possible. In some case, technological problems resulting from the processing, led to piston seizure problems during the engine tests; thus, no detailed answer concerning the effects on the friction could be discerned so far. A detailed analysis showed that, in some cases, the final honing procedure taking place after the coating process destroyed the coating, or at least, seriously damaged the structure. Moreover, seizures between the components of the coating material and the compression rings (chrome components) were identified as the underlying cause for some of the problems. Nonetheless, compared to liner from series production, at least in some of these measurements showed a potential for friction reduction. Thus, further research should focus on the technological problems as well as on the optimal combination of materials in the liner structure and on the piston rings in order to provide good tribological results.

Microstructures in the cylinder liner surface were expected to modify the amount of oil and the oil film distribution on the liner. Therefore, it was suspected that structured liners may lead to enhanced oil emissions. Thus, the emissions caused by unburned oil were measured by means of a mass spectrometer, in cooperation with the Institut für Messtechnik from TU Hamburg-Harburg. These measurements detected the long chained hydrocarbons resulting from unburned oil in the exhaust section of the engine. Against expectations, it was found out that all investigated microstructured liners exhibited significantly lower oil emission than the plateau honed liner from series production for the low and medium load cases and only slightly enhanced oil emission for highest load.

It can be concluded that the realisation of this subproject was essentially successful. The operational effort was high, as the tribological investigations under fired engine conditions required careful procedure planning to reduce the influence of parasitic effects and ensure the measurement of the friction effect of the liners. Nevertheless, these measurements conducted under realistic fired engine conditions are of significant importance for the determination of the application potential of microstructured cylinder liners in internal combustion engines.

9 Own publications

- [BAC07] Bach, Fr.-W.; Möhwald, K.; Drößler, B.: Thermally Sprayed Coatings with Stochastic Microstructure for Improved Lubricant Retention. 6th International conference, Hannover, October 25th-26th 2007, p. 317-322, 2007
- [BAC08] Bach, Fr.-W.; Möhwald, K.; Drößler, B.: Thermally Sprayed Coatings with Stochastic Microstructures for Thermomechanically High Stressed Surfaces. International Thermal Spray Conference and Exposition (ITSC), Maastricht (Netherlands), June 2nd-4th, 2008
- [BRA10] Brand, S.: Tribologische Charakterisierung deterministischer Oberflächen mittels des Lattice-Boltzmann-Verfahrens und Simulation der Ölemission von Verbrennungsmotoren unter Berücksichtigung der Schmierölformulierung. Dr.-Ing. Dissertation, Universität Kassel, 2010
- [DEN07a] Denkena, B.; Reichstein, M.; Kästner, J.: Micro Structuring of Functional Surfaces via Cutting Processes. 7th euspen conference, Bremen, Band 1, May 20th-24th 2007, p. 123-126, 2007
- [DEN07b] Denkena, B.; Reichstein, M.; Kästner, J.: Spanende Mikrostrukturierung duktiler Werkstoffe. Jahrbuch Schleifen, Honen, Läppen und Polieren. Herausgeber Hans-Werner Hoffmeister, Berend Denkena, 63. Ausgabe, p. 245-254, 2007
- [DEN07c] Denkena, B.; Kramer, N.; Siegel, F.; Kästner, J.: Leistungsoptimierung an der Schneidkante, VDI-Z, 2. Ausgabe, p. 24-26, 2007
- [DEN08a] Denkena, B., Boehnke, D., Kästner, J.: Microstructuring of functional surfaces by means of cutting processes. Production Engineering - Research and Development (WGP), Ausgabe 2, p. 21-25, 2008
- [DEN08b] Denkena, B., Boehnke, D., Kästner, J.: Investigation of Chip Formation during Microstructuring by Means of Cutting. 10th anniversary international conference of the european society for precision engineering and nanotechnology (euspen), Band 2, Zürich (Switzerland), May 18th-22nd 2008, p. 134-137, 2008
- [DEN08c] Denkena, B.; Boehnke, D.; Kästner, J.: Surface Functionalization Using Piezo-Driven Tools. 1st International Symposium of the Volkswagen Foundation on Functional Surfaces, Bremen, June 18th - 19th, 2008
- [DEN08d] Denkena, B.; Knoll, G.; Bach, F.; Reithmeier, E.; Kästner, J.; Brandt, S.; Drößler, B.; Bretschneider, M.: Mikrostrukturierung funktionaler Oberflächen, wt Werkstatttechnik online, Heft 6, p. 486-494, 2008

- [DEN09c] Denkena, B.; de Leon, L.; Kästner, J.: Burr Formation in Microstructuring Processes. Conference on Burrs, Kaiserslautern, April 2nd-3rd, 2009
- [DEN10a] Denkena, B.; Kästner, J.; Wang, B.: Advanced Microstructures and its Production through Cutting and Grinding. CIRP – General Assembly, Ausgabe 59 (1), p. 67-72, 2010
- [DEN10b] Denkena, B.; de Leon, L.; Kästner, J.: Precise Machining of Micro Dimples in Large Scale Areas, 10th euspens conference, Band 2, Delft (Holland), May 31st - June 6st 2010, p. 111-115, 2010
- [DEN12] Denkena, B.; Köhler, J.; Kästner, J.: Efficient Machining of Micro Dimples for Friction Reduction. 7th International Conference on Micro-manufacturing, Illinois USA, March 12nd-14th, 2012
- [DEN13] Denkena, B.; Köhler, J.; Kästner, J.; Götttsching, T.; Dinkelacker, F.; Ulmer, H.: Efficient Machining of Micro-dimples for Friction Reduction, ASME Journal of Micro and Nano-Manufacturing, **in press**
- [KNO08b] Knoll, G.; Brandt, S.; Schlerenge, F.; Umbach, S.: Berechnung der Reibungszustände an Kolbenringen. Gesellschaft für Tribologie e.V., Tagungsband Tribologie Fachtagung, p. 60-71, 2008
- [REI08] Reithmeier, E.; Fahlbusch, T.; Bretschneider, M.; Püschmann, D.: Chromatische Punktsensoren in der Kontur- und Oberflächenmesstechnik. 109. Jahrestagung der Deutschen Gesellschaft für angewandte Optik, Esslingen a. N., May 13th-17th, 2008
- [REI09a] Reithmeier, E.; Kästner, M.; Bretschneider, M.: Metrology and Characterisation of Microstructures made by Cutting Processes, 9. International euspens Conference, San Sebastian, July 2nd-5th, 2009
- [REI09b] Reithmeier, E.; Kästner, M.; Bretschneider, M.: Metrology and Characterisation of Thermal Sprayed Coatings. 12th International Conference on Metrology and Properties of Engineering Surfaces, Rzeszow, July 8th-10th, 2009
- [REI11] Hübsch, C.; Erne, M.; Möhwald, K.; Bach, Fr.-W.; Bretschneider, M.; Kästner, M.; Reithmeier, E.: Optische Oberflächencharakterisierung von plasmagespritzten stochastischen Strukturen. Materialwissenschaft und Werkstofftechnik, Ausgabe 42 (6), p. 519-530, 2011
- [REI12] Abo-Namous, O.; Kästner, M.; Reithmeier, E.: Feature recognition in 2D-images using 3D-thinning methods. Optimess, Antwerpen (Belgien), April 4th-5th, 2012

- [ULM12] Ulmer, H.; Dinkelacker, F.; Kästner, J.; Denkena, B.: Tribologische Optimierung von Zylinderlaufbuchsen durch spanend eingebrachte Mikroschmieraschen. Tribologie Fachtagung Göttingen, September 25th - 26th, 2012
- [ULM13] Ulmer, H.; Dinkelacker, F.; Kästner, J.; Denkena, B., Hübsch, Ch.; Bach, F-W.: Investigation of Microstructured Cylinder Liner Surfaces for Friction Reduction. 13th CIMAC Congress, Shanghai (China) May 13th-16th, 2013, **in press**

10 Quoted literature

- [ABD74] Abdelmoneim, M. Es., Scrutton, R.F.: Tool Edge Roundness and Stable Build-Up Formation in Finish Machining, Transaction of the ASME, p. 1258-1267, 1974
- [ABE06] Abeln, T.: Reibungsminimierung durch Laseroberflächenstrukturierung im Motorenbau. 3. VDI Fachtagung "Zylinderlaufbahn. Kolben, Pleul", Böblingen, 7.-8.3. 2006
- [AHN97] Ahn, J-H.; Lim, H.S.; Dornfeld, D.A.: Burr and Shape Disortion in Microgrooving of Optical Components. Proceedings of the 11th ASPE Annual Meeting, Monterey (California), p. 496-499, 1996
- [ALB60] Albrecht, P.: New developments in the theory of the metal cutting process - Part I: The ploughing process in metal cutting. ASME - Journal of Engineering and Industry, 81, p. 348-358, 1960
- [BAR05] Barbezat, G.: Advanced thermal spray technology and coating for light-weight engine blocks for the automotive industry, Surface and Coatings Technology 200, p. 1990 – 1993, 2005
- [BEN02] Ben Amor, R.: Thermomechanische Wirkmechanismen und Spanbildung bei der Hochgeschwindigkeitszerspanung. Dr.-Ing. Dissertation, Universität Hannover, 2002
- [BIC12] Bichmann S.; Depiereux, F.; König, N.: „Rauheitsmesstechnik zu Automatisierten 100-Prozent-Prüfung - Berührungslos durch Berg und Tal“, QZ 57, p.54-56, 2012
- [BOD98] Bodschnwinna, H.: Beurteilung und Optimierung technischer Funktionsflächen, Habilitation, Universität Hannover, 1998.
- [BRE04] Brecher, C.; Wenzel, C.; Wolf, F.: Großflächige Mikrostrukturierung optischer Oberflächen. Photonik, 5, p. 48-51, 2004
- [BRI02] Brinkmann, S.: Funktionsorientierte Beurteilung von Zylinderlaufflächen durch 3-dimensionale Oberflächenmesstechnik, Dissertation, Universität Hannover, Dissertation, 2002
- [BRI07] Brinksmeier, E.; Gläbe, R.; Flucke, C.: Manufacturing of molds for the replication of prismatic microstructures by a novel diamond cutting process, Industrial Diamond Review, 1/07, p. 25-30, 2007
- [BRO04] Brotka, K. : Aus der Forschung in die Praxis. In: Quality Engineering 9 p. 16-18, 2004
- [COS09] Costa; H.L.; Hutchings, I.M.: Development of maskless electrochemical texturing method. Journal of Machining Processing Technology, p. 3869-3878, 2009

- [CZI10] Czichos, H. and Habig, K.-H.: Tribologie-Hanbuch: Tribometrie Tribomaterialien, Tribotechnik, Springer Fachmedien, Wiesbaden, 2010
- [DER94] Derstroff, B.: Spanungsgeometrie und Zerspankräfte beim achsparallelen Drehfräsen. Dr.-Ing. Dissertation, Technische Hochschule Darmstadt, 1994
- [DES12] <https://www.destatis.de/DE/ZahlenFakten/Wirtschaftsbereiche/TransportVerkehr/UnternehmenInfrastrukturFahrzeugbestand/Tabellen/Fahrzeugbestand.html>, last visit May 2012
- [DEU10] Deuss, T.; Enhis, H.; Freier, R.; Künzel, R.: Reibleistungsmessung am befeuerten Dieselmotor. Potentiale der Kolbengruppe. Motorentechische Zeitschrift, 71/5, p. 326-330, 2010
- [DON95b] Dong, W. P., Davis E. J., Butler, D. L., Stout, K. J.: Topographic features of cylinder liners - an application of three – dimensional techniques, Tribology International, Band 28, Heft 7, 1995
- [ETS04] Etsion, I.; Halperin, V.; Brizmer, V; Kligermann, Y.: Experimental Investigation of laser surface textured parallel thrust bearings. Tribology Letters, 17/2, S. 295-300, 2004
- [ETS05] Etsion, I.: State of the Art in Laser Surface Texturing. Journal of Tribology, 127, p. 248-253, 2005
- [ETS09] Etsion, I; Shinkarevko, A; Kligermann, Y: The effect of surface texturing in soft elasto-hydrodynamic lubrication. Tribology International, 42, p. 284-292, 2009
- [ETS99a] Etsion, I.; Kligermann, Y.; Halperin, G.: Analytical and Experimental Investigation of Laser-Textured Mechanical Seal Faces. Tribology Transactions, 42, p. 511-516; 1999
- [ETS99b] Etsion, I; Sher, E: Improving fuel efficiency with laser surface textured piston rings. Tribology International, 42, p. 542-547, 2009
- [FLO03] Flor, Stephan: Beitrag zum Verschleißverhalten von plasmagespritzten Zylinderlaufflächen im Diesel Motorenbetrieb. Dr.-Ing. Dissertation, Universität Hannover, 2003
- [FLO11] Flores, G.: Prozesskette zur Herstellung thermisch beschichteter Zylinderbohrungen, Thermal Spray Bulletin 1, p. 35-39, 2011
- [FLO85] Flores, G.: Plateauhohlen von Kolbenlaufbahnen. Motortechnische Zeitschrift, 46/1, 1985
- [GAH81] zum Gahr, K. Z.: Abrasiver Verschleiß metallischer Werkstoffe, Fortschrittsberichte der VDI - Reihe Grund- und Werkstoffe, p. 35 et seq., 1981

- [GLA04] Gläbe, R.: Prozess- und Schneidstoffentwicklung zur ultrapräzisen Bearbeitung von Stahl, Dr.-Ing. Dissertation, Universität Bremen, 2004
- [GOL04] Golloch, R; Merker; G.P.; Kessen, U; Brinkmann, S.: Benefits of Laser-Structured Cylinder Liners for Internal Combustion Engines. 14th International Colloquium Tribology - Tribology and Lubricants Engineering, Technische Akademie Esslingen, January 13th-15th, 2004
- [GRU97] Gruber, H.-P.: Komponenten für μ -Systeme durch die μ -EDM. Tagungsband Micro-Engineering, Stuttgart, 1997
- [HEU07] Heuberger, A.: Neue Werkstoffe und Oberflächengestaltung bei Zylinderlaufbahnen zur Absenkung der Reibung der Kolbengruppe bei Verbrennungsmotoren. Dr.-Ing. Dissertation, Universität Kassel, 2007
- [HIR07] Hirt, G; Thome, M: Large Area Rolling of Functional Metallic Micro Structures. Production Engineering - Research and Development, 1/4, p. 351-356, 2007
- [KLO07] Klocke, F.; Feldhaus, B; Hirt, G.; Thome, M.; Klumpp, S.; Schröder, W.: Development of Two Innovative Rolling Processes for the Production of Defined Riblet Structures in Consideration of Common Fluid Dynamic Requirements. ICNFT, International Conference on new Forming Technology, Bremen, p. 185-194, 2007
- [KNO01] Knoll, G.; Lechtape-Grüter, R.: Ölverbrauchssimulation – Rechnerische Simulation der Ölverbrauchs- und Öltransportwege im Bereich Kolben-Kolbenring-Zylinderwand; FVV-Abschlussbericht zum Vorhaben Nr. 646, Heft 707, 2001
- [KNO06] Knoll, G.; Matz, G.; Thiemann, W.; v. Hollen, P.; Krause, S.; Schlerege, F.: Ölverdampfung; FVV-Forschungsheft 873, 2006
- [KNO08] Knoll, G.; Matz, G.; Thiemann, W.; v. Hollen, P.; Krause, S.; Schlerege, F.; Brandt, S.: Ölverdampfung im Brennraum von Verbrennungsmotoren, Messung und Modellierung; FVV-Zwischenbericht Heft R 541, Frühjahrstagung, Frankfurt, p. 263-299, 2008
- [KNO92] Peeken, H.; Knoll, G.; Lechtape-Grüter, R.: Kolbenringreibung I, FVV-Forschungsheft 502, 1992 und 513, 1993
- [KNO94] Knoll, G.; Lechtape-Grüter, R.: Kolbenringreibung II; FVV-Forschungsheft 570-1, 1994 und 570-2, 1995
- [KRA09] Krause, S.: Massenspektrometrisches Verfahren zur Charakterisierung der Ölverdampfung im Brennraum von Ottomotoren, Dr.-Ing. Dissertation, Technische Universität Hamburg-Harburg, 2009
- [KRO69] Kronenberg, M.: Grundzüge der Zerspanungslehre – Mehrschneidige Zerspanung (Umfangsfräsen, Räumen), Band 3, Springer Verlag, 1969

- [KRY04] Krystek, M.: Morphological filters in surface texture analysis. In: Proceedings of the XI. International Colloquium on Surfaces-Part I, Aachen: Shaker, 2004
- [LAG00] Lagemann, V.; Numerische Verfahren zur tribologischen Charakterisierung bearbeitungsbedingter rauher Oberflächen bei Mikrohydrodynamik und Mischreibung, Universität Kassel, Dissertation, 2000
- [LAN87] Lankford, J., Wei W. and Kossowsky R.: Friction and wear behavior of ion beam modified ceramics, Journal of Materials Science 22, p. 2069-2078, 1987
- [LEE90] Lee, M and Flom D.G.: Hardness of Polycrystalline Tungsten and Molybdenum Oxides at Elevated Temperatures, Journal of the American Ceramic Society 73 [7], p. 2117-2118, 1990
- [MAS89] Masaki, T.: Micro-Electro-Discharge-Machining. Proceedings of the International Symposium for Electro-Machining, Nagoya, Japan, the Japan Society of Electrical-Machining Engineers, p. 26-29, 1989
- [MOK82] Mokhtar, M.O.A.: The effect of hardness on the frictional behavior of metals, Wear 78, p. 297-304, 1982
- [NIR10] Niranatlumpong P. and Koiprasert H.: The effect of Mo content in plasma-sprayed Mo-NiCrBSi coating on the tribological behavior, Surface and Coatings Technology 205, p. 483-489, 2010
- [OFE07] Ofen, R.: 3-D-Erfassung von Radien und Kanten an Werkzeugen und Bauteilen. In: Optische Messung technischer Oberflächen in der Praxis – Bestimmung von Geometrie und Topographie, VDI-Gesellschaft Mess- und Automatisierungstechnik, (VDI-Berichte Nr. 1996), p. 53-68, 2007
- [ORE79] Oversm, M.P., Harris S.J. and Waterhouse R.B.: The Fretting Wear of Sprayed Molybdenum Coatings at Temperatures up to 300 C, Wear of Materials, in: K.C. Ludema, W.A. Glaeser, S.K. Rhee (Editors), ASME, New York, p. 379-387, 1979
- [PAT78] Patir, N. und Cheng H.S.: An Average Flow Model for Determining Effects of Three-Dimensional Roughness on Partial Hydrodynamic Lubrication, Journal of Lubrication Technology, 100 (1978), p. 12-17, 1978
- [PET05] Pettersson, U.; Jacobson, S.: Tribological texturing of steel surfaces with a novel diamond embossing tool technique. Tribology International, 39/7, p. 695-700, 2005
- [RIE95] Rienäcker, A.: Instationäre Elastohydrodynamik von Gleitlagern mit rauhen Oberflächen und inverse Bestimmung der Warmkonturen, Universität Kassel, Dissertation, 1995

- [SCH02] Schwenke, H.; Neuschaefer-Rube, U.; Pfeifer, T.; Kunzmann, H. : Optical methods for dimensional metrology in production engineering. In : Annals of the CIRP 51, p. 199-207, 2002
- [SCH07] Schmitt, J.: Praktischer Einsatz der optischen Messtechnik zur Beurteilung der Haptik von Oberflächen. In: Optische Messung technischer Oberflächen in der Praxis – Bestimmung von Geometrie und Topographie, VDI-Gesellschaft Mess- und Automatisierungstechnik, (VDI-Berichte Nr. 1996), p. 35-44, 2007
- [SCH11] Schommers, J.; Weller, R.; Böttcher, M.; Ruisinger, W.: Downsizing beim Dieselmotor. Motorentechnische Zeitschrift, 72/2, p. 100-105, 2011
- [SCO75] Scott, D., Smith, A.I., Tait, J. and Tremain, G.R.: Materials and Metallurgical aspects of piston ring scuffing - a literature survey, Wear 33, p. 293-315, 1975
- [SIE09] Siegel, F.; Klug, U.; Kling, R.: Extensive Micro-Structuring of Metals using Picosecond Pulses – Ablation Behavior and Industrial Relevance. Journal of Laser Micro/Nanoengineering, 4/2, p. 104-110, 2009
- [STÖ08] Stöver, M.; Wintermantel, E.: Oberflächenstrukturierung metallischer Werkstoffe. Medizintechnik – Life Science Engineering, Springer DOI: 10.107/978-3-540-74925-7, p. 769-775, 2008
- [STO93] Stout, K.J, Sullivan, P.J., Mainsah, E., Mou, N., Mathia, T., Zahouani, H.: The Development of Methods for the Characterisation of Roughness in Three Dimensions, European Commission, Report EUR 15178 EN, Brüssel, 1993
- [STR02] Stribeck, R.: Die wesentlichen Eigenschaften der Gleit- und Rollenlager, Z. Verein. Deut. Ing. Vol. 46, p. 38 et seq., p. 1341-1348, 1902
- [SZE06] Szeliski, R.: Image Alignment and Stitching: A Tutorial p. 22 et seq., 2006
- [TAG86] Taguchi, G.: Introduction to Quality Engineering, Asian Productivity Organisation, Tokyo, 1986
- [TOE11] Tönshoff, H.K.: Spanen Grundlagen, Springer Verlag, 2011
- [TOM08] Tomanik, E.: Friction and wear bench tests of different engine liner surface finishes. Tribology International 41, p. 1032-1038, 2008
- [UHL06] Uhlmann, E.; Piltz, S.; Doll, U.: Funkenerosion in der Mikrotechnik. Einsatzgebiete und Verfahrensgrenzen. Werkstatttechnik wt-online, 12, p. 733-737, 2004
- [UMW12] <http://www.umweltbundesamt-daten-zur-umwelt.de/umweltdaten/public>, last visit: May 2012

- [VEN09] Venci A., Mrdak M. and Banjac M.: Correlation of Microstructures and Tribological Properties of Ferrous Coatings Deposited by Atmospheric Plasma Spraying on Al-Si Cast Alloy Substrate, *Metallurgical and Materials Transactions A* 40A, p. 398-405, 2009
- [VIN91] Vincent, L. ; Soille, P. : Watersheds in digital spaces: an efficient algorithm based on immersion simulations, *IEEE Transactions on Pattern Analysis and Machine Intelligence* 13, Nr. 6, p. 583–598, 1991
- [VOL05] Volk, R.: *Rauheitsmessung – Theorie und Praxis*. DIN – Beuth Verlag Berlin Köln, 2005
- [WAN03] Wang, X.; Kato, K.; Adachi, K.; Aizawa, K.: Loads carrying capacity map for the surface texture design of SiC thrust bearing sliding in water, *Tribology International*, 36/3, p.189– 97, 2003
- [WAN04] Wang, X.; Kato, K; Adachi, K.: The critical condition for the transition from HL to ML in water-lubricated SiC. *Tribology Letters* 16/4, p. 253-258, 2004
- [WEI06] Weidner, A.: *Strukturorientierte dreidimensionale Rauheitsmesstechnik von optisch vermessenen Zylinderlaufbahnen*, Dissertation, Universität Hannover, 2006
- [XIN09] Xin, B.: *Auswertung und Charakterisierung dreidimensionaler Messdaten technischer Oberflächen mit Riefenstruktur*, Universität Karlsruhe, Dissertation, 2009